



Provided by the author(s) and University of Galway in accordance with publisher policies. Please cite the published version when available.

Title	Experimental Investigation of the Response of Osteoblasts to Static and Dynamic Loading using a Modified Atomic Force Microscope
Author(s)	Weafer, Paul
Publication Date	2013-02-07
Item record	<a href="http://hdl.handle.net/10379/3590">http://hdl.handle.net/10379/3590</a>

Downloaded 2024-04-27T01:28:04Z

Some rights reserved. For more information, please see the item record link above.



Experimental Investigation of the Response of Osteoblasts to  
Static and Dynamic Loading using a Modified Atomic Force  
Microscope

*by*

Paul Weafer, B.E.

A thesis submitted to the National University of Ireland as fulfilment  
of the requirements for the Degree of Doctor of Philosophy



Department of Mechanical and Biomedical Engineering  
National University of Ireland, Galway

2012

Supervisor of Research: Dr. J. P. McGarry

Co-Supervisor: Prof. S. P. Jarvis (University College Dublin)

# Abstract

Cells and tissues continuously experience mechanical loading during daily activity. However, the mechanisms by which cells respond to mechanical stimuli are poorly understood. The focus of this thesis is to develop atomic force microscopy (AFM) techniques to investigate whole cell mechanics over physiologically relevant time scales, providing an in-depth understanding of the role of the actin cytoskeleton in osteoblast biomechanics. The work presented in this thesis can be divided into two categories: instrument development, and experimental cell biomechanics.

In terms of instrument development, the first key contribution of this thesis is the adaptation of a standard AFM to apply high precision mechanical loading at the whole cell level. Correction factors for AFM force and indentation measurements are developed, for the first time, to account for constraints imposed on AFM cantilever bending due to the attachment of a sphere at the cantilever's free-end. It is demonstrated that uncorrected force-indentation data may result in a dramatic ~18 fold underestimation of a sample's elastic modulus.

Using this modified AFM cantilever, high precision whole cell monotonic compression is applied to osteoblasts. It is found that the actin cytoskeleton contributes significantly (~40-60%) to the whole cell compression force. Additionally it is shown that the actively generated contractility of the actin cytoskeleton has a pronounced influence on cell and nucleus morphology.

The second key contribution in terms of instrument development is the stability enhancement of a standard AFM system to achieve accurate displacement control over long time scales. The methodology developed in this thesis for the reduction of thermal drift provides a significant 17-fold enhancement in z-drift stability. Furthermore, a customised fluid cell setup is developed to eliminate liquid instabilities during long term cell mechanics experiments.

This enhanced AFM system is used to implement cyclic single cell deformation, with a constant loading and unloading strain rate being applied to the cell. The range of applied deformation is altered during the experiment without altering the strain rate. It is demonstrated that steady state cell forces are largely unaffected by this change in deformation range. This phenomenon is not observed for non-contractile passive cells; measured forces for cells treated with cyto-D are found to be highly dependent on the applied deformation range.

# Table of Contents

Acknowledgements .....	vi
<b>Introduction.....</b>	<b>1</b>
1.1 Background and Motivation .....	2
1.2 Objectives of this Thesis.....	3
1.3 Thesis Overview .....	4
1.4 References .....	7
<b>Background and Related Work.....</b>	<b>9</b>
2.1 Introduction .....	10
2.2 Cell Structure.....	11
2.3 Cellular Response to Mechanical Stimulation.....	17
2.4 Experimental Techniques to Investigate Cell Mechanics.....	20
2.4.1 <i>Micropipette Aspiration</i> .....	21
2.4.2 <i>Substrate Stretching</i> .....	23
2.4.3 <i>Microplates</i> .....	25
2.4.4 <i>Atomic Force Microscopy</i> .....	28
2.5 Mechanical Stimulation in Bone .....	32
2.6 Conclusions .....	34
2.7 References .....	36
<b>Atomic Force Microscope Cantilever Modifications to apply Whole Cell Deformation</b>	<b>48</b>
3.1 Introduction .....	49
3.2 Investigating Cell Mechanics using an AFM .....	51
3.2.1 <i>The Integrated AFM/Fluorescence Microscopy System</i> .....	51
3.2.2 <i>Calibration of Cantilever Spring Constant and Deflection Sensitivity</i> .....	53
3.3 Adaption of an AFM Cantilever to Measure Whole Cell Mechanics.....	55
3.3.1 <i>Large Sphere Attachment: Design Considerations</i> .....	56
3.4 Modified Cantilever Calibration.....	63
3.4.1 <i>Optical Lever Sensitivity</i> .....	63
3.4.2 <i>Spring Constant</i> .....	64
3.4.3 <i>Cantilever Bending Profiles: ‘Sliding’ versus ‘Constrained’</i> .....	66
3.4.4 <i>Correction of Force-Indentation Measurements</i> .....	70

3.4.5	<i>Validation of Correction Factors</i> .....	74
3.5	Discussion.....	75
3.6	References .....	77

**The Role of Actin Cytoskeleton Contractility in the Resistance of Osteoblasts to Compression..... 80**

4.1	Introduction .....	81
4.2	Materials and Methods .....	82
4.2.1	<i>Cell Culture</i> .....	82
4.2.2	<i>Cell Preparation</i> .....	83
4.2.3	<i>Experimental Procedure</i> .....	83
4.2.4	<i>Cytoskeleton Morphology Analysis</i> .....	86
4.2.5	<i>Statistical Analysis of Data</i> .....	87
4.3	Results .....	87
4.3.1	<i>Cell Morphology Change</i> .....	87
4.3.2	<i>Monotonic Compression</i> .....	91
4.3.3	<i>Strain Rate Dependence</i> .....	93
4.4	Discussion.....	94
4.5	References .....	100
4.6	Appendix .....	104

**Stability Enhancement of an Atomic Force Microscope for Long-Term Force Measurement..... 111**

5.1	Introduction .....	112
5.2	Materials and Methods .....	114
5.2.1	<i>Stability Criteria</i> .....	114
5.2.2	<i>Stability Measurement</i> .....	115
5.3	Stability under Standard Operating Conditions.....	115
5.4	System Stabilisation .....	117
5.4.1	<i>Stability in Air: Active Temperature Control</i> .....	118
5.4.2	<i>Stability in Liquid: Customised Fluid Cell</i> .....	122
5.5	Stability Enhancement versus Standard Operating Conditions .....	127
5.5.1	<i>Introduction</i> .....	127
5.5.2	<i>Materials and Methods</i> .....	127
5.5.3	<i>Results</i> .....	129
5.6	Discussion.....	132

5.7	References .....	134
5.8	Appendix .....	136
<b>Investigation of the Cellular Response to Cyclic Deformation .....</b>		<b>138</b>
6.1	Introduction .....	139
6.2	Materials and Methods .....	140
6.2.1	<i>AFM and Fluid Cell Setup</i> .....	140
6.2.2	<i>Cell Preparation</i> .....	141
6.2.3	<i>Experimental Procedure</i> .....	142
6.2.4	<i>Data Analysis and Data Presentation</i> .....	143
6.2.5	<i>Statistical Analysis</i> .....	145
6.3	Results .....	145
6.3.1	<i>Cell Morphology Changes</i> .....	145
6.3.2	<i>Effects of Cyclic Deformation over 120 min</i> .....	149
6.3.3	<i>Effects of Cyclic Deformation at <math>T_0</math></i> .....	152
6.3.4	<i>Effects of Cyclic Deformation at <math>T_{RC}</math></i> .....	154
6.4	Discussion.....	162
6.5	References .....	169
6.6	Appendix .....	173
<b>Discussion .....</b>		<b>188</b>
7.1	Discussion.....	189
7.2	References .....	198

## **Acknowledgements**

Firstly, the biggest thank you must go to Dr. Pat McGarry. Pat has guided, motivated and inspired me all the way through this PhD and as a supervisor he has gone far beyond the call of duty. His constant optimism has made this tough journey a lot less stressful.

I would also like to thank my fellow colleagues in the McGarry group; Enda, Will, Eamo, Nicola, Emer, Dave and Noel. It has all been a team effort! Additionally, I would also like to acknowledge everyone in the Department of Mechanical and Biomedical Engineering in NUI Galway who have guided and assisted me over the years both as an undergraduate student and during my PhD.

A special thank you to Prof. Suzi Jarvis and all at the Nanoscale Function Group (NFG) for having me in their group during my time in UCD. Being surrounded by world experts in AFM, who have collectively come across all the countless issues regarding AFM, has made this PhD a lot easier. In particular, I would like to acknowledge Dr. Maarten van Es and Dr. Jason Kilpatrick for sharing their vast technical knowledge. To the other members of the NFG, both past and present (Liam, Denise, Tracy, Kate, Brian, Pdraig, Sabine, Tim, Nigel, Lorraine, Laila, Bart, Liz, Anika, etc.), thanks for all the help, advice and the laughs over the years.

To my parents and sisters, knowing you are always there for me whenever I need help and advice makes life a lot easier, so thank you! To Ruthie, thanks for being there when I needed distracting and for making my life complete.

Thanks to my friends whom I have progressively abandoned over the past few years, and the new friends I've made during my time in Dublin, particularly, Lisa, Keith, Michelle and John.

Finally, I would also like to acknowledge Science Foundation Ireland for funding this project.

# **Chapter 1**

## **Introduction**

## 1.1 Background and Motivation

Cells and tissues continuously experience mechanical loading during normal daily activity. This mechanical loading can involve many different loading configurations, peak loads and loading rates. Mechanical loading plays a vital role in many physiological behaviours, for example, strenuous exercise increases bone mass (Lanyon (1996), Courteix et al. (1998)) whereas disuse by inactivity reduces bone mass (Zerwekh et al. (2009)). However, to date, very little is known about the underlying biomechanisms involved in the load-induced ‘mechanosensitivity’ of bone. In fact, the contribution of intracellular components to the mechanical response of osteoblasts to loading has not been widely investigated.

Studies have demonstrated that the response of cells to mechanical loading is dependent on cell geometry, cell phenotype, and cell contractility (Janmey and McCulloch (2007)). As an example, highly contractile myoblasts exhibit a strong resistance to compressive deformation (Peeters et al. (2005)) whereas less contractile fibroblasts exhibit a relatively weak resistance to compression (Deng et al. (2010)). Additionally, rounded chondrocytes exhibit a low resistance to shear induced substrate detachment in comparison to spread chondrocytes (Huang et al. (2003)). Furthermore, it has been shown that the cytoskeleton, in particular the actin cytoskeleton, plays a key role in the biomechanical behaviour of cells (Fletcher and Mullins (2010)). The actin cytoskeleton has also been shown to contribute to cellular processes including growth (Roca-Cusachs et al. (2008)), mechanosignalling transduction (McGarry et al. (2008)) and gene expression (Thomas et al. (2002)). However, the contribution of the actin cytoskeleton to the mechanical response of cells to applied static and dynamic loading has not been well established, and consequently the constitutive behaviour of the actin cytoskeleton is not well understood. Enhanced knowledge of specific cellular responses to mechanical loading is vital for understanding mechanotransduction and is critical for advancement of the field of tissue engineering (Huang et al. (2004), Ingber (2006)). In addition, understanding how mechanical loading leads to specific cellular responses is critical in the development of therapeutic solutions to diseases such as

osteoporosis which is attributed, at least in part, to a reduction in mechanical stimulation (Zerwekh et al. (2009), Burr (1997)).

Numerous experimental techniques have been developed or adapted to apply mechanical loading to cells. For example, the atomic force microscope (AFM) was initially developed as a high resolution imaging technique (Binnig et al. (1986)) but has since emerged as an important technique for investigating cell mechanics due to its unrivalled force resolution and displacement precision (Mostaert et al. (2006), Fukuma et al. (2006)). In general, AFM is used to investigate cell mechanics by applying highly localised deformation, via an AFM cantilever with a sharp tip, to specific regions of the cell membrane (Rotsch and Radmacher (2000), Prabhune et al. (2012)). However, physiological mechanical loading is typically applied to the whole cell via the extracellular matrix (i.e. fluid shear and matrix deformation), and not at localised points of the membrane, as typically applied by AFM indentation. The *in vitro* implementation of whole cell deformation provides a more accurate representation of cell deformation due to physiological loading. Techniques such as microplates manipulation (Thoumine et al. (1999)), substrate stretching (Wang et al. (2001)) and micropipette aspiration (Hochmuth (2000)) have been developed to apply deformation at the whole cell level. However these systems are somewhat crude in terms of accuracy of applied deformation and force measurement, in comparison to the precision offered by AFM systems. Adapting the AFM to apply non-localised whole cell deformation would provide physiologically relevant loadings with unrivalled precision in terms of applied displacement and measured force.

## 1.2 Objectives of this Thesis

The focus of this thesis is to advance the AFM technique to investigate whole cell mechanics over physiologically relevant time scales. This modified system will then be used to gain a more in-depth understanding of the role of the actin cytoskeleton in cell biomechanics under static and dynamic loading by performing novel *in vitro* whole cell experiments that take advantage of the high force precision and displacement resolution of the AFM.

The objectives of this thesis are as follows:

- Modification of a standard AFM to implement high precision deformation-controlled loading of single cells, where the deformation is applied at the whole cell level over physiologically relevant time scales.
- Experimental investigation of the role of the actin cytoskeleton in the single cell response to monotonic compressive deformation applied at the whole cell level.
- Experimental investigation of the role of the actin cytoskeleton in the single cell response to constant strain rate cyclic deformation applied at the whole cell level over physiologically relevant time scales.

### **1.3 Thesis Overview**

Figure 1.1 shows a flowchart portraying the overall structure of this thesis. The work reported in this thesis can be broadly divided into two categories: (i) AFM instrumentation modifications (Chapters 3 & 5), and (ii) novel single cell static (Chapter 4) and dynamic (Chapter 6) experiments using the modified AFM.

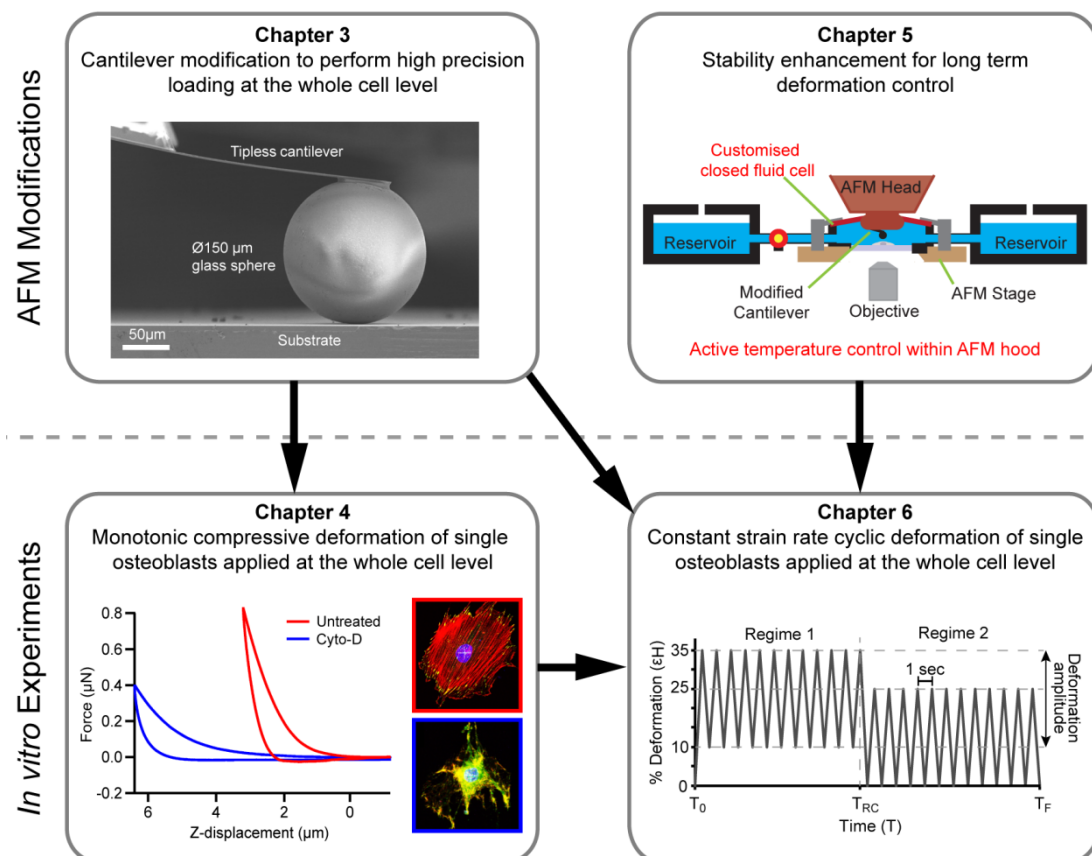


Figure 1.1: Flowchart showing the overall structure of this thesis. The thesis can be divided into two sections; (i) the AFM system enhancing modifications to implement novel single cell experiments, and (ii) the application of the modified system to perform these novel single cell experiments.

In **Chapter 2**, firstly a brief description of the structure of the cell is provided (Section 2.2). An outline of the cellular response to mechanical stimuli is then presented in Section 2.3. Next, a broad overview of *in vitro* techniques for mechanical manipulation of cells is presented in Section 2.4. Finally, an overview of the role of mechanical stimulation in bone mechanics is presented. In addition to the background literature presented in Chapter 2, the reader should note that detailed and focused discussion of directly relevant literature is provided in each technical chapter of this thesis (Chapters 3-6).

In **Chapter 3**, AFM cantilever modifications performed to facilitate the application of deformation controlled loading at a whole cell level are presented. A large sphere is attached to the free-end of a tipless AFM cantilever, such that the bottom of the sphere permits mechanical loading at the whole cell level. For the first

time, an extensive investigation of the effects of sphere attachment to an AFM cantilever bending profile is performed. Correction factors necessary for the accurate interpretation of force-indentation data for modified AFM cantilevers are proposed.

In **Chapter 4**, a series of *in vitro* experiments are performed in which single osteoblasts are subjected to high precision monotonic compressive deformation using the modified AFM cantilever developed in Chapter 3. Experiments are repeated on the same cells following treatment with the actin cytoskeleton disrupting agent, Cytochalasin-D (cyto-D), to elucidate the role of the actin cytoskeleton in the resistance of cells to compressive deformation. Additionally, detailed confocal microscopy is performed to establish the effect of the actin cytoskeleton on cell and nucleus morphology.

In **Chapter 5**, a readily implementable, cost effective method of modifying a standard AFM for deformation controlled operation over long time scales is developed. This involves a novel combination of (i) active temperature control and (ii) a customised closed fluid cell to eliminate thermal drift and liquid related instabilities in the AFM system.

In **Chapter 6**, a series of novel *in vitro* experiments are performed in which single osteoblasts are subjected to deformation controlled cyclic loading using the AFM modifications developed in Chapter 3 and Chapter 5. Experiments are repeated on cells treated with the actin cytoskeleton disrupting agent, cyto-D, to elucidate the role of the actin cytoskeleton in the response of cells to deformation controlled cyclic loading.

In **Chapter 7**, a discussion of the main findings of this thesis is presented together with concluding remarks and future considerations arising from the work.

## 1.4 References

- Binnig, G., Quate, C. F. and Gerber, C. (1986) Atomic force microscope. *Physical Review Letters*. 56 (9), 930-933
- Burr, D. B. (1997) Muscle strength, bone mass, and age-related bone loss. *Journal of Bone and Mineral Research*. 12 (10), 1547-1551
- Courteix, D., Lespessailles, E., Peres, S. L., Obert, P., Germain, P. and Benhamou, C. (1998) Effect of physical training on bone mineral density in prepubertal girls: A comparative study between impact-loading and non-impact-loading sports. *Osteoporosis international*. 8 (2), 152-158
- Deng, Z., Lulevich, V., Liu, F.-T. and Liu, G.-Y. (2010) Applications of atomic force microscopy in biophysical chemistry of cells. *The Journal of Physical Chemistry B*. 114 (18), 5971-5982
- Fletcher, D. A. and Mullins, R. D. (2010) Cell mechanics and the cytoskeleton. *Nature*. 463 (7280), 485-492
- Fukuma, T., Mostaert, A. S. and Jarvis, S. P. (2006) Explanation for the mechanical strength of amyloid fibrils. *Tribology Letters*. 22 (3), 233-237
- Hochmuth, R. M. (2000) Micropipette aspiration of living cells. *Journal of Biomechanics*. 33 (1), 15-22
- Huang, H., Kamm, R. D. and Lee, R. T. (2004) Cell mechanics and mechanotransduction: Pathways, probes, and physiology. *American Journal of Physiology-Cell Physiology*. 287 (1), C1-C11
- Huang, W., Anvari, B., Torres, J. H., Lebaron, R. G. and Athanasiou, K. A. (2003) Temporal effects of cell adhesion on mechanical characteristics of the single chondrocyte. *Journal of Orthopaedic Research*. 21 (1), 88-95
- Ingber, D. E. (2006) Cellular mechanotransduction: Putting all the pieces together again. *The FASEB journal*. 20 (7), 811-827
- Janmey, P. A. and McCulloch, C. A. (2007) Cell mechanics: Integrating cell responses to mechanical stimuli. *Annu. Rev. Biomed. Eng.* 9, 1-34
- Lanyon, L. (1996) Using functional loading to influence bone mass and architecture: Objectives, mechanisms, and relationship with estrogen of the mechanically adaptive process in bone. *Bone*. 18 (1), S37-S43
- McGarry, J. G., Maguire, P., Campbell, V. A., O'Connell, B. C., Prendergast, P. J. and Jarvis, S. P. (2008) Stimulation of nitric oxide mechanotransduction in single osteoblasts using atomic force microscopy. *J. Orthop. Res.* 26 (4), 513-521

- Mostaert, A., Higgins, M., Fukuma, T., Rindi, F. and Jarvis, S. (2006) Nanoscale mechanical characterisation of amyloid fibrils discovered in a natural adhesive. *Journal of Biological Physics*. 32 (5), 393-401
- Peeters, E. A. G., Oomens, C. W. J., Bouten, C. V. C., Bader, D. L. and Baaijens, F. P. T. (2005) Mechanical and failure properties of single attached cells under compression. *J. Biomech*. 38 (8), 1685-1693
- Prabhune, M., Belge, G., Dotzauer, A., Bullerdiek, J. and Radmacher, M. (2012) Comparison of mechanical properties of normal and malignant thyroid cells. *Micron*. 43 (12), 1267-1272
- Roca-Cusachs, P., Alcaraz, J., Sunyer, R., Samitier, J., Farré, R. and Navajas, D. (2008) Micropatterning of single endothelial cell shape reveals a tight coupling between nuclear volume in g1 and proliferation. *Biophysical Journal*. 94 (12), 4984-4995
- Rotsch, C. and Radmacher, M. (2000) Drug-induced changes of cytoskeletal structure and mechanics in fibroblasts: An atomic force microscopy study. *Biophysical Journal*. 78 (1), 520-535
- Thomas, C. H., Collier, J. H., Sfeir, C. S. and Healy, K. E. (2002) Engineering gene expression and protein synthesis by modulation of nuclear shape. *Proceedings of the National Academy of Sciences*. 99 (4), 1972-1977
- Thoumine, O., Ott, A., Cardoso, O. and Meister, J. J. (1999) Microplates: A new tool for manipulation and mechanical perturbation of individual cells. *J. Biochem. Bioph. Meth.* 39 (1-2), 47-62
- Wang, J. H. C., Goldschmidt-Clermont, P., Wille, J. and Yin, F. C. P. (2001) Specificity of endothelial cell reorientation in response to cyclic mechanical stretching. *J. Biomech*. 34 (12), 1563-1572
- Zerwekh, J. E., Ruml, L. A., Gottschalk, F. and Pak, C. Y. C. (2009) The effects of twelve weeks of bed rest on bone histology, biochemical markers of bone turnover, and calcium homeostasis in eleven normal subjects. *Journal of Bone and Mineral Research*. 13 (10), 1594-1601

## Chapter 2

### **Background and Related Work**

## 2.1 Introduction

The importance of mechanotransduction in regulating numerous physiological processes has become increasingly evident in recent years (Ingber (2003), Ramaekers and Bosman (2004), Ingber (2006)). Mechanical stimuli have been found to play a significant role in the cellular pathology of numerous diseases, including osteoporosis (Burr (1997), Zerwekh et al. (2009)), arthritis (Lammi (2004)), and cancer (Makale (2007), Prabhune et al. (2012)). These findings highlight the importance of research in the field of cell mechanics, and emphasise the necessity of understanding the complex mechanical behaviour of cells (Van Vliet et al. (2003), Lim et al. (2006), Discher et al. (2009)). Numerous *in vitro* studies have demonstrated that cells actively respond to mechanical stimuli (Wang et al. (2001), Shieh and Athanasiou (2007), Adachi et al. (2008), Balestrini et al. (2010), Watanabe-Nakayama et al. (2011)). Specifically, the role of the cytoskeleton in response to mechanical loading has been demonstrated through the use of chemical agents that disrupt individual cytoskeletal components (Ujihara et al. (2008), Ofek et al. (2009), Dowling et al. (2012)) or using fluorescent imaging techniques (Wang et al. (2008), Huang et al. (2010), Pravincumar et al. (2012)). However, despite such extensive *in vitro* investigation, the biomechanical response of cells to mechanical loading is still poorly understood.

In this chapter, an overview of the structural components of the cell is first presented in Section 2.2, with a particular emphasis on the actin cytoskeleton. Leading on from this, the processes by which a cell senses and responds to forces are discussed in Section 2.3. In Section 2.4 experimental techniques used to investigate single cell mechanics are reviewed. In addition, relevant findings obtained using these techniques are highlighted. Finally, the important effects of mechanical stimuli in bone mechanics are outlined in Section 2.5. The reader should note that, in addition to the background literature presented in this chapter, a detailed and focused discussion of directly relevant literature is provided in each technical chapter of this thesis (Chapters 3-6). Finally, in the final chapter of the thesis (Chapter 7) the key

findings of the thesis are discussed in the broad context of cell mechanics and AFM experimentation, with further discussion of relevant literature being provided.

## 2.2 Cell Structure

The cell cytoskeleton provides the key mechanical components of the cell, providing resistance to deformation, active contractility, maintenance of morphology, intracellular transport, regulation of adhesion, spreading and motility. The three components of the cytoskeleton are shown in Figure 2.1, namely the actin cytoskeleton, microtubules, and intermediate filaments. The cytoskeleton has been the subject of extensive investigation in recent years, given its important role in the physical properties and biomechanical behaviours of cells. However, a cell's membrane, nucleus, and cytoplasm also contribute to its mechanic behaviour.

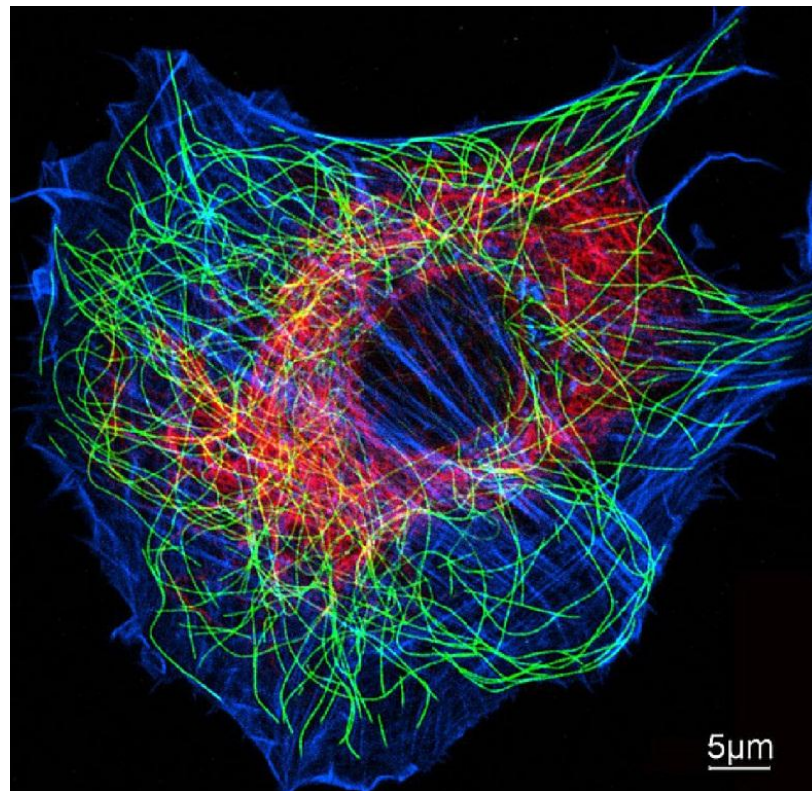


Figure 2.1: The cytoskeleton of the cell consists of three filamentous protein groups: actin filaments (blue), microtubule (green) and intermediate filaments (red). Image courtesy of Cora-Ann Schoenenberger and Rosmarie Suetterlin, Biozentrum, University of Basel. Reproduced with permission.

The nucleus is the largest organelle within a eukaryotic cell. The main role of a cell's nucleus is to regulate gene expression, but it also has a degree of structural stiffness and plasticity that can play a role in cell mechanics and mechanotransduction (Guilak et al. (2000), Caille et al. (2002), Lammerding (2011)). The cytoplasm is the intracellular material between the cell membrane and the nucleus. It contains a crowded microenvironment of proteins, protein complexes, and organelles (Martini (2004)). Due to its mainly liquid composition, the cytoplasm is often considered to be incompressible. The cell membrane is the outer boundary of the cell that separates the cytoplasm from the extracellular environment. It is composed of a thin lipid bilayer, approximately 5 to 10 nm thick. Besides acting as a physical barrier, the cell membrane also plays many other important roles. It contains protein structures that act as receptors for signalling molecules, transport channels for ions, and connection points between a cell's cytoskeleton and the extracellular environment (Alberts et al. (2002), Martini (2004)).

The cytoskeleton lies within the cytoplasm and, as mentioned above, consists of three groups of protein filaments; intermediate filaments, microtubules, and actin filaments, as shown in Figure 2.1 and Figure 2.2. Due to the cytoskeleton's ability to resist, transmit, and generate cellular forces (Fletcher and Mullins (2010)), interactions between these interconnected cytoskeletal components dynamically influences cell shape, motility, adhesion and stiffness (Mofrad (2009)). Intermediate filaments are composed of tetramer subunits which bundle together to form filamental structures with an intermediate diameter of 8 to 12 nm relative to the other cytoskeletal filaments. These filaments are arranged in a network surrounding the nucleus (Figure 2.1), providing strength and organisation to both the cell and nucleus (Alberts et al. (2002), Lammerding (2011)). It is believed this filament group contributes to the overall mechanical response of the cell during large cell deformation, when intermediate filaments become fully extended and stretched (Wang and Stamenović (2000), Stamenović (2008)). Microtubules are stiff, hollow structures with filament diameter of 24 nm (Alberts et al. (2002), Martini (2004)). These filaments are composed of alternating helical layers of its monomer protein, tubulin (Wade and Hyman (1997)). Microtubules radiate outwards from the

centrosome (also known as a microtubule-organising centre) which is a central organelle near the nucleus. Microtubules serve as the transportation pathway for molecular motor proteins to shuttle cargo around the cell (Hirokawa (1998)) and to separate chromosomes during cell division (Anaphase (2000)). In most adherent cells, they play only a minor mechanical role in stabilising the cytoskeleton and balancing stress fluctuations (Stamenović (2008)).

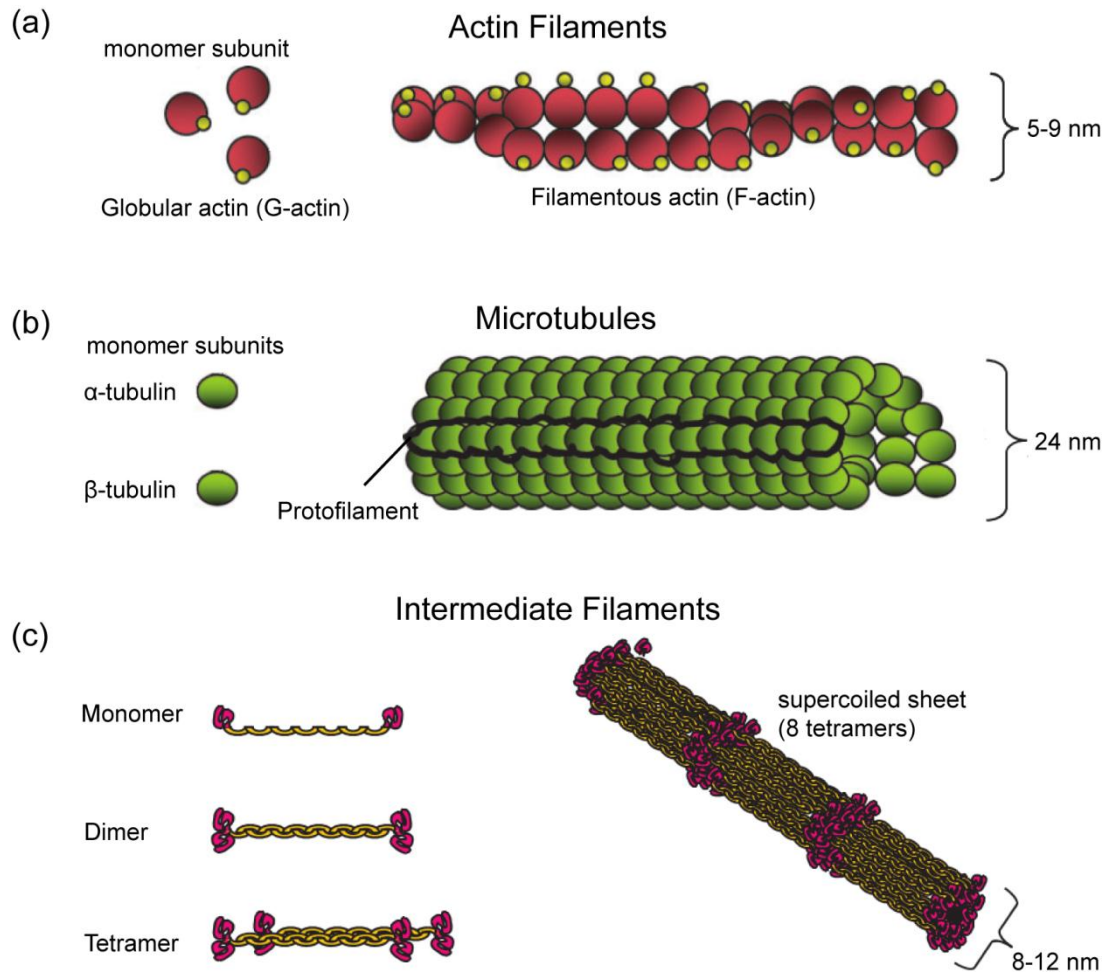


Figure 2.2: The three filamentous groups that make up the cell cytoskeleton; (a) actin filaments, (b) microtubules, and (c) intermediate filaments. Adapted from Blain (2009).

Actin filaments act as the primary structural component of the cytoskeleton, and with the aid of myosin motor molecules, are integral in creating and maintaining the forces required for cellular movement and contraction (Kumar et al. (2006), Sato et al. (2006), Fletcher and Mullins (2010)). Actin filaments are double-helical arrangements (F-actin) composed of polymerised globular actin monomers (G-actin),

and are reported to be the most abundant protein in eukaryotic cells with a diameter of 5-9 nm (Alberts et al. (2002)). It is known that the actin cytoskeleton is essential for cellular functions such as morphology, motility, adhesion and contractility (Guilak (1995), Fernández et al. (2006), Blain (2009), Ofek et al. (2009), Fletcher and Mullins (2010)). In a suspended or resting state, the cytoplasm contains short actin filaments (capped by the protein CapZ), actin monomers, and myosin II (in an inactive state). Consequently any interaction between actin and myosin is prevented. In response to an activation signal, several intracellular pathways (Cdc42, Rho and Rac) stimulate actin filament growth and myosin II activation. This signal stimulates the release of calcium ions from endoplasmic reticulum into the cell cytosol, which then results in the activation of gelsolin, which cleaves capped actin filaments into small fragments. This process of severing and uncapping leads to the formation of long actin filaments which are then bundled together (10-30 filaments) to either fimbrin or  $\alpha$ -actinin (Burrige and Wennerberg (2004)). Fimbrin causes actin filaments to be tightly bundled and thus prevents any interaction with myosin II, whereas  $\alpha$ -actinin loosely bundles actin filaments together, allowing myosin II (active state) to enter and form contractile actin filament bundles known as stress fibres, Figure 2.3. Phosphorylation of myosin II into an active state is the result of either a response to the influx of calcium ions (light-chain-kinase) or due to an externally applied signal (Rho-kinase). Active state myosin II then assembles into bipolar filaments and interacts with actin filaments that are bundled together by  $\alpha$ -actinin, resulting in the formation of stress fibres (Alberts et al. (2002)). The cross-bridge interaction between the bipolar myosin II and actin filaments leads to contractile force generation in a cell, analogous to the shortening of sarcomeres in muscle cells (Burrige and Wennerberg (2004)). Contractile forces have been measured in the range of 25-50 nN for fibroblasts and 150 nN for myofibroblasts (Balaban et al. (2001), Goffin et al. (2006)).

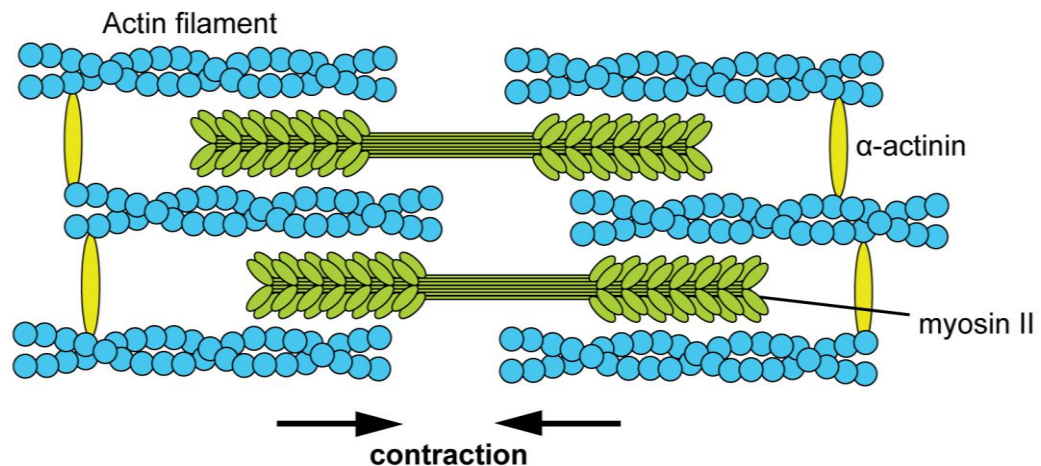


Figure 2.3: Stress fibres are the contractile force generating structures in a cell which are composed of actin filaments, myosin II and  $\alpha$ -actinin.

The shortening of many stress fibres in a cell can lead to tension at points of contact outside the cell, e.g. cell-matrix adhesions and/or cell-cell junctions, Figure 2.4. This membrane tension gives rise to a pre-tension, or prestress, within the cell. Tension at cell-cell junctions acts predominately at adherens junctions, which connects the actin filaments of adjacent cells through cadherin proteins (Alberts et al. (2002)). Tension at cell-matrix junctions acts predominately at focal adhesions, which are protein complexes that have both a structural and mechano-signalling role (Shemesh et al. (2005)). Focal adhesions proteins, like vinculin, talin and focal adhesion kinase, connect F-actin to transmembrane receptors known as integrins, which subsequently connect to ligands in the extracellular matrix (Geiger and Bershadsky (2001)). The reorganisation of actin filaments into stress fibres causes more focal adhesions, thus enhancing the extracellular matrix binding in a positive feedback system (F  r  ol et al. (2009), Mofrad (2009)). The interconnected relationship of the actin cytoskeleton, cell shape and the number of focal adhesion complexes formed may perhaps explain why a highly spread cell is much stiffer than when rounded (Caille et al. (2002), Bacabac et al. (2008)). Contractile forces are believed to be necessary for this cell spreading process, as it has been shown that cell area decreases in the absence of contractile forces (Wakatsuki et al. (2003)).

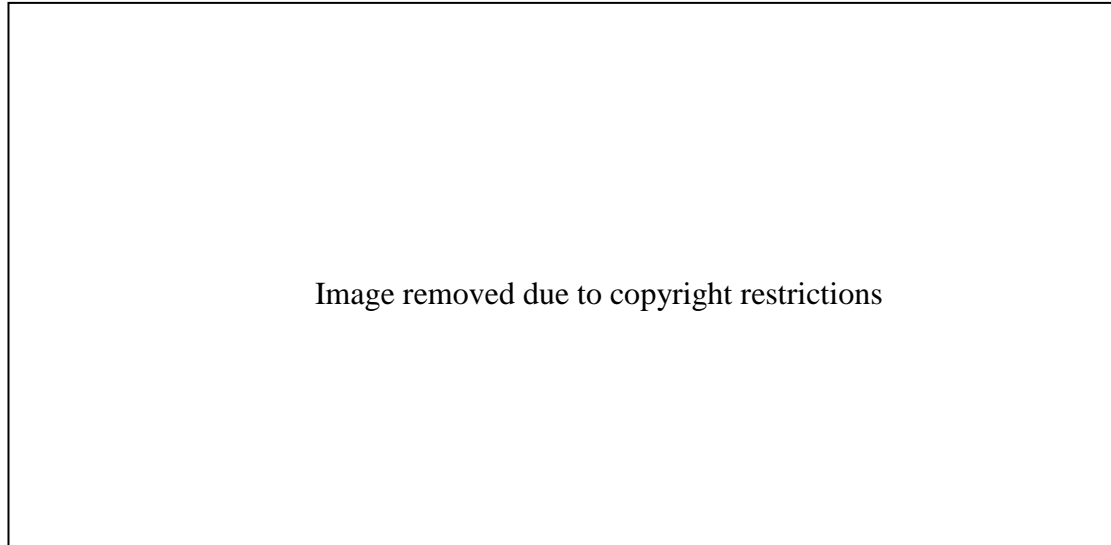


Figure 2.4: Schematic showing cell-cell junctions (adheren junctions) and cell-matrix adhesions (focal adhesions) and their interconnected relationship with the actin cytoskeleton. Reproduced from Girard et al. (2007).

Mechanical loading can either be directly applied to the cell or transmitted to the cell via the extracellular matrix or adjacent cells. These forces can be sensed by the same mechanosensory structures that detect internal forces, that is, focal adhesions and/or adherens junctions (Shemesh et al. (2005)), but they can also be sensed by structures like the stereocilia, primary cilium, and stretch ion channels (Alberts et al. (2002)), as highlighted in Figure 2.5. Stereocilia and primary cilia are protrusions of the cell membrane that deflect much like cantilever beams when subjected to fluid flow. Stretch ion channels are protein complexes in the cell membrane that open their central pores in response to externally applied strains (Sachs (2010)). It is believed that forces applied to the cell membrane leads to an increase in membrane tension which in turn opens the stretch ion channels, thus increasing the transfer of extracellular ions and activating signalling pathways that affect cell function and gene expression ((Ingber (2006), Janmey and McCulloch (2007)).

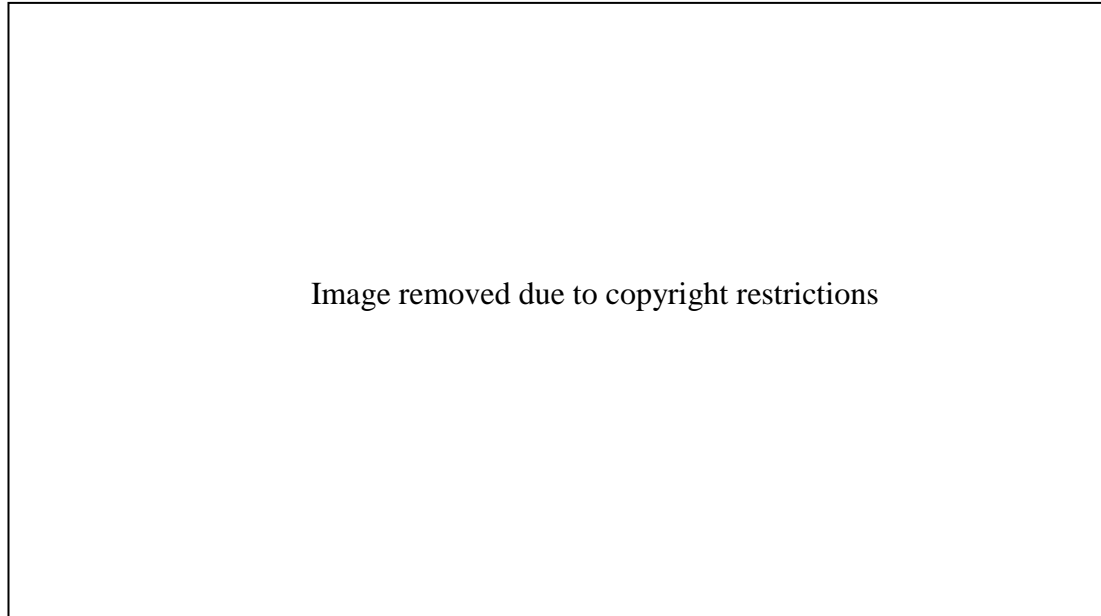


Figure 2.5: Mechanosensory structures of the cell. Adapted from Ingber (2006).

### 2.3 Cellular Response to Mechanical Stimulation

It is well established that cells respond to mechanical loading (Orr et al. (2006)). Changes at the cell-environment interface, due to a variety of chemical and mechanical signals present in the extracellular environment, are sensed by cells and converted into biochemical responses in a process known as mechanotransduction (Ingber (2006)). Although the response of cells to mechanical stimulation may differ between cell phenotypes, common signalling mechanisms have been identified. Specifically, integrins interacting with the extracellular matrix mediate increases in intracellular  $\text{Ca}^{2+}$  levels and activate cascades of mitogen-activated protein kinases, ultimately resulting in the phosphorylation of two members of a subclass of this family, namely extracellular signal-regulated kinase (ERK) 1 and 2. This occurs irrespective of the mechanosensitive cell phenotype involved (Iqbal and Zaidi (2005)). Phosphorylated ERK 1/2 then causes the activation of the activator protein-1 family of transcription factors, the major components of which are the Fos and c-Jun protein families. AP-1 binds to the promoter of various mechanosensitive genes (Liedert et al. (2006)), ultimately leading to a cellular response. Although much is known about the signalling cascades related to mechanotransduction (Burrige and

Wennerberg (2004)), less is understood about the underlying mechanisms by which cells feel and response to mechanical stimulation.

Cells in tissues adhere to and interact with the extracellular environment via specialised cell-cell and cell-extracellular matrix contacts (Alberts et al. (2002)). Cells sense their environment through ion channels and other mechanosensors present on the cell membrane (Shemesh et al. (2005), Ingber (2006)). Some transmembrane receptors form clusters and associate intra-cellularly with groups of proteins which link them to the cytoskeleton. For example, focal adhesions are specialised areas of the cell membrane involved in cell-extracellular matrix adhesion. Structurally, these complexes link a cell to the underlying matrix through the association of transmembrane integrin receptors with specific extracellular matrix ligands (Geiger and Bershadsky (2001), Shemesh et al. (2005)). For cell-cell adhesion, adherens junctions are involved in coupling adjacent cells through  $\text{Ca}^{2+}$  dependant linkage of transmembrane cadherin molecules. The cytoplasmic domain of cadherins associates with catenins, which link the complex to the actin cytoskeleton (Girard et al. (2007)). Therefore, in anchorage-dependent cells, mechanical stimuli may be sensed at sites of cell-cell and cell-extracellular matrix adhesion due to the physical deformation of the membrane surface. Furthermore, as the cytoskeleton is connected to these cell-cell and cell-extracellular matrix junctions, mechanical stimuli are therefore transferred through the cell via these structural components (Burrige and Chrzanowska-Wodnicka (1996)).

Studies have highlighted the effects of mechanical stimuli such as tension, compression and shear stress at the single cell level (Lehenkari et al. (2000), Huang et al. (2004), Barron et al. (2007), Janmey and McCulloch (2007), Shieh and Athanasiou (2007), Dowling et al. (2012)). Stress applied to a cell will deform the cell according to the mechanical properties of its internal architecture. This mechanical response is known as the passive mechanical behaviour of the cell and it is widely assumed that this response falls in the class of viscoelastic bodies (Thoumine and Ott (1997), Alcaraz et al. (2003), Peeters et al. (2005b), Darling et al. (2006)). However, in contrast to inert matter, cells may also exhibit an active response to mechanical stimulation. Thus, cells may develop internal stresses from

different motor proteins associated to the cytoskeleton, such as acto-myosin cross-bridging. In addition, cells may reorganise their internal structure and modify their stiffness dramatically without the existence of any external force, as occurs during cell migration and cell division (Small et al. (1998), Fletcher and Mullins (2010)). Studies have shown that it is possible to distinguish the active and passive processes on a time scale basis (Thoumine and Ott (1997), Fernández et al. (2006), Watanabe-Nakayama et al. (2011)). A study by Thoumine and Ott (1997) demonstrated that the immediate mechanical response following an applied whole cell deformation (in the first minutes) comes from the passive viscoelastic response, whereas the response several tens of minutes after applying an external force falls in a contractile regime, in which actin-dependent traction forces were developed in response to uniaxial load.

Although it is unclear how cells modify their internal structure to exhibit such different mechanical properties, evidence suggests that the cytoskeleton, in particular the actin cytoskeleton, of the cell is mainly responsible for this complex mechanical behaviour (Rotsch and Radmacher (2000), Charras and Horton (2002), Kumar et al. (2006)). The whole cytoskeleton is embedded in the viscous cytoplasm and it is mechanically coupled to the cell nucleus, as well as attached to the cell membrane at specialised sites. However, it is still not clear how the cytoskeletal filaments, their associated proteins and other cell structures are organised and coupled to respond to a mechanical stimulus. Despite the complexity of cell mechanical behaviour, some mechanical aspects have been identified, such as the existence of a prestress. The stress bearing elements, such as stress fibres of the actin cytoskeleton, within the cell carry a pre-existing tension that is developed prior to the application of an external load. A major implication of this is that because stress bearing elements of the cell are prestressed, forces can be transmitted effectively across the cytoplasm. Thus, pre-tension provides a structural basis for cell mechanotransduction processes in response to changes in the extracellular environment around the cell. In addition to biochemical mediators, intracellular tension has been proposed as a candidate mechanical mediator for stress fibre reorganisation (Kumar et al. (2006), Sato et al. (2007)). The intracellular tension within a cell is influenced by the force of myosin contraction, the deformability of the actin cytoskeleton, and the constraints on the

deformability of the cell due to matrix attachment and external force. The interplay between these factors and the resulting formation of stress fibres provides the basis for a cell's response to mechanical stimulation. For instance, the cell selectively strengthens stress fibres along the direction of maximum resistance to myosin contractility. This not only allows the cell to stiffen itself in a particular direction to protect against excess stress and strains, but it also allows the cell to feel the matrix rigidity and migrate towards the stiffest direction. (Lo et al. (2000), Saez et al. (2007)). Furthermore, changes in stress fibre patterns affect cell shape and orientation (Noria et al. (2004), Flavahan et al. (2005), Kumar et al. (2006)).

Although much is known about the biochemical signalling pathways related to mechanotransduction (BurrIDGE and Wennerberg (2004)), and the role of the cytoskeleton, particularly the actin cytoskeleton, in response to mechanical loading, it is still unclear how and what cells sense, if cell behaviour is dependent on stress, strain, strain rate, or a combination of such effects. Additionally, it is unclear what cellular structures are responsible for cell mechanical behaviour. The exact mechanisms by which a cell senses and actively generates forces remains to be determined.

## **2.4 Experimental Techniques to Investigate Cell Mechanics**

An extensive range of techniques have been developed to investigate cell mechanics at both the tissue and single cell level. Experiments in which a mechanical stimulus is applied at the tissue level (Hillam and Skerry (1995), Lanyon (1996), Hsieh and Turner (2001)) or on cell-populated constructs (Wille et al. (2006), Nekouzadeh et al. (2008), Balestrini and Billiar (2009), Buxboim et al. (2010), Thorpe et al. (2010)) have the ability, in a reproducible and efficient manner, to show that applied mechanical stress alters cell structure and function. However, the heterogeneity among cell responses is largely ignored. Furthermore, the response of a single cell to mechanical signals cannot be decoupled easily from the response of the entire population. Furthermore, the contribution of the extracellular matrix cannot be trivially decoupled from the active cell response to mechanical loading. In order to measure the response of cells to mechanical stimuli, experiments must be performed

at the single cell level. The single cell approach allows for the observation of resulting changes in cellular behaviour after the application of specific mechanical stimuli. This may include examining mechanical properties, cellular signalling, and intracellular structural changes such as remodelling of the cytoskeleton.

Localised deformation is applied to cells to investigate the biomechanical response to location specific loading and/or to measure the mechanical properties of specific structures or parts of a cell (AFM, cell poking, optical tweezers). In the body, mechanical loading is typically applied to the whole cell via the extracellular matrix (i.e. fluid shear and matrix deformation). The cellular response to whole cell deformation on single cells is therefore a more accurate method of mimicking physiologically relevant loading experienced by cells. Several experimental systems have been developed or adapted in order to examine the effect of whole cell deformation on cell behaviour. In this section, these techniques are reviewed and the most relevant findings obtained using each technique discussed.

#### **2.4.1 Micropipette Aspiration**

This technique uses a suction pressure to partially or wholly pull a single cell into a micropipette. The cell elongation into the pipette as a result of suction pressure is measured using video analysis from which the whole cell mechanical properties can be evaluated. In general, this technique is used for cells in solution, although it can also be used on cells adhered to a substrate.

This technique has been used to investigate the mechanical properties of the cell and the contribution of the cytoskeleton to these properties. A study by Zhou et al. (2005) found a decrease in cell stiffness for fibroblasts following disruption of the actin cytoskeleton using cyto-D, indicating that the actin cytoskeleton is an important load bearing structure of the cell. This finding is consistent with the recent work of Reynolds et al. (2012) in which the role of the stress fibre contractility and nucleus geometry in response to micropipette aspiration has been investigated. Furthermore, a study by Trickey et al. (2006) found that disruption of the actin filaments significantly increased the deformability of chondrocytes, whereas the disruption of

microtubule and intermediate filaments did not significantly affect the cells deformability.

A recent study by Pravin Kumar et al. (2012) using micropipette aspiration combined with fluorescence microscopy found that cell deformation involved distortion, disassembly and subsequent reassembly of the actin cytoskeleton (Figure 2.6). Furthermore, it was shown that the cell mechanical properties and actin remodelling were dependent on the rate of applied pressure. The micropipette aspiration technique has also been used to study nuclear mechanics by gently extracting the nucleus from the cell and testing it with a pipette. It is suggested that the nucleus is 3-4 times stiffer than the cell cytoplasm and almost twice as viscous (Guilak et al. (2000)). However, it is difficult to definitively quantify the nucleus stiffness, since studies have demonstrated that the nucleus stiffness changes significantly when extracted from the cell (Caille et al. (2002)).

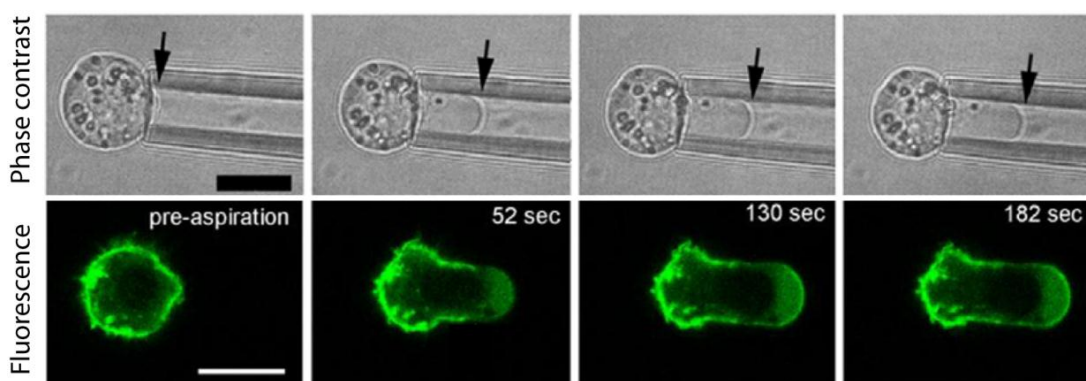


Figure 2.6: Selected images from time series showing a GFP-actin transfected chondrocyte during micropipette aspiration. Scale bars represent 10  $\mu$ m. Adapted from Pravin Kumar et al. (2012).

Micropipette aspiration is a relatively simple and cost effective technique to use. The main disadvantages of this technique are the stress concentration at the pipette lumen and friction between the micropipette and cell membrane, which can both affect the accuracy of the forces calculated. Additionally, drift in the pressure zero setting can arise (Hochmuth (2000)).

### 2.4.2 Substrate Stretching

The substrate stretching technique involves the application of a global strain to an elastic membrane or gel and is typically applied using a vacuum or substrate indenter. This static or cyclic strain can be applied in one direction (uniaxially), in two directions (biaxially), or equal strain in all direction (equiaxially) to single cells or a population of cells. Substrate stretching has been used to investigate the phenomena of strain-induced cell morphology and cytoskeleton changes (Krishnan et al. (2009) Balestrini et al. (2010) DiPaolo et al. (2010)). It has been demonstrated that both the cell morphology and actin cytoskeleton re-align in response to the applied deformation and this reorientation is in the direction of the minimal substrate strain (Figure 2.7) (Kaunas et al. (2005), Barron et al. (2007)). Furthermore, it has been demonstrated that cell and actin cytoskeleton reorganisation and realignment are strain rate dependent, with increased realignment with increased strain rate (Lee et al. (2010), Hsu et al. (2010)). A study by Throm-Quinlan et al. (2011) have investigated the response of cells to combined dynamic stretch and tunable substrate stiffness. It was found that inhibition of spreading due to a lack of matrix stiffness surround the cell may be overcome by externally applying a stretching load. This suggests that similar mechanotransduction mechanisms are used by cells to sense stretch and stiffness.

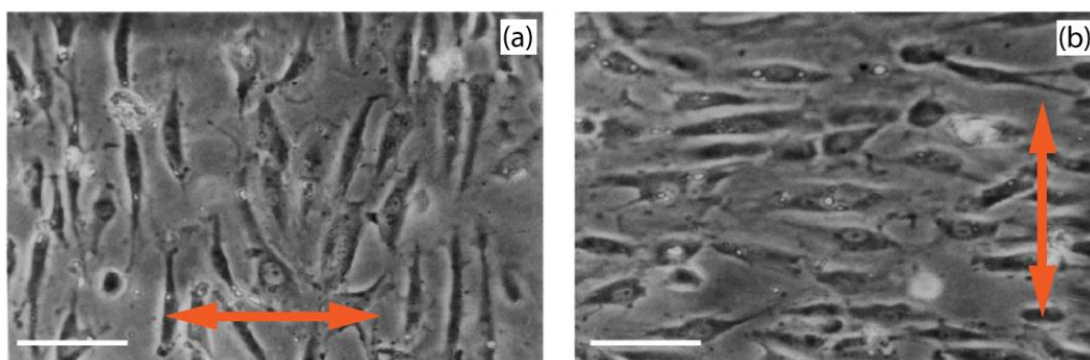


Figure 2.7: Phase contrast images of endothelial cells in response to cyclic stretching. (a) After 3 hr of 10% pure uniaxial stretching, the cells reoriented perpendicular to the stretching direction. (b) The stretching direction was then changed 90 degrees. Cells again reoriented perpendicular to the stretching direction. Scale bar represents 100  $\mu\text{m}$ . Adapted from Wang et al. (2001).

The substrate stretching technique has also been used to investigate the biochemical response of cells to static and dynamic loading. A study by Wang et al. (2004) demonstrated that tendon fibroblasts up-regulate the expression of  $\alpha$ -smooth muscle actin when actin cytoskeleton reorientation occurs during cyclic stretching. A similar finding has been reported by O'Cearbhaill et al. (2008) following the realignment of the actin cytoskeleton in MSCs, with an up-regulation of calponin also being reported. Similarly, Kurpinski et al. (2006) have demonstrated that MSCs, which were forced to align parallel to the strain direction, induced an up-regulation of calponin. However, this was not induced in cells forced to align perpendicular to the strain direction. This suggests that the effects of mechanotransduction depend on the orientation of the cells with respect to the applied loading.

As presented above, the substrate stretching technique is an important technique for investigating the morphological, cytoskeletal, and biochemical response of cells to dynamic loading. However, the biomechanical response of individual cells is not easily measured using this technique in its standard form. A recent study by Mann et al. (2012) have advanced the substrate stretching technique by investigating the contractile response of smooth muscle cells to stretch using an elastomeric substrate micro-fabricated with microposts. In response to an equi-biaxial static stretch, the cells first increased their contractility (~20 min), before gradually softening. Furthermore, combining substrate stretching with AFM and confocal microscopy, Na et al. (2008) have demonstrated that cyclic stretching (10% at 0.25 Hz) rapidly altered the cell stiffness and focal adhesion associated paxillin and vinculin. This suggests that remodelling of focal adhesions plays a critical role in regulating cell stiffness by recruiting and anchoring actin filaments.

The main advantages of this technique are its relative ease of use and low cost, the wide variety of different strain profiles possible, control over the stiffness of the substrate that the cells are seeded upon, and the ability to observe the cell during testing. The disadvantages of this technique include the non-uniformity of the applied strain at the grip regions, and the inherent heterogeneity of the elastin substrates used in this technique.

### 2.4.3 Microplates

The microplates technique is used to measure mechanical responses to unidirectional unidirectional whole cell compression, tension and shear. Several different versions of this technique have been developed (Thoumine and Ott (1997), Shin and Athanasiou (1999), Miyazaki et al. (2000), Peeters et al. (2003), Nagayama et al. (2007)). Thoumine and Ott (1997) developed a microplate manipulation system in which the cell to be tested was placed between two parallel plates, one stiff and other flexible (

Figure 2.8 (a)). Similarly, Shin and Athanasiou (1999) developed a system, referred to as a cytoindenter, in which the cell to be tested was grown on a rigid substrate and indented with a tungsten probe. However, each technique follows the same basic methodology. Cell indentation is performed using a probe that is larger than the size of the cell. A piezoelectric actuator drives the probe a set displacement and cantilever beam theory is generally used to determine the applied force based on the deflection of the beam. The deformation imparted on the cell may be either force-controlled or strain controlled.

Using this technique, a study by Caille et al. (2002) showed that spread endothelial cells are much stiffer than rounded endothelial cells. Furthermore, it was reported that the endothelial nuclei are ~10-fold stiffer than the cytoplasm. By globally compressing myoblasts until rupture, the mechanical and failure properties of myoblasts were demonstrated by Peeters et al. (2005a). It was found that compression beyond ~72% resulted in cell membrane bulging and subsequent bursting. The reaction force measured at 60% whole cell compression was 2300 nN for these highly contractile myoblasts. This is in comparison to lower forces reported for less contractile cells (at the same level of whole cell compression); 500 nN for endothelial cells (Caille et al. (2002)) and 350 nN for fibroblasts (Deng et al. (2010)). This trend suggests that highly contractile cells provide a greater resistance to applied whole cell compression. This technique has also been used to investigate the role of the cytoskeleton to global compressive deformation using selective cytoskeletal inhibitors. Ofek et al. (2009) found that the actin cytoskeleton plays a

significant role (~50%) in the compressive stiffness of cell, whereas microtubules and intermediate filaments had little effect on this parameter.

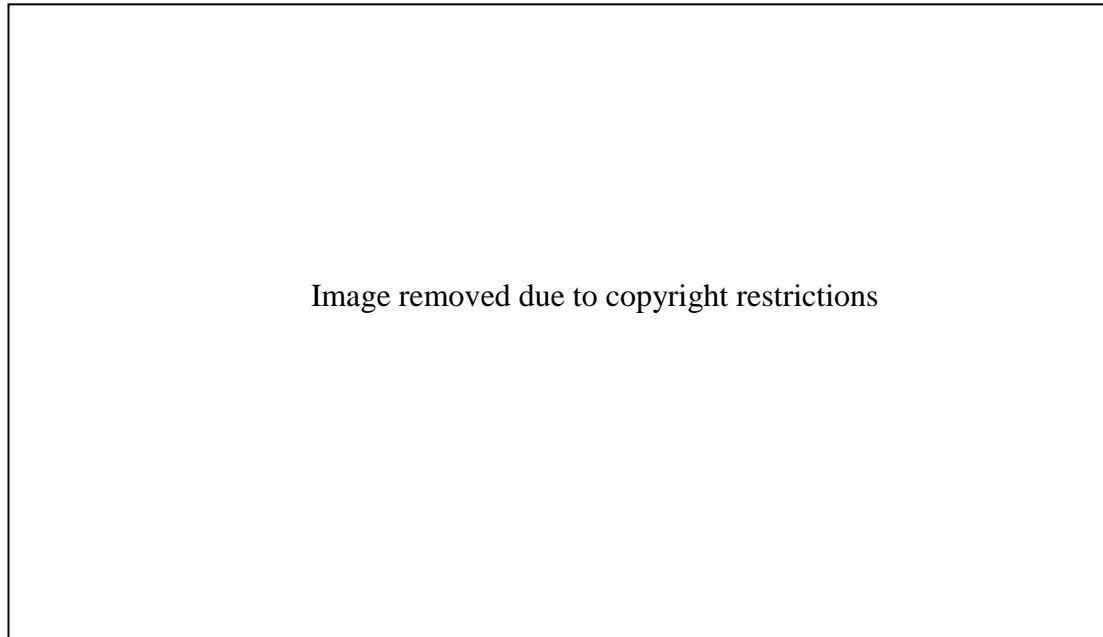


Figure 2.8: (a) The microplate manipulation system and (b) images of a fibroblast between the microplates. The cell was lowered towards the flexible plate (bottom plate) and incubated for 6 min. At time 0, the rigid plate was moved upwards through 12  $\mu\text{m}$  in 10 s and maintained for 1 hr. The scale bar represents 5  $\mu\text{m}$ . Adapted from Thoumine and Ott (1997).

The specific contribution of passive viscoelasticity and active cell contraction has been distinguished in cells using the aforementioned technique (Thoumine and Ott (1997), Micoulet et al. (2005), Peeters et al. (2005b), Fernández and Ott (2008)).

By performing dynamic compression and stretch experiments (

Figure 2.8 (b)), Thoumine and Ott (1997) found that fibroblasts have an initial elastic response (seconds), followed by a viscous behaviour (minutes), and finally a contractile regime in which actin-dependent traction forces were developed (tens of minutes). It is also suggested that the time scale and the rate of applied load are critical determinants of the resultant mechanical measurements, as also suggested by the findings of Peeters et al. (2005b) on myoblast cells. The cellular response to cyclic loading has also been investigated using this technique. Fernández et al. (2006) have shown that applying small amplitude oscillations on a mechanically prestressed fibroblast resulted in a transition from viscoelastic behaviour to a stress

stiffening behaviour. A study by Micoulet et al. (2005) demonstrated that repeated step-stretching resulted in the recruitment of cell-contractile elements upon mechanical stimulation, and the actin cytoskeleton becomes increasingly cross-linked in response to mechanical stretch. Furthermore, Mitrossilis et al. (2009) found that the response of myoblasts to stiffness exhibited a muscle-like behaviour, Figure 2.9. Isolated myoblasts were seeded between a rigid plate and flexible probes. The stiffness ( $k$ ) of the flexible probe varied between experiments. It was demonstrated that the tension-velocity relationship of the cells obeyed a Hill-type relationship, similar to that observed for skeletal muscle (Hill (1938)). The biochemical response of cells to whole cell static and cyclic stimulation has also been demonstrated with the microplates. Shieh and Athanasiou (2007) report that static compression of chondrocytes results in a decrease in gene expression (aggrecan and collagen), however interestingly, an up-regulation of gene expression is observed during dynamic compression of the same cell type.

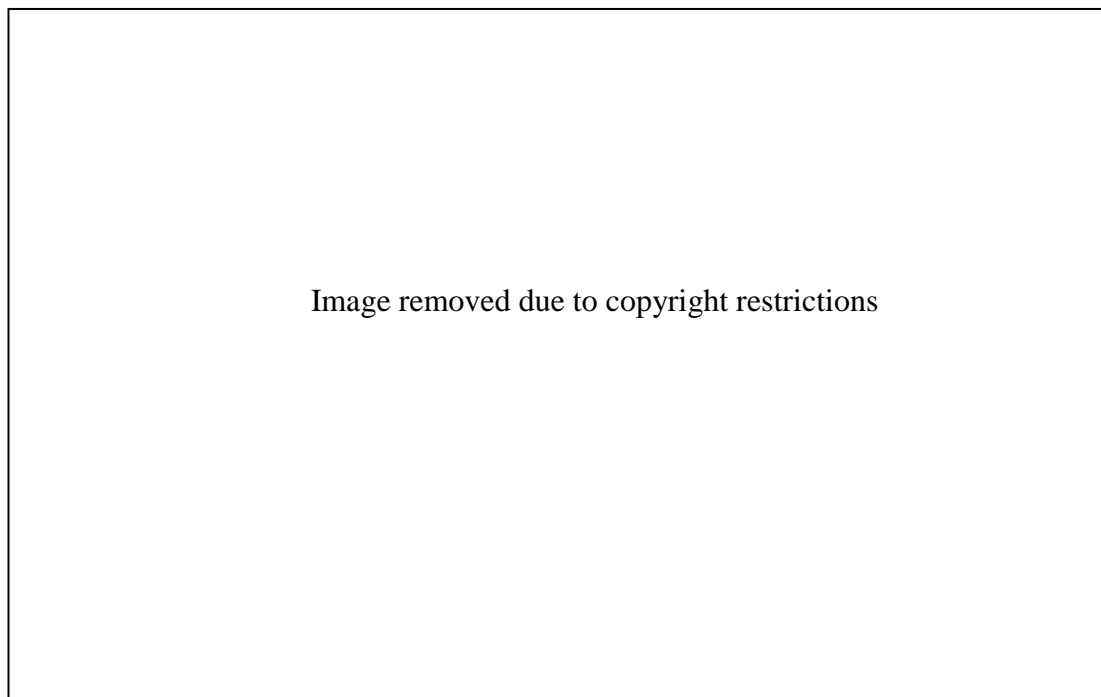


Figure 2.9: (a) Cell traction forces measured over time for a myoblast seeded between two plates. The stiffness ( $k$ ) of the flexible (top) probe was changed for each experiment. The plateau force ( $F_p$ ) and rate of force increase ( $\frac{dF}{dt}$ ) increased with increased probe stiffness ( $k$ ). (b) Following normalisation of the data, the speed of cell shortening (open squares) and mechanical power (filled circles) as a

function of the load were found to fit the Hill equation of muscle contraction (solid lines). Adapted from Mitrossilis et al. (2009).

The advantage of the microplate technique is that it allows a wide range of different mechanical stimulation profiles to be tested. However, as force measurements are generally calculated by video analysis of probe deflection the accuracy is limited to a maximum precision of 1-10 nN and measurements are susceptible to human error during deflection interpretation. Additionally, the nominal strain imparted on the cell cannot be accurately controlled due to significant deflections of the flexible probe during compression.

#### **2.4.4 Atomic Force Microscopy**

Developed originally by Binnig et al. (1986), AFM is a high resolution form of scanning probe microscopy. AFM was originally developed to be a qualitative imaging tool, in which information about the sample is gathered by ‘feeling’ the surface with a mechanical probe. However, AFM is now also an established technique in the field of cell mechanics for measuring localised cell mechanics with unrivalled force and displacement precision (Colton et al. (1997), Lim et al. (2006), Simon and Durrieu (2006)). As will be presented in Chapter 3, this system also has the potential to be an important technique for measuring whole cell mechanics.

The principle components of the AFM are (i) the flexible cantilever at the end of which a sharp tip is typically mounted (mechanical probe), (ii) the cantilever deflection detection system, usually consisting of a laser diode and a position sensitive detector (PSD), and (iii) the sub-nanometre precision positioning of the cantilever (z-axis) and sample stage (x-y axis) using piezoelectric actuation (Figure 2.10). As illustrated in Figure 2.10, a laser beam is reflected off the back of the cantilever onto a four quadrant PSD, permitting the measurement of both normal (vertical) bending and torsion of the cantilever with accuracy on the order of 0.1 nm (Lim et al. (2006), Mostaert et al. (2006)). Forces of between  $10^{-7}$  and  $10^{-15}$  N can be measured using AFM (Colton et al. (1997), Simon and Durrieu (2006)). During AFM operation, the position of the cantilever is controlled by a piezoelectric actuator which moves relative to the sample in three dimensions.

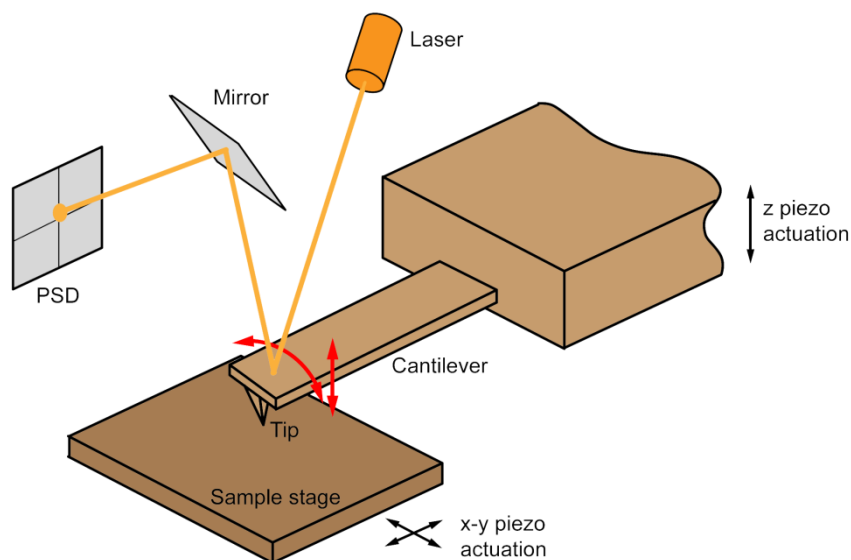


Figure 2.10: Schematic illustrating the basic principles of AFM.

Since the AFM was adapted for use in liquid environments, it has become a valuable tool for studying biological materials (Alessandrini and Facci (2005)). Its most common use in the field of cell mechanics has been to measure and compare the characteristic differences in both the elastic and viscous properties of various cell types (Radmacher et al. (1996), Rotsch et al. (1997), Hofmann et al. (1997), Lulevich et al. (2006), Jaasma et al. (2007), Darling et al. (2008), Deng et al. (2010), Prabhune et al. (2012)). As the technique is typically used to apply highly localised deformation to the cell membrane, it has also proved useful in confirming that cells are highly heterogeneous, with differences in the observed stiffness of the nucleus and cytoplasm (Sato et al. (2000), Yamane et al. (2000)) and due to the underlying cytoskeleton (McGarry et al. (2008)). Furthermore, AFM has been used to investigate the difference in mechanical properties between normal and diseases cells (Cross et al. (2008), Li et al. (2008)). A study by Prabhune et al. (2012) found that malignant thyroid cells were  $\sim 5$ -fold softer than primary normal thyroid cells. Additionally, the observed actin cytoskeleton was also found to be different between the healthy and diseased cells. The change in mechanical properties of cells has also been investigated during the cell cycle. A study by Kelly et al. (2011) reports that both the elasticity and morphology of bone cells changes during the cell cycle. Cells in S phase were found to have a modulus 1.7 times that of G1 cells, this correlated

with an increase in actin concentration during the cell cycle. It was also found that both the cytoplasm and overall cell height increased between G1 and S phase.

To elucidate how the mechanical properties of a cell are related to the structure and function of the underlying cytoskeleton a number of studies have employed chemical treatments or genetic mutations that target particular cytoskeletal components (Hofmann et al. (1997), Goldmann et al. (1998), Charras and Horton (2002), Roca-Cusachs et al. (2008), Watanabe-Nakayama et al. (2011)). A study by Rotsch and Radmacher (2000) investigated the effects of disrupting different cytoskeleton components on the stiffness of fibroblasts. It was found that the addition of actin-targeted drugs made the cell softer whereas microtubule-targeted drugs produced no mechanical changes. Additionally, Goldmann et al. (1998) reported that the elastic modulus of vinculin-deficient cells was lower than that of control cells, but when vinculin expression was reinstated, cells recovered an elastic modulus close to that of the control cells. This result shows that vinculin, known to connect integrins to the actin filaments, stabilises the focal adhesion structure as well as transferring mechanical stresses to the cytoskeleton network. An AFM study by Wakatsuki et al. (2003) found that inhibiting myosin activation reduced the stiffness of spreading fibroblasts. It is proposed that this was due to a decrease in the crosslinking of actin filaments and myosin. It was also found that this decrease in stiffness resulted in an increased cell deformability and an increased rate of cell spreading. AFM indentation has also been used to investigate the mechanical properties of stem cells during differentiation. Titushkin and Cho (2007) found that osteo-differentiation of human mesenchymal stem cells (hMSC) caused a decrease in cell elasticity and an increase in membrane-cytoskeleton interaction. These modulations were related to remodelling of the actin cytoskeleton from thick stress fibres in stem cells into the thinner filamentous networks in osteoblasts.

Further enhancing the importance of AFM as a technique for cell mechanics, AFM can be combined with fluorescent microscopy to simultaneously apply localised strain and visualise the cells response (Trache and Meininger (2005), Haupt et al. (2006), Pelling et al. (2007)). Using this combined technique, studies have monitored the real-time intracellular nitric oxide and calcium ion response to applied

loading, thus allowing the correlation of localised mechanical deformation and biochemical signal transduction. McGarry et al. (2008) observed a location specific response to applied indentation. It was found that indentation on rigid locations of the osteoblast membrane correlated with activation of nitric oxide, suggesting that the cytoskeleton is involvement in nitric oxide transduction. A similar study was performed by Charras and Horton (2002) to stimulate intracellular calcium responses in osteoblasts. Two cell response pathways were found; during AFM probe contact with the cell (dependent on activation of stretch-activated ion channels) and following stress relaxation (required an intact microtubule cytoskeleton). Furthermore, it was found that the cell response was dependent on the indentation strain magnitude. More recently, Sato et al. (2007) found that the calcium response was deformation velocity dependent and the cells responded with a higher sensitivity to a higher velocity. Using the aforementioned technique, Watanabe-Nakayama et al. (2011) applied step-stretching to localised regions of fibroblasts. When the cytoskeleton was disrupted using cyto-D or blebbistatin (an inhibitor of myosin II ATPase activity), a passive viscoelastic type relaxation of the cell force over time was observed. For untreated cells, with an intact contractile actin cytoskeleton, a passive force relaxation was not observed; rather, a gradual increase in measured force was reported, which correlated with an increase in F-actin in the cell. Similar findings were also reported in the microplate studies by Micoulet et al. (2005) and Thoumine and Ott (1997).

AFM force spectroscopy measurements are typically performed using a sharp tip or small colloid to measure the response of cells to localised deformation (Bao and Suresh (2003), Titushkin and Cho (2007), Darling et al. (2008), Roca-Cusachs et al. (2008), Prabhune et al. (2012)). However, this technique can be extended to the study of whole cell mechanics by taking force map arrays over the entire cell surface (Radmacher et al. (1996), Hofmann et al. (1997), Rotsch and Radmacher (2000), Kelly et al. (2011)). Although measuring data over large areas with sufficient resolution generally requires acquisition times comparable to those associated with remodelling of the cytoskeleton. Also, individual curves within a force map depend greatly upon the local environment and its position relative to the underlying

cytoskeletal components, often resulting in measurements spanning an order of magnitude within a single force map. In an effort to overcome these problems, a number of studies have attached a sphere (less than  $\text{\O}60\ \mu\text{m}$ ) to the end of the AFM cantilever (Lehenkari et al. (2000), Lulevich et al. (2006), Jaasma et al. (2006), Zimmer et al. (2012)). While providing an improvement on AFM tip measurements, the contact radius between these spheres and the cell will typically be smaller than the cell diameter, hence measurements still suffer the drawback of significant localisation. In Chapter 3, a significantly larger sphere of diameter  $150\ \mu\text{m}$  is attached to an AFM cantilever in order to perform whole cell compression of osteoblasts. The contact radius between such a large sphere and a cell is of the same order as the cell radius. Hence, compression of a cell with such a large sphere provides a reasonable approximation of parallel plate cell compression.

## 2.5 Mechanical Stimulation in Bone

Mechanical stimulation is considered essential for bone homeostasis, growth, healing and remodelling (Frost (2004)). Age-related bone loss and subsequent osteoporosis have been attributed, at least in part, to a reduction in muscle mass/function and the resultant decrease in mechanical usage of the skeleton (Zerwekh et al. (2009), Burr (1997)). On the other hand, mechanical overloading has been shown to enhance bone formation and cause an overall gain in cancellous bone mass, the major structural component of skeletal load-bearing sites (Lanyon (1996), Courteix et al. (1998)). In the body, bone cells are exposed to a dense matrix composed primarily of mineralised type I collagen. As osteoblasts deposit this matrix, they become trapped and differentiate into osteocytes. Osteocytes live in pockets of un-mineralised matrix known as lacunae and connect with adjacent osteocytes and bone-lining cells through small protrusions known as canaliculi, forming an interconnected network of cells throughout the bone.

The response of bone cells to mechanical loading occurs over a range of time scales; from seconds to days (Charras and Horton (2002), Gabbay et al. (2006), Sato et al. (2007), Rath et al. (2008)). Mechanosensitive responses include changes in gene expression, proteins, enzymes, and signalling molecules associated with

osteoblasts and osteocyte function. Mechanical stimulation of bone is transmitted through the extracellular matrix to resident osteocytes, osteoblasts, and osteoclast; however it is still unclear what form of mechanical loading bone cells are subjected to during physiological loading. It is generally accepted to be a strain as a result of deformation of the extracellular matrix (Duncan and Turner (1995), Owan et al. (1997)) and strain-induced fluid flow through the lacunar-canalicular network (Burger and Klein-Nulend (1999), Hillsley and Frangos (2004)). Furthermore, it remains to be elucidated what bone cell type are the main regulator of bone mechanotransduction. Mechanically stimulated osteocytes are known to express multiple paracrine factors that stimulate osteoblast function and bone formation including nitric oxide, prostaglandin E2 (PGE2), and insulin-like growth factor. Osteoclast activity is decreased in mechanically stimulated bone through both positive and negative factors released by osteocytes, though little is known about these factors (Raisz (1999)).

*In vivo* studies have demonstrated the effects of compressive forces on bone, which include increased mineralisation and fracture stiffness during fracture healing (Egger et al. (1993), Rubin et al. (2006), Gardner et al. (2006)). Furthermore, animal studies have demonstrated that strain rate is more important than strain amplitude to induce bone formation in response to loading (Mosley and Lanyon (1998)). This is consistent with pulsatile fluid flow studies of cell *in vitro* (Kaspar et al. (2002), Bacabac et al. (2004), Mullender et al. (2006)). Furthermore, studies using tissue constructs have shown that long-term compressive forces induced mineralisation (Gabbay et al. (2006)) while cyclic loading enhanced differentiation of osteoblastic cells (Rath et al. (2008)). A study by Mullender et al. (2004) describe the response of primary osteoblasts to both pulsatile fluid flow and cyclic mechanical strain over 1 hr timeframes. In the strain experiments, it was found that collagen type I significantly increased, however nitric oxide and prostaglandin responses were unchanged. Interestingly, in the fluid flow experiments, the opposite responses were observed: an increase in nitric oxide and prostaglandin, and down-regulation of collagen type I. This suggests that bone cells can distinguish modes of loading, perhaps via activation of different signal transduction pathways.

Studies in which osteoblasts have been investigated at the single cell level have also demonstrated responses to mechanical loading. Localised probing of the cell membrane was found to result in intracellular calcium ion and nitric oxide signalling (Charras and Horton (2002), Sato et al. (2007), Adachi et al. (2008), McGarry et al. (2008). Interestingly, McGarry et al. (2008) reports that nitric oxide signalling was associated with the application of force to more rigid membrane sites, suggesting cytoskeletal involvement in mechanotransduction. Furthermore, Sato et al. (2007) reported that the cellular response was more sensitive to higher deformation velocity.

Although such studies highlight the importance of mechanical stimuli in bone homeostasis and remodelling, the underlying mechanisms in which osteoblasts respond to mechanical stimuli are still poorly understood. Based on the literature discussed in this chapter, it is hypothesised that the cytoskeleton, in particular the actin cytoskeleton, plays an important role in the cellular response to mechanical stimulation. The studies reported in the thesis aim to parse the contribution of the actin cytoskeleton in osteoblasts to mechanical deformation in order to gain further insight into the biomechanical behaviour of cells to mechanical stimuli. This could provide unique insight into bone remodelling mechanisms, diseases in which they are affected, as well as bone tissue engineering.

## **2.6 Conclusions**

In this chapter, an overview of the structural components of the cell is presented. A particular emphasis is placed on the actin cytoskeleton since it has been shown to play a critical role in the behaviour of cells to mechanical stimuli. The processes by which a cell responds to mechanical loading are also discussed. Furthermore, a review of experimental techniques in which mechanical stimulation is directly applied at the single cell level is presented. Relevant findings obtained using these techniques are also highlighted. Finally, an outline of the important role of mechanical stimulation in bone biomechanics is presented. It should again be noted that further detailed and focused discussion of directly relevant literature is provided in each technical chapter of this thesis (Chapters 3-6).

Despite the numerous experimental techniques developed to investigate cell mechanics, the biomechanical response of cells to mechanical stimuli is still poorly understood. A technique which is becoming increasingly important in the field of cell mechanics is AFM. However, standard AFM systems apply highly localised nano-scale deformation of the cell membrane, hence provide limited insight into biomechanical behaviour at a whole cell level. Adapting the AFM to apply non-localised whole cell deformation would provide physiologically relevant loadings with unrivalled precision in terms of applied displacement and measured force. In this thesis, the developmental steps to enhance the AFM technique to investigate whole cell mechanics are presented. This modified system is then used to gain a more in-depth understanding of the role of the actin cytoskeleton in cell biomechanics under both static and dynamic loading conditions by performing novel *in vitro* whole cell experiments.

## 2.7 References

- Adachi, T., Sato, K., Higashi, N., Tomita, Y. and Hojo, M. (2008) Simultaneous observation of calcium signaling response and membrane deformation due to localized mechanical stimulus in single osteoblast-like cells. *Journal of the Mechanical Behavior of Biomedical Materials*. 1 (1), 43-50
- Alberts, B., Bray, D., Lewis, J., Raff, M., Roberts, K. and Watson, J., (2002) Molecular biology of the cell, Garland Publishing Inc., New York, 4th Edition.
- Alcaraz, J., Buscemi, L., Grabulosa, M., Trepast, X., Fabry, B., Farré, R. and Navajas, D. (2003) Microrheology of human lung epithelial cells measured by atomic force microscopy. 84 (3), 2071-2079
- Alessandrini, A. and Facci, P. (2005) Afm: A versatile tool in biophysics. *Measurement science and technology*. 16 (6), R65
- Anaphase, B. (2000) Microtubule motors in mitosis. *Nature*. 407 (1), 41-47
- Bacabac, R. G., Mizuno, D., Schmidt, C. F., MacKintosh, F. C., Van Loon, J. J. W. A., Klein-Nulend, J. and Smit, T. H. (2008) Round versus flat: Bone cell morphology, elasticity, and mechanosensing. *Journal of Biomechanics*. 41 (7), 1590-1598
- Bacabac, R. G., Smit, T. H., Mullender, M. G., Dijcks, S. J., Van Loon, J. J. W. A. and Klein-Nulend, J. (2004) Nitric oxide production by bone cells is fluid shear stress rate dependent. *Biochemical and Biophysical Research Communications*. 315 (4), 823-829
- Balaban, N. Q., Schwarz, U. S., Riveline, D., Goichberg, P., Tzur, G., Sabanay, I., Mahalu, D., Safran, S., Bershadsky, A. and Addadi, L. (2001) Force and focal adhesion assembly: A close relationship studied using elastic micropatterned substrates. *Nat Cell Biol*. 3 (5), 466-472
- Balestrini, J. L. and Billiar, K. L. (2009) Magnitude and duration of stretch modulate fibroblast remodeling. *Journal of Biomechanical Engineering*. 131 (5), 51005
- Balestrini, J. L., Skorinko, J. K., Hera, A., Gaudette, G. R. and Billiar, K. L. (2010) Applying controlled non-uniform deformation for in vitro studies of cell mechanobiology. *Biomechanics and Modeling in Mechanobiology*. 9 (3), 329-344
- Bao, G. and Suresh, S. (2003) Cell and molecular mechanics of biological materials. *Nature materials*. 2 (11), 715-725
- Barron, V., Brougham, C., Coghlan, K., McLucas, E., O'Mahoney, D., Stenson-Cox, C. and McHugh, P. (2007) The effect of physiological cyclic stretch on the

- cell morphology, cell orientation and protein expression of endothelial cells. *Journal of Materials Science: Materials in Medicine*. 18 (10), 1973-1981
- Binnig, G., Quate, C. F. and Gerber, C. (1986) Atomic force microscope. *Physical Review Letters*. 56 (9), 930-933
- Blain, E. J. (2009) Involvement of the cytoskeletal elements in articular cartilage homeostasis and pathology. *International journal of experimental pathology*. 90 (1), 1-15
- Burger, E. H. and Klein-Nulend, J. (1999) Mechanotransduction in bone-role of the lacuno-canalicular network. *The FASEB journal*. 13 (9001), S101-S112
- Burr, D. B. (1997) Muscle strength, bone mass, and age-related bone loss. *Journal of Bone and Mineral Research*. 12 (10), 1547-1551
- Burridge, K. and Chrzanowska-Wodnicka, M. (1996) Focal adhesions, contractility, and signaling. *Annual review of cell and developmental biology*. 12 (1), 463-519
- Burridge, K. and Wennerberg, K. (2004) Rho and rac take center stage. *Cell*. 116 (2), 167-179
- Buxboim, A., Rajagopal, K., Brown, A. E. and Discher, D. E. (2010) How deeply cells feel: Methods for thin gels. *J Phys Condens Matter*. 22 (19), 194116
- Caille, N., Thoumine, O., Tardy, Y. and Meister, J. J. (2002) Contribution of the nucleus to the mechanical properties of endothelial cells. *J. Biomech*. 35 (2), 177-187
- Charras, G. T. and Horton, M. A. (2002) Single cell mechanotransduction and its modulation analyzed by atomic force microscope indentation. *Biophys. J*. 82 (6), 2970-2981
- Colton, R. J., Baselt, D. R., Dufrêne, Y. F., Green, J. B. D. and Lee, G. U. (1997) Scanning probe microscopy. *Current opinion in chemical biology*. 1 (3), 370-377
- Courteix, D., Lespessailles, E., Peres, S. L., Obert, P., Germain, P. and Benhamou, C. (1998) Effect of physical training on bone mineral density in prepubertal girls: A comparative study between impact-loading and non-impact-loading sports. *Osteoporosis international*. 8 (2), 152-158
- Cross, S. E., Jin, Y. S., Tondre, J., Wong, R., Rao, J. Y. and Gimzewski, J. K. (2008) Afm-based analysis of human metastatic cancer cells. *Nanotechnology*. 19 (38), 384003

- Darling, E., Zauscher, S. and Guilak, F. (2006) Viscoelastic properties of zonal articular chondrocytes measured by atomic force microscopy. *Osteoarthritis and Cartilage*. 14 (6), 571-579
- Darling, E. M., Topel, M., Zauscher, S., Vail, T. P. and Guilak, F. (2008) Viscoelastic properties of human mesenchymally-derived stem cells and primary osteoblasts, chondrocytes, and adipocytes. *J. biomech.* 41 (2), 454-464
- Deng, Z., Lulevich, V., Liu, F.-T. and Liu, G.-Y. (2010) Applications of atomic force microscopy in biophysical chemistry of cells. *The Journal of Physical Chemistry B*. 114 (18), 5971-5982
- Discher, D., Dong, C., Fredberg, J. J., Guilak, F., Ingber, D., Janmey, P., Kamm, R. D., Schmid-Schönbein, G. W. and Weinbaum, S. (2009) Biomechanics: Cell research and applications for the next decade. *Annals of biomedical engineering*. 37 (5), 847-859
- Dowling, E. P., Ronan, W., Ofek, G., Deshpande, V. S., Athanasiou, K. A., McMeeking, R. M. and McGarry, J. P. (2012) The effect of remodelling and contractility of the actin cytoskeleton on the shear resistance of single cells: A computational and experimental investigation. *J. R. Soc. Interface*. 9 (77), 3469-3479
- Duncan, R. and Turner, C. (1995) Mechanotransduction and the functional response of bone to mechanical strain. *Calcified tissue international*. 57 (5), 344-358
- Egger, E. L., Gottsauner-Wolf, F., Palmer, J., Aro, H. T. and Chao, E. (1993) Effects of axial dynamization on bone healing. *The Journal of trauma*. 34 (2), 185
- Féréol, S., Fodil, R., Laurent, V. M., Balland, M., Louis, B., Pelle, G., Hénon, S., Planus, E. and Isabey, D. (2009) Prestress and adhesion site dynamics control cell sensitivity to extracellular stiffness. *Biophysical Journal*. 96 (5), 2009-2022
- Fernández, P. and Ott, A. (2008) Single cell mechanics: Stress stiffening and kinematic hardening. *Physical Review Letters*. 100 (23), 238102
- Fernández, P., Pullarkat, P. A. and Ott, A. (2006) A master relation defines the nonlinear viscoelasticity of single fibroblasts. *Biophysical Journal*. 90 (10), 3796-3805
- Flavahan, N. A., Bailey, S. R., Flavahan, W. A., Mitra, S. and Flavahan, S. (2005) Imaging remodeling of the actin cytoskeleton in vascular smooth muscle cells after mechanosensitive arteriolar constriction. *American Journal of Physiology-Heart and Circulatory Physiology*. 288 (2), H660-H669
- Fletcher, D. A. and Mullins, R. D. (2010) Cell mechanics and the cytoskeleton. *Nature*. 463 (7280), 485-492

- Frost, H. M. (2004) A 2003 update of bone physiology and Wolff's law for clinicians. *The Angle Orthodontist*. 74 (1), 3-15
- Gabbay, J. S., Zuk, P. A., Tahernia, A., Askari, M., O'Hara, C. M., Karthikeyan, T., Azari, K., Hollinger, J. O. and Bradley, J. P. (2006) In vitro microdistraction of preosteoblasts: Distraction promotes proliferation and oscillation promotes differentiation. *Tissue Engineering*. 12 (11), 3055-3065
- Gardner, M. J., van der Meulen, M. C. H., Demetrakopoulos, D., Wright, T. M., Myers, E. R. and Bostrom, M. P. (2006) In vivo cyclic axial compression affects bone healing in the mouse tibia. *Journal of Orthopaedic Research*. 24 (8), 1679-1686
- Geiger, B. and Bershadsky, A. (2001) Assembly and mechanosensory function of focal contacts. *Current Opinion in Cell Biology*. 13 (5), 584-592
- Girard, P. P., Cavalcanti-Adam, E. A., Kemkemer, R. and Spatz, J. P. (2007) Cellular chemomechanics at interfaces: Sensing, integration and response. *Soft Matter*. 3 (3), 307-326
- Goffin, J. M., Pittet, P., Csucs, G., Lussi, J. W., Meister, J. J. and Hinz, B. (2006) Focal adhesion size controls tension-dependent recruitment of  $\alpha$ -smooth muscle actin to stress fibers. *The Journal of Cell Biology*. 172 (2), 259-268
- Goldmann, W. H., Galneder, R., Ludwig, M., Xu, W., Adamson, E. D., Wang, N. and Ezzell, R. M. (1998) Differences in elasticity of vinculin-deficient f9 cells measured by magnetometry and atomic force microscopy. *Experimental Cell Research*. 239 (2), 235-242
- Guilak, F. (1995) Compression-induced changes in the shape and volume of the chondrocyte nucleus. *Journal of Biomechanics*. 28 (12), 1529-1541
- Guilak, F., Tedrow, J. R. and Burgkart, R. (2000) Viscoelastic properties of the cell nucleus. *Biochemical and Biophysical Research Communications*. 269 (3), 781-786
- Haupt, B. J., Pelling, A. E. and Horton, M. A. (2006) Integrated confocal and scanning probe microscopy for biomedical research. *The Scientific World Journal*. 6, 1609-1618
- Hill, A. (1938) The heat of shortening and the dynamic constants of muscle. *Proceedings of the Royal Society of London. Series B, Biological Sciences*. 126 (843), 136-195
- Hillam, R. A. and Skerry, T. M. (1995) Inhibition of bone resorption and stimulation of formation by mechanical loading of the modeling rat ulna in vivo. *Journal of Bone and Mineral Research*. 10 (5), 683-689

- Hillsley, M. and Frangos, J. (2004) Review: Bone tissue engineering: The role of interstitial fluid flow. *Biotechnology and Bioengineering*. 43 (7), 573-581
- Hirokawa, N. (1998) Kinesin and dynein superfamily proteins and the mechanism of organelle transport. *Science*. 279 (5350), 519-526
- Hochmuth, R. M. (2000) Micropipette aspiration of living cells. *Journal of Biomechanics*. 33 (1), 15-22
- Hofmann, U. G., Rotsch, C., Parak, W. J. and Radmacher, M. (1997) Investigating the cytoskeleton of chicken cardiocytes with the atomic force microscope. *Journal of Structural Biology*. 119 (2), 84-91
- Hsieh, Y. F. and Turner, C. H. (2001) Effects of loading frequency on mechanically induced bone formation. *Journal of Bone and Mineral Research*. 16 (5), 918-924
- Hsu, H. J., Lee, C. F., Locke, A., Vanderzyl, S. Q. and Kaunas, R. (2010) Stretch-induced stress fiber remodeling and the activations of jnk and erk depend on mechanical strain rate, but not fak. *PLoS One*. 5 (8),
- Huang, H., Kamm, R. D. and Lee, R. T. (2004) Cell mechanics and mechanotransduction: Pathways, probes, and physiology. *American Journal of Physiology-Cell Physiology*. 287 (1), C1-C11
- Huang, L., Mathieu, P. S. and Helmke, B. P. (2010) A stretching device for high-resolution live-cell imaging. *Annals of biomedical engineering*. 38 (5), 1728-1740
- Ingber, D. E. (2003) Mechanobiology and diseases of mechanotransduction. *Annals of Medicine*. 35 (8), 564-577
- Ingber, D. E. (2006) Cellular mechanotransduction: Putting all the pieces together again. *The FASEB journal*. 20 (7), 811-827
- Iqbal, J. and Zaidi, M. (2005) Molecular regulation of mechanotransduction. *Biochemical and Biophysical Research Communications*. 328 (3), 751-755
- Jaasma, M. J., Jackson, W. M. and Keaveny, T. M. (2006) Measurement and characterization of whole-cell mechanical behavior. *Annals of biomedical engineering*. 34 (5), 748-758
- Jaasma, M. J., Jackson, W. M., Tang, R. Y. and Keaveny, T. M. (2007) Adaptation of cellular mechanical behavior to mechanical loading for osteoblastic cells. *Journal of Biomechanics*. 40 (9), 1938-1945
- Janmey, P. A. and McCulloch, C. A. (2007) Cell mechanics: Integrating cell responses to mechanical stimuli. *Annu. Rev. Biomed. Eng.* 9, 1-34

- Kaspar, D., Seidl, W., Neidlinger-Wilke, C., Beck, A., Claes, L. and Ignatius, A. (2002) Proliferation of human-derived osteoblast-like cells depends on the cycle number and frequency of uniaxial strain. *Journal of Biomechanics*. 35 (7), 873-880
- Kaunas, R., Nguyen, P., Usami, S. and Chien, S. (2005) Cooperative effects of rho and mechanical stretch on stress fiber organization. *Proc. Natl. Acad. Sci.* 102 (44), 15895-15900
- Kelly, G. M., Kilpatrick, J. I., van Es, M. H., Weafer, P. P., Prendergast, P. J. and Jarvis, S. P. (2011) Bone cell elasticity and morphology changes during the cell cycle. *J. Biomech.* 44 (8), 1484-1490
- Krishnan, R., Park, C. Y., Lin, Y. C., Mead, J., Jaspers, R. T., Trepatt, X., Lenormand, G., Tambe, D., Smolensky, A. V. and Knoll, A. H. (2009) Reinforcement versus fluidization in cytoskeletal mechanoresponsiveness. *PLoS One*. 4 (5), e5486
- Kumar, S., Maxwell, I. Z., Heisterkamp, A., Polte, T. R., Lele, T. P., Salanga, M., Mazur, E. and Ingber, D. E. (2006) Viscoelastic retraction of single living stress fibers and its impact on cell shape, cytoskeletal organization, and extracellular matrix mechanics. *Biophysical Journal*. 90 (10), 3762-3773
- Kurpinski, K., Chu, J., Hashi, C. and Li, S. (2006) Anisotropic mechanosensing by mesenchymal stem cells. *Proceedings of the National Academy of Sciences*. 103 (44), 16095-16100
- Lammerding, J. (2011) Mechanics of the nucleus. *Comprehensive Physiology*. 783-807
- Lammi, M. J. (2004) Current perspectives on cartilage and chondrocyte mechanobiology. *Biorheology*. 41 (3-4), 593-596
- Lanyon, L. (1996) Using functional loading to influence bone mass and architecture: Objectives, mechanisms, and relationship with estrogen of the mechanically adaptive process in bone. *Bone*. 18 (1), S37-S43
- Lee, C. F., Haase, C., Deguchi, S. and Kaunas, R. (2010) Cyclic stretch-induced stress fiber dynamics - dependence on strain rate, rho-kinase and mlck. *Biochemical and Biophysical Research Communications*. 401 (3), 344-349
- Lehenkari, P. P., Charras, G. T., Nykänen, A. and Horton, M. A. (2000) Adapting atomic force microscopy for cell biology. *Ultramicroscopy*. 82 (1-4), 289-295
- Li, Q., Lee, G., Ong, C. and Lim, C. (2008) Afm indentation study of breast cancer cells. *Biochemical and Biophysical Research Communications*. 374 (4), 609-613

- Liedert, A., Kaspar, D., Blakytyn, R., Claes, L. and Ignatius, A. (2006) Signal transduction pathways involved in mechanotransduction in bone cells. *Biochemical and Biophysical Research Communications*. 349 (1), 1-5
- Lim, C. T., Zhou, E. H., Li, A., Vedula, S. R. K. and Fu, H. X. (2006) Experimental techniques for single cell and single molecule biomechanics. *Materials Science and Engineering: C*. 26 (8), 1278-1288
- Lo, C. M., Wang, H. B., Dembo, M. and Wang, Y. (2000) Cell movement is guided by the rigidity of the substrate. *Biophysical Journal*. 79 (1), 144-152
- Lulevich, V., Zink, T., Chen, H. Y., Liu, F. T. and Liu, G. (2006) Cell mechanics using atomic force microscopy-based single-cell compression. *Langmuir*. 22 (19), 8151-8155
- Makale, M. (2007) Cellular mechanobiology and cancer metastasis. *Birth Defects Res C Embryo Today*. 81 (4), 329-43
- Mann, J. M., Lam, R. H. W., Weng, S., Sun, Y. and Fu, J. (2012) A silicone-based stretchable micropost array membrane for monitoring live-cell subcellular cytoskeletal response. *Lab on a Chip*. 12 (4), 731-740
- Martini, F. H., (2004) Fundamentals of anatomy and physiology, Benjamin Cummings Inc., San Francisco, 6th Edition.
- McGarry, J. G., Maguire, P., Campbell, V. A., O'Connell, B. C., Prendergast, P. J. and Jarvis, S. P. (2008) Stimulation of nitric oxide mechanotransduction in single osteoblasts using atomic force microscopy. *J. Orthop. Res*. 26 (4), 513-521
- Micoulet, A., Spatz, J. P. and Ott, A. (2005) Mechanical response analysis and power generation by single-cell stretching. *ChemPhysChem*. 6 (4), 663-670
- Mitrossilis, D., Fouchard, J., Guirouy, A., Desprat, N., Rodriguez, N., Fabry, B. and Asnacios, A. (2009) Single-cell response to stiffness exhibits muscle-like behavior. *Proceedings of the National Academy of Sciences*. 106 (43), 18243-18248
- Miyazaki, H., Hasegawa, Y. and Hayashi, K. (2000) A newly designed tensile tester for cells and its application to fibroblasts. *Journal of Biomechanics*. 33 (1), 97-104
- Mofrad, M. R. K. (2009) Rheology of the cytoskeleton. *Annual Review of Fluid Mechanics*. 41 (1), 433-453
- Mosley, J. R. and Lanyon, L. E. (1998) Strain rate as a controlling influence on adaptive modeling in response to dynamic loading of the ulna in growing male rats. *Bone*. 23 (4), 313-318

- Mostaert, A., Higgins, M., Fukuma, T., Rindi, F. and Jarvis, S. (2006) Nanoscale mechanical characterisation of amyloid fibrils discovered in a natural adhesive. *Journal of Biological Physics*. 32 (5), 393-401
- Mullender, M., El Haj, A., Yang, Y., van Duin, M., Burger, E. and Klein-Nulend, J. (2004) Mechanotransduction of bone cells in vitro: Mechanobiology of bone tissue. *Medical and biological engineering and computing*. 42 (1), 14-21
- Mullender, M. G., Dijcks, S. J., Bacabac, R. G., Semeins, C. M., Van Loon, J. J. W. A. and Klein-Nulend, J. (2006) Release of nitric oxide, but not prostaglandin e2, by bone cells depends on fluid flow frequency. *Journal of Orthopaedic Research*. 24 (6), 1170-1177
- Na, S., Trache, A., Trzeciakowski, J., Sun, Z., Meininger, G. and Humphrey, J. (2008) Time-dependent changes in smooth muscle cell stiffness and focal adhesion area in response to cyclic equibiaxial stretch. *Annals of biomedical engineering*. 36 (3), 369-380
- Nagayama, K., Yanagihara, S. and Matsumoto, T. (2007) A novel micro tensile tester with feed-back control for viscoelastic analysis of single isolated smooth muscle cells. *Medical engineering & physics*. 29 (5), 620-628
- Nekouzadeh, A., Pryse, K. M., Elson, E. L. and Genin, G. M. (2008) Stretch-activated force shedding, force recovery, and cytoskeletal remodeling in contractile fibroblasts. *Journal of Biomechanics*. 41 (14), 2964-2971
- Noria, S., Xu, F., McCue, S., Jones, M., Gotlieb, A. I. and Langille, B. L. (2004) Assembly and reorientation of stress fibers drives morphological changes to endothelial cells exposed to shear stress. *The American journal of pathology*. 164 (4), 1211-1223
- O'Cearbhaill, E. D., Punchard, M. A., Murphy, M., Barry, F. P., McHugh, P. E. and Barron, V. (2008) Response of mesenchymal stem cells to the biomechanical environment of the endothelium on a flexible tubular silicone substrate. *Biomaterials*. 29 (11), 1610-1619
- Ofek, G., Wiltz, D. C. and Athanasiou, K. A. (2009) Contribution of the cytoskeleton to the compressive properties and recovery behavior of single cells. *Biophys. J*. 97 (7), 1873-1882
- Orr, A. W., Helmke, B. P., Blackman, B. R. and Schwartz, M. A. (2006) Mechanisms of mechanotransduction. *Developmental Cell*. 10 (1), 11-20
- Owan, I., Burr, D. B., Turner, C. H., Qiu, J., Tu, Y., Onyia, J. E. and Duncan, R. L. (1997) Mechanotransduction in bone: Osteoblasts are more responsive to fluid forces than mechanical strain. *American Journal of Physiology-Cell Physiology*. 273 (3), C810-C815

- Peeters, E. A. G., Bouten, C. V. C., Oomens, C. W. J. and Baaijens, F. P. T. (2003) Monitoring the biomechanical response of individual cells under compression: A new compression device. *Medical and biological engineering and computing*. 41 (4), 498-503
- Peeters, E. A. G., Oomens, C. W. J., Bouten, C. V. C., Bader, D. L. and Baaijens, F. P. T. (2005a) Mechanical and failure properties of single attached cells under compression. *J. Biomech.* 38 (8), 1685-1693
- Peeters, E. A. G., Oomens, C. W. J., Bouten, C. V. C., Bader, D. L. and Baaijens, F. P. T. (2005b) Viscoelastic properties of single attached cells under compression. *J Biomech Eng.* 127 (2), 237-243
- Prabhune, M., Belge, G., Dotzauer, A., Bullerdiek, J. and Radmacher, M. (2012) Comparison of mechanical properties of normal and malignant thyroid cells. *Micron*. 43 (12), 1267-1272
- Pravincumar, P., Bader, D. L. and Knight, M. M. (2012) Viscoelastic cell mechanics and actin remodelling are dependent on the rate of applied pressure. *PLoS One*. 7 (9), e43938
- Radmacher, M., Fritz, M., Kacher, C. M., Cleveland, J. P. and Hansma, P. K. (1996) Measuring the viscoelastic properties of human platelets with the atomic force microscope. *Biophys. J.* 70 (1), 556-567
- Raisz, L. G. (1999) Physiology and pathophysiology of bone remodeling. *Clinical Chemistry*. 45 (8), 1353-1358
- Ramaekers, F. and Bosman, F. T. (2004) The cytoskeleton and disease. *The Journal of pathology*. 204 (4), 351-354
- Rath, B., Nam, J., Knobloch, T. J., Lannutti, J. J. and Agarwal, S. (2008) Compressive forces induce osteogenic gene expression in calvarial osteoblasts. *Journal of biomechanics*. 41 (5), 1095-1103
- Reynolds, N. H., Ronan, W., Dowling, E. P. and McGarry, J. P., (2012) Investigation of the role of stress fiber contractility and nucleus geometry in the response of cells to micropipette aspiration, *Proceedings of the ASME Summer Bioengineering Conference*, El Conquistador Resort, Fajardo, Puerto Rico, USA, p. SBC2012-80899
- Roca-Cusachs, P., Alcaraz, J., Sunyer, R., Samitier, J., Farré, R. and Navajas, D. (2008) Micropatterning of single endothelial cell shape reveals a tight coupling between nuclear volume in g1 and proliferation. *Biophysical Journal*. 94 (12), 4984-4995
- Rotsch, C., Braet, F., Wisse, E. and Radmacher, M. (1997) Afm imaging and elasticity measurements on living rat liver macrophages. *Cell biology international*. 21 (11), 685-696

- Rotsch, C. and Radmacher, M. (2000) Drug-induced changes of cytoskeletal structure and mechanics in fibroblasts: An atomic force microscopy study. *Biophysical Journal*. 78 (1), 520-535
- Rubin, J., Rubin, C. and Jacobs, C. R. (2006) Molecular pathways mediating mechanical signaling in bone. *Gene*. 367, 1-16
- Sachs, F. (2010) Stretch-activated ion channels: What are they? *Physiology*. 25 (1), 50-56
- Saez, A., Ghibaudo, M., Buguin, A., Silberzan, P. and Ladoux, B. (2007) Rigidity-driven growth and migration of epithelial cells on microstructured anisotropic substrates. *Proceedings of the National Academy of Sciences*. 104 (20), 8281-8286
- Sato, K., Adachi, T., Shirai, Y., Saito, N. and Tomita, Y. (2006) Local disassembly of actin stress fibers induced by selected release of intracellular tension in osteoblastic cell. *Journal of Biomechanical Science and Engineering*. 1 (1), 204-214
- Sato, K., Adachi, T., Ueda, D., Hojo, M. and Tomita, Y. (2007) Measurement of local strain on cell membrane at initiation point of calcium signaling response to applied mechanical stimulus in osteoblastic cells. *Journal of Biomechanics*. 40 (6), 1246-1255
- Sato, M., Nagayama, K., Kataoka, N., Sasaki, M. and Hane, K. (2000) Local mechanical properties measured by atomic force microscopy for cultured bovine endothelial cells exposed to shear stress. *Journal of Biomechanics*. 33 (1), 127-135
- Shemesh, T., Geiger, B., Bershadsky, A. D. and Kozlov, M. M. (2005) Focal adhesions as mechanosensors: A physical mechanism. *Proc Natl Acad Sci U S A*. 102 (35), 12383-8
- Shieh, A. C. and Athanasiou, K. A. (2007) Dynamic compression of single cells. *Osteoarthritis and Cartilage*. 15 (3), 328-334
- Shin, D. and Athanasiou, K. A. (1999) Cytoindentation for obtaining cell biomechanical properties. *Journal of Orthopaedic Research*. 17 (6), 880-890
- Simon, A. and Durrieu, M. C. (2006) Strategies and results of atomic force microscopy in the study of cellular adhesion. *Micron*. 37 (1), 1-13
- Small, J. V., Rottner, K., Kaverina, I. and Anderson, K. (1998) Assembling an actin cytoskeleton for cell attachment and movement. *Biochimica et Biophysica Acta-Molecular Cell Research*. 1404 (3), 271-281
- Stamenović, D. (2008) Rheological behavior of mammalian cells. *Cellular and molecular life sciences*. 65 (22), 3592-3605

- Thorpe, S. D., Buckley, C. T., Vinardell, T., O'Brien, F. J., Campbell, V. A. and Kelly, D. J. (2010) The response of bone marrow-derived mesenchymal stem cells to dynamic compression following  $\text{tgf-}\beta\text{3}$  induced chondrogenic differentiation. *Annals of biomedical engineering*. 38 (9), 2896-2909
- Thoumine, O. and Ott, A. (1997) Time scale dependent viscoelastic and contractile regimes in fibroblasts probed by microplate manipulation. *J Cell Sci*. 110 (17), 2109-2116
- Throm-Quinlan, A. M., Sierad, L. N., Capulli, A. K., Firstenberg, L. E. and Billiar, K. L. (2011) Combining dynamic stretch and tunable stiffness to probe cell mechanobiology in vitro. *PLoS One*. 6 (8), e23272
- Titushkin, I. and Cho, M. (2007) Modulation of cellular mechanics during osteogenic differentiation of human mesenchymal stem cells. *Biophysical Journal*. 93 (10), 3693-3702
- Trache, A. and Meininger, G. A. (2005) Atomic force-multi-optical imaging integrated microscope for monitoring molecular dynamics in live cells. *Journal of Biomedical Optics*. 10 (6), 064023
- Trickey, W. R., Vail, T. P. and Guilak, F. (2006) The role of the cytoskeleton in the viscoelastic properties of human articular chondrocytes. *Journal of Orthopaedic Research*. 22 (1), 131-139
- Ujihara, Y., Miyazaki, H. and Wada, S. (2008) Morphological study of fibroblasts treated with cytochalasin d and colchicine using a confocal laser scanning microscopy. *The journal of physiological sciences: JPS*. 58 (7), 499
- Van Vliet, K., Bao, G. and Suresh, S. (2003) The biomechanics toolbox: Experimental approaches for living cells and biomolecules. *Acta Materialia*. 51 (19), 5881-5905
- Wade, R. H. and Hyman, A. A. (1997) Microtubule structure and dynamics. *Current Opinion in Cell Biology*. 9 (1), 12-17
- Wakatsuki, T., Wysolmerski, R. B. and Elson, E. L. (2003) Mechanics of cell spreading: Role of myosin ii. *Journal of Cell Science*. 116 (8), 1617-1625
- Wang, J. H. C., Goldschmidt-Clermont, P., Wille, J. and Yin, F. C. P. (2001) Specificity of endothelial cell reorientation in response to cyclic mechanical stretching. *J. Biomech*. 34 (12), 1563-1572
- Wang, J. H. C., Yang, G., Li, Z. and Shen, W. (2004) Fibroblast responses to cyclic mechanical stretching depend on cell orientation to the stretching direction. *Journal of Biomechanics*. 37 (4), 573-576

- Wang, N. and Stamenović, D. (2000) Contribution of intermediate filaments to cell stiffness, stiffening, and growth. *American Journal of Physiology-Cell Physiology*. 279 (1), C188-C194
- Wang, Y., Shyy J.Y-J. and Chien S. (2008) Fluorescence proteins, live-cell imaging, and mechanobiology: Seeing is believing. *Annual Review of Biomedical Engineering*. 10, 1-38
- Watanabe-Nakayama, T., Machida, S., Harada, I., Sekiguchi, H., Afrin, R. and Ikai, A. (2011) Direct detection of cellular adaptation to local cyclic stretching at the single cell level by atomic force microscopy. *Biophys. J.* 100 (3), 564-572
- Wille, J. J., Elson, E. L. and Okamoto, R. J. (2006) Cellular and matrix mechanics of bioartificial tissues during continuous cyclic stretch. *Ann. Biomed. Eng.* 34 (11), 1678-1690
- Yamane, Y., Shiga, H., Haga, H., Kawabata, K., Abe, K. and Ito, E. (2000) Quantitative analyses of topography and elasticity of living and fixed astrocytes. *Journal of electron microscopy*. 49 (3), 463-471
- Zerwekh, J. E., Ruml, L. A., Gottschalk, F. and Pak, C. Y. C. (2009) The effects of twelve weeks of bed rest on bone histology, biochemical markers of bone turnover, and calcium homeostasis in eleven normal subjects. *Journal of Bone and Mineral Research*. 13 (10), 1594-1601
- Zhou, E. H., Lim, C. T., Ng, S. M. and Quek, S. T. (2005) Micropipette aspiration of fibroblasts. *Proceedings of the 3rd International Conference on Materials for Advanced Technologies*.
- Zimmer, C. C., Shi, L. F., Shih, Y. P., Li, J. R., Jin, L. W., Lo, S. H. and Liu, G. Y. (2012) F-actin reassembly during focal adhesion impacts single cell mechanics and nanoscale membrane structure. *Science China Chemistry*. 1-11

## Chapter 3

# **Atomic Force Microscope Cantilever Modifications to apply Whole Cell Deformation**

### 3.1 Introduction

The use of whole cell compression testing to determine mechanical properties was initially reported by Thoumine and Ott (1997) in which fibroblasts were monotonically compressed between two parallel plates to examine cell viscoelasticity. Parallel plate compression was also used by Caille et al. (2002) in order to characterise the elastic properties of endothelial cells and their isolated nuclei. Similar studies have been performed by Ofek et al. (2009) on chondrocytes and Peeters et al. (2005) on myoblasts. Typically, cell compression experiments are performed by seeding cells on stiff substrates. A flexible probe, that is initially parallel to the substrate, is used to impart a compressive deformation on the cell. By observing the deflection of the probe using a microscope, the compressive force is computed using beam theory. The maximum accuracy of such force measurements is typically in the range of 1-10 nN. Additionally, the nominal strain imparted on the cell cannot be accurately controlled due to significant deflection and bending of the flexible probe during compression of the cell.

AFM is widely used to investigate the mechanical behaviour of cells (Hofmann et al. (1997), Rotsch and Radmacher (2000), Cross et al. (2008), Roca-Cusachs et al. (2008), Kelly et al. (2011)). AFM systems can accurately measure forces of the order of pico-Newton (Lim et al. (2006), Mostaert et al. (2006)). Additionally, sub-nanometre displacements can be accurately applied to cells (Colton et al. (1997), Simon and Durrieu (2006)). However, previous implementations of AFM based force spectroscopy for the mechanical characterisation of cells have used sharp nano-scale probes that apply a highly localised deformation to the cell membrane. Such an approach suffers from a number of setbacks: applied deformations are restricted to the upper surface of the cell, measured forces are highly influenced by cell inhomogeneity, and large deformations occur in a highly localised region of the cell. These issues make it difficult to characterise the applied strain field and to interpret measured forces.

Efforts to overcome problems associated with highly localised measurements using standard AFM systems have involved the measurement of force map arrays

over the entire cell surface (Radmacher et al. (1996)). However measuring data over large areas with sufficient resolution generally requires acquisition times comparable to those associated with remodelling of the cytoskeleton. Individual curves within a force map depend greatly upon the local environment and its position relative to the underlying cytoskeletal components, often resulting in measurements spanning an order of magnitude within a single force map (Hofmann et al. (1997), Rotsch and Radmacher (2000)). Additionally, localised nano-scale deformations are highly influenced by cell structures in the membrane, and immediately below the membrane layer. Consequently, whilst force maps offer great details about intracellular mechanical heterogeneity along the cell membrane, the interpretation of such data as being representative of mechanical properties on the whole cell scale is highly questionable. In an effort to overcome these problems, a number of studies have attached a sphere ( $\varnothing$  10-60  $\mu\text{m}$ ) to the end of the AFM cantilever to increase the contact area between the cell and probe (Lehenkari et al. (2000), Lulevich et al. (2006), Jaasma et al. (2006), Zimmer et al. (2012)). While providing an improvement on AFM tip measurements, the contact radius between these spheres and the cell will typically be smaller than the cell diameter, hence measurements will still suffer the drawback of significant localisation. In this chapter, a significantly larger sphere of  $\varnothing$  150  $\mu\text{m}$  is attached to an AFM cantilever in order to perform whole cell compression of osteoblasts. The contact radius between such a large sphere and a cell is of the same order as the cell radius. Hence, compression of a cell with such a large sphere provides a reasonable approximation of parallel plate cell compression. However, this modified AFM system offers an advantage over previous parallel plate compression devices given its high level of precision in terms of control of applied cell deformation and measurement of reaction forces.

In this chapter, the progressive developmental steps to achieve whole cell loading using a standard AFM system are presented. Firstly, a description of the AFM system used in this thesis is presented (Section 3.2). In Section 3.3, a modification of the AFM cantilever to facilitate whole cell deformation experiments is proposed. An initial assessment of the design issues is also presented in this section. In Section 3.4, an extensive investigation of the effects of sphere attachment

on AFM data is presented. Examination of the cantilever bending profile reveals that the optical lever system assumption of free-ended cantilevering is inappropriate as the sphere introduces additional constraints; this important effect has not been considered in previous studies. In Section 3.4, correction factors necessary for the accurate interpretation of force-indentation data for the modified AFM cantilever are determined. Throughout each section of this technical chapter, presented results and analyses are discussed with reference to previous studies. A brief summary of the key points is then provided in Section 3.5.

## **3.2 Investigating Cell Mechanics using an AFM**

Following from the general introduction to the AFM technique presented in Section 2.4.4, the standard AFM system used in the current study is described in Section 3.2.1. AFM calibration techniques are outlined in Section 3.2.2.

### **3.2.1 The Integrated AFM/Fluorescence Microscopy System**

All work presented in this thesis is performed using a MFP-3D AFM (Asylum Research, CA, USA) combined with an Eclipse Ti fluorescent microscope and A1R confocal system (Nikon, Japan), Figure 3.1. The system is configured such that the AFM head is positioned above the stage of the inverted microscope (Figure 3.1 (a)), thus allowing independent movement of the sample and the AFM cantilever relative to the objective lens of the microscope. The major advantage of this system is that it facilitates concurrent viewing of the sample and AFM cantilever, hence allowing appropriate positioning of the cantilever relative to the sample during experiments. In addition, this system allows real-time measurement of the sample within the field of view of the objective lens, allowing cellular responses to be monitored and quantified during AFM indentation experiments. To minimise thermal and acoustic noise, the system is positioned on a vibration isolation table (Micro 60, Halcyonics, Germany) and housed within a large acoustic isolation hood (BCH-45, Asylum Research, USA), Figure 3.1 (b). Air conditioning maintained the lab temperature at  $21 \pm 1$  °C.

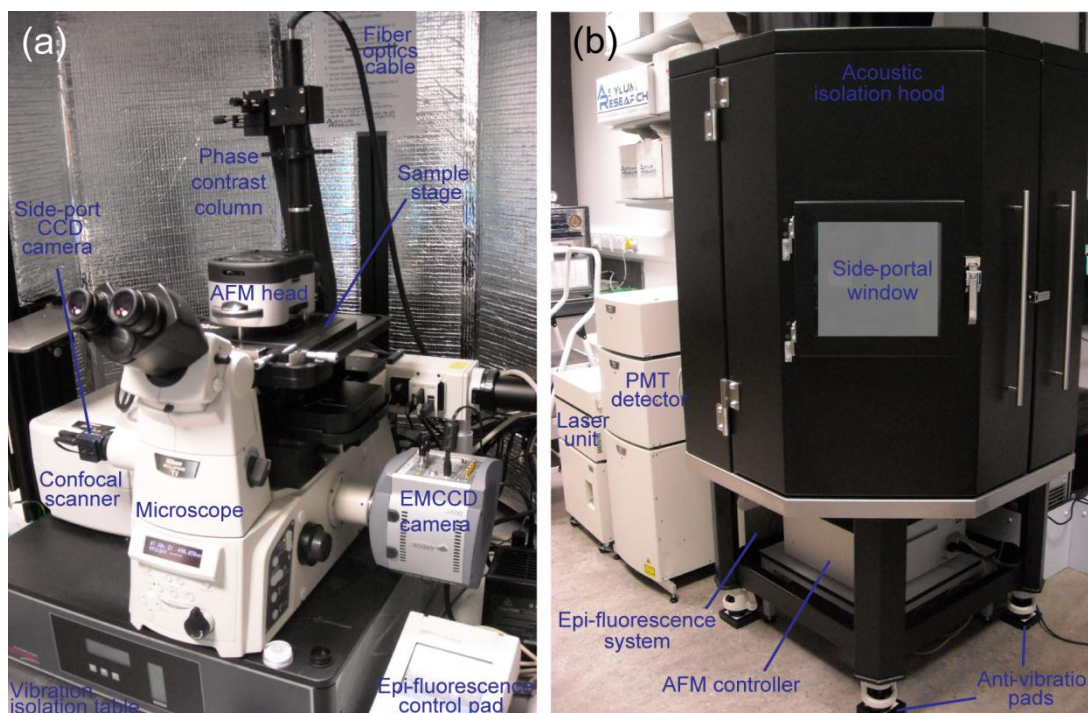


Figure 3.1: The integrated AFM/fluorescence microscopy system. (a) shows the AFM head positioned above the confocal/fluorescence setup. The system is positioned on a vibration isolation table, which aids to reduce the amount of noise experienced during AFM measurements. (b) shows the AFM/fluorescence system components positioned outside of the acoustic isolation hood. The components shown in (a) are set up within the acoustic isolation hood that stands on anti-vibration pads, further reducing acoustic noise within the hood.

Prior to experiments, organic contaminants are removed from the cantilever using UV/Ozone cleaning (UV/Ozone Procleaner<sup>TM</sup>, BioForce Nanosciences, Iowa, USA) for a period of 20 min. This is followed by cantilever immersion in 70% ethanol for 5 min and rinsing (x3) with ultrapure water (Milli-Q Integral System, Merck Millipore, Ireland). Additionally, the cantilever holder is cleaned by sonication in 70% ethanol for 15 min and rinsed (x3) with ultrapure water.

The cantilever is positioned in the cantilever holder, which is then attached to the AFM head. A clean sample holder is placed on the AFM stage, directly above the lens of the inverted optical microscope. The AFM head is placed in position on the stage and care is taken not to allow the cantilever tip to contact the sample. Laser intensity reflected from the cantilever, detected by the PSD (position sensitive detector) is maximised, while deflection signal is minimised. The height of the AFM

head is initially lowered so that the tip is positioned a few millimetres above the surface of the sample. At this point, the cantilever is approached to the surface. Briefly, cantilever deflection is set at 0 (i.e. the laser spot is centred on the PSD), while a setpoint of 0.5 V is chosen as the criteria for engaging the surface. With the z-feedback loop enabled, the AFM head is manually lowered until the setpoint condition is met.

### 3.2.2 Calibration of Cantilever Spring Constant and Deflection Sensitivity

A schematic of an AFM cantilever is shown in Figure 3.2. In AFM force spectroscopy experiments the force applied to the AFM tip (reaction force),  $F$ , is calculated from the measured cantilever deflection ( $\delta$ ). Typically, a linear Hooke's law relationship is applicable whereby the reaction force  $F$  is given as  $F = k \delta$ . The cantilever stiffness  $k$  must be accurately calibrated to provide precise values of  $F$ .

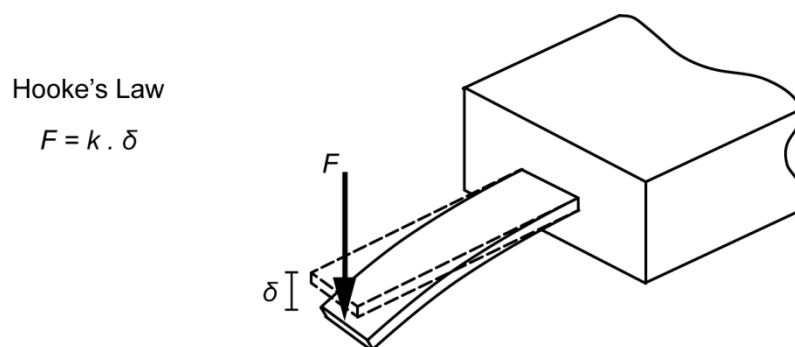


Figure 3.2: Schematic illustrating Hooke's Law. The cantilever spring constant ( $k$ ) must be known to relate the measured deflection ( $\delta$ ) to an applied force ( $F$ ).

Cantilever deflection ( $\delta$ ) is measured using the optical lever technique proposed by Meyer and Amer (1988) whereby a laser beam hits the cantilever at a cantilever position ( $x = LS$ ) and the reflected laser beam is directed onto a PSD (Figure 3.3). When the cantilever deflects, the slope of the cantilever at position  $x$ ,  $\theta(x)$ , changes, where  $x$  is the axial coordinate along the length of the cantilever. As a result, the reflected angle of the laser beam changes and its position on the PSD is consequently altered. The position change of the laser beam on the PSD is proportional to the change in slope of the cantilever at position  $x$ ,  $\theta(x)$ . Additionally, when the deflection of the cantilever is much lower than the length of the cantilever,

the cantilever deflection at point  $x$ ,  $\delta(x)$ , is proportional to the cantilever slope at point  $x$ ,  $\theta(x)$ . Therefore, the change in laser beam on the PSD is proportional to  $\delta(x)$  (Butt et al. (2005), Evans and Craig (2006)).

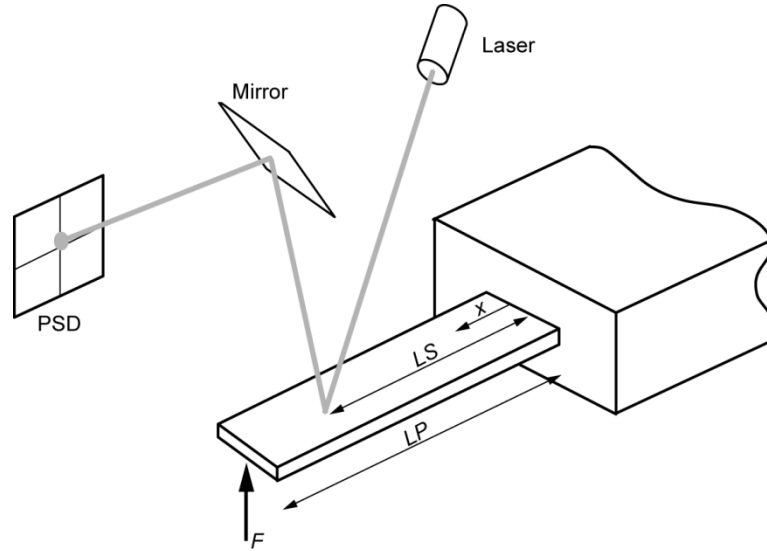


Figure 3.3: Schematic of the optical lever system employed to measure deflection ( $\delta$ ) of a cantilever, where  $x$  is the axial coordinate along the length of the cantilever and  $LS$  is the laser spot position.  $LP$  is the loading point against the surface.

The difference in laser beam intensity between the top and bottom quadrants of the PSD leads to a change of the PSD output voltage ( $V$ ). This voltage change is proportional to  $\delta(x)$ , and therefore:

$$dV \propto \delta(x) \quad (3.1)$$

Cantilever deflection calibration is performed by calculating the optical lever sensitivity (OLS). This is achieved by applying a load that moves the cantilever a known distance. Typically, this is performed by probing a hard surface until the cantilever deflects at the loading point ( $x = LP$ ) by a known distance relative to its fixed end. The deflection change at the loading point is proportional to the deflection change at the laser spot ( $x$ ) (again with the constant of proportionality being dependent on the specific choice of  $x = LS$  and  $x = LP$ ). Hence, the ratio of the change in voltage signal from the PSD to  $\delta(LS)$  is provided by the OLS calibration

(Equation (3.2)), typically the loading point (LP) is at the free-end of the cantilever for a standard AFM setup.

$$OLS = \frac{dV}{\delta(LP)} \quad (3.2)$$

As described above, while AFM measurements are reported in terms of deflection, based on OLS calibration, it is in fact the change in cantilever slope that is actually detected on the PSD. Any variation in the optical arrangement, such as movement of the laser spot position ( $LS$ ), will result in a different OLS, as the ratio of cantilever deflection to cantilever slope is a function of the axial coordinate  $x$  along the cantilever. Following from the background AFM theory outlined in this section, a detailed description of the methodology used to calibrate the OLS for the modified cantilevers used in this thesis is later provided in Section 3.4.1.

Cantilever spring constant nominal values (provided by the manufacturer) tend to differ significantly from the precise value associated with a given cantilever, thus, calibration of the cantilevers stiffness is also a prerequisite for quantitative AFM force measurements. Numerous calibration methods have been developed to determine the spring constant of AFM cantilevers. The most common methods are are; (i) the *thermal method* (Butt and Jaschke (1995)) which uses equi-partition theorem to deduce the spring constant from the thermal vibration spectrum of a cantilever, (ii) the *Sader (Dublin) method* (Sader et al. (1995)) which uses geometrical dimensions and a quality factor to calculate the stiffness, and (iii) the *added mass method* (Cleveland et al. (1993)) which measures the change in resonance frequency at different loads to deduce the cantilever spring constant. In Section 3.4.2, a detailed description of the methodology used to calibrate the spring constant for the modified cantilever used in this study is given.

### 3.3 Adaption of an AFM Cantilever to Measure Whole Cell

#### Mechanics

AFM measurement of whole cell mechanical behaviour, via the application of an approximately uniform deformation field to the cell, is not possible using a

standard AFM tipless cantilever. This is due to (i) its narrow geometry, resulting in deformation of only a localised section of the cell (Figure 3.4 (a)), and (ii) its angle of inclination (typically 10–15°), which results in a non-uniform applied deformation (Figure 3.4 (b)). Modification of an AFM cantilever, as proposed in this section, is required to overcome these issues in order to achieve a system comparable to a parallel plate compression setup.

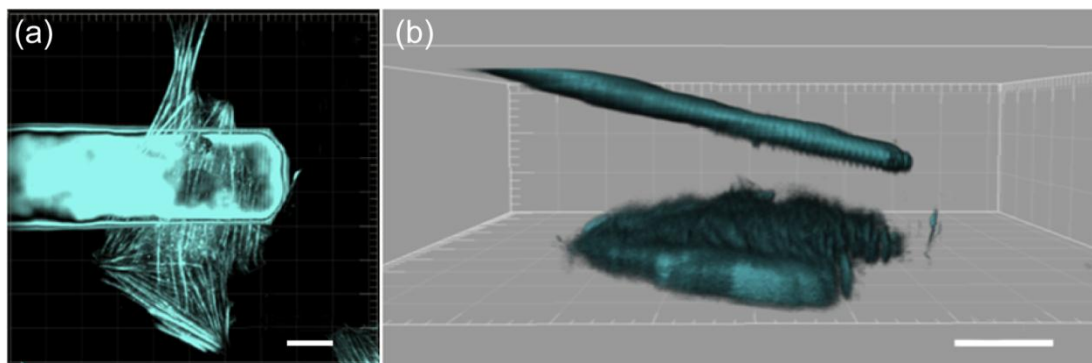


Figure 3.4: Image of an actin-transfected osteoblast under a NSC12 tipless cantilever. (a) The top-down view highlights the narrow geometry of the cantilever relative to the cell below. (b) The side view highlights the cantilever's angle of inclination (typically 10–15°). Z-stacks are taken with confocal mode for the cell and reflection-confocal mode for the cantilever. Both z-stacks are combined to produce this 3D visualisation using the Imaris software package (Bitplane, Switzerland). Scale bar represents 10  $\mu\text{m}$ .

### 3.3.1 Large Sphere Attachment: Design Considerations

In the current study, whole cell deformation is achieved by attaching a large sphere to the cantilever's free-end, Figure 3.5. By choosing a sphere of sufficiently large diameter, the bottom surface of the sphere can be approximated as a planar surface relative to the dimensions of the cell.

A number of considerations and issues must be addressed when using a modified cantilever with a sphere of the scale required to perform whole cell deformation:

- (i) A cantilever must be chosen that is sufficiently stiff to support an attached sphere, while on the other hand being sufficiently compliant to allow for accurate force measurements for the sample being tested (Section 3.3.1.1).

- (ii) A sphere radius must be chosen that is sufficiently large to approximate a planar surface for whole cell deformation, without becoming oversized relative to the cantilever length (Section 3.3.1.1).
- (iii) Hydrodynamic force effects must be examined (Section 3.3.1.2).
- (iv) A sphere attachment criterion must be developed (Section 3.3.1.3).
- (v) The effects of sphere attachment on cantilever calibration must be examined (Section 3.4).

The remainder of this Chapter is devoted to addressing these considerations and issues.

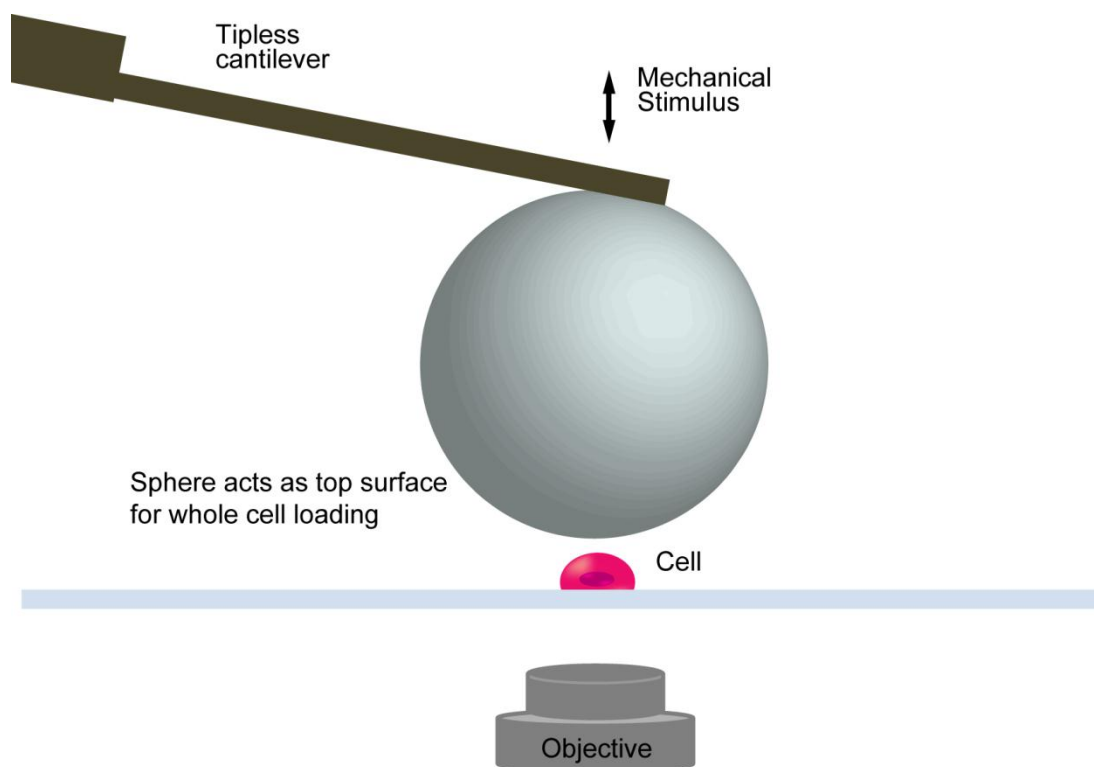


Figure 3.5: Schematic of proposed cantilever modification to achieve whole cell loading by use of a large microsphere attached to the cantilever's free-end. By choosing a sufficiently large sphere relative to the cell dimensions, it will act as the top (approximately) planar surface for mechanical loading at a whole cell level.

### 3.3.1.1 Cantilever and Sphere Selection

Figure 3.6 shows a scanning electron microscopy (SEM) image of the cantilever (Lever F, NSC12/Tipless/AIBS,  $k \approx 0.65$  N/m, MikroMasch, Spain) selected for use with an attached large sphere to perform whole cell deformation. Selecting a tipless cantilever allowed sphere positioning at the free-end of the cantilever. The aluminium coating on the backside (the side the laser reflects on) enhances the signal to noise ratio. Table 3.1 shows the cantilever specifications reported by the manufacturer.

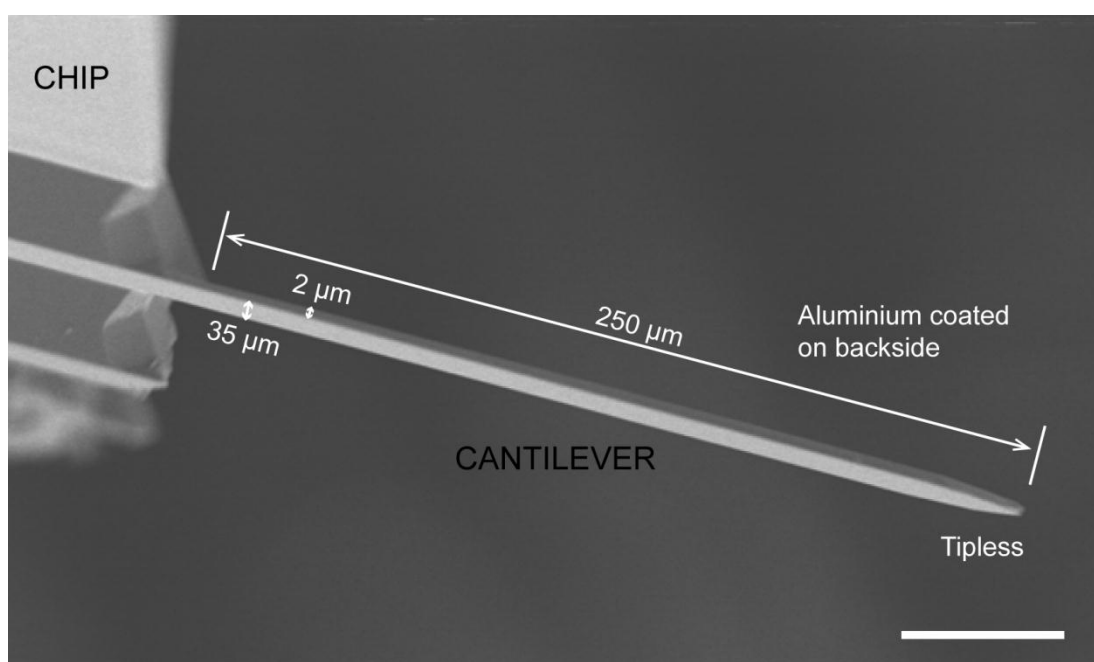


Figure 3.6: SEM image of the NSC12 tipless cantilever. The cantilever is aluminium coated on the backside to increase reflection of the laser. The laser is positioned on the backside at an axial position ( $x$ ) from the base of the cantilever. The scale bar represents 25  $\mu\text{m}$ .

Table 3.1: Resonant frequency, spring constant and dimensional details for the NSC12 cantilever.

Resonant frequency (kHz)			Spring Constant (N/m)			Dimensions ( $\mu\text{m}$ )		
Min	Nominal	Max	Min	Nominal	Max	Length	Width	Thickness
33	41	49	0.35	0.65	1.2	$250 \pm 5$	$35 \pm 3$	$2.0 \pm 0.5$

The sphere selected for attachment to the cantilever is a  $\text{\O} 150 \text{ }\mu\text{m}$  glass monodisperse standard (MS0156, Whitehouse Scientific, UK). The sphere radius is such that it is less than the length of the cantilever, but greater than the size of a typical osteoblast, so that whole cell deformation is achieved. As illustrated in Figure 3.7, for a contact radius of  $10 \text{ }\mu\text{m}$  between the cell and the sphere, the contact point elevation differs by  $0.67 \text{ }\mu\text{m}$  at the outer limit of the contact area than at the sphere centre.

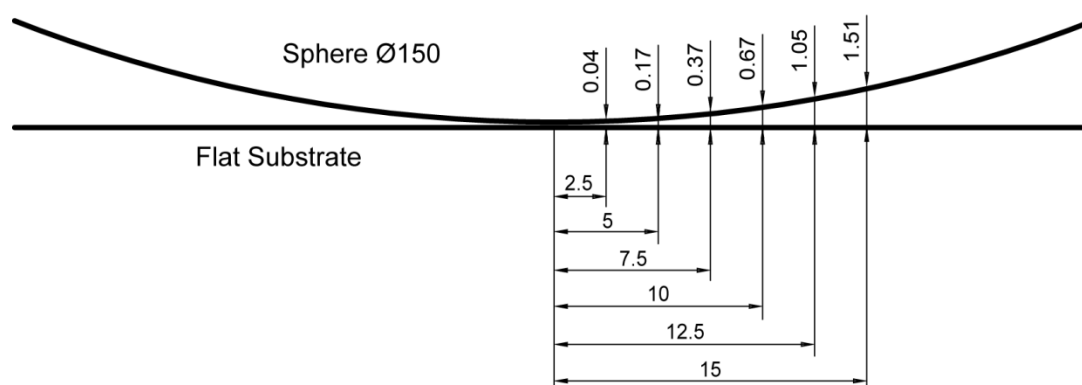


Figure 3.7: Relationship between elevation of outer contact points and contact radius for a  $\text{\O} 150 \text{ }\mu\text{m}$  sphere. Dimensions in  $\mu\text{m}$ .

### 3.3.1.2 Hydrodynamic Force

A sphere approaching a substrate through a liquid medium must displace a certain quantity of liquid. The force required to displace liquid is known as the hydrodynamic force. The hydrodynamic force is proportional to the velocity of the sphere, the square of the sphere radius, and the fluid viscosity. Additionally the hydrodynamic force is inversely proportional to the distance of the sphere from the substrate surface (Butt et al. (2005)). When the distance between the sphere and substrate is small in comparison to the radius of the sphere, the hydrodynamic drag force ( $F_H$ ) is given by the equation;

$$F_H = \frac{6\pi\eta R^2 U}{D} \quad (3.3)$$

where  $\eta$  is the viscosity of the fluid (Newtonian fluid),  $R$  is the radius of the sphere,  $U$  is the velocity of approach, and  $D$  is the surface separation (Shannon et al. (2003)).

It is necessary to consider hydrodynamic force effects when performing AFM experiments with a large sphere in liquid. Figure 3.8 shows the hydrodynamic force calculated using Equation (3.3) for a  $\varnothing$  150  $\mu\text{m}$  sphere moving towards a planar substrate in water at three velocities: 1  $\mu\text{m/s}$ , 10  $\mu\text{m/s}$  and 100  $\mu\text{m/s}$ . When the sphere is 0.5  $\mu\text{m}$  from the surface, the hydrodynamic drag force is  $\sim 0.2$  nN at a velocity of 1  $\mu\text{m/s}$  (blue),  $\sim 1.8$  nN at 10  $\mu\text{m/s}$  (red) and  $\sim 18.1$  nN at 100  $\mu\text{m/s}$  (green). Therefore, the velocity of the cantilever during experiments is restricted to a maximum of 20  $\mu\text{m/s}$  in order to minimise any hydrodynamic force contribution (Fan and Fedorov (2003), Attard (2007)).

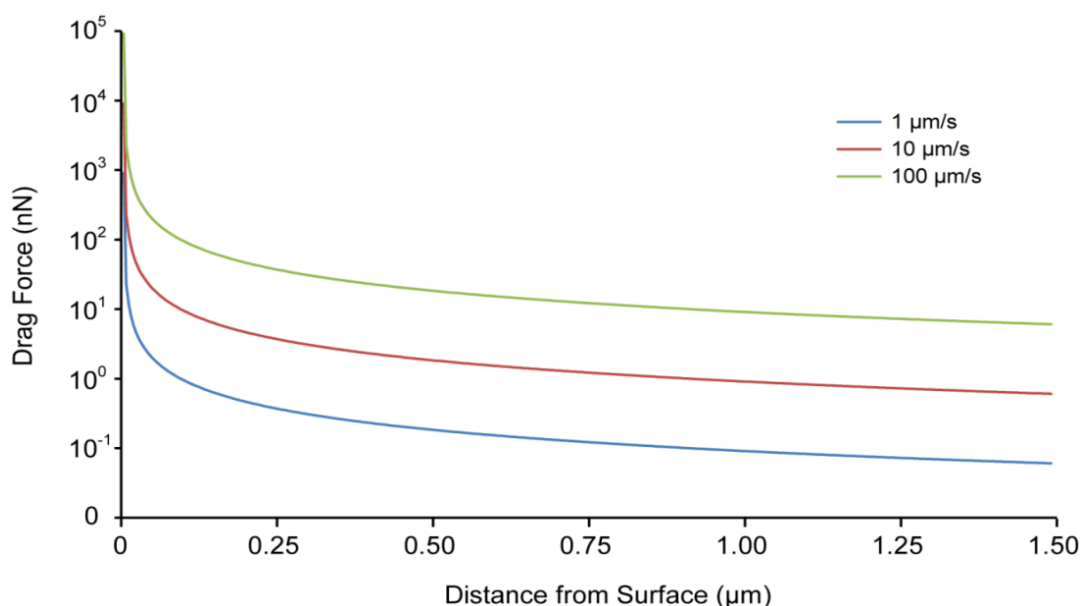


Figure 3.8: Hydrodynamic force calculated for a  $\varnothing 150$   $\mu\text{m}$  sphere approaching a planar surface in water at three different velocities: 1  $\mu\text{m/s}$  (blue); 10  $\mu\text{m/s}$  (red); 100  $\mu\text{m/s}$  (green).

### 3.3.1.3 Sphere Attachment

Figure 3.9 shows a SEM image of the modified cantilever, whereby the large sphere is attached to the free-end of the tipless cantilever. Sphere attachment is performed using a glass micropipette on a three-way micro-positioner over an optical microscope, as illustrated in Figure 3.10. The micropipettes are formed by pulling  $\varnothing$  1 mm glass tubules (Bilbate, UK) over a small Bunsen burner flame. Firstly, using the setup shown in Figure 3.10, a small quantity of epoxy (Loctite 3430, Henkel, Germany) is placed at the free-end of the cantilever using a micropipette. The sphere

is then promptly positioned on the epoxy spot (epoxy initial setting time of 5 min) using a clean micropipette. It is found that an electrostatic interaction between the micropipette and the glass sphere is strong enough to move and position the sphere on the cantilever. The epoxy is left to fully cure for a minimum of 24 hr.

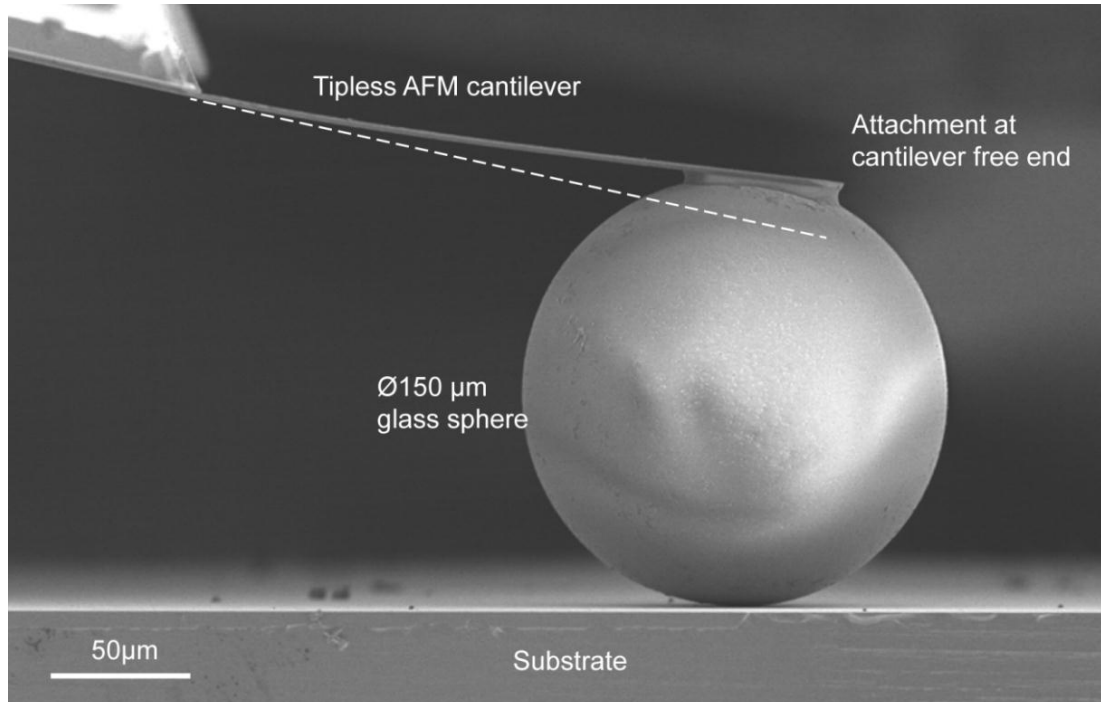


Figure 3.9: SEM image of the modified AFM cantilever: A  $\text{Ø } 150 \text{ }\mu\text{m}$  glass microsphere is attached to the free-end of an AFM tipless cantilever. In this image the sphere is compressed into a flat substrate resulting in a deflection of the cantilever.

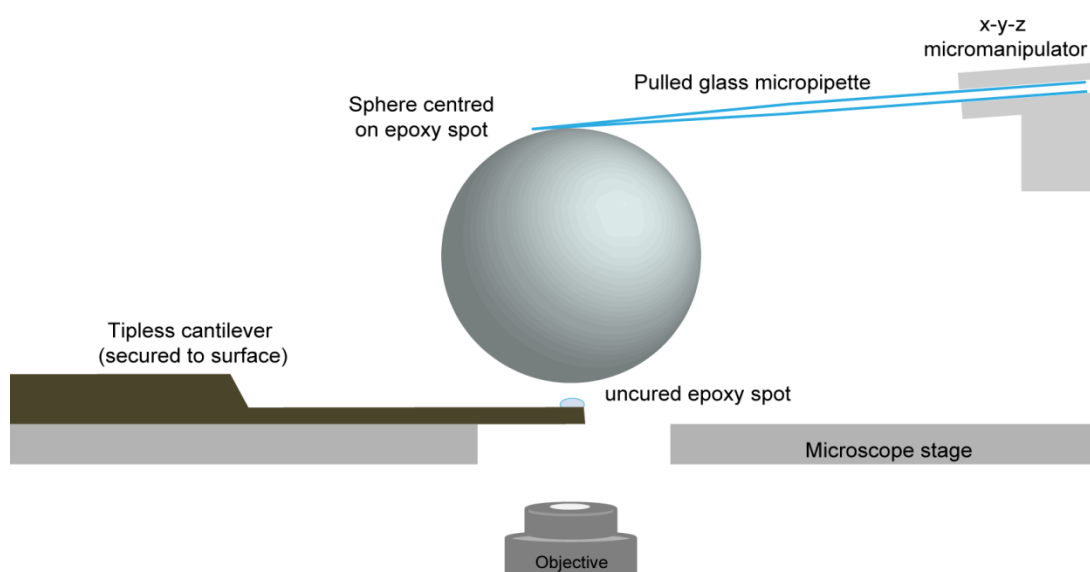


Figure 3.10: Schematic illustrating the sphere attachment procedure.

SEM with a customised sample stage is used to verify sphere attachment, based on the following criteria:

- The sphere is positioned sufficiently close to the free-end of the cantilever (distance from centre of attachment to free-end of cantilever  $< 10 \mu\text{m}$ ).
- The centre of the sphere is aligned with the axis of the cantilever.
- A minimum quantity of epoxy is used.
- There is no epoxy on the sphere or on the cantilever other than at the attachment point.
- The sphere is smooth and free of defects.

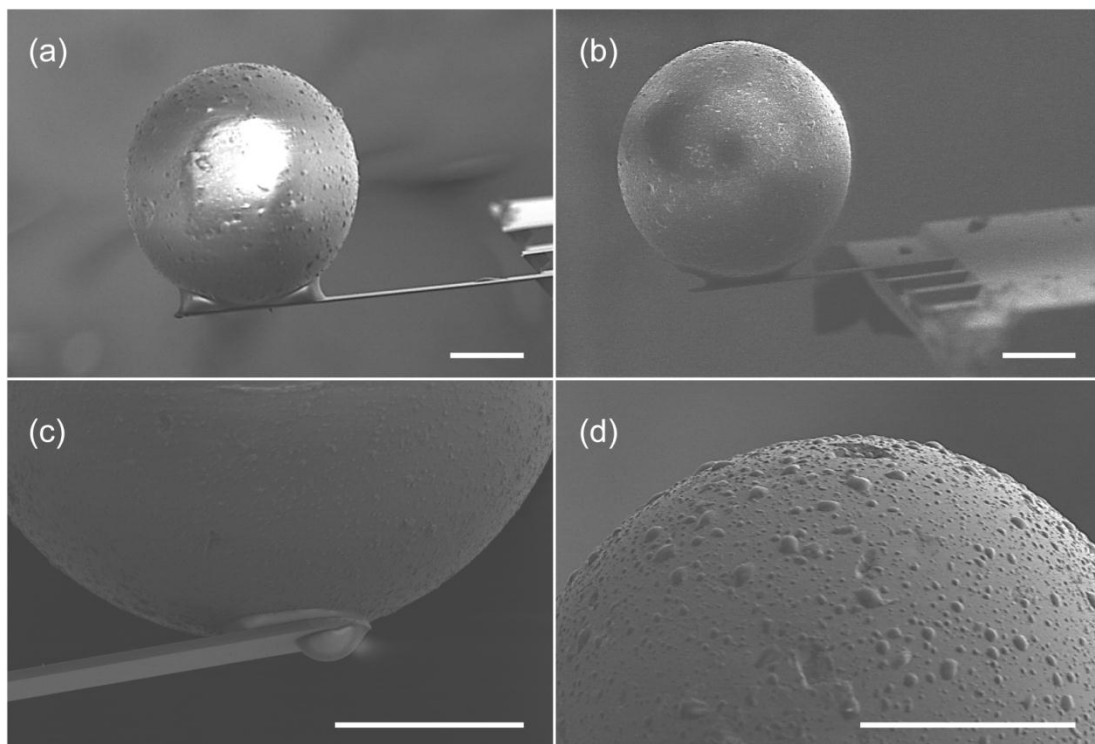


Figure 3.11: Examples of modified cantilevers rejected following SEM assessment: (a) excessive quantity of epoxy is used; ((a), (b)) distance from centre of attachment to free-end of cantilever  $> 10 \mu\text{m}$ ; (c) epoxy on the backside of the cantilever; (d) the sphere surface is uneven and defective (also observed in (a)). The scale bar represents  $50 \mu\text{m}$ .

### 3.4 Modified Cantilever Calibration

Quantitative AFM force measurement requires accurate calibration of the cantilever. For optical lever systems, this involves calculating (i) the cantilever stiffness and (ii) optical lever sensitivity, OLS. The methods used to determine these values (discussed in Section 3.2.2) require careful consideration and adaptation when using a modified cantilever. In this section, the methods used to determine the cantilever stiffness and OLS for the modified cantilever are outlined and discussed.

#### 3.4.1 Optical Lever Sensitivity

OLS calibration is taken as the ratio of the change in voltage signal from the photodetector to the distance moved by the cantilever when pressed against a rigid substrate. The linear slope of the resulting voltage-displacement curve provides the OLS in units of V/nm. Friction between the sphere and substrate results in uncharacteristic voltage-displacement curves. As the sphere slides along the substrate, friction results in the loading and unloading sections of the curve often exhibiting a substantial hysteresis, as previously reported by Chung et al. (2009), Hoh and Engel (1993), and Stiernstedt et al. (2005). Consequently, obtaining an accurate linear slope of the voltage-displacement curves can prove difficult. In this study, the mean of the slopes of the loading and unloading data is calculated as the best estimate of OLS (Figure 3.12), as previously reported by Chung et al. (2009).

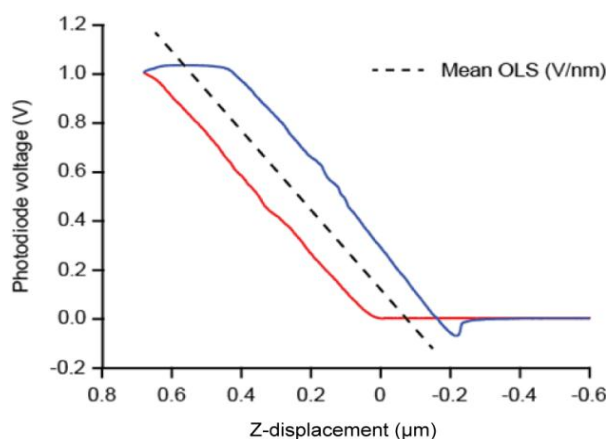


Figure 3.12: Representative example of the photodiode voltage response observed when probing a clean glass slide in liquid with the sphere-attached-cantilever. The slope of the response curve (OLS) is estimated from both the loading (red) and unloading (blue) data. The mean of these two values is calculated as a best estimate of the OLS.

It is important to note that, even though optical lever measurements are usually reported as a deflection, it is the change in slope of the cantilever that is actually detected. When the cantilever deflects, the slope changes and this causes the laser to move across the detector.

### 3.4.2 Spring Constant

Due to the scale of the attached microsphere, standard AFM calibration methods could not be utilised to calculate the spring constant of the AFM cantilever. In the current study accurate calculation of the cantilever spring constant is not achievable using the thermal method (Butt and Jaschke (1995)) or the Sader method (Sader et al. (1995)) due to the additional mass of the attached sphere. Instead, the spring constant is determined after sphere attachment according to the added mass method proposed by Cleveland et al. (1993). The added mass method calculates a cantilever's spring constant by measuring the change in resonance frequency at different loads, according to Equation (3.4). Briefly, calculation of cantilever spring constant ( $k_{am}$ ) due to the addition of a mass ( $M$ ) to the cantilever's free-end results in a resonant frequency shift from the resonant frequency without an added mass ( $V_0$ ) and to that with an added mass ( $V_1$ ).

$$k_{am} = (2\pi)^2 \frac{M}{\frac{1}{V_1^2} - \frac{1}{V_0^2}} \quad (3.4)$$

A thermal noise spectrum is collected for the cantilever prior to sphere attachment ( $V_0$ ) and following sphere attachment ( $V_1$ ). A thermal noise spectrum determines the natural resonant frequency of the cantilever by monitoring the spontaneous vibration of the cantilever (amplitude) over a user defined frequency range while it is excited by the Brownian motion of either the air or water molecules in its vicinity. Spectra data recorded represent the average of 100 samples (Figure 3.13). The mass of the sphere ( $M$ ) is taken as the nominal value specified by the manufacturer as 4.87 ng. Calculated spring constant ( $k_{am}$ ) values range from 0.3 - 0.5 N/m and are within 20% of values obtained prior to sphere attachment via the

thermal method ( $k_t$ ), as shown in Table 3.2. Measured values are within the lower tolerance specified by the manufacturer (Table 3.1).

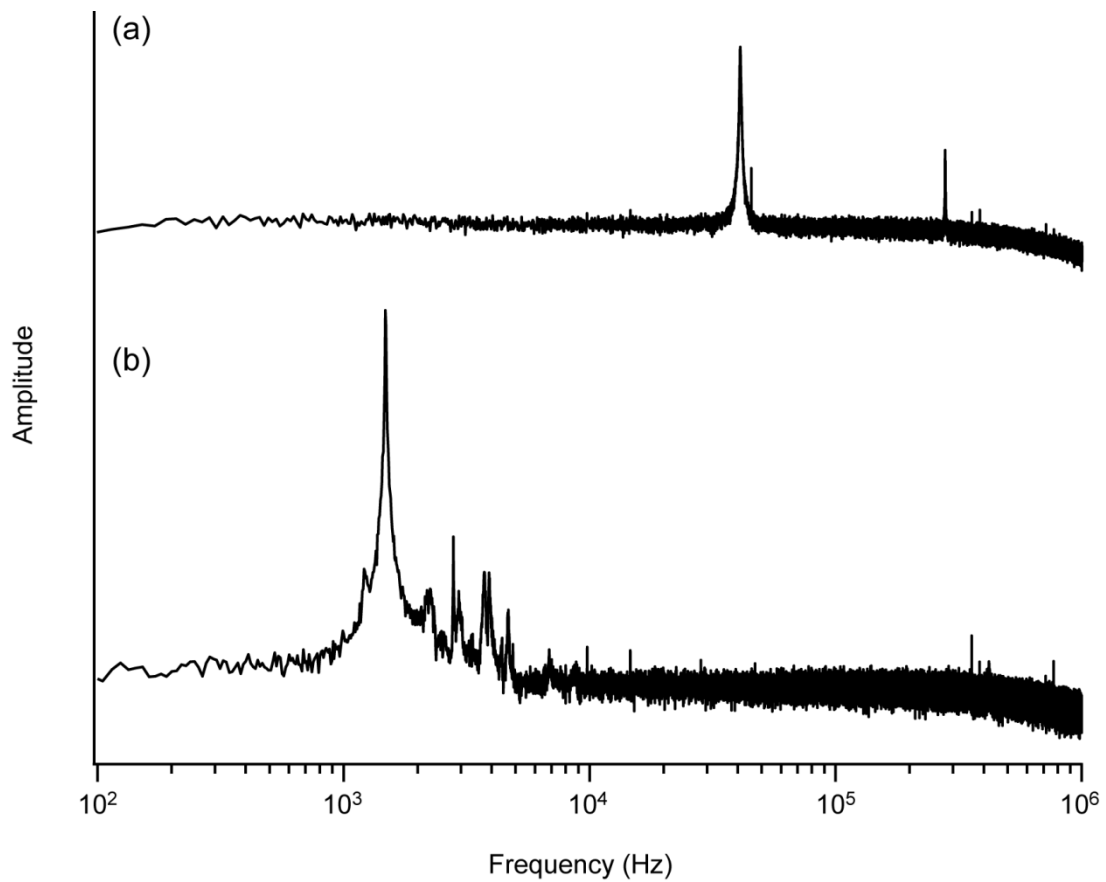


Figure 3.13: Resonance spectra of the same cantilever in air (a) without and (b) with an attached  $\text{\O}150$   $\mu\text{m}$  sphere. (a) The spectrum for the cantilever without an attached sphere shows a peak at 40.9 kHz ( $V_0$ ), and (b) the spectrum with an attached sphere shows a peak at 1.5 kHz ( $V_1$ ). In accordance with the added mass method, this frequency shift of 39.4 kHz results in a calibrated cantilever spring constant of 0.42 N/m.

Table 3.2: Mean and standard deviation of the resonant frequency before ( $V_0$ ) and after ( $V_1$ ) sphere attachment, which are used to calculate the spring constant of modified cantilevers ( $n = 21$ ) using the added mass method. Spring constant values ( $k_{am}$ ) calculated using the added mass method are comparable to those calculated using the thermal method prior to sphere attachment ( $k_t$ ).

	$V_0$	$V_1$	$k_{am}$	$k_t$
Mean	39.6 kHz	1.5 kHz	0.41 N/m	0.42 N/m
Standard dev. ( $\pm$ )	2.7 kHz	0.2 kHz	0.08 N/m	0.11 N/m

### 3.4.3 Cantilever Bending Profiles: ‘Sliding’ versus ‘Constrained’

Application of the calibrated cantilever stiffness and OLS in order to obtain the applied force is accurate only if the cantilever behaves as a free-ended cantilever. If friction between the sphere and substrate is sufficient to inhibit sphere sliding, the cantilever will no longer act as a free-ended cantilever due to a rotation constraint at the cantilever's free-end. To illustrate this important point, Figure 3.13 shows SEM images obtained using a modified sample stage of a cantilever, inclined at  $11^\circ$ , with a sphere attached to the free-end. In Figure 3.13 (a) the cantilever is lowered vertically until it is compressed into a smooth horizontal glass surface. The friction coefficient between the sphere and the rigid substrate is sufficiently low to allow sliding of the sphere along the substrate, herein referred to as a ‘*sliding sphere*’ (Figure 3.14 (a)). In contrast, in Figure 3.13 (b) the sphere is in contact with a fixed inverted AFM tip, which prevents horizontal movement of the sphere as the cantilever is lowered vertically (i.e. the contact point at the bottom of the sphere is fixed in space). A similar effect is achieved if the sphere contacts a rough surface with sufficiently high friction coefficient to prevent sliding of the sphere. The term ‘*constrained sphere*’ is used herein to describe a sphere that does not slide along the substrate, leading to a rotational constraint on the end of the cantilever.

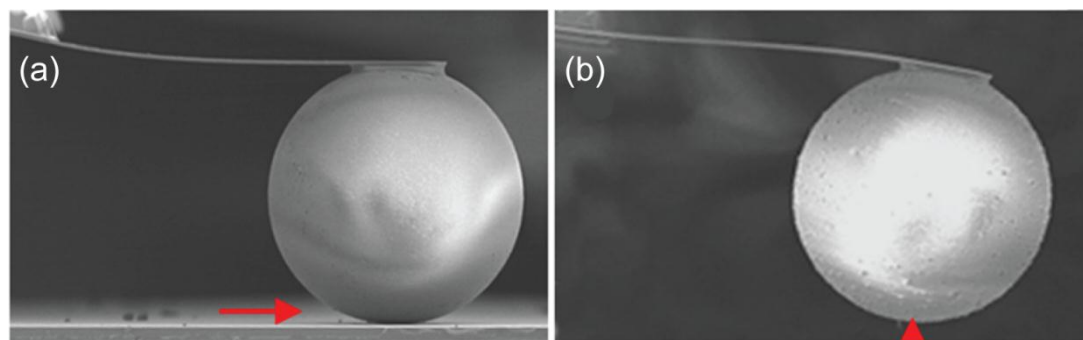


Figure 3.14: SEM images of a cantilever with a (a) sliding and (b) constrained sphere. In (a) the arrow indicates the sliding direction. In (b) the arrow indicates the point of constraint. The cantilever is inclined to  $11^\circ$  to represent its angle during AFM measurement.

The SEM images uncover a fundamental difference in the cantilever bending profile between the case of the sliding sphere and the constrained sphere. In the case of the sliding sphere, the bending profile is similar to that of a free-ended cantilever

(Figure 3.14 (a)). In the case of the constrained sphere, a moment is applied by the constrained sphere to the cantilever, preventing rotation at the “free-end” of the cantilever; essentially the cantilever undergoes zero rotation at both ends (also described as encastre at both ends) (Figure 3.14 (b)).

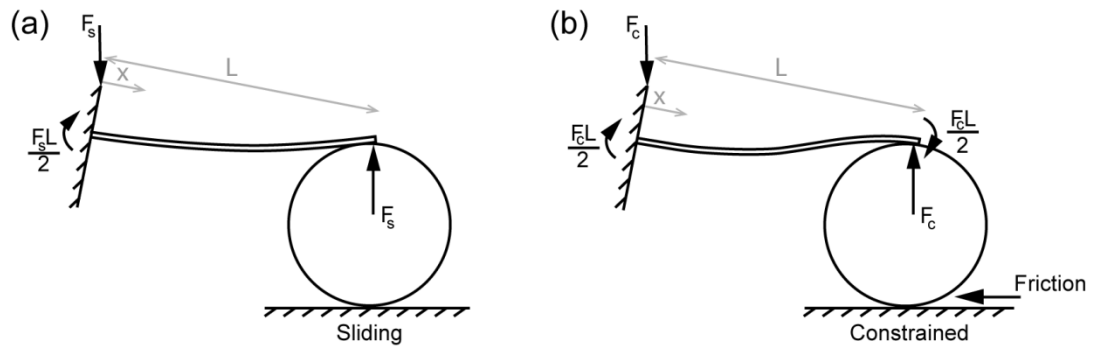


Figure 3.15: (a) A sliding sphere allows the cantilever to behave as a free-ended beam. (b) A constrained sphere results in the cantilever to behave as a rotation constrained beam.

As outlined above, a sliding sphere allows the cantilever to behave as a free-ended beam, whereas a constrained sphere results in a beam that has rotation fully constrained at both ends, as indicated in Figure 3.15. From simple beam theory, cantilever deflection and slope can be determined for each case. For a sliding sphere, cantilever deflection ( $\delta_s$ ) and slope ( $\theta_s$ ) (subscript  $s$  indicates sliding) are as follows.

$$\delta_s = \frac{F_s x^2}{6EI} (3L - x) \quad (3.5)$$

$$\theta_s = \frac{F_s x}{EI} \left(L - \frac{x}{2}\right) \quad (3.6)$$

where  $F_s$  is the force applied at the cantilever free-end,  $x$  is the axial position along the cantilever,  $L$  is the length of the cantilever,  $E$  is the elastic modulus and  $I$  is the moment of inertia.

In the case of the constrained sphere, cantilever deflection ( $\delta_c$ ) and slope ( $\theta_c$ ) (subscript  $c$  for constrained) can also be calculated from simple beam theory:

$$\delta_c = \frac{F_c x^2}{12EI} (3L - 2x) \quad (3.7)$$

$$\theta_c = \frac{F_c x}{2EI} (L - x) \quad (3.8)$$

Following from the demonstrational SEM images presented in Figure 3.13, the influence of substrate material on cantilever bending shape next investigated by side profiling the cantilever during indentation of glass (Figure 3.16 (b)) and silicone (Figure 3.16 (c)). Confocal reflection microscopy is used to create z-stacks of the cantilever (the attached sphere is not shown in Figure 3.16 for clarity). A clear difference in the cantilever bending profile for glass and silicone is evident even though the cantilever deflection ( $\delta$ ) is identical for both materials. The cantilever bending profile against glass appears similar to that of a free-ended cantilever and is comparable to that shown in Figure 3.14 (a) suggesting sphere sliding is not inhibited by the glass substrate. The cantilever bending profile for silicone suggests a constrained sphere, thus constraining rotation of the end of the cantilever (similar to the SEM image in Figure 3.14 (b)). This difference in bending profile results in the PSD measuring a larger change in voltage (slope change) for a glass substrate (Figure 3.16 (b)) than for a silicone substrate (Figure 3.16 (c)) even though the actual deflection ( $\delta$ ) is identical for both. Therefore, the conversion of measured voltage change (slope) to cantilever deflection is not applicable for a constrained sphere, as this conversion is based on the assumption of a free-ended cantilever.

As it is not possible to characterise the bending profile of the cantilever during the course of an AFM experiment, it is proposed that monitoring of the horizontal displacement of the sphere during indentation will indicate if a sphere is constrained. Image analysis (ImageJ, National Institutes of Health, USA) of the spheres front edge during substrate loading in PBS found that 1  $\mu\text{m}$  of cantilever z-displacement resulted in sphere forward displacement of  $0.61 \pm 0.03 \mu\text{m}$  for glass ( $n = 5$ ). In contrast, no detectable sphere forward displacement ( $0.04 \pm 0.08 \mu\text{m}$ ) is observed for a silicone substrate ( $n = 5$ ). Furthermore, importantly, inspection of the sphere during 2  $\mu\text{m}$  cell indentation also showed no detectable forward displacement of the sphere

$(0.00 \pm 0.13 \mu\text{m})$  ( $n = 5$ ), indicating the necessity of developing a method to account for a constrained sphere during cell indentation experiments.

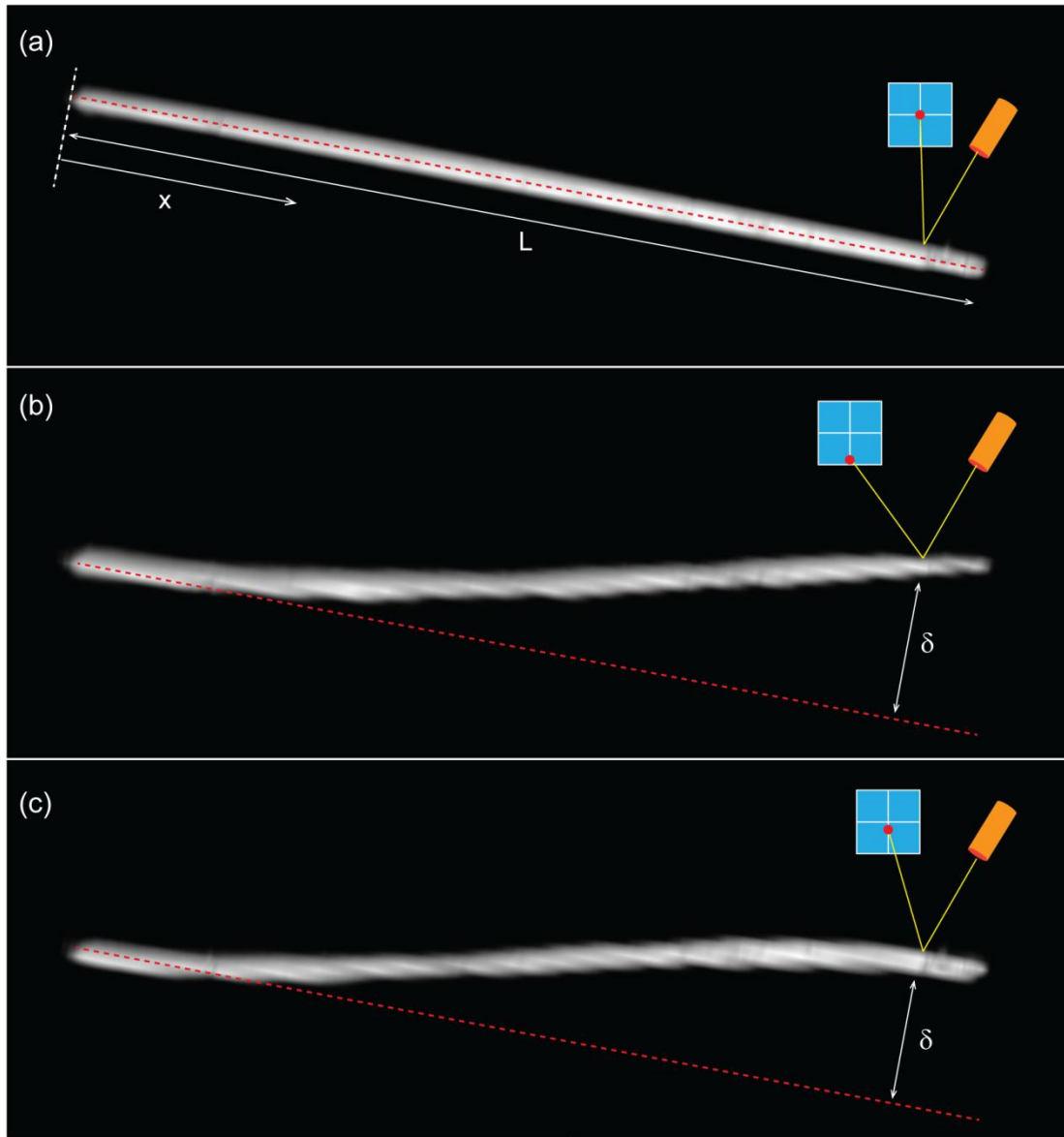


Figure 3.16: Side profiling of a cantilever (a) not in contact with a substrate, (b) in contact with glass (sliding sphere profile) and (c) in contact with silicone (constrained sphere profile). Images are created from z-stacks captured using confocal reflection microscopy (attached sphere not visible). The photodetector measures a larger change in voltage for (b) compared to (c) even though deflection ( $\delta$ ) is the same in each case. The cantilever is length  $L$  with axial position  $x$ .

### 3.4.4 Correction of Force-Indentation Measurements

It is demonstrated that the cantilever does not act as a free-ended cantilever for the case of a constrained sphere. A constrained sphere applies an additional moment at the free-end of the cantilever and thus affects AFM measurements in two ways:

- (i) The force-deflection relationship changes. Rotation at the cantilevers free-end is prevented by a constrained sphere, resulting in cantilevering at both ends. Hence, the spring constant of an equivalent free-ended cantilever cannot be used to convert deflection to applied force. The calculation of an appropriate force-deflection relationship correction factor will be presented in Section 3.4.4.1.
- (ii) The conversion of measured slope to reported deflection does not follow that of a conventional AFM, where free rotation of the cantilever is assumed. As will be demonstrated in Section 3.4.4.2, the determination of an appropriate correction factor is dependent on laser spot positioning on the cantilever.

Accounting for these relationship changes is vital for accurate determination of AFM measurements for a constrained sphere, i.e. when standard calibration for a sliding sphere scenario (e.g. OLS calibration on glass) is no longer sufficient. Here, the steps required to correctly determine AFM measurements for the case of a constrained sphere are presented.

#### 3.4.4.1 (i) Force-deflection relationship

The force-deflection relationship differs for a sliding sphere and for a constrained sphere. The correction factor that accounts for the different force-deflection relationship may be determined by comparing the analytical solutions for identical cantilever deflections for constrained and sliding beams, Equations (3.5) and (3.7).

$$\delta_s = \delta_c \tag{3.9}$$

As discussed above, simple beam theory allows the sliding sphere case to behave as a free-ended beam and the constrained sphere case to behave as a beam with rotation fully constrained at both ends.

$$\frac{F_s x^2}{6EI} (3L - x) = \frac{F_c x^2}{12EI} (3L - 2x) \quad (3.10)$$

If it is assumed that force is applied at the cantilever free-end,  $x = L$ .

$$\frac{F_s L^3}{3EI} = \frac{F_c L^3}{12EI} \quad (3.11)$$

Elastic modulus ( $E$ ), moment of inertia ( $I$ ) and cantilever length ( $L$ ) are identical for all cases, hence, for a given deflection of the free-end of the cantilever, the applied force is four times higher in the case of a constrained sphere:

$$4F_s = F_c \quad (3.12)$$

#### 3.4.4.2 (ii) Relationship between measured slope and cantilever deflection

Conversion of the reported change in voltage from the photodiode to the actual cantilever deflection is dependent upon identifying whether a constrained sphere or a sliding sphere case is present. This is due to the difference in slope along the cantilever between the case of a sliding sphere and that of a constrained sphere, as shown in Figure 3.16. The difference in slope (slope correction factor ( $C$ )) for a sliding ( $\theta_s$ ) and constrained sphere ( $\theta_c$ ) is calculated as follows.

$$C = \frac{\theta_s}{\theta_c} \quad (3.13)$$

For each case, slope is calculated as the first derivative w.r.t.  $x$  of cantilever deflection (Equations (3.6) and (3.8)).

$$C = \frac{\frac{F_s x}{EI} (L - \frac{x}{2})}{\frac{F_c x}{2EI} (L - x)} \quad (3.14)$$

Equation (3.12) shows that the force applied by a cantilever for a sliding sphere ( $F_c$ ) is four times lower than the force applied by a cantilever for a constrained sphere ( $F_s$ ) for the same cantilever free-end deflection.

$$C = \frac{\frac{F_s x}{EI} (L - \frac{x}{2})}{\frac{4F_s x}{2EI} (L - x)} \quad (3.15)$$

Again, assuming identical Elastic modulus ( $E$ ) and moment of inertia ( $I$ ) for both cases:

$$C = \frac{(L - \frac{x}{2})}{\frac{4}{2}(L - x)} \quad (3.16)$$

Hence, the correction factor for cantilever slope as a function of normalised axial position along the cantilever ( $x/L$ ) is given as:

$$C = \frac{(2 - \frac{x}{L})}{4(1 - \frac{x}{L})} \quad (3.17)$$

The slope correction factor ( $C$ ) depends only on  $x/L$ , i.e. it depends only on the position of the laser along the axis of the cantilever.

Analytical solutions from simple beam theory are used to compute the slope profiles along the axis of a cantilever (Equations (3.6) and (3.8)) when identical end deflections are imposed in both cases shown in Figure 3.17 (a). Clearly, the difference in slope between the constrained sphere and sliding sphere is a function of axial position ( $x$ ) along a cantilever of length ( $L$ ). Only at a cantilever position of  $x/L = 0.66$  is the slope identical for both cases. The ratio of slope between a sliding sphere and a constrained sphere (i.e. the slope correction factor ( $C$ )) is shown in

Figure 3.17 (b). It can be observed that the slope ratio is highly sensitive to axial position near the free-end of the cantilever ( $x/L > 0.9$ ).

As demonstrated in Figure 3.17, in order to determine the correct deflection for the case of a constrained sphere, it is essential that the laser spot position on the cantilever is known. For all experiments reported in this thesis a laser spot position of  $x/L = 0.8$  is chosen. This position is selected as a compromise between the maximum OLS at the free-end of a cantilever ( $x/L = 1$ ) for the sliding sphere (i.e. during calibration on glass) and the maximum OLS at the middle of the cantilever ( $x/L = 0.5$ ) for the constrained sphere (e.g. during subsequent experimental measurement of cells or silicone). At  $x/L = 0.8$  a constrained sphere profile will result in the measurement of a slope that is 1.5 times lower than the slope that would be measured at this position for a sliding sphere (as indicated by the dashed line in Figure 3.17 (b)), assuming an identical end deflection in both cases. Therefore, for constrained spheres, when the laser spot position is at  $x/L = 0.8$ , a correction factor of 1.5 must be applied to the default AFM deflection measurement in order to obtain the correct deflection.

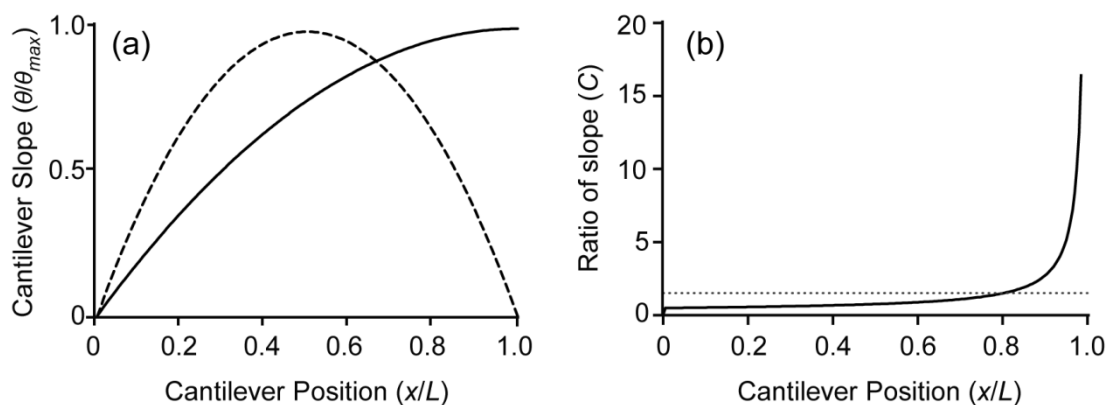


Figure 3.17: (a) Cantilever slope along the axis of a cantilever which has a sliding sphere (solid) and constrained sphere (dashed) bending profile. Identical end deflections are imposed in each case. (b) At a cantilever position of  $x/L = 0.8$  the difference in slope is  $\times 1.5$  (dotted).

In summary, to correctly determine the deflection and force measured for the case of a constrained sphere, (i) the slope change recorded by the AFM has to be corrected according to Figure 3.17 (b) and is only dependent on the relative axial position of the laser spot along the cantilever. In all experiments performed herein,

the laser is positioned at  $x/L = 0.8$ , therefore a slope-deflection correction factor of 1.5 is applied to default AFM measured deflection values. (ii) Due to rotation constraint at the cantilever free-end, the cantilever stiffness is four times higher than that of a free-ended cantilever.

### 3.4.5 Validation of Correction Factors

Validation of the slope-deflection and force-deflection relationship changes is achieved by indenting a flat silicone substrate of known Young's modulus. Tensile testing (0-10% strain) of four sections of the silicone substrate indicates the Young's modulus to be  $0.92 \pm 0.08$  MPa. To calculate the Young's modulus of the silicone using the AFM, the OLS is calibrated on glass in PBS according to Section 3.4.1. Force-deformation measurements are performed on the silicone in PBS at five separate locations at an approach velocity of  $0.5 \mu\text{m/s}$ . Figure 3.18 shows the force (mean  $\pm$  standard deviation) at 10 sample indentation depths for both the uncorrected and corrected data. The uncorrected default AFM data reports a maximum force of  $0.48 \pm 0.08 \mu\text{N}$  at an indentation of  $0.9 \mu\text{m}$ . This results in a calculated Young's modulus of 0.05 MPa using standard Hertzian contact theory. Application of the correction factors, determined above, to the data results in a maximum force of  $2.88 \pm 0.47 \mu\text{N}$  at a corrected indentation depth of  $0.4 \mu\text{m}$ . This results in a calculated Young's modulus of 0.94 MPa, which is within 2% of the Young's modulus calculated from the tensile testing experiments. The uncorrected AFM data results in a substantial (18-fold) underestimation of the silicone's elastic modulus. This highlights the significant error that can arise if cantilever modification, resulting in an altered bending profile, is not carefully analysed, illustrating the necessity of careful interpretation and in-depth analysis of reported default AFM measurements.

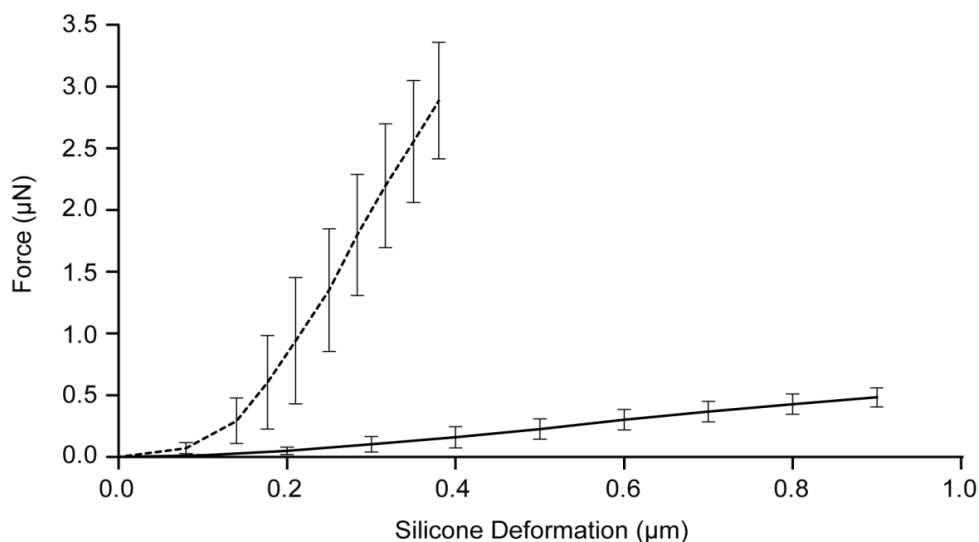


Figure 3.18: Uncorrected (solid) and corrected (dashed) AFM force-deformation data. The Young's moduli are calculated as 0.05 MPa and 0.94 MPa, respectively.

### 3.5 Discussion

In this chapter, a method of performing whole cell deformation using an AFM is successfully developed, whereby a large sphere is attached to the end of a tipless cantilever. The bottom of the sphere forms the effective top planar surface, providing more uniform applied cell deformation. The sphere used in this study is significantly larger ( $\text{\O} 150 \mu\text{m}$ ) than those used in previous studies ( $< \text{\O} 60 \mu\text{m}$ ), and as such provide a closer approximation to the planar surface assumption over the contact area (Lehenkari et al. (2000), Lulevich et al. (2006), Jaasma et al. (2006), Zimmer et al. (2012)).

It is found that careful reinterpretation of reported AFM data is required to account for a constrained sphere. A constrained sphere applies a moment to the cantilever, preventing rotation of the free-end of the cantilever. This in turn changes the slope-deflection and force-deflection relationships. This serious issue, which can significantly alter the reported force measurements and perceived indentation depth, has not been considered in previous AFM studies where a sphere is attached to the cantilever (Lehenkari et al. (2000), Lulevich et al. (2006), Jaasma et al. (2006), Zimmer et al. (2012)). In this chapter, a methodology is outlined in order to correctly determine force and indentation values when sphere sliding is prevented and a

rotational constraint is applied to the free-end of the cantilever. Furthermore, it is demonstrated that observation of the front edge of the sphere is sufficient to determine if the correction factor is applicable. Previous studies have attempted to account for the effects of altered cantilever bending. A theoretical paper by Edwards et al. (2008) developed correction factors to account for the effects of cantilever tilt and induced torque on force measurements. Furthermore, Evans and Craig (2006) proposed equations to determine cantilever deflection for different loading scenarios; uniformly distributed loading and moment loading. However, the current study presents, for the first time, a practical methodology that accounts for both altered cantilever stiffness and altered cantilever slope-deflection relationship for the correct interpretation of AFM force-indentation measurement. The methodology described here requires only the monitoring of the forward displacement of the sphere during loading in order to determine if correction factors for a constrained sphere should be used. It is demonstrated in this chapter that uncorrected default AFM force and indentation measurements result in an 18-fold underestimation of the Young's modulus of a silicone sample, where sphere-substrate friction was sufficient to prevent sphere sliding. In conclusion, this chapter illustrates, for the first time, the necessity of careful interpretation of default AFM measurements if a sphere is attached to a cantilever. The work presented in this Chapter is published in the *Review of Scientific Instruments* (Weafer et al. (2012)).

### 3.6 References

- Attard, P. (2007) Measurement and interpretation of elastic and viscoelastic properties with the atomic force microscope. *J. Phys. Condens. Matter.* 19 (47), 3201-3233
- Butt, H. J., Cappella, B. and Kappl, M. (2005) Force measurements with the atomic force microscope: Technique, interpretation and applications. *Surface Science Reports.* 59 (1-6), 1-152
- Butt, H. J. and Jaschke, M. (1995) Calculation of thermal noise in atomic force microscopy. *Nanotechnology.* 6 (1), 1-7
- Caille, N., Thoumine, O., Tardy, Y. and Meister, J. J. (2002) Contribution of the nucleus to the mechanical properties of endothelial cells. *J. Biomech.* 35 (2), 177-187
- Chung, K. H., Shaw, G. A. and Pratt, J. R. (2009) Accurate noncontact calibration of colloidal probe sensitivities in atomic force microscopy. *Rev. Sci. Instrum.* 80, 065107
- Cleveland, J. P., Manne, S., Bocek, D. and Hansma, P. K. (1993) A nondestructive method for determining the spring constant of cantilevers for scanning force microscopy. *Rev. Sci. Instrum.* 64 (2), 403-405
- Colton, R. J., Baselt, D. R., Dufrêne, Y. F., Green, J. B. D. and Lee, G. U. (1997) Scanning probe microscopy. *Current opinion in chemical biology.* 1 (3), 370-377
- Cross, S. E., Jin, Y. S., Tondre, J., Wong, R., Rao, J. Y. and Gimzewski, J. K. (2008) Afm-based analysis of human metastatic cancer cells. *Nanotechnology.* 19 (38), 384003
- Edwards, S. A., Ducker, W. A. and Sader, J. E. (2008) Influence of atomic force microscope cantilever tilt and induced torque on force measurements. *J. Appl. Phys.* 103, 064513
- Evans, D. R. and Craig, V. S. J. (2006) Sensing cantilever beam bending by the optical lever technique and its application to surface stress. *J. Phys. Chem. B.* 110 (11), 5450-5461
- Fan, T. H. and Fedorov, A. G. (2003) Analysis of hydrodynamic interactions during afm imaging of biological membranes. *Langmuir.* 19 (4), 1347-1356
- Hofmann, U. G., Rotsch, C., Parak, W. J. and Radmacher, M. (1997) Investigating the cytoskeleton of chicken cardiocytes with the atomic force microscope. *Journal of Structural Biology.* 119 (2), 84-91

- Hoh, J. H. and Engel, A. (1993) Friction effects on force measurements with an atomic force microscope. *Langmuir*. 9 (11), 3310-3312
- Jaasma, M. J., Jackson, W. M. and Keaveny, T. M. (2006) Measurement and characterization of whole-cell mechanical behavior. *Annals of biomedical engineering*. 34 (5), 748-758
- Kelly, G. M., Kilpatrick, J. I., van Es, M. H., Weafer, P. P., Prendergast, P. J. and Jarvis, S. P. (2011) Bone cell elasticity and morphology changes during the cell cycle. *J. Biomech*. 44 (8), 1484-1490
- Lehenkari, P. P., Charras, G. T., Nykänen, A. and Horton, M. A. (2000) Adapting atomic force microscopy for cell biology. *Ultramicroscopy*. 82 (1-4), 289-295
- Lim, C. T., Zhou, E. H., Li, A., Vedula, S. R. K. and Fu, H. X. (2006) Experimental techniques for single cell and single molecule biomechanics. *Materials Science and Engineering: C*. 26 (8), 1278-1288
- Lulevich, V., Zink, T., Chen, H. Y., Liu, F. T. and Liu, G. (2006) Cell mechanics using atomic force microscopy-based single-cell compression. *Langmuir*. 22 (19), 8151-8155
- Meyer, G. and Amer, N. M. (1988) Novel optical approach to atomic force microscopy. *Applied physics letters*. 53 (12), 1045-1047
- Mostaert, A., Higgins, M., Fukuma, T., Rindi, F. and Jarvis, S. (2006) Nanoscale mechanical characterisation of amyloid fibrils discovered in a natural adhesive. *Journal of Biological Physics*. 32 (5), 393-401
- Ofek, G., Natoli, R. M. and Athanasiou, K. A. (2009) In situ mechanical properties of the chondrocyte cytoplasm and nucleus. *J Biomech*. 42 (7), 873-877
- Peeters, E. A. G., Oomens, C. W. J., Bouten, C. V. C., Bader, D. L. and Baaijens, F. P. T. (2005) Viscoelastic properties of single attached cells under compression. *J Biomech Eng*. 127 (2), 237-243
- Radmacher, M., Fritz, M., Kacher, C. M., Cleveland, J. P. and Hansma, P. K. (1996) Measuring the viscoelastic properties of human platelets with the atomic force microscope. *Biophys. J*. 70 (1), 556-567
- Roca-Cusachs, P., Alcaraz, J., Sunyer, R., Samitier, J., Farré, R. and Navajas, D. (2008) Micropatterning of single endothelial cell shape reveals a tight coupling between nuclear volume in g1 and proliferation. *Biophysical Journal*. 94 (12), 4984-4995
- Rotsch, C. and Radmacher, M. (2000) Drug-induced changes of cytoskeletal structure and mechanics in fibroblasts: An atomic force microscopy study. *Biophysical Journal*. 78 (1), 520-535

- Sader, J. E., Larson, I., Mulvaney, P. and White, L. R. (1995) Method for the calibration of atomic force microscope cantilevers. *Rev. Sci. Instrum.* 66 (7), 3789-3798
- Shannon, M. N., Simon, B. and Vincent, S. J. C. (2003) Calibration of colloid probe cantilevers using the dynamic viscous response of a confined liquid. *Review of Scientific Instruments.* 74 (9), 4026-4032
- Simon, A. and Durrieu, M. C. (2006) Strategies and results of atomic force microscopy in the study of cellular adhesion. *Micron.* 37 (1), 1-13
- Stiernstedt, J., Rutland, M. W. and Attard, P. (2005) A novel technique for the in situ calibration and measurement of friction with the atomic force microscope. *Rev. Sci. Instrum.* 76, 083710
- Thoumine, O. and Ott, A. (1997) Time scale dependent viscoelastic and contractile regimes in fibroblasts probed by microplate manipulation. *J Cell Sci.* 110 (17), 2109-2116
- Weafer, P. P., McGarry, J. P., van Es, M. H., Kilpatrick, J. I., Ronan, W., Nolan, D. R. and Jarvis, S. P. (2012) Stability enhancement of an atomic force microscope for long-term force measurement including cantilever modification for whole cell deformation. *Review of Scientific Instruments.* 83 (9), 093709
- Zimmer, C. C., Shi, L. F., Shih, Y. P., Li, J. R., Jin, L. W., Lo, S. H. and Liu, G. Y. (2012) F-actin reassembly during focal adhesion impacts single cell mechanics and nanoscale membrane structure. *Science China Chemistry.* 1-11

## Chapter 4

# **The Role of Actin Cytoskeleton Contractility in the Resistance of Osteoblasts to Compression**

## 4.1 Introduction

Mechanical loading is necessary for the healthy function of many cell types. For instance, mechanical deformation is considered essential for bone remodelling (Frost (2004)). The response of osteoblasts to mechanical loading is attributed to deformation of the cell and its surrounding matrix (Duncan and Turner (1995), Owan et al. (1997)). Previous studies have shown that compressive deformation induces mineralisation of osteoblastic cells (Gabbay et al. (2006)) and is an effective up-regulator of osteogenesis (Rath et al. (2008)). Furthermore, localised deformation of osteoblasts has been found to induce calcium and nitric oxide signalling, both of which are important in bone function (Charras and Horton (2002), Sato et al. (2007), McGarry et al. (2008)). While the role of mechanical loading on cell function has been reported, the basic mechanisms underlying these cellular mechanosensitive responses are still not fully understood. In order to elucidate the effect of mechanical loading on cell function it is essential to accurately characterise the biomechanical behaviour of the cell.

The resistance of a cell to compressive deformation largely depends on the mechanical properties of the cell, which are determined by its intracellular components (cytoskeleton, nucleus, cytoplasm, and several other organelles) (Thoumine and Ott (1997), Rotsch and Radmacher (2000), Ofek et al. (2009)) and its interactions with the environment around it ((Engler et al. (2006), Roca-Cusachs et al. (2008), Janmey et al. (2011)). Ofek et al. (2009) investigated the contribution of the cytoskeletal components of chondrocytes to compressive deformation using selective cytoskeletal inhibitors. It was found that the actin cytoskeleton significantly contributes to the compressive stiffness of cell, whereas microtubules and intermediate filaments provide little resistance to cell compression. Furthermore, it has been shown that the nucleus contributes significantly to a cells ability to resist compression (Caille et al. (2002)). Additionally, resistance to compressive deformation has been shown to be highly dependent on cell phenotype. Peeters et al. (2005a) reported high levels of resistance to compressive deformation for highly contractile myoblasts, whereas the less contractile endothelial cells (Caille et al. (2002)) and fibroblasts (Deng et al. (2010)) were found to have significantly reduced

compression resistance. This link between compression resistance and contractility further highlights the importance of the actin cytoskeleton in the mechanical behaviour of cells.

The objective of this study is to investigate the role of the actin cytoskeleton in the resistance of osteoblasts to compression. Specifically, experiments are performed in which the resistance of single spread osteoblasts to monotonic whole cell compression is observed. Additionally, tests are also performed on osteoblasts following the inhibition of the cell actin cytoskeleton using cyto-D. Whole cell compression is applied using the modified AFM cantilever described in Chapter 3. It is found that the contractile actin cytoskeleton plays a significant role in the cells ability to resist compression. Furthermore, detailed confocal microscopy demonstrates that the contractile nature of the actin cytoskeleton has a pronounced effect on cell and nucleus morphology.

## **4.2 Materials and Methods**

### **4.2.1 Cell Culture**

The cells investigated in this study are a secondary cell line known as MC3T3-E1, subclone 4 (ATCC-LGC, Middlesex, UK). These adherent pre-osteoblasts are derived from the calvarial tissue of newborn mice and are known to behave similarly to primary calvarial osteoblasts (Wang et al. (1999)). This cell line is robust, homogeneous, and the predominant choice in bone cell mechanotransduction research (Pavalko et al. (1998), Charras and Horton (2002), McGarry et al. (2008), Adachi et al. (2008)).

Cells are cultured in monolayer in alpha minimum essential medium ( $\alpha$ -MEM; Sigma-Aldrich, UK) supplemented with 10% foetal bovine serum (FBS), 1% penicillin-streptomycin, 2% 2 mM L-glutamine and 1% 100 mM sodium pyruvate (Invitrogen, Ireland). Cells are maintained in an incubator at 37 °C, with 95% humidity and 5% CO<sub>2</sub>. Medium is changed every 2-3 days. Cell subculture is routinely performed at 80-90% confluency, as assessed by visual inspection of cultures. Cell are used when the confluence is less than 80% at passages 10 to 20.

### 4.2.2 Cell Preparation

MC3T3-E1 osteoblasts are cultured according to the method described in Section 4.2.1. Prior to experiments, cells are seeded at a single cell level and allowed to spread for 24 hr. Briefly, the medium is removed and culture flasks rinsed in pre-warmed sterile phosphate buffered saline (Oxoid, UK) in order to remove any traces of medium. To detach cells from the surface of flasks, 5-7 ml of pre-warmed 0.25% trypsin EDTA (Sigma-Aldrich, UK) is added, and flasks are placed in an incubator at 37 °C, for 4 min. Cultures are then briefly re-examined under a light microscope to ensure sufficient cell detachment had occurred. The suspension is collected in a 15 ml falcon tube containing 5-7 ml pre-warmed medium and centrifuged at 2000 g for 5 min. The supernatant is discarded and the pellet resuspended in 10 ml supplemented  $\alpha$ -MEM. This suspension is aspirated through a 1 ml pipette three times to obtain a single cell suspension. The cell concentration is counted using a haemocytometer. Cells are seeded on a sterile  $\emptyset$  35  $\mu$ m petri-dish at a density of 3,500 cells/cm<sup>2</sup> and left to spread in an incubator for 24 hr.

### 4.2.3 Experimental Procedure

The AFM is setup according to Section 3.2.1. A modified cantilever is used to measure whole cell mechanics, as previously described in Section 3.4. The coverslip to which the cells are adhered is placed within a BioHeater™ (Asylum Research, CL, USA), which is in turn secured to the stage of the AFM. Experiments are performed at 37 °C with cells remaining immersed in culture medium for the duration of the experiments.

The AFM head is centred on the stage and the modified cantilever lowered into the media until a few millimetres from the surface. Air bubble formation on the cantilever or sphere is assessed by visual inspection. If required, bubbles are removed by raising the AFM head until the cantilever is removed from the media and then lowered again. Laser alignment on the cantilever and cantilever calibration are performed according to Section 3.4. The modified cantilever is examined during experiments to assess that the sphere remains constrained during cell indentation. Consequently, all measured force data are corrected using the factors identified in

Section 3.4.4. All force-displacement curves are performed in closed loop mode at an approach velocity of 500 nm/s, unless otherwise stated.

#### 4.2.3.1 Cell Height Measurement

The height of the cell of interest is measured directly before each deformation test. As demonstrated in Figure 4.1, the sample stage is moved via the x-y stage positioners until the cell of interest is located adjacent to the modified cantilever. Cell height is determined as the difference in z-piezo position between the point of contact for a force-displacement curve taken on the glass substrate beside a cell ( $z_{piezo_{substrate}}$ ) and that taken over the cell of interest ( $z_{piezo_{cell}}$ ), as shown in Figure 4.2. This is represented in Equation (4.1) below. Phase contrast optical microscopy allows aligning of the microsphere above the centre of the cell.

$$Cell\ height = z_{piezo_{cell}} - z_{piezo_{substrate}} \quad (4.1)$$

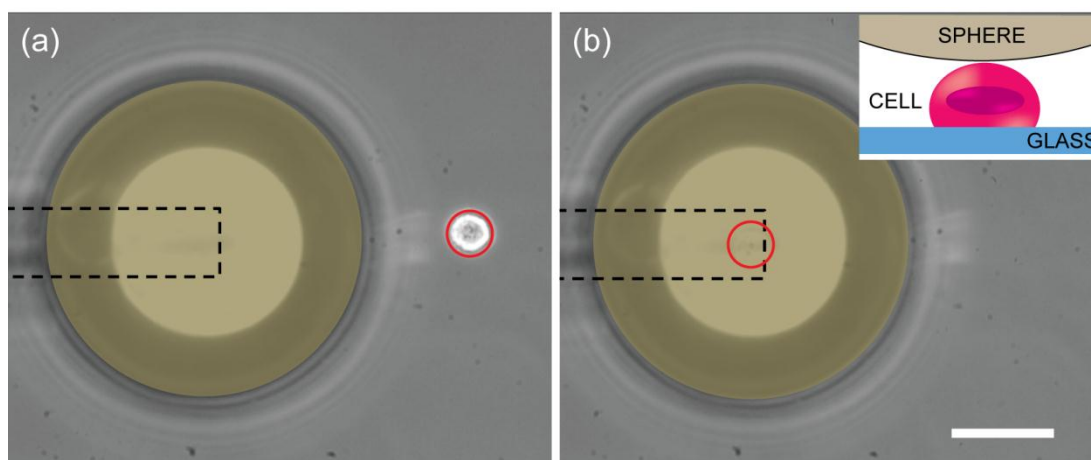


Figure 4.1: Bottom-view phase contrast images of the modified cantilever showing outline of tipless cantilever (dashed), attached sphere (brown), and a cell adhered to the glass substrate (red circle). (a) shows the modified cantilever beside a cell of interest, and (b) centred above the same cell. Inset: schematic representation of sphere in contact with the top of the cell. The scale bar represents 50  $\mu\text{m}$ .

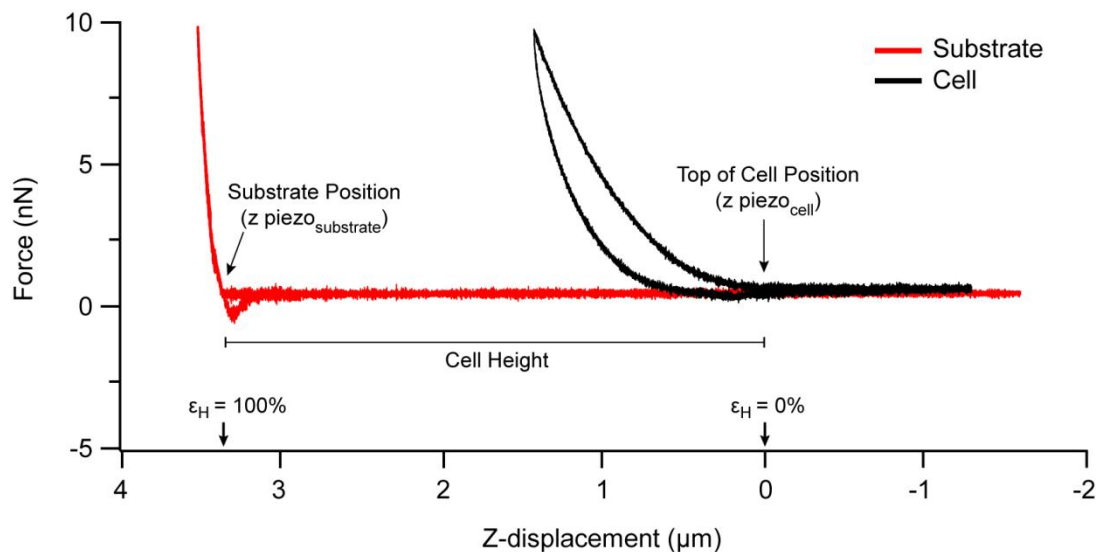


Figure 4.2: Force-displacement curves taken on the glass substrate beside the cell of interest (red) and over the cell of interest (black). The cell height is calculated as the difference between the contact points from each curve.

#### 4.2.3.2 Cell Deformation

In this thesis cell deformation ( $\epsilon_H$ ) is defined as the change in cell height normalised by the measured cell height prior to applied compression (i.e. nominal strain in the compressive direction), given as:

$$\epsilon_H = \frac{\text{change in cell height}}{\text{undeformed cell height}} \quad (4.2)$$

Each cell ( $n = 11$ ) is subjected to a monotonic deformation at a constant strain rate ( $\frac{d\epsilon_H}{dt} = \dot{\epsilon}_H = 0.1 \text{ s}^{-1}$ ) until a compressive deformation of  $\epsilon_H = 60\%$  is achieved. An identical (negative) strain rate is used for unloading of cells (probe withdrawal). Each cell is subjected to a monotonic deformation under two sample conditions; untreated control and cyto-D treated. Firstly, untreated cells are tested, prepared according to Section 4.2.2. Secondly, following 30 min of actin cytoskeleton disruption, using 10  $\mu\text{M}$  cyto-D, deformation is repeated for the same cells (referred to hereafter as “cyto-D cells”). In each case, phase contrast images are taken to record cell spreading morphology.

#### 4.2.4 Cytoskeleton Morphology Analysis

Cells are prepared as described in Section 4.2.2. Following incubation for 24 hr, cells are (i) fixed (untreated cells) or (ii) treated with 10  $\mu$ M cyto-D for 30 min and then fixed (cyto-D cells). Fixation is achieved by incubating samples in 4% paraformaldehyde (EMS, PA, USA) for 20 min at room temperature. Samples are washed two times in wash buffer (PBS containing 0.5% Tween-20) and permeabilised with 0.1% Triton X-100 in PBS for 5 min. Cells are then washed two times in wash buffer, and non-reactive sites are blocked by applying blocking solution (1% BSA in PBS) for 30 min. Samples are incubated with an anti-vinculin primary antibody (Chemicon, Ireland), diluted to the optimal titre (1:200) in blocking solution for 1 hr. Vinculin is found in protein complexes reported to be associated with the intracellular domains of integrin receptors which form focal adhesion complexes. Thus, vinculin is considered to be a universal marker for focal adhesions (Burridge et al. (1990)). Cells are washed three times (5 min each) with wash buffer, following which cells are incubated with Gt x Ms FITC-conjugated secondary antibody (1:200 in PBS) and rhodamine-conjugated phalloidin (1:50 in PBS) for 1 hr in the dark. Phalloidin is a naturally occurring organic molecule that binds to actin filaments. Therefore, conjugation of phalloidin with a fluorophore, such as rhodamine, allows visualisation of the actin cytoskeleton in cells (Cooper (1987)). Cells are washed three times in wash buffer (5 min each) and counterstained using the nuclear stain DAPI (1:10,000 in PBS) for 5 min in the dark. Samples are again washed 3 times (5 min each) in wash buffer and maintained in PBS at 4 °C.

Samples are imaged the following day. DAPI, FITC and Rhodamine are excited at 402, 488 and 561 nm, respectively, while emitted fluorescence is collected at 470, 525 and 590 nm for each fluorophore, respectively. Z-stacks of untreated cells (n = 5) and cyto-D cells (n = 7) are acquired using a Nikon A1R confocal microscope (Nikon, UK) with intervals of 200 nm between z-stack steps. The Nikon NIS-Elements AR 3.0 software package (Nikon, UK) is used to quantify cytoskeletal and cell morphology details.

### 4.2.5 Statistical Analysis of Data

All data is presented as mean  $\pm$  standard error of the mean (sem). Statistical differences between the means of two experimental groups are determined using Student's t-tests. Paired t-tests are used to investigate statistical differences between the means of dependent groups, i.e. AFM measurements taken before and after cyto-D treatment on the same cells (Section 4.2.3). Unpaired t-tests are used to investigate statistical significance between the means of independent experimental groups, i.e. morphology changes of fluorescently stained cells (Section 4.2.4). One-way analysis of variance (ANOVA) tests are employed to determine statistical differences between the means of the three independent cell groups, i.e. difference between three different strain rates. The associated  $p$ -value is also determined in each case, and the null hypothesis rejected if  $p > 0.05$ . Significant differences between groups are indicated by  $*p < 0.01$ ,  $**p < 0.001$ ,  $***p < 0.0001$ .

## 4.3 Results

### 4.3.1 Cell Morphology Change

Untreated cells (Figure 4.3) and cyto-D treated cells (Figure 4.5) are stained to observe the effect of disrupting the actin cytoskeleton on cell morphology. Figure 4.3 shows the stained morphology of untreated cells. The untreated cells are highly spread with polymerised actin (red) visible as long, linear bundles of filaments that traverse the cytoplasm of the cell surrounding and crossing over the nucleus (blue). Focal adhesions (green) are observed as intense spots at the terminal ends of actin filaments. In Figure 4.3 (a), the actin filaments are mostly aligned parallel with the long axis of the cell. In Figure 4.3 (b), the actin filaments are traversing the cell in all directions with the majority of the filaments focused around the periphery of the cell. In both Figure 4.3 (a) and (b), the cross-sectional views show that the cells and nuclei are highly flattened. Additionally, the actin filaments are observed to traverse over and under the nucleus. In order to further demonstrate the 3D distribution of the actin cytoskeleton a 3D reconstruction of an untreated osteoblast is shown in Figure 4.4. The highly spread cell morphology is apparent, with the polymerised actin visible as

long, linear bundles of filaments that traverse the cytoplasm of the cell surrounding and crossing over the nucleus (nucleus not visible).

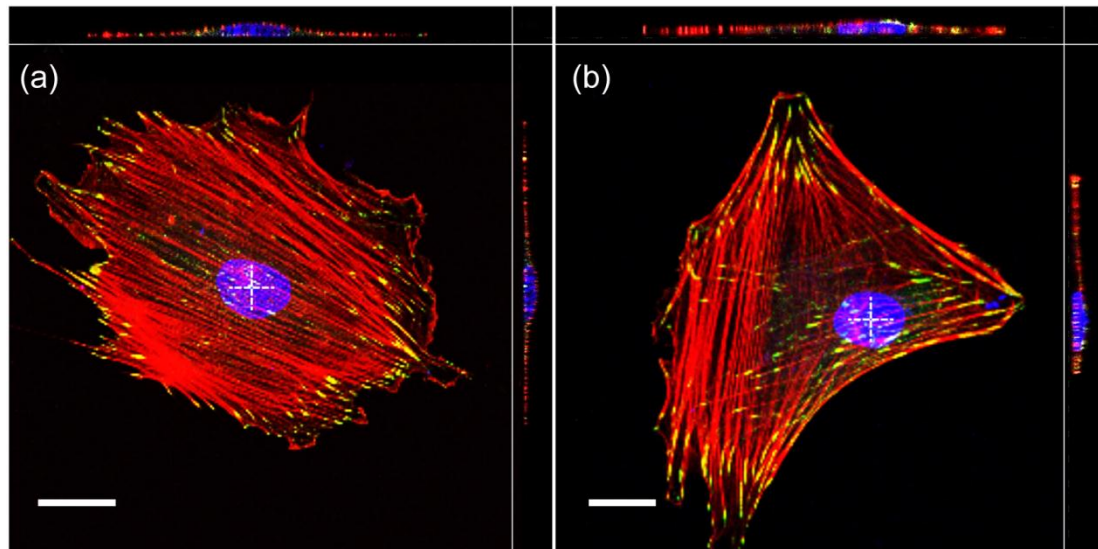


Figure 4.3: Stained cell images of untreated cells. Cells are stained for actin (red), vinculin (green) and nuclei (blue). Cross-sectional views are taken across the nucleus centre (dashed lines) in all cases. The scale bar represents 20  $\mu\text{m}$ .

Figure 4.5 (a) and (b) shows that the cell morphology changes drastically due to the addition of cyto-D. The cells are significantly less spread and appear spindly. Cross-sectional views show the less flattened morphology, with a larger thickness of cytoplasm being observed both above and below the more rounded nuclei. Cyto-D results in actin depolymerisation to its monomer form, which causes the disassembly of the linear bundles of actin filaments and corresponding focal adhesions. The actin and focal adhesion protein monomers appear to be concentrated together mostly around the nucleus, indicated by the yellow/orange colour.

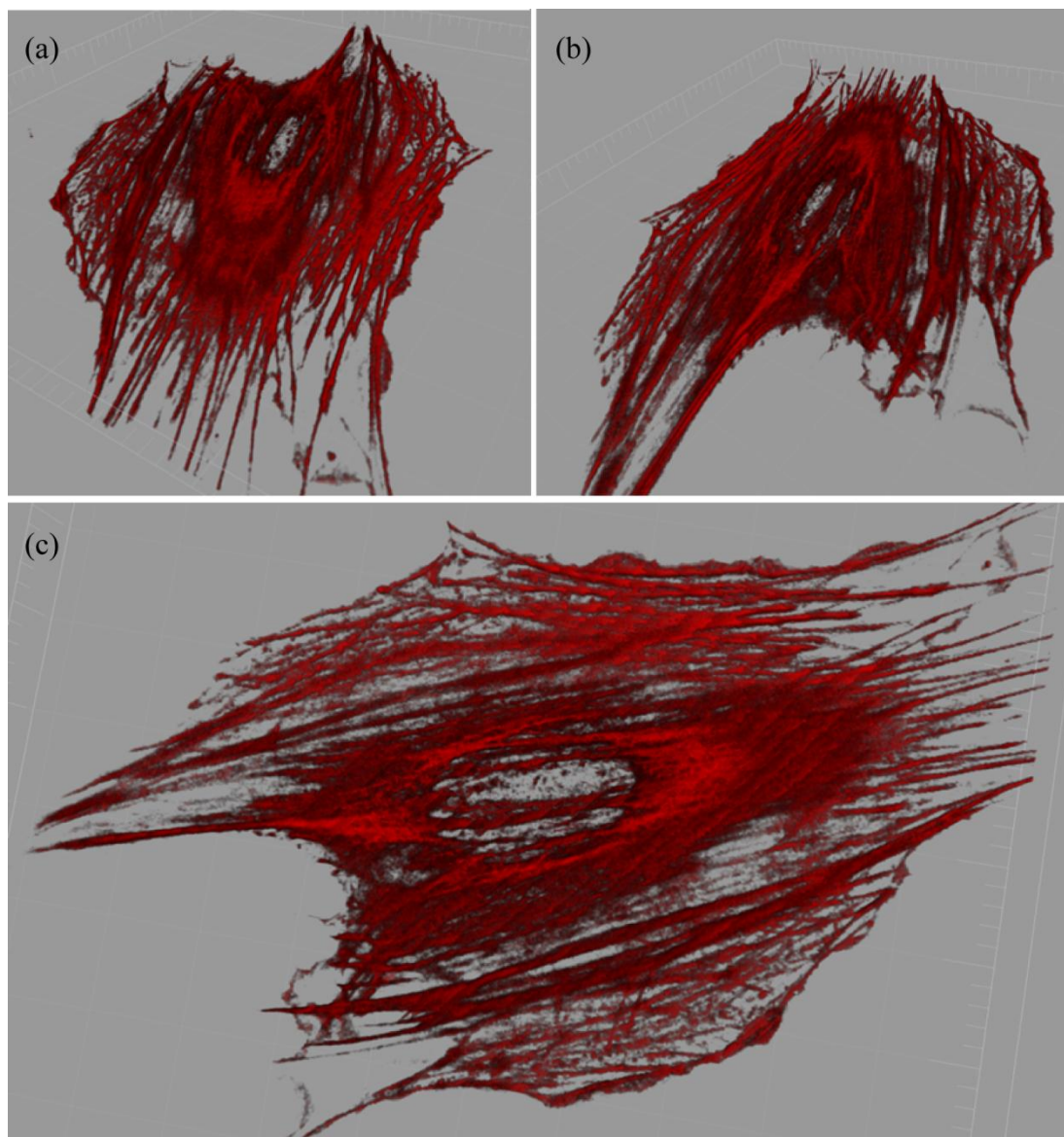


Figure 4.4: 3D reconstruction of the actin cytoskeleton created from a z-stack of a stained osteoblast. Three perspective views of the 3D reconstruction are shown; (a) and (b) show the actin cytoskeleton along the long axis of the cell in both directions and (c) shows the top-down view. Images are reconstructed using the Imaris software package (Bitplane, Switzerland).

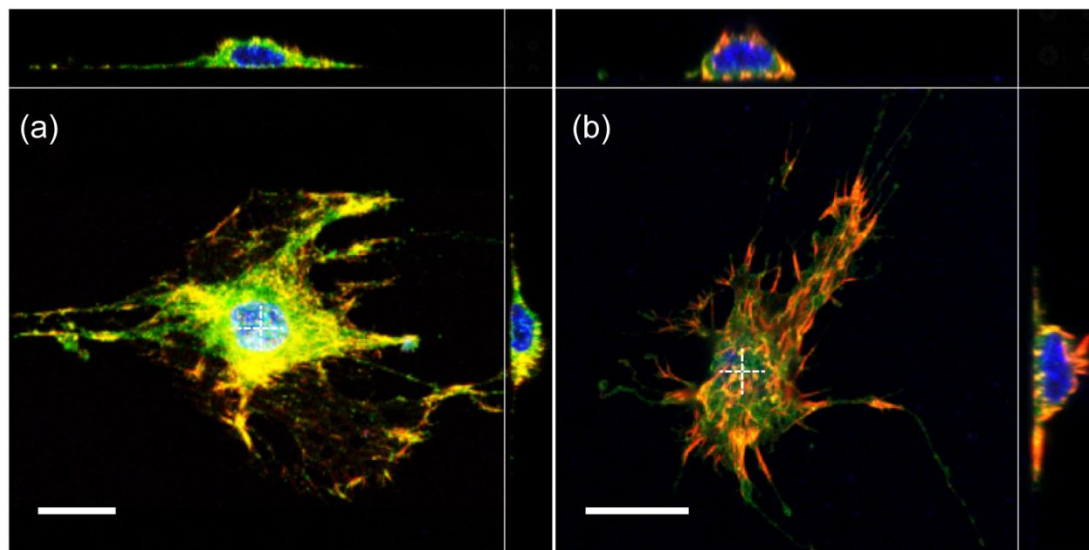


Figure 4.5: Stained cell images of cyto-D cells. Cells are stained for actin (red), vinculin (green) and nuclei (blue). Cross-sectional views are taken across the nucleus centre (dashed lines) in all cases. The scale bar represents 20  $\mu\text{m}$ .

The main geometrical characteristics of untreated and cyto-D cells are shown in Figure 4.6. Analysis of experimental measurements reveals that the cell height increases by 71% in response to cyto-D treatment. Additionally, phase contrast images of the cell show that the cell base area decreases by 29% following the addition of cyto-D. Analysis of the stained cells shows that the nucleus height increases by 57% and that the nucleus diameter decreases by 41% in response to cyto-D treatment. It is also observed that the cytoplasm thickness above and below the nucleus increased by over 200%. Further details of cell morphological changes are presented in tabular form in Appendix 4.A.

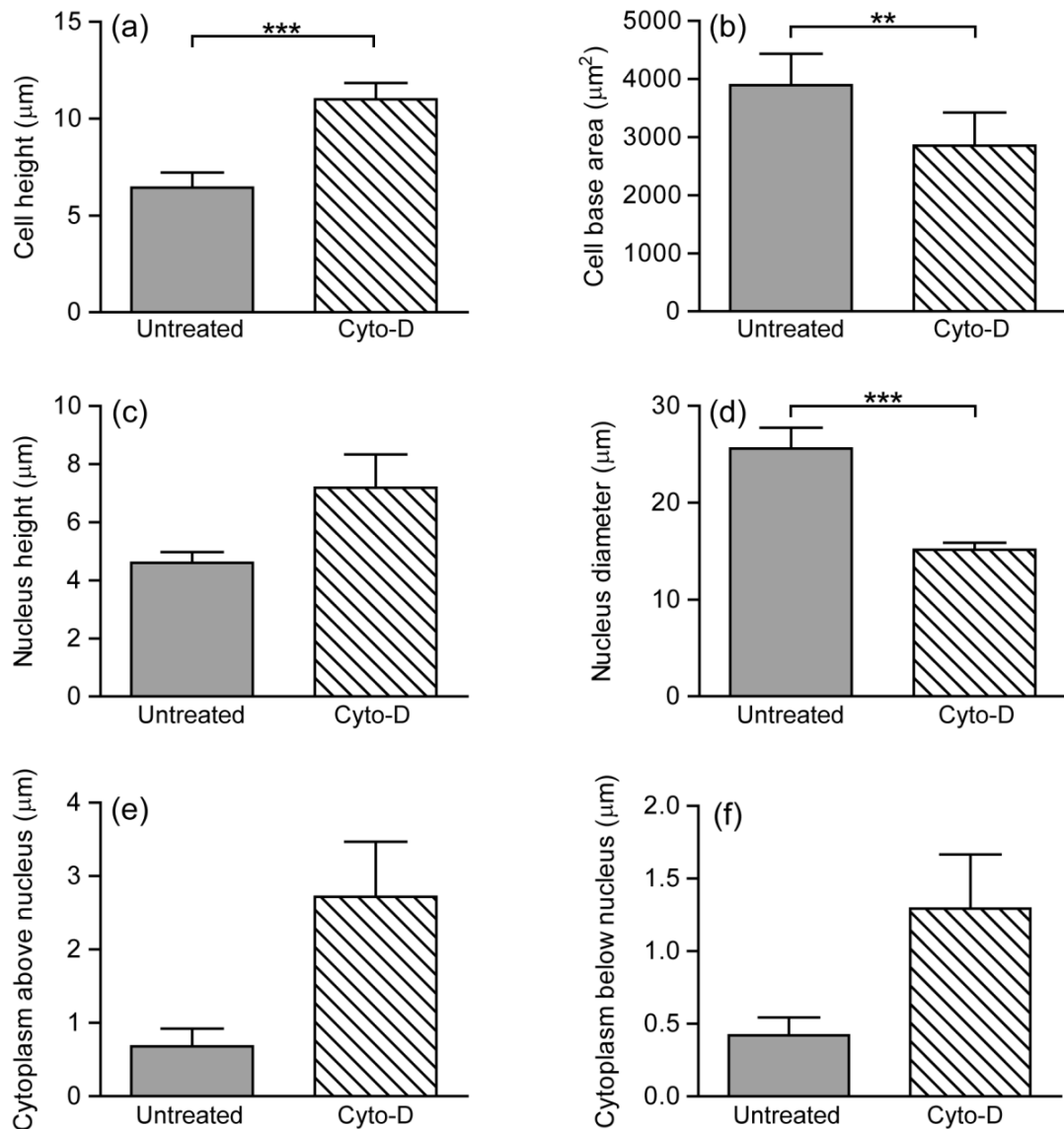


Figure 4.6: Cell geometry characteristics for untreated and cyto-D cells. (a) Cell height is measured using the AFM immediately before monotonic deformation ( $n = 11$ ). Cell base area is calculated from phase contrast images taken during AFM experiments ( $n = 11$ ). The (c) nucleus height, (d) nucleus diameter, and cytoplasm (e) above and (f) below the nucleus are all calculated from the stained cells ( $n = 5$ ) and cyto-D cells ( $n = 7$ ).

### 4.3.2 Monotonic Compression

The mean force versus compressive deformation curves measured at a constant strain rate ( $n = 11$ ) for untreated (round markers) and cyto-D (square markers) cells are shown in Figure 4.7. The raw AFM data used to derive results presented in Figure 4.7 is shown in Appendix 4.B. Mean forces are calculated at compressive deformation increments of  $\epsilon_H = 10\%$ . It is evident that the force increases non-

linearly with the imposed compressive deformation for both the untreated cells and cyto-D cells. For the loading half of the curve, a statistically significant difference is measured between the untreated cells and cyto-D cells for  $40\% \leq \varepsilon_H \leq 60\%$ . At  $\varepsilon_H = 60\%$ , the mean force recorded for the untreated cells is  $756 \pm 42$  nN versus  $467 \pm 47$  nN for the cyto-D cells. This is a statistically significant difference of 38% (Table 4.1). It can be observed from Table 4.1 that the mean compression force is  $\sim 60\%$  higher for untreated cells at lower deformation levels ( $\varepsilon_H \leq 40\%$ ). Additionally, hysteresis is observed between the loading and unloading halves of the cycle which is similar for both the untreated cells and the cyto-D cells, suggesting visco-hyperelastic behaviour (Appendix 4.B). This suggests that measured force is dependent on loading rate. It is important to note that, due to the difference in cell height between untreated and cyto-D cells, probe velocities of  $0.63 \pm 0.07$   $\mu\text{m/s}$  (untreated) and  $1.08 \pm 0.08$   $\mu\text{m/s}$  (cyto-D) were implemented to enforce a constant loading strain rate of  $\dot{\varepsilon}_H = 0.1$   $\text{s}^{-1}$  for all experiments. Strain rate dependence is investigated in more detail in Section 4.3.3 below.

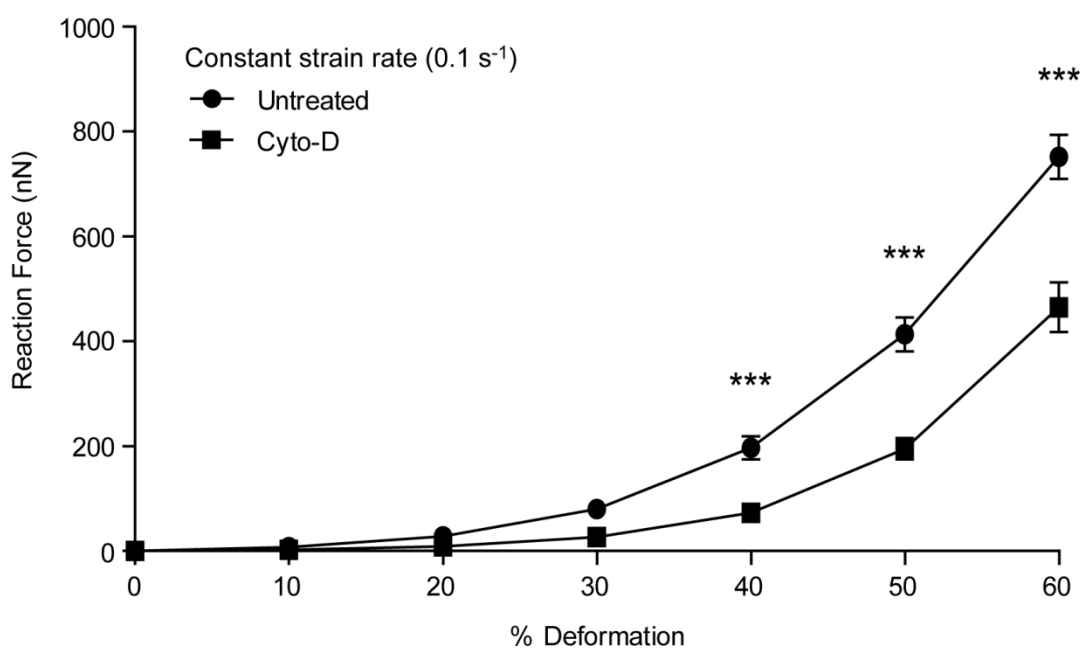


Figure 4.7: Reaction force versus % deformation ( $\varepsilon_H$ ) curves ( $n = 11$ ) obtained at a constant strain rate ( $\dot{\varepsilon}_H = 0.1$   $\text{s}^{-1}$ ) for untreated cells (round marker) and cyto-D cells (square marker). Significant differences between the untreated and cyto-D cell groups at each 10% deformation increment is indicated by  $***p < 0.0001$ .

Table 4.1: Difference (%) in mean reaction force at 10% increments for the untreated cells and the cyto-D cells

$\varepsilon_H$ (%)	10	20	30	40	50	60
Reaction force for untreated cells (nN)	7.7	28.4	80.4	197.8	415.3	755.5
Reaction force for cyto-D cells (nN)	2.8	9.3	27.2	73.6	195.9	467.3
% Difference	64%	67%	66%	63%	53%	38%

### 4.3.3 Strain Rate Dependence

The effect of strain rate ( $\dot{\varepsilon}_H$ ) on the measured cell compression force is next investigated. In Figure 4.8 force-deformation curves are shown for three strain rates ( $\dot{\varepsilon}_H = 0.1 \text{ s}^{-1}$ ,  $1.0 \text{ s}^{-1}$ , and  $5.0 \text{ s}^{-1}$ ) for untreated cells ( $n = 10$ ). The raw AFM data used to derive Figure 4.8 is shown in Appendix 4.C. Again, it is evident that the force increases non-linearly with the imposed compressive deformation for each strain rate. Additionally, hysteresis is observed between the loading and unloading halves of the cycle which is similar for the three strain rates tested, suggesting viscoelastic behaviour (Appendix 4.C). The reaction forces are statistically different for  $40\% \leq \varepsilon_H \leq 60\%$  between each of the three different strain rates. At  $\varepsilon_H = 60\%$ , the mean maximum force recorded is  $615 \pm 74 \text{ nN}$  at a strain rate of  $0.1 \text{ s}^{-1}$ ,  $917 \pm 73 \text{ nN}$  at a strain rate of  $1.0 \text{ s}^{-1}$ , and  $1366 \pm 99 \text{ nN}$  at a strain rate of  $5.0 \text{ s}^{-1}$ . Hydrodynamic drag effects, previously discussed in Section 3.3.1.2, are considered insignificant since the maximum velocity of  $19.4 \text{ }\mu\text{m/s}$  at  $5.0 \text{ s}^{-1}$  results in a drag force of less than  $3.5 \text{ nN}$  at  $0.5 \text{ }\mu\text{m}$  from the surface.

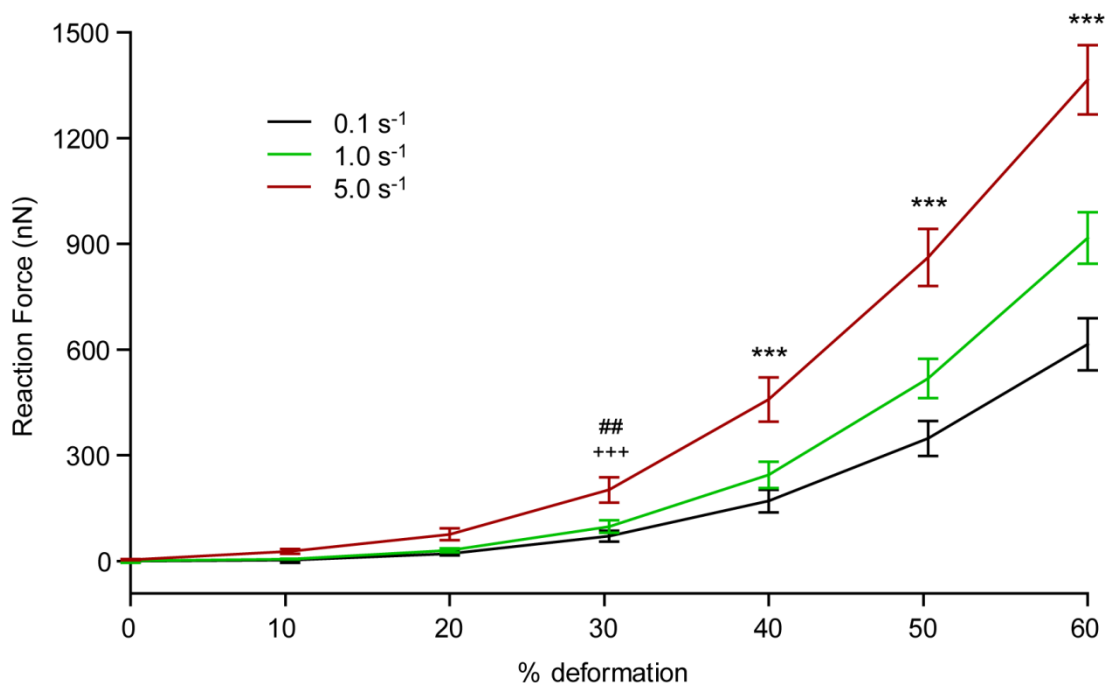


Figure 4.8: The effects of strain rate on the measured cell deformation reaction force. Cells ( $n = 10$ ) are deformed to  $\epsilon_H = 60\%$  at three different strain rates:  $0.1 \text{ s}^{-1}$  (black),  $1.0 \text{ s}^{-1}$  (green) and  $5.0 \text{ s}^{-1}$  (red). Significant differences are indicated at each 10% deformation increment by  $***p < 0.0001$  between all groups,  $##p < 0.001$  between  $1.0 \text{ s}^{-1}$  and  $5.0 \text{ s}^{-1}$ , and  $+++p < 0.0001$  between  $0.1 \text{ s}^{-1}$  and  $5.0 \text{ s}^{-1}$ .

#### 4.4 Discussion

In this study it is clearly demonstrated that the actin cytoskeleton plays a critical role in the resistance of osteoblasts to compression. Its removal results in a significant decrease ( $\sim 40\text{-}60\%$ ) in the mean cell compression force compared to untreated cells. This is in agreement with the whole cell compression study of Ofek et al. (2009), in which it was demonstrated that the actin cytoskeleton contributes significantly ( $\sim 50\%$ ) to the compressive stiffness of chondrocytes. The results of the current study are also in broad agreement with the findings of Hofmann et al. (1997) on cardiocytes and Rotsch and Radmacher (2000) on fibroblasts. Using AFM probing of the cell surface, both studies report that untreated cells are  $\sim 3$  times stiffer than cells treated with cyto-D. In these studies, localised cell indentation with an AFM tip was used to determine cell stiffness using standard Hertzian contact theory. Due to the localised nature of AFM tip indentation it was required in these studies to perform cell indentation at  $\sim 5000$  locations (force mapping) over a time period of 7

min in an effort to establish an average stiffness value for untreated and cyto-D cells. Such localised probing of the cell is known to result in a wide range of reaction forces across the cell due to its heterogeneous nature (McGarry et al. (2008)). Therefore, averaging of highly localised measurements taken in a force map cannot give a true measurement of the whole cell stiffness. More importantly, AFM tip indentation (typically  $< 1 \mu\text{m}$ ) merely deforms the cell membrane and a small region of the underlying cytoplasm. In the current study, these issues do not arise as the whole cell reaction force is recorded in a single global measurement. The contact area between the bottom of the sphere and the cell is approximated from the cross-sectional views of the stained control cells (Figure 4.3) and cyto-D cells (Figure 4.5). These images show that the contact area (when the sphere is centred over the cell nucleus) is similar for both the control and cyto-D cells, with the contact radius no greater than  $\sim 15 \mu\text{m}$ . The approximation of the sphere as a planar surface over this contact radius is illustrated in Figure 3.7. For a contact radius of  $15 \mu\text{m}$ , the contact point elevation differs by  $1.51 \mu\text{m}$  at the outer limit of the contact area than at the sphere centre.

Experimentally measured whole cell compression forces are found to be highly dependent on cell phenotype. Peak reaction forces at 60% compression of 2300 nN are reported for highly contractile myoblasts (Peeters et al. (2005a)), while lower forces are reported for less contractile cells: 500 nN for endothelial cells (Caille et al. (2002)) and 350 nN for fibroblasts (Deng et al. (2010)). This trend suggests that highly contractile cells provide a greater resistance to applied compression. A direct comparison of compression reaction forces between studies is difficult given that the allocated time for cell spreading, the loading conditions, and the environmental conditions may be different in each study. However, the compression value measured for osteoblasts in the current study ( $\sim 756 \text{ nN}$  at  $\epsilon_H = 60\%$ ) is 2-fold higher than the aforementioned reported compression forces for fibroblasts and 1.5-fold higher than that reported for endothelial cells, suggesting that osteoblasts may be more contractile. The current study shows that removal of the actin cytoskeleton reduces the compression force by  $\sim 40\text{-}60\%$ , demonstrating the significant contribution of the contractile actin cytoskeleton to the mechanical behaviour of osteoblasts. The high

level of tension in osteoblast stress fibres is demonstrated in Appendix 4.D. Severing of a single stress fibre results in a rapid recoil/retraction followed by depolymerisation. Pellegrin and Mellor (2007) suggest that the level of contractility differs among cell phenotypes due to the different levels of organisation of the actin cytoskeleton. Highly contractile cells, like myoblasts, have very well organised actin filament arrays, whereas fibroblasts which are less contractile, have sparse and poorly organised contractile actin filament bundles. The present study reinforces the link between contractility, organisation of the actin cytoskeleton, and compression resistance, demonstrating that the highly contractile, highly organised actin cytoskeleton of osteoblasts results in high levels of compression force. A computational investigation by Ronan et al. (2012) suggests a mechanism by which highly contractile aligned stress fibres provide significant resistance to cell compression. The data presented in this chapter has been used in a joint experimental-computational study (Weafer and Ronan et al. (2013)) to provide, for the first time, a full mechanical characterisation of the active actin cytoskeleton and the passive cytoplasm for osteoblasts.

The current study also demonstrates that the contractility of the actin cytoskeleton has a pronounced effect on cell morphology. Both cell height and nucleus height increase significantly when the actin cytoskeleton is disrupted using cyto-D. Ujihara et al. (2008) also reported significant changes in fibroblast cell height following cyto-D treatment, further demonstrating the link between cell height and actin cytoskeleton contractility. The study by Dowling et al. (2012) demonstrates that chondrocytes, which exhibit very low levels of contractility, do not significantly change height following cyto-D treatment. Furthermore, Ujihara et al. (2008) observed that disruption of microtubule did not affect cell height. In the current study, cells appeared spindly and fragmented following cyto-D treatment. A similar configuration was observed by Higuchi et al. (2009) following initial cyto-D treatment of osteoblasts. Importantly, this study also reported that the subsequent removal of cyto-D resulted in cell morphology and cytoskeleton recovery, demonstrating that the osteoblasts are not adversely affected by cyto-D treatment, despite their spindly appearance.

Significant nucleus deformation due to actin cytoskeleton contractility is observed in the present study. Similarly, in the work of Avalos et al. (2011), nuclei in contractile cells are shown to be significantly flatter than spherical nuclei observed in treated cyto-D cells. The findings of the current study clearly demonstrate the interconnected relationship between the actin cytoskeleton, nuclear deformation, and cell deformability. Interactions between the nucleus and cytoskeleton have been shown to significantly contribute to the mechanical regulation of the cell (Houben et al. (2007)). Previous studies have demonstrated that the removal of nuclear lamins leads to a significant decrease in the compressive strength of cells (Broers et al. (2004)) and disruption of the actin cytoskeleton (Khatau et al. (2009)). Knockdown of the nuclear protein nesprin-1 has also been shown to alter the cytoskeleton and inhibit cell reorientation under applied cyclic strain in endothelial cells (Chancellor et al. (2010)). The detailed measurement of nucleus shape change following disruption of the actin cytoskeleton reported in this chapter is of particular importance in light of studies that have reported a link between nucleus deformation and gene expression (Roca-Cusachs et al. (2008), Makale (2007), Vergani et al. (2004)). A study by Thomas et al. (2002) demonstrates that connections between the cytoskeleton and the nucleus shape of osteoblasts results in alterations to gene expression and protein synthesis (collagen I and osteocalcin).

The mean compression force is ~60% higher for the control cells compared to the cyto-D cells for  $\varepsilon_H \leq 40\%$ , as shown in Table 4.1. However, the difference in mean compression force between the two cell groups decreases with increased deformation levels ( $40\% \leq \varepsilon_H \leq 60\%$ ). At  $\varepsilon_H = 60\%$ , the mean compression force is ~40% higher for the control cells compared to the cyto-D cells. The larger difference in the mean compression forces at the lower deformation levels ( $\varepsilon_H \leq 40\%$ ) may be explained by the differing cell geometries between the control cells and cyto-D cells. As shown in Figure 4.6, the cytoplasm thickness above the nucleus is 2.7  $\mu\text{m}$  for the cyto-D cells (cell height of 10.8  $\mu\text{m}$ ). Therefore, the sphere does not compress the nucleus until  $\varepsilon_H \approx 38\%$ . In comparison, the cytoplasm thickness above the nucleus is 0.7  $\mu\text{m}$  for the control cells (cell height of 6.3  $\mu\text{m}$ ). Therefore, the sphere begins to compress the nucleus from  $\varepsilon_H \approx 11\%$ . The differing deformation levels at which the

two cell groups interact with the nucleus would explain the larger difference in the mean compression force at the lower deformation levels ( $\varepsilon_H \leq 40\%$ ). This is supported by previous studies which indicate that the nucleus is  $\sim 3$ - $4$  times stiffer than the surrounding cytoplasm (Guilak et al. (2000), Caille et al. (2002)). After  $\varepsilon_H \leq 40\%$ , the reaction force is dominated by the nucleus deformation for both cell groups. For the control cells, nucleus deformation is resisted by the actin cytoskeleton surrounding the nucleus, whereas for the cyto-D cells, which do not have a contractile actin cytoskeleton, nucleus deformation is less restricted, hence reaction forces measured are lower.

Strain rate dependence is also investigated in the current study. Experiments are performed over a range of loading rates to characterise the rate dependence of cell deformation. It is found that measured reaction forces are strain rate dependent. Cell deformation to  $\varepsilon_H = 60\%$  at a strain rate of  $\dot{\varepsilon}_H = 5.0 \text{ s}^{-1}$  (mean velocity of  $19.4 \text{ }\mu\text{m/s}$ ) resulted in a 2-fold increase in the measured reaction force compared to cell deformation at  $\dot{\varepsilon}_H = 0.1 \text{ s}^{-1}$  (mean velocity of  $0.4 \text{ }\mu\text{m/s}$ ). This increase in the measured reaction force with increased strain rate is likely due to the viscoelastic behaviour of the cell given the short timescale of the experiments. Previous studies have shown that the viscoelastic response dominates the measured forces for the initial  $\sim 10$  mins of loading with subsequent active remodelling contributing thereafter (Wang et al. (2001), Kaunas et al. (2005), Wille et al. (2006)). Similar strain rate dependence is reported in the dynamic whole cell compression experiments of Peeters et al. (2005b) in which a wide range of compression velocities ranging from  $0.1$  to  $20 \text{ }\mu\text{m/s}$  were investigated. It was shown that the resulting strain rate dependence was due to the viscoelastic properties of the cell, with the resulting force-displacement curves fitting a non-linear viscoelastic model. The findings of the current chapter indicate that the strain rate is an important parameter for *in vitro* cell deformation experiments. In Chapter 6, the effects of altering strain amplitude, while maintaining a constant strain rate, during dynamic loading of cells will be investigated.

In conclusion, detailed whole cell measurements are successfully obtained by exploiting the high precision of an AFM which was adapted to apply whole cell deformation (Chapter 3). The importance of the actin cytoskeleton in the resistance of osteoblasts to compressive deformation is clearly illustrated in the current study. It is demonstrated that the actin cytoskeleton contributed to ~40-60% of the cells ability to resist compression. Furthermore, the findings of this study demonstrate the interconnected relationship between the actin cytoskeleton, cell shape and nucleus deformation, highlighting the important role of the actin cytoskeleton, not only in the structural response of cells, but in regulation of nucleus morphology. The latter finding is of particular importance given that gene expression and protein synthesis have been linked to nucleus morphology. Thomas et al. (2002) have demonstrated that a nucleus of a bone cell which is less deformed synthesises increased levels of collagen type I. This suggests a link between the contractile forces generated by the actin cytoskeleton and bone formation and remodelling, given that collagen type I is the main extracellular component in newly formed bone.

## 4.5 References

- Adachi, T., Sato, K., Higashi, N., Tomita, Y. and Hojo, M. (2008) Simultaneous observation of calcium signaling response and membrane deformation due to localized mechanical stimulus in single osteoblast-like cells. *Journal of the Mechanical Behavior of Biomedical Materials*. 1 (1), 43-50
- Avalos, P. G., Reichenzeller, M., Eils, R. and Gladilin, E. (2011) Probing compressibility of the nuclear interior in wild-type and lamin deficient cells using microscopic imaging and computational modeling. *J. Biomech.* 44 (15), 2642-2648
- Broers, J. L. V., Peeters, E. A. G., Kuijpers, H. J. H., Endert, J., Bouten, C. V. C., Oomens, C. W. J., Baaijens, F. P. T. and Ramaekers, F. C. S. (2004) Decreased mechanical stiffness in *Imna*<sup>-/-</sup> cells is caused by defective nucleo-cytoskeletal integrity: Implications for the development of laminopathies. *Human Molecular Genetics*. 13 (21), 2567-2580
- Burridge, K., Nuckolls, G., Otey, C., Pavalko, F., Simon, K. and Turner, C. (1990) Actin-membrane interaction in focal adhesions. *Cell Differentiation and Development*. 32 (3), 337-342
- Caille, N., Thoumine, O., Tardy, Y. and Meister, J. J. (2002) Contribution of the nucleus to the mechanical properties of endothelial cells. *J. Biomech.* 35 (2), 177-187
- Chancellor, T., Lee, J., Thodeti, C. K. and Lele, T. (2010) Actomyosin tension exerted on the nucleus through nesprin-1 connections influences endothelial cell adhesion, migration, and cyclic strain-induced reorientation. *Biophysical Journal*. 99 (1), 115-123
- Charras, G. T. and Horton, M. A. (2002) Single cell mechanotransduction and its modulation analyzed by atomic force microscope indentation. *Biophys. J.* 82 (6), 2970-2981
- Cooper, J. A. (1987) Effects of cytochalasin and phalloidin on actin. *The Journal of cell biology*. 105 (4), 1473-1478
- Deng, Z., Lulevich, V., Liu, F.-T. and Liu, G.-Y. (2010) Applications of atomic force microscopy in biophysical chemistry of cells. *The Journal of Physical Chemistry B*. 114 (18), 5971-5982
- Dowling, E. P., Ronan, W., Ofek, G., Deshpande, V. S., Athanasiou, K. A., McMeeking, R. M. and McGarry, J. P. (2012) The effect of remodelling and contractility of the actin cytoskeleton on the shear resistance of single cells: A computational and experimental investigation. *J. R. Soc. Interface*. 9 (77), 3469-3479

- Duncan, R. and Turner, C. (1995) Mechanotransduction and the functional response of bone to mechanical strain. *Calcified tissue international*. 57 (5), 344-358
- Engler, A. J., Sen, S., Sweeney, H. L. and Discher, D. E. (2006) Matrix elasticity directs stem cell lineage specification. *Cell*. 126 (4), 677-89
- Frost, H. M. (2004) A 2003 update of bone physiology and wolff's law for clinicians. *The Angle Orthodontist*. 74 (1), 3-15
- Gabbay, J. S., Zuk, P. A., Tahernia, A., Askari, M., O'Hara, C. M., Karthikeyan, T., Azari, K., Hollinger, J. O. and Bradley, J. P. (2006) In vitro microdistraction of preosteoblasts: Distraction promotes proliferation and oscillation promotes differentiation. *Tissue engineering*. 12 (11), 3055-3065
- Guilak, F., Tedrow, J. R. and Burgkart, R. (2000) Viscoelastic properties of the cell nucleus. *Biochemical and Biophysical Research Communications*. 269 (3), 781-786
- Higuchi, C., Nakamura, N., Yoshikawa, H. and Itoh, K. (2009) Transient dynamic actin cytoskeletal change stimulates the osteoblastic differentiation. *Journal of bone and mineral metabolism*. 27 (2), 158-167
- Hofmann, U. G., Rotsch, C., Parak, W. J. and Radmacher, M. (1997) Investigating the cytoskeleton of chicken cardiocytes with the atomic force microscope. *Journal of Structural Biology*. 119 (2), 84-91
- Houben, F., Ramaekers, F. C. S., Snoeckx, L. H. E. H. and Broers, J. L. V. (2007) Role of nuclear lamina-cytoskeleton interactions in the maintenance of cellular strength. *Biochimica et Biophysica Acta (BBA) - Molecular Cell Research*. 1773 (5), 675-686
- Janmey, P. A., Tee, S. Y., Fu, J. P. and Chen, C. S. (2011) Cell shape and substrate rigidity both regulate cell stiffness. *Biophysical Journal*. 100 (5), L25-L27
- Kaunas, R., Nguyen, P., Usami, S. and Chien, S. (2005) Cooperative effects of rho and mechanical stretch on stress fiber organization. *Proc. Natl. Acad. Sci*. 102 (44), 15895-15900
- Khatau, S. B., Hale, C. M., Stewart-Hutchinson, P. J., Patel, M. S., Stewart, C. L., Searson, P. C., Hodzic, D. and Wirtz, D. (2009) A perinuclear actin cap regulates nuclear shape. *Proceedings of the National Academy of Sciences*. 106 (45), 19017-19022
- Makale, M. (2007) Cellular mechanobiology and cancer metastasis. *Birth Defects Res C Embryo Today*. 81 (4), 329-43
- McGarry, J. G., Maguire, P., Campbell, V. A., O'Connell, B. C., Prendergast, P. J. and Jarvis, S. P. (2008) Stimulation of nitric oxide mechanotransduction in

- single osteoblasts using atomic force microscopy. *J. Orthop. Res.* 26 (4), 513-521
- Ofek, G., Wiltz, D. C. and Athanasiou, K. A. (2009) Contribution of the cytoskeleton to the compressive properties and recovery behavior of single cells. *Biophys. J.* 97 (7), 1873-1882
- Owan, I., Burr, D. B., Turner, C. H., Qiu, J., Tu, Y., Onyia, J. E. and Duncan, R. L. (1997) Mechanotransduction in bone: Osteoblasts are more responsive to fluid forces than mechanical strain. *American Journal of Physiology-Cell Physiology.* 273 (3), C810-C815
- Pavalko, F. M., Chen, N. X., Turner, C. H., Burr, D. B., Atkinson, S., Hsieh, Y. F., Qiu, J. and Duncan, R. L. (1998) Fluid shear-induced mechanical signaling in mc3t3-e1 osteoblasts requires cytoskeleton-integrin interactions. *American Journal of Physiology-Cell Physiology.* 275 (6), C1591-C1601
- Peeters, E. A. G., Oomens, C. W. J., Bouten, C. V. C., Bader, D. L. and Baaijens, F. P. T. (2005a) Mechanical and failure properties of single attached cells under compression. *J. Biomech.* 38 (8), 1685-1693
- Peeters, E. A. G., Oomens, C. W. J., Bouten, C. V. C., Bader, D. L. and Baaijens, F. P. T. (2005b) Viscoelastic properties of single attached cells under compression. *J Biomech Eng.* 127 (2), 237-243
- Pellegrin, S. and Mellor, H. (2007) Actin stress fibres. *Journal of Cell Science.* 120 (20), 3491-3499
- Rath, B., Nam, J., Knobloch, T. J., Lannutti, J. J. and Agarwal, S. (2008) Compressive forces induce osteogenic gene expression in calvarial osteoblasts. *Journal of biomechanics.* 41 (5), 1095-1103
- Roca-Cusachs, P., Alcaraz, J., Sunyer, R., Samitier, J., Farré, R. and Navajas, D. (2008) Micropatterning of single endothelial cell shape reveals a tight coupling between nuclear volume in g1 and proliferation. *Biophysical Journal.* 94 (12), 4984-4995
- Ronan, W., Deshpande, V. S., McMeeking, R. M. and McGarry, J. P. (2012) Numerical investigation of the active role of the actin cytoskeleton in the compression resistance of cells. *Journal of the Mechanical Behavior of Biomedical Materials.* 14, 143-157
- Rotsch, C. and Radmacher, M. (2000) Drug-induced changes of cytoskeletal structure and mechanics in fibroblasts: An atomic force microscopy study. *Biophysical Journal.* 78 (1), 520-535
- Sato, K., Adachi, T., Ueda, D., Hojo, M. and Tomita, Y. (2007) Measurement of local strain on cell membrane at initiation point of calcium signaling response

- to applied mechanical stimulus in osteoblastic cells. *Journal of Biomechanics*. 40 (6), 1246-1255
- Thomas, C. H., Collier, J. H., Sfeir, C. S. and Healy, K. E. (2002) Engineering gene expression and protein synthesis by modulation of nuclear shape. *Proceedings of the National Academy of Sciences*. 99 (4), 1972-1977
- Thoumine, O. and Ott, A. (1997) Time scale dependent viscoelastic and contractile regimes in fibroblasts probed by microplate manipulation. *J Cell Sci*. 110 (17), 2109-2116
- Ujihara, Y., Miyazaki, H. and Wada, S. (2008) Morphological study of fibroblasts treated with cytochalasin d and colchicine using a confocal laser scanning microscopy. *The journal of physiological sciences: JPS*. 58 (7), 499
- Vergani, L., Grattarola, M. and Nicolini, C. (2004) Modifications of chromatin structure and gene expression following induced alterations of cellular shape. *The international journal of biochemistry & cell biology*. 36 (8), 1447-1461
- Wang, D., Christensen, K., Chawla, K., Xiao, G., Krebsbach, P. H. and Franceschi, R. T. (1999) Isolation and characterization of mc3t3-e1 preosteoblast subclones with distinct in vitro and in vivo differentiation/mineralization potential. *Journal of Bone and Mineral Research*. 14 (6), 893-903
- Wang, J. H. C., Goldschmidt-Clermont, P., Wille, J. and Yin, F. C. P. (2001) Specificity of endothelial cell reorientation in response to cyclic mechanical stretching. *J. Biomech*. 34 (12), 1563-1572
- Weafer, P. P., Ronan, W., Jarvis, S. P. and McGarry, J. P. (2013) Experimental and computational investigation of the role of stress fiber contractility in the resistance of osteoblasts to compression. *Bulletin of Mathematical Biology*. DOI: 10.1007/s11538-013-9812-y
- Wille, J. J., Elson, E. L. and Okamoto, R. J. (2006) Cellular and matrix mechanics of bioartificial tissues during continuous cyclic stretch. *Ann. Biomed. Eng.* 34 (11), 1678-1690

## 4.6 Appendix

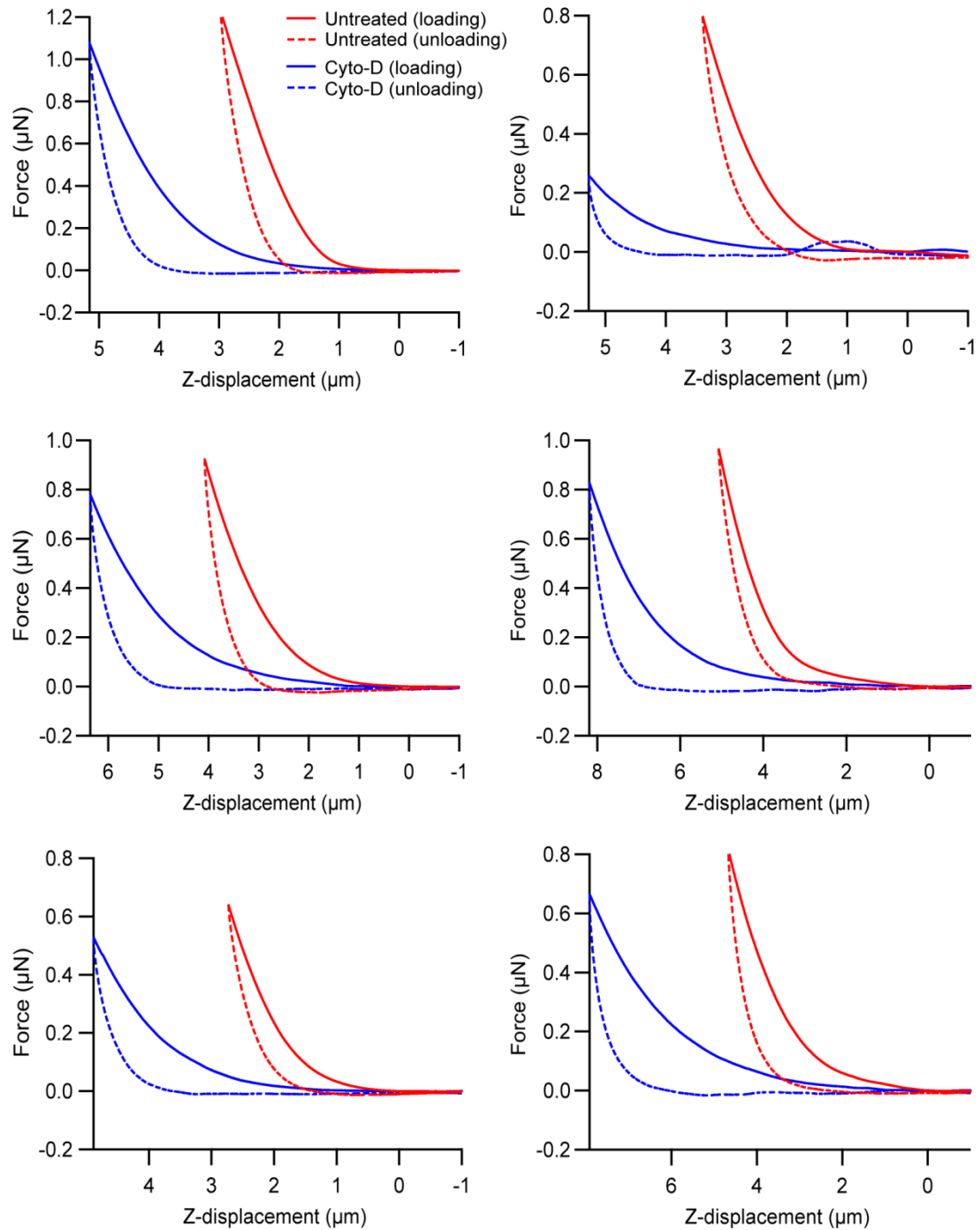
### 4.A Cell Geometry Details

Table 4-A: Cell geometry characteristics for untreated and cyto-D cells (mean  $\pm$  sem). % difference of mean values signifies the difference in mean cell geometric values following the addition of cyto-D.

	Untreated	Cyto-D	% difference of mean values
Cell height ( $\mu\text{m}$ )	6.3 $\pm$ 0.8	10.8 $\pm$ 0.9	+71.4%
Cell base area ( $\mu\text{m}^2$ )	3898 $\pm$ 536	2776 $\pm$ 571	-28.8%
Nucleus Height ( $\mu\text{m}$ )	4.6 $\pm$ 0.4	7.2 $\pm$ 1.1	+56.5%
Nucleus Diameter ( $\mu\text{m}$ )	25.6 $\pm$ 2.2	15.1 $\pm$ 0.7	-41.0%
Cytoplasm above nucleus ( $\mu\text{m}$ )	0.7 $\pm$ 0.2	2.7 $\pm$ 0.8	+285.7%
Cytoplasm below nucleus ( $\mu\text{m}$ )	0.4 $\pm$ 0.1	1.3 $\pm$ 0.4	+225.0%

### 4.B Monotonic Compression Force-Displacement Curves

Force-displacement curves for 11 osteoblasts compressed ( $\varepsilon_H = 60\%$ ) at a constant strain rate ( $\dot{\varepsilon}_H = 0.1 \text{ s}^{-1}$ ). Each graph shows the loading-unloading curve for a cell which is untreated (red) and subsequently treated with cyto-D (blue). This data was used to derive the plot in Figure 4.7.



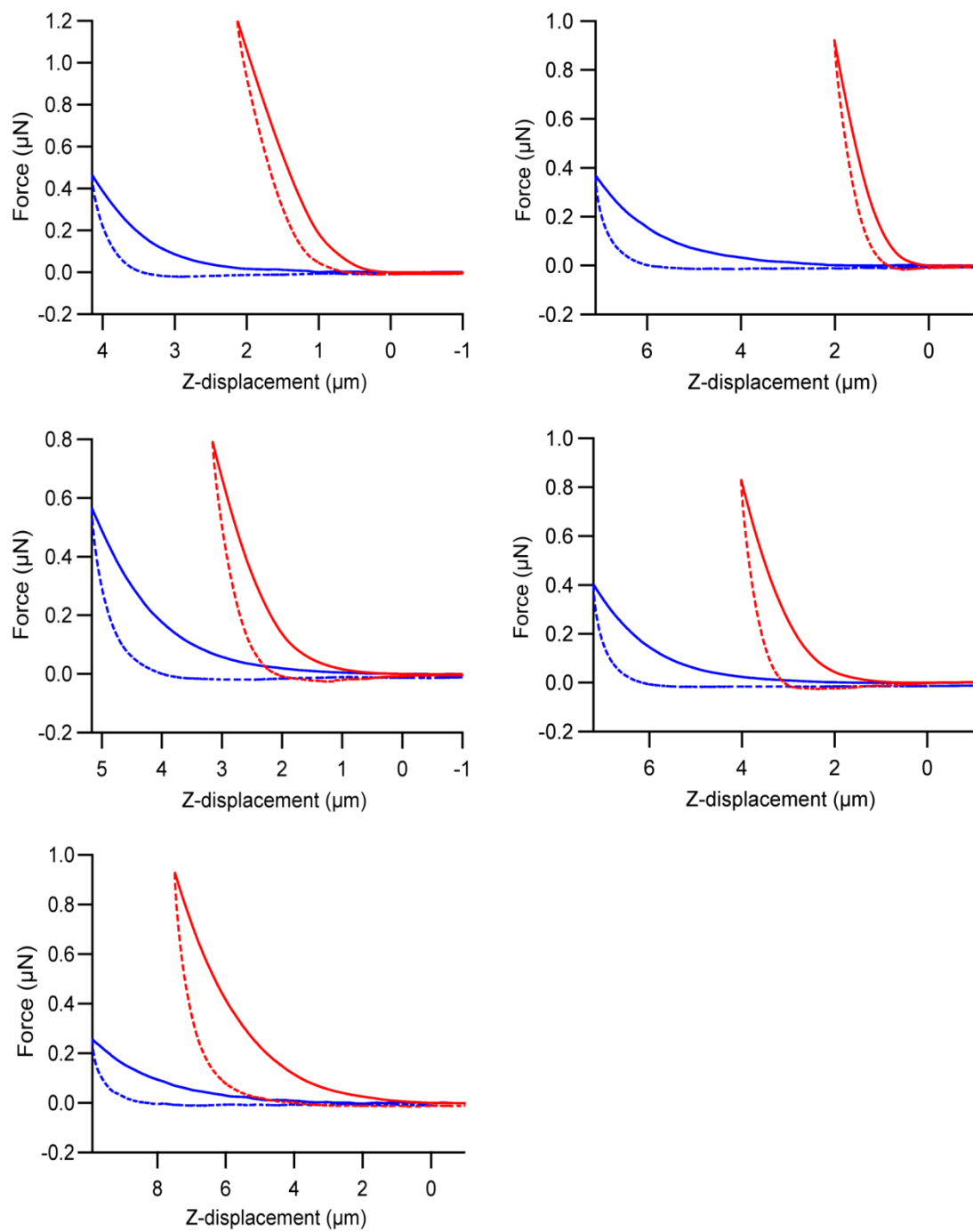
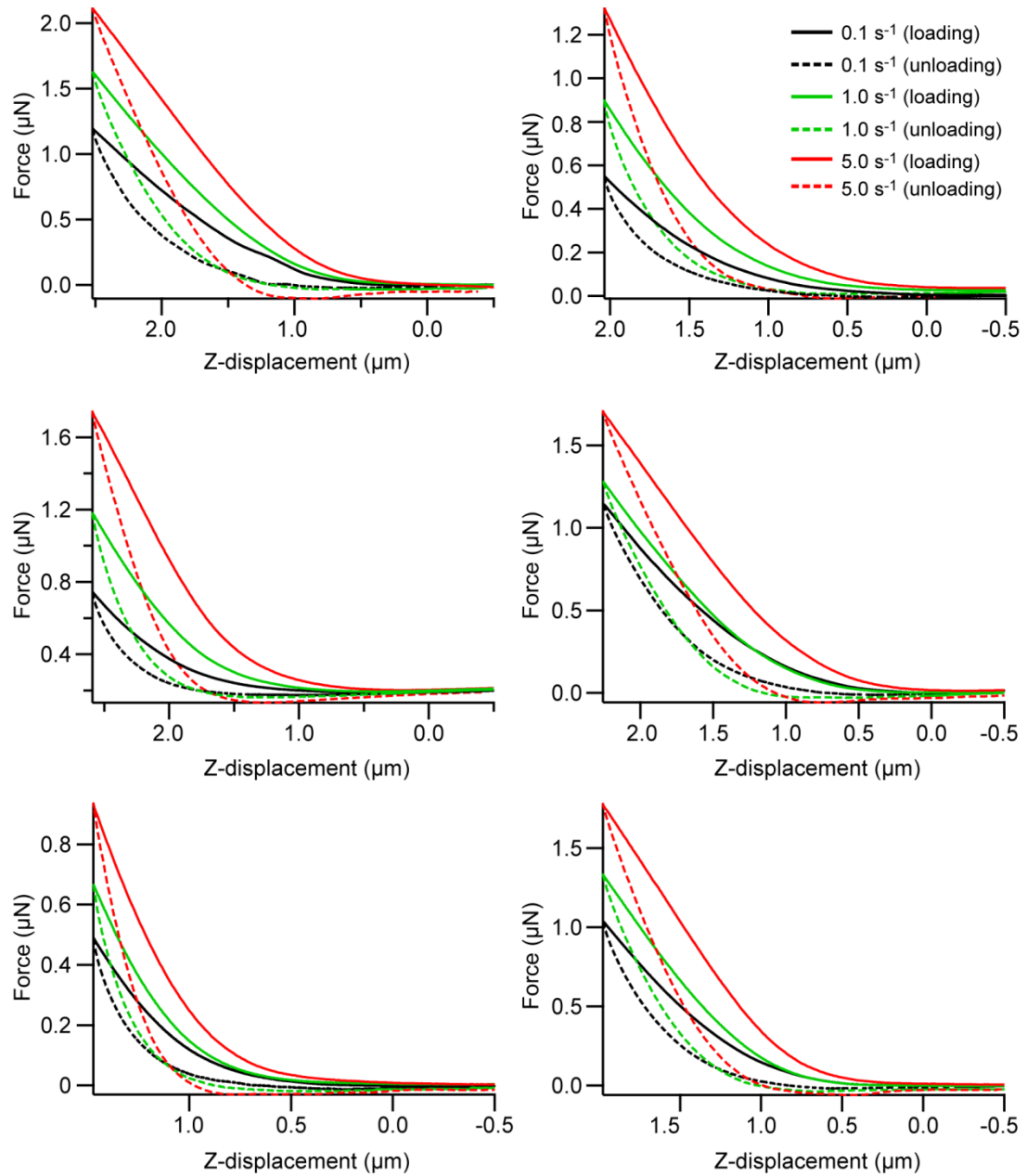


Figure 4-B: Force-displacement curves for 11 osteoblasts compressed ( $\varepsilon_H = 60\%$ ) at a constant strain rate ( $\dot{\varepsilon}_H = 0.1 \text{ s}^{-1}$ ).

### 4.C Strain Rate Dependence Force-Displacement Curves

Force-displacement curves for 10 untreated osteoblasts compressed ( $\epsilon_H = 60\%$ ) at three strain rates;  $\dot{\epsilon}_H = 0.1 \text{ s}^{-1}$ ,  $1.0 \text{ s}^{-1}$ , and  $5.0 \text{ s}^{-1}$ . This data was used to derive the plot in Figure 4.8.



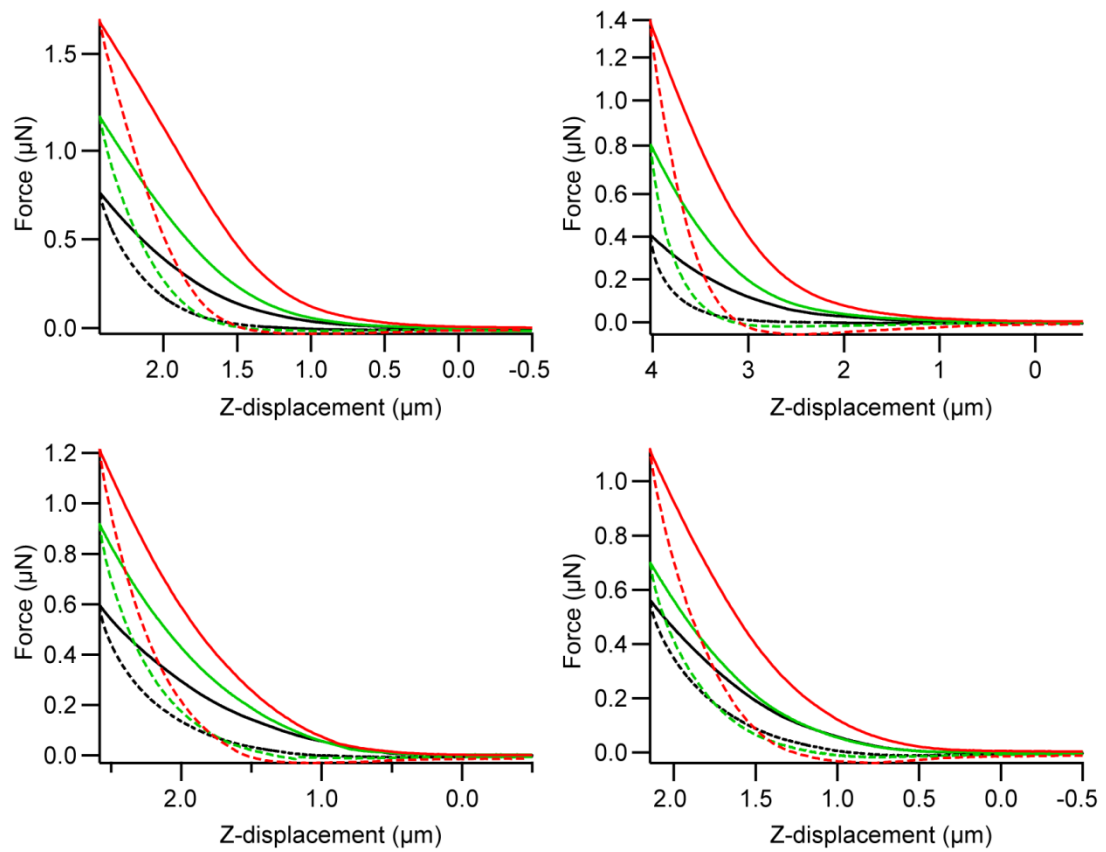


Figure 4-C: Force-displacement curves for 10 untreated osteoblasts compressed ( $\epsilon_H = 60\%$ ) at three strain rates;  $\dot{\epsilon}_H = 0.1 \text{ s}^{-1}$ ,  $1.0 \text{ s}^{-1}$ , and  $5.0 \text{ s}^{-1}$ .

#### 4.D Actin Cytoskeleton Contractility: Severance of a Single Stress Fibre

The contractile nature of the actin cytoskeleton is demonstrated by severing a single stress fibre in a living osteoblast. The actin cytoskeleton of the living cell is visualised by transient transfection with the plasmid vector pGFP2-actin (Evrogen, Russia). Cells are seeded at a concentration of  $1.5 \times 10^5$  cells per Ø35 mm glass-bottomed petri dishes (FluoroDish, WRI, Florida) 24 hr prior to transfection. Transfection is performed using GeneJuice (Novagen, Germany) according to the manufacturer's guidelines, at an optimised ratio of 3:1 (reagent: vector). Experiments are performed using a combined AFM-fluorescence system.

Figure 4-D shows the severance of a single stress fibre. A tipless cantilever (NSC12, MikroMesch, Spain) is positioned beside the cell of choice. Using the stage x-y positioners, the cantilever is then slowly moved into the side of the cell until stress fibre severance is observed ( $t = 0$  s). Following initial stress fibre severance, the stress fibre is observed to rapidly retract, suggesting a release of isometric tension. The further retraction of the stress fibre until  $t = 240$  s is most likely due to the disassembly of the polymerised actin into its monomer form in response to the tension dissipation. This demonstration highlights the contractile nature of the actin cytoskeleton and also shows that tension is essential in maintain actin filaments in their polymerised form.

The findings of this demonstration are very similar to those observed by Kumar et al. (2006), where a laser 'nanoscissor' was used to severe a stress fibre in an endothelial cell. A comparable rate of stress fibre retraction ( $\sim 3 \mu\text{m}$  in 10 s) is observed in both cases.

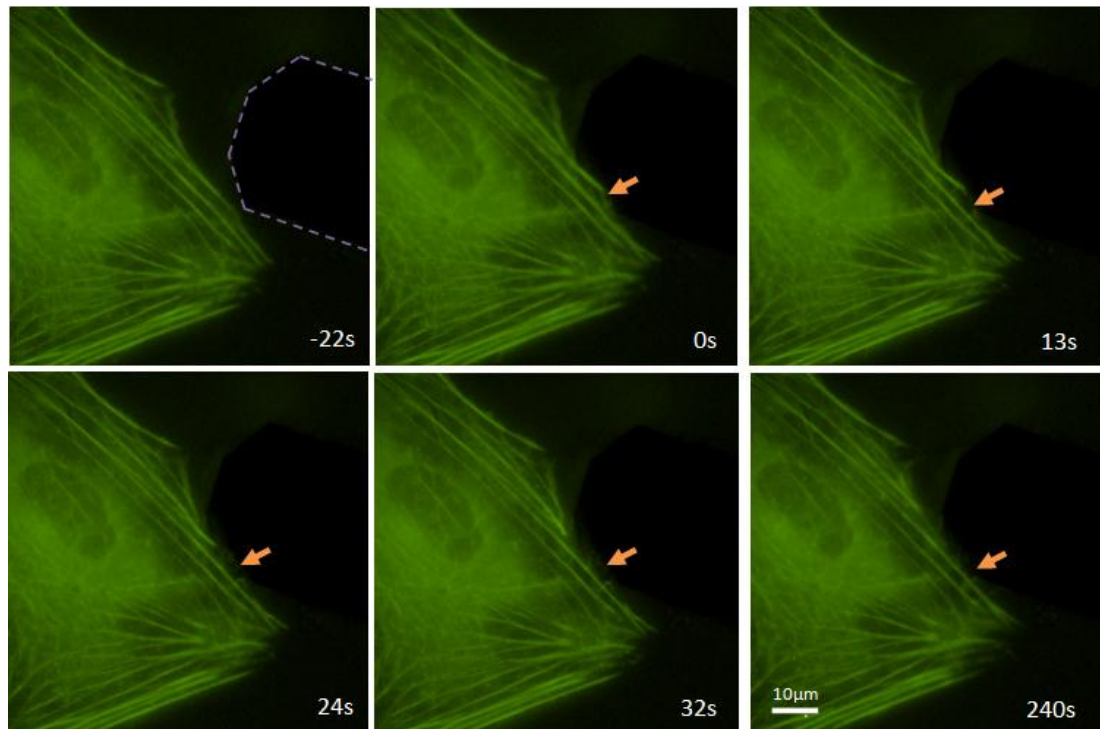


Figure 4-D: Time-lapse image sequence of a stress fibre being severed using a tipless AFM cantilever (which is at the surface). From 0 to 240 s, the stress fibre is shown to retract and depolymerise. Arrow indicates the point of stress fibre severance. The dashed line indicates the position of the tipless cantilever at the start of the experiment. The osteoblast is transiently transfected with GFP-actin.

## Reference

Kumar, S., Maxwell, I. Z., Heisterkamp, A., Polte, T. R., Lele, T. P., Salanga, M., Mazur, E. and Ingber, D. E. (2006) Viscoelastic retraction of single living stress fibers and its impact on cell shape, cytoskeletal organization, and extracellular matrix mechanics. *Biophysical Journal*. 90 (10), 3762-3773

## Chapter 5

# **Stability Enhancement of an Atomic Force Microscope for Long-Term Force Measurement**

## 5.1 Introduction

AFM has been utilised extensively in the investigation of single cell mechanics over time scales of seconds to minutes (Charras and Horton (2002), McGarry et al. (2008)). However, other experimental techniques have revealed that remodelling of the cell actin cytoskeleton can occur on a time scale of tens of minutes to hours. For example, the actin cytoskeleton of endothelial cells seeded on silicone membranes has been shown to change alignment following approximately 1 hr of cyclic substrate stretching (Kaunas et al. (2005), Wang et al. (2001)). Additionally, Wille et al. (2006) has demonstrated that active stress fibre contractility of fibroblasts seeded in 3D gels alters during the first 30 min of cyclic deformation before reaching a steady state. In order to further understand the mechanisms underlying the biomechanical response of cells to mechanical loading, a key requirement is the ability to perform single cell experiments over physiologically relevant time scales. Such measurements are generally not trivially implemented using standard AFM systems due to uncertainty in the tip-sample distance over long time scales.

In the current chapter, it is demonstrated that uncertainties in the tip-sample distance occur due to thermal drift (z-drift), and perturbations in the z-axis occur due to instabilities associated with liquid motion (liquid instability). Both effects impose severe limitations on the application of AFM over large time scales, the extent of which is often not considered. These limitations prohibit quantitative, long time scale single cell experiments due to an inability to reliably specify displacement controlled motion. For this condition to be satisfied the aforementioned z-drift and any liquid instability effects must be eliminated, such that the reference positions of the sample and z-piezo remain at a fixed distance over the course of the entire experiment.

Z-drift is characterised as a change in the tip-sample distance due to environmental temperature variations. The two main components of this motion are (i) cantilevers with composite construction (e.g. a metal coating) which may deflect due to the bimetallic effect (Thundat et al. (1994)) and (ii) the tip-sample distance which may change due to thermal expansion/contraction of components within the AFM frame. For experiments where the position of the substrate cannot be directly

measured and therefore used as a reference (e.g. cell indentation studies) such effects may result in significant errors in the calculated tip-sample distance thus limiting the ability to perform deformation controlled experiments over long time scales. Liquid instabilities may also be present due to evaporation, convection, and air currents in open fluid cell systems, and may also arise in closed fluid cell system if any air bubbles are present. Here it is demonstrated, for the first time, that such fluid motion effects can give rise to perturbations in the apparent z-displacement greater than 100 nm. The elimination of both z-drift and liquid instabilities is critical for experiments where the precise control of cell deformation and the precise measurement of reaction force is required over long time scales is required.

Previous drift related studies have primarily focused on thermal drift in the lateral (XY) plane for imaging purposes, which can be compensated for by using Kalman filtering (Mokaberi and Requicha (2006)) or correlation methods (Kindt et al. (2002)), and/or reduced by instrument modifications (Oulevey et al. (1999)). Similar approaches have also been applied to the alleviation of z-drift. Spagnoli et al. (2007) utilised a software routine whereby the cantilever is repositioned to reference the substrate between force measurements by moving laterally away from the sample before recalibrating the substrate position. However, this method is unsuitable when the cell dimensions exceed the lateral range of the AFM scanner, or if a continuous cyclic deformation must be applied to the sample. Reference sensors have also been used to provide tip-sample distance information in parallel by monitoring either an additional cantilever adjacent to the measurement cantilever (Choy et al. (2007), Altmann et al. (2001)) or a proximity sensor (Schitter and Stemmer (2002), Sparks and Manalis (2004)). The reference sensor method provides real-time information for the compensation of the effects of z-drift; however, great care must be taken to ensure that the sensor itself is inert to thermal effects. Such reference sensor systems often require substantial modifications of existing instrumentation. Customised systems have also been developed whereby thermal motion in one component counteracts thermal motion in another, resulting in an inherently stable instrument (Hoogeman et al. (1998), Torun et al. (2009)). Furthermore, there are commercially available products designed specifically to manage thermal drift by controlling

environmental conditions (Park Systems ([www.parkafm.com](http://www.parkafm.com)); Agilent Technologies ([www.agilent.com](http://www.agilent.com)); Nanosurf ([www.nanosurf.com](http://www.nanosurf.com))) and/or demonstrate ultra-low drift as a function of temperature change (THead ([www.ntmdt.com](http://www.ntmdt.com)); Dimension Edge ([www.bruker-axs.com](http://www.bruker-axs.com)); Cypher ([www.asylumresearch.com](http://www.asylumresearch.com))). Such systems represent significant advancements in instrumentation but there is still a pressing need to develop a reliable, cost effective and easily implemented method of adapting any existing AFM for the purpose of long term displacement controlled experiments.

In this chapter, the progressive developmental steps to obtain displacement controlled operation in a liquid environment over long time scales using a standard AFM are presented. Firstly, the methodology used to monitor stability in an AFM is described in Section 5.2. This methodology is then used to measure the extent of z-drift within a standard AFM under standard operating conditions (Section 5.3). In Section 5.4, the progressive steps to enhanced stability within the AFM is presented, firstly for measurements in air, and then for measurements within a liquid environment. The AFM modifications presented here involve the use of an active temperature control setup combined with a customised fluid cell and reservoir system. Finally, to highlight the importance of precise displacement control, cyclic single cell deformation is performed for both an unmodified and modified system (Section 5.5). It is important to note that a comprehensive single cell investigation will be presented in Chapter 6; the sole purpose of the cell experiments presented in the current chapter is simply to demonstrate the significant errors that can occur in applied cell deformation and measured reaction force when an unmodified system is used. Throughout each section of this technical chapter, presented results are discussed with reference to previous studies. A brief summary of the key points are then provided Section 5.6.

## **5.2 Materials and Methods**

### **5.2.1 Stability Criteria**

The goal of this chapter is to minimise z-drift in the instrument without sacrificing system stability or incorporating any additional noise. It should be noted in this section that: (i) Z-drift is the rate of change of the z-displacement of the

cantilever relative to the surface, which is reported as the slope of a linear fit to 1 hr of z-displacement data, and (ii) the relative noise in the system is indicated by the parameter z-sdev, which is the standard deviation of 1 hr of z-displacement data after subtracting a linear fit. By subtracting the fit from the data a more accurate indication of system stability can be obtained since the impact of drift on this value is minimised. In the case of both parameters, values are reported as mean  $\pm$  standard deviation. Here, long term performance is defined as z-drift and z-sdev over a 5 hr period as it approximates the time limit for the cells used in this study to remain viable on the AFM stage.

### 5.2.2 Stability Measurement

The AFM is setup according to Section 3.2.1. Stability measurements are performed by monitoring the z-displacement required to maintain a constant force ( $\approx 60$  nN) on a substrate (z integral gain = 1.0) in response to the deflection of a cantilever (Lever C, NSC36/AIBS,  $k \approx 0.6$  N/m, MikroMasch, Spain).

Temperatures are recorded via a USB-TC interface (Measurement Computing, USA) into the AFM software program, Igor Pro (Wavemetrics, USA), by in-house custom software at five discrete locations on the AFM (K-type thermocouples, Radionics, Ireland). All temperature and z-displacement data are collected using a sampling rate of 1.0 Hz. Air conditioning maintained the lab at  $21 \pm 1$  °C. The acoustic isolation hood doors are kept closed during all experiments unless stated otherwise. All measurements are performed from the same initial system configuration (*cold system*) defined as having the hood doors closed, the inverted microscope powered off and AFM controller on with the laser off for a period of 10 hr.

## 5.3 Stability under Standard Operating Conditions

To elucidate the extent of z-drift under standard operating conditions (unmodified system), measurements are performed on a glass slide in air over a period of 18 hr using the setup described in Section 5.2.2. Starting from a *cold system*, the laser and inverted microscope are powered on, and temperatures within

the isolation hood are observed to rise due to thermal dissipation. An offset is observed between thermocouple locations; however, the rate of temperature increase is similar for all positions. The AFM head temperature is observed to increase to a maximum value of 33.04 °C (Figure 5.1 (a), black). After 5 hr of equilibration the temperature is  $32.62 \pm 0.31$  °C with a linear rate of change of  $0.09 \pm 0.08$  °C/hr. The z-displacement is seen to closely match the corresponding temperature change (Figure 5.1 (a), grey). After 5 hr of equilibration, the z-drift is found to be  $111.56 \pm 112.97$  nm/hr (Figure 5.1 (b)) with a z-sdev of  $4.62 \pm 1.08$  nm (Figure 5.1 (c)). The substantial standard deviation of the z-drift should be noted.

The stability measurements shown for an unmodified system (Figure 5.1) indicate that z-drift of this magnitude would significantly affect any long term experiments where a known tip-substrate displacement is required at all times. Previous studies frequently state thermal equilibration times ranging from 60 min (Munday et al. (2009), Zepeda et al. (2001)) to a few hours (Rachlin et al. (1992), Gan (2009)); however, it is clear from the results presented here that substantially longer times may be required in order to reach thermal equilibrium in the absence of stability enhancement. These results highlight the need for a more systematic approach to alleviating z-drift when conducting measurements over long time periods.

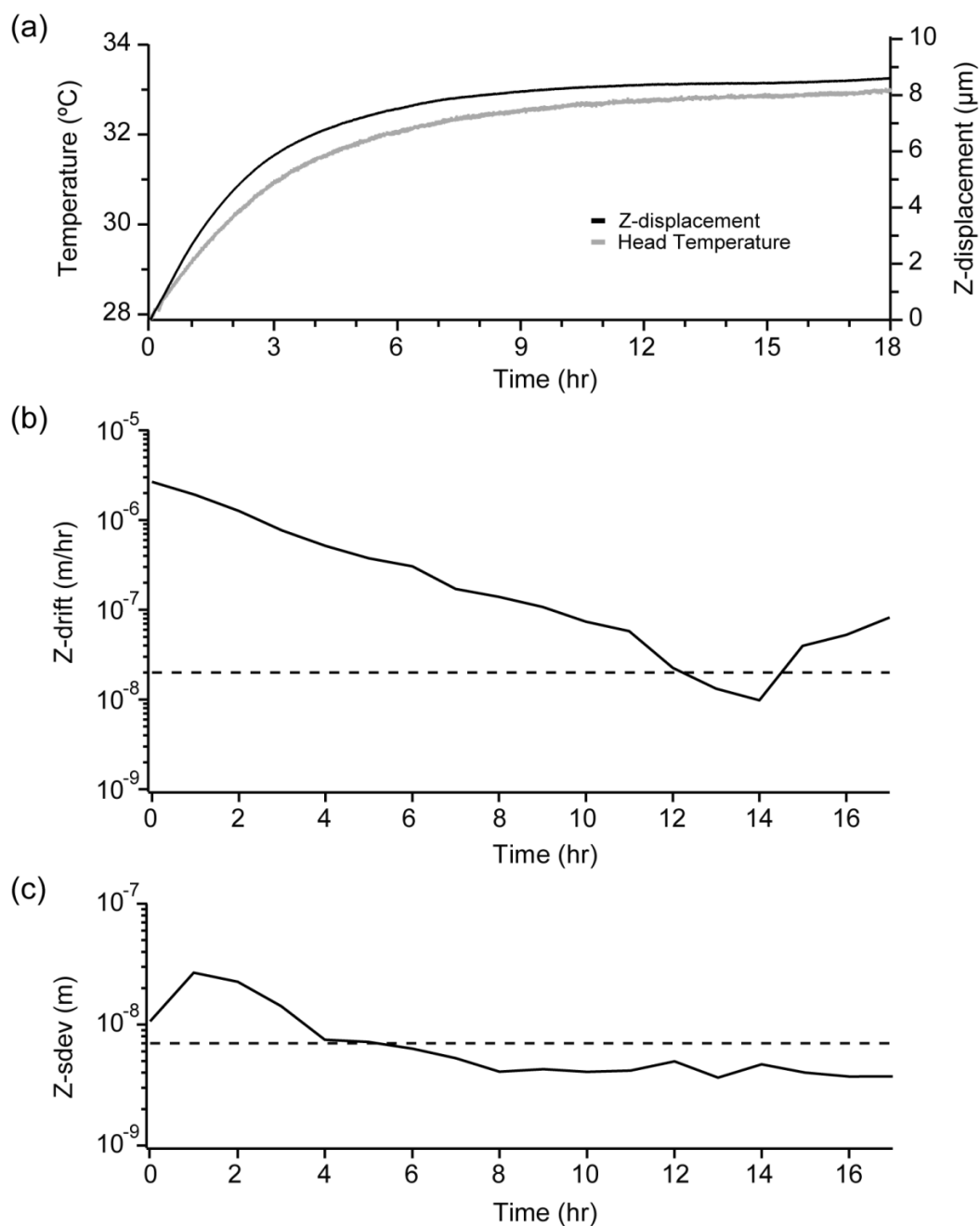


Figure 5.1: (a) AFM head temperature and measured z-displacement, (b) z-drift and (c) z-sdev over 18 hr under standard operating conditions. For (b) and (c) increments of 1 hr are used for each data point. Dashed lines are included as indicators only and are defined as 20 nm/hr for (b) and 7 nm for (c).

## 5.4 System Stabilisation

The developmental steps towards achieving system stability are discussed in this section. Enhanced stability is first established for measurements in air (Section 5.4.1), and then for measurements in a liquid environment (Section 5.4.2).

### 5.4.1 Stability in Air: Active Temperature Control

Initial attempts to stabilise the AFM involved counteracting drift based on the system temperature change (see Appendix 5.A for details). However, it is found that the most effective method to stabilise the AFM is to prevent drift rather than counteract it. Drift prevention could be established if the system temperature is increased to a value greater than the equilibration temperature using an active temperature control system.

Active temperature control is implemented using a TempControl 37-2 digital controller and heating unit (Zeiss, Germany), Figure 5.2. The temperature control unit is mechanically isolated from the AFM system to suppress acoustic and vibration noise. An operating temperature of 35 °C is chosen to ensure the instrument is kept above room temperature to reduce the influence of external temperature fluctuations whilst keeping below the maximum operating temperature of 40 °C. This temperature resulted in a liquid temperature of 37 °C within the fluid cell.

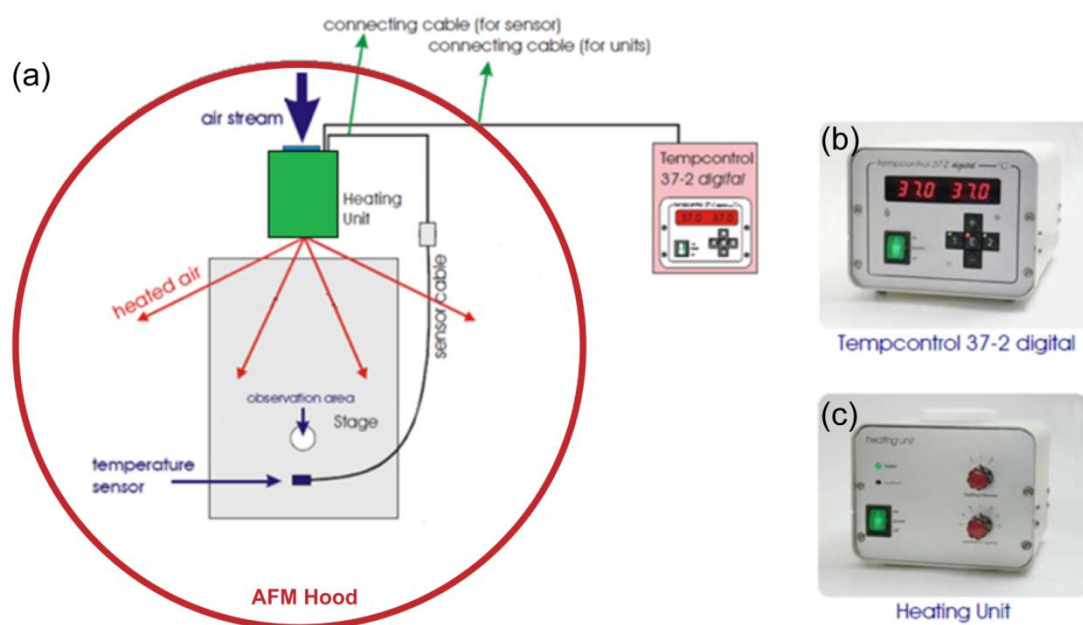


Figure 5.2: (a) Connection diagram of active temperature control system, (b) temperature control unit and (c) heating unit. Adapted from Pecon incubator BL manual ([www.pecon.biz](http://www.pecon.biz)).

To elucidate the magnitude of z-drift when active temperature control is implemented, stability measurements are performed on a glass slide in air over a

period of 18 hr, as shown in Figure 5.3. Starting from a *cold system*, the laser, inverted microscope, and active temperature control system are powered on. The temperatures within the isolation hood are observed to rise rapidly, in contrast to the unmodified system. The AFM head temperature increased to a maximum value of 35.51 °C. After 5 hr of equilibration the temperature is  $35.28 \pm 0.03$  °C with a rate of change of  $0.02 \pm 0.02$  °C/hr. After 5 hr of equilibration, the z-drift for the modified system is found to be  $9.28 \pm 5.41$  nm/hr compared to  $111.56 \pm 112.97$  nm/hr for the unmodified system (Figure 5.3 (b)). This significant improvement in performance is primarily due to system operation at a temperature greater than the unmodified equilibration temperature of the system, which negates the impact of slow variations in temperature due to instrument heat dissipation. No significant difference in system relative noise stability is observed, with a z-sdev of  $4.94 \pm 0.46$  nm for the modified system compared to z-sdev of  $4.62 \pm 1.08$  nm for the unmodified system, as shown in Figure 5.3 (c).

In the case of the modified system it is found that fully opening the acoustic isolation hood doors for 10 min required a period of 5 hr to re-establish stability. As such, all major adjustments to samples and cantilevers are performed within a 10 min period, after which the system is left for 5 hr to equilibrate. The system is defined as a *warm system* when thermal stability is reached. Minor adjustments such as laser positioning, cell injection, AFM head and sample stage positioning may also be performed through the side portal window of the acoustic isolation hood. Such operations are not found to affect stability if performed in time periods less than 1 min.

For biological experiments under physiologically relevant conditions the addition of a fluid cell is required. As such, the performance of two fluid cells: a BioHeater™ fluid cell (Asylum Research, USA) and a glass bottomed petri dish (GBPD) (FluoroDish 35 mm, WRI, Florida) are also measured using a *warm system* in air over a period of 5 hr for comparison, Figure 5.4.

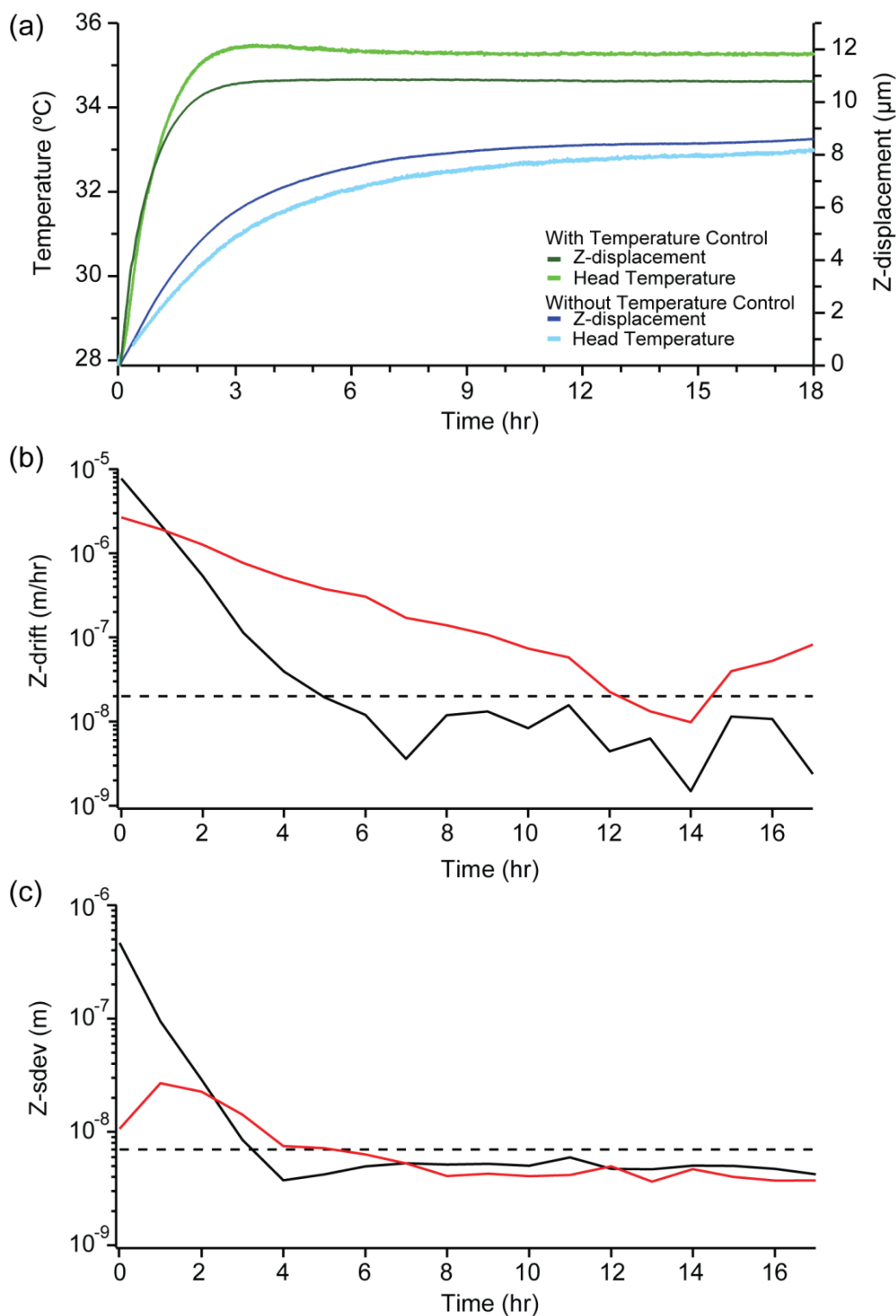


Figure 5.3: (a) AFM head temperature and measured z-displacement over 18 hr with and without active temperature control. (b) z-drift with (black) and without (red) active temperature control. (c) z-sdev with (black) and without (red) active temperature control. For (b) and (c), increments of 1 hr are used for each data point. Dashed lines are included as indicators only and are defined as 20 nm/hr for (b) and 7 nm for (c).

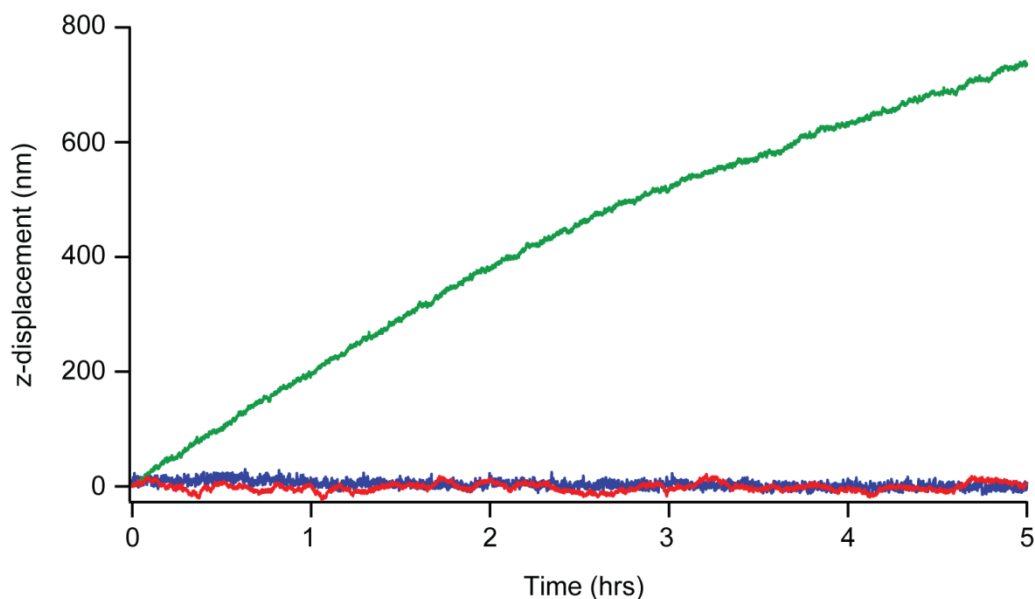


Figure 5.4: Z-displacement in air using a *warm system* on a glass slide (red)  $z$ -drift =  $12.51 \pm 5.26$  nm/hr with  $z$ -sdev =  $5.86 \pm 0.52$  nm, a GBPD (blue)  $z$ -drift =  $2.98 \pm 2.82$  nm/hr with  $z$ -sdev =  $4.90 \pm 0.28$  nm, and a BioHeater™ (green)  $z$ -drift =  $148.37 \pm 41.72$  nm/hr with  $z$ -sdev =  $3.37 \pm 0.49$  nm.

Best  $z$ -drift performance is found using the GBPD with a value of  $2.98 \pm 2.82$  nm/hr compared to  $12.51 \pm 5.26$  nm/hr for the glass slide and  $148.37 \pm 41.72$  nm/hr for the BioHeater™. Again the relative noise stability of the system (sdev) is found to be comparable in all cases. The origin of the high  $z$ -drift in the BioHeater™ system is unknown but may be attributed to the complexity of the design with a range of thermal expansion coefficients present (PEEK body, glass coverslip, O-ring, and a metal retaining ring), as illustrated in Figure 5.5. From these results, it is evident that the GBPD has the lowest drift rate and so represented the best candidate for stable operation in liquid.

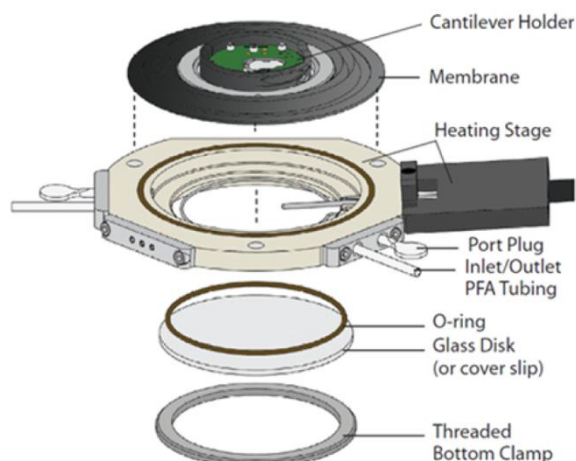


Figure 5.5: Schematic of BioHeater™ assembly. Adapted from Asylum Research Data Sheet 04 - BioHeater™ Closed Fluid Cell.

#### 5.4.2 Stability in Liquid: Customised Fluid Cell

Having demonstrated good stability in air (Figure 5.4), the GBPD is then tested in liquid (PBS) in a *warm system* over a period of 5 hr. With the GBPD open to the environment, the system is unstable with changes in z-displacement of over 100 nm observed, as shown in Figure 5.6. These perturbations are attributed to liquid instabilities arising from evaporation.

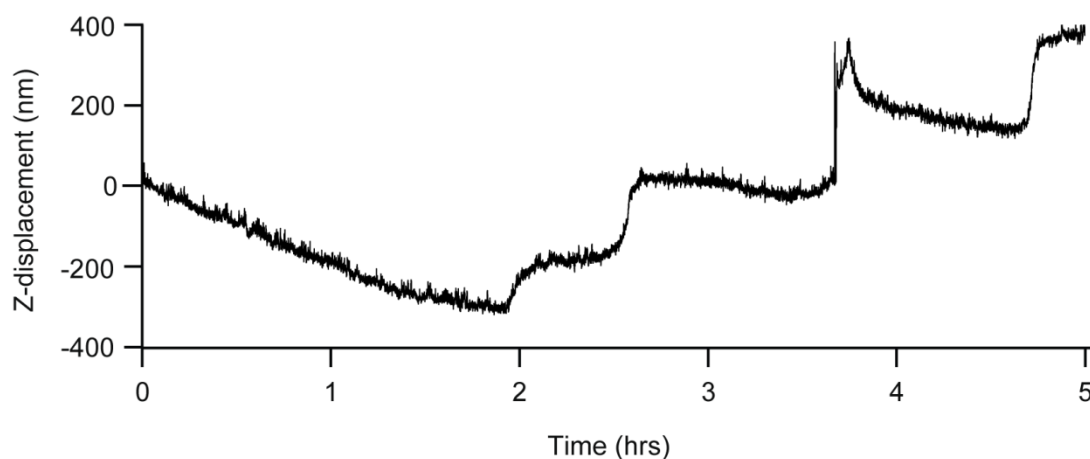


Figure 5.6: Z-displacement in a *warm system* in PBS using an open GBPD.

Figure 5.6 highlights the necessity of a closed fluid cell setup to prevent liquid instabilities. However, as indicated in Figure 5.5, the Asylum Research BioHeater™ (a closed fluid cell) demonstrated very poor stability. Therefore, a modified closed

fluid cell is developed to minimise z-drift whilst maintaining system stability and additionally to provide:

- (i) The ability to inject cells/chemical agents into the fluid cell with minimal disruption
- (ii) Optical access from below to allow sample observation via the inverted optical microscope.

Briefly, the closed fluid cell design (Figure 5.7) consists of a reservoir (Sarstedt, Germany) with an inlet tube (ID = 1 mm) (Cole-Parmer, IL, USA) containing a 3-way valve (Cole-Parmer, IL, USA) inserted into the side of the GBPD. The fluid cell itself is made up of a GBPD with a flexible silicone membrane (Asylum Research, USA) clamped around the top circumference of the dish. This encapsulated the AFM cantilever holder within the fluid cell. The fluid cell is fixed to the AFM stage by a magnetic petri dish clamp assembly (Asylum Research, CA, USA). A wider bore tube (ID = 5 mm) (Cole-Parmer, IL, USA) exits the dish and finishes within a second fluid reservoir. Reservoirs are positioned such that the liquid levels (~125 ml) are the same in each reservoir. Each reservoir has an opening to allow for pressure equilibration during setup, and for cell/chemical injection through the 3-way valve. During experiments the valve is closed to eliminate liquid flow and any associated temperature changes and/or liquid instabilities. By placing the reservoirs in the active temperature controlled hood, thermal gradients within the fluid are also eliminated.

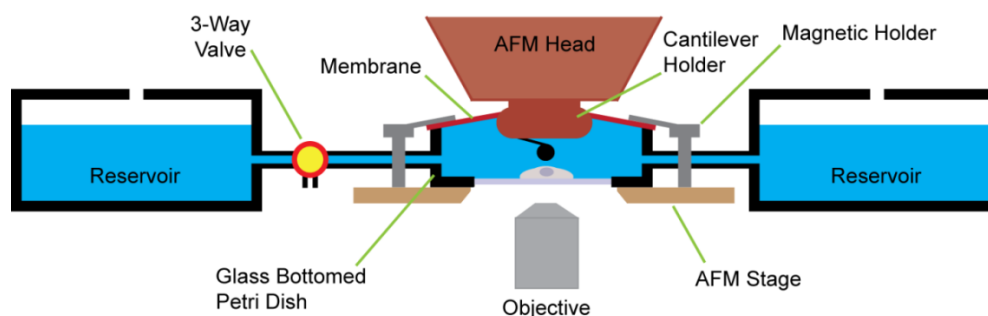


Figure 5.7: Customised fluid cell; setup consists of a sealed GBPD clamped to the AFM stage using a magnetic dish clamp assembly. The design is a closed system, air-free within the fluid cell. A 3-way valve is connected to an inlet tube to allow cell/chemical agent addition without further system restabilisation.

Figure 5.8 illustrates the performance of the customised fluid cell with trapped air present when tested in liquid (PBS) in a *warm system* over a period of 5 hr. Liquid instabilities due to the trapped air results in sudden z-displacement jumps of hundreds of nanometres. Further investigation found that movement of trapped air (not removed during setup) or air bubbles forming (due to nucleation or when highly gas permeable tubing is used) within the system results in liquid instability ( $n = 10$ ). Liquid instability tests show that the addition of even a small volume of air ( $0.008 \text{ cm}^3$ , 0.1% of the fluid cell volume) to the closed fluid cell results in instability, as shown in Figure 5.9. Stability tests with gas permeable tubing are also performed. Air that permeates into an initially stabilised system results in system instability with large jumps of over 100 nm in the z-displacement (Figure 5.10). Quantifying the amount of air within the system was performed according to Appendix 5.B.

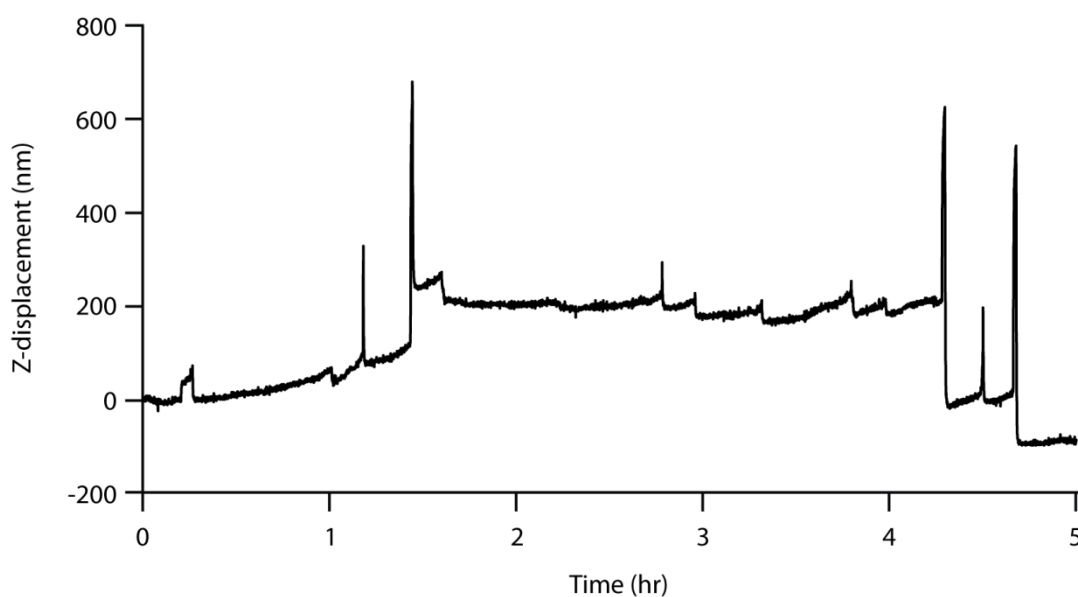


Figure 5.8: Z-displacement using a *warm system* in PBS of a customised closed fluid cell with trapped air bubbles.

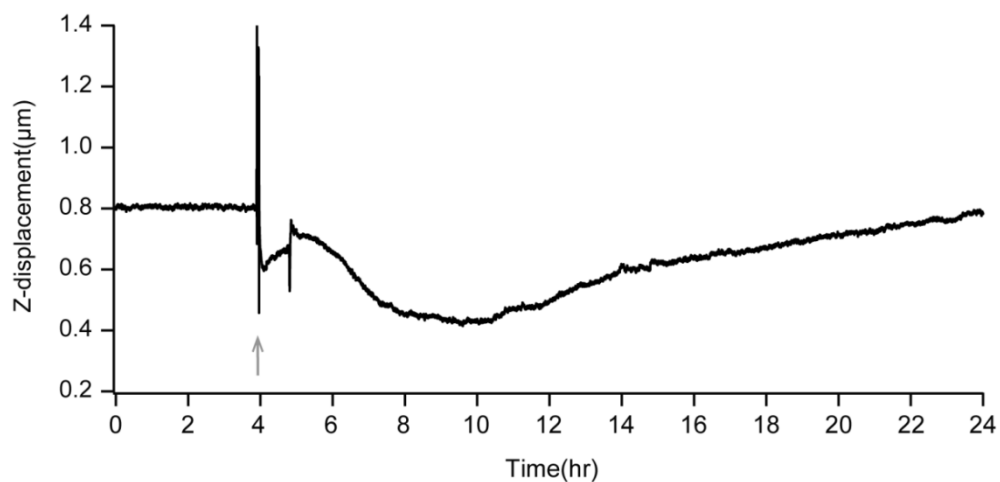


Figure 5.9: Stabilised system (all air expelled during setup) becomes unstable due to the addition of  $0.008 \text{ cm}^3$  of air into the fluid cell (0.1% of the fluid cell volume), indicated by an arrow at 4 hr. Z-displacement never re-stabilises after this point and a 200 nm jump occurs 1 hr after air injection. Further spontaneous z-displacement jumps are not observed in this case.

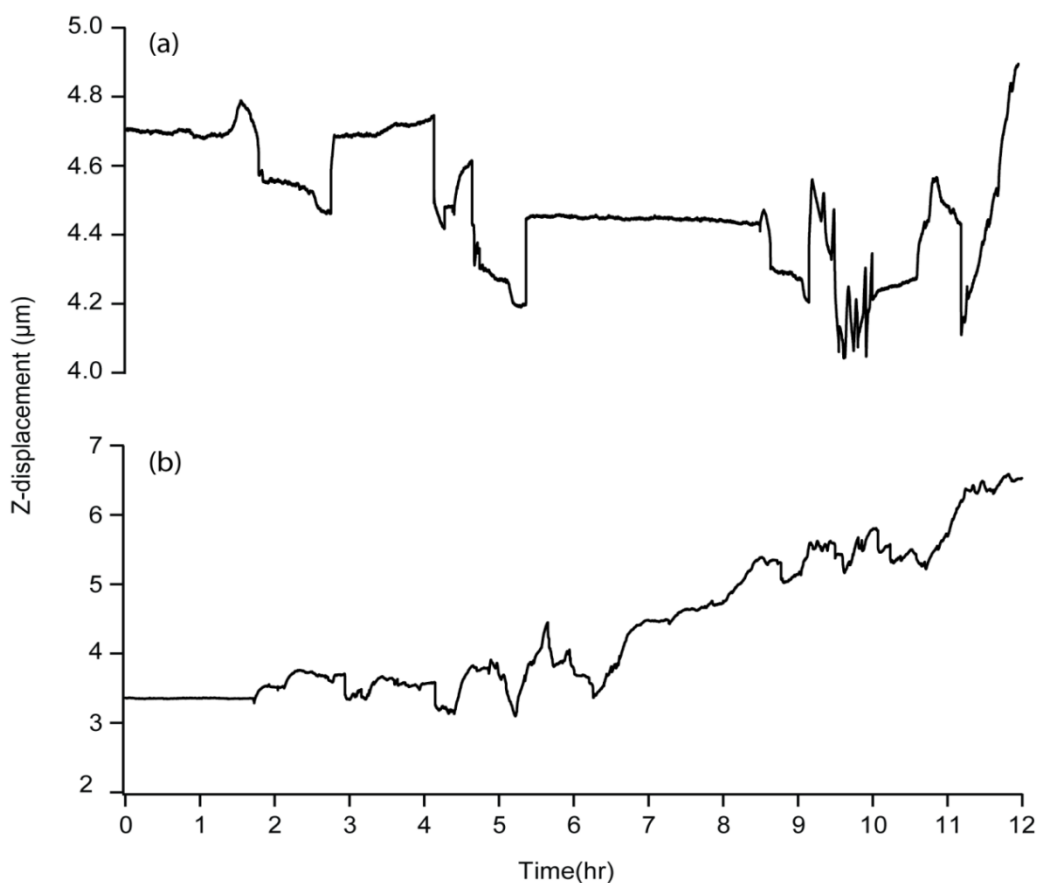


Figure 5.10: Examples of stabilised systems (all air expelled during setup) becoming unstable over time when gas permeable tubing is used. In (a) and (b), the quantity of air measured within the system changes from 0 to  $1.0\text{--}1.5 \text{ cm}^3$  (measured after experiments).

From these liquid instability tests, it is established that the use of gas impermeable tubing is critically important, in addition to the requirement increasing the liquid temperature to the system temperature prior to use (avoiding nucleation). Additionally, prior to experiments, it is essential that air is completely expelled from the system. This is achieved by positioning the setup at such an angle that trapped air is forced through the system, exiting via the outlet tubing. Visual inspection of the transparent tubing and fluid cell verifies that the system remains air free. No liquid instability is observed when the above steps are followed, as demonstrated in Figure 5.11.

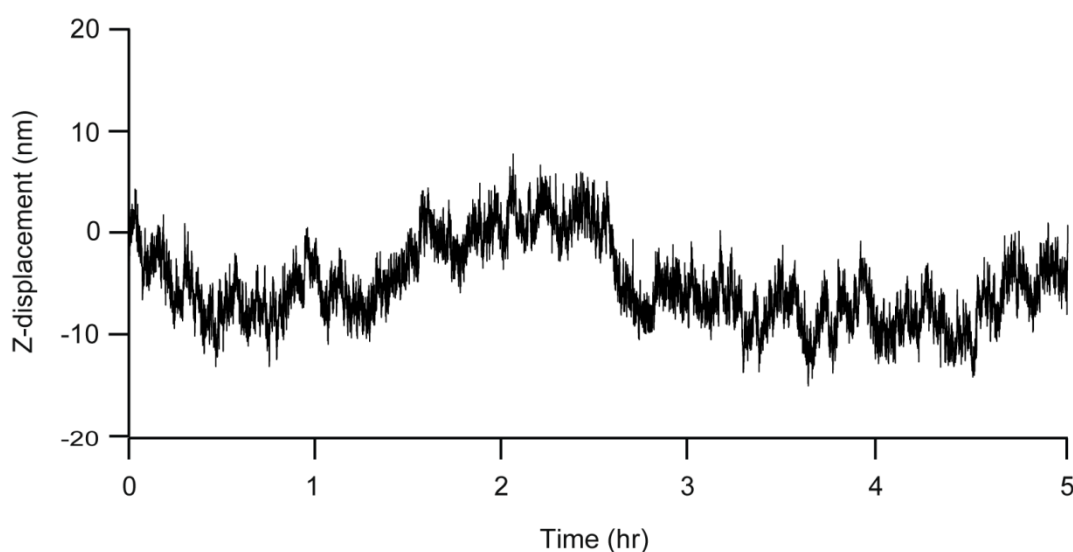


Figure 5.11: Z-displacement using a *warm system* in PBS of a customised closed fluid cell with all air expelled.

By combining this customised closed fluid cell with active temperature control a practical method for achieving displacement controlled AFM over long time scales, with readily implementable modifications to a commercial system, has been established. The z-drift performance under physiologically relevant conditions is found to be  $6.33 \pm 3.90$  nm/hr with a z-sdev of  $2.40 \pm 0.29$  nm over a 5 hr period. This represents a 17-fold improvement in z-drift and 2-fold improvement in system noise stability when compared to the operation of an unmodified AFM system in air (Figure 5.1).

## 5.5 Stability Enhancement versus Standard Operating Conditions

### 5.5.1 Introduction

To highlight the importance of precise displacement control, cyclic cell deformation is performed for both an unmodified (open GBPD and no temperature control) and modified system (active temperature control with customised fluid cell). It is important to note that a comprehensive single cell investigation will be presented in Chapter 6. Here it is simply demonstrated that the stabilised system developed in this chapter must be used for single cell deformation controlled cyclic loading, highlighting the significant errors that can occur in applied cell strain when an unmodified system is used.

### 5.5.2 Materials and Methods

#### 5.5.2.1 AFM and Fluid Cell Setup

The AFM cantilever holder and modified cantilever are cleaned according to Section 3.2.1. The fluid cell system components are cleaned by immersion in 70% ethanol for 15 min, followed by three rinses with ultrapure water. They are then placed under UV in a laminar flow hood (NuAire, Minnesota, USA) for a further 15 min.

The fluid cell system is assembled in the laminar flow hood to maintain sterility. Briefly, the cleaned cantilever holder is sealed to the top section of the fluid cell (magnetic holder with attached silicone membrane). Following cantilever loading, the bottom section of the fluid cell (modified GBPD with tubing ports) is then securely sealed to the magnetic holder. Care is taken not to allow the sphere-attached-cantilever come into contact with the glass bottom of the fluid cell. The fluid cell setup is filled with pre-warmed sterilised PBS via the 3-way valve. The assembled fluid cell setup is transferred to the AFM system and attached to the AFM head via the cantilever holder, which is in turn carefully centred on the stage over the inverted microscope. Visual inspection of the transparent tubing and fluid cell verifies the system is air free. The AFM head is lowered until the sphere-attached-cantilever is only millimetres from the glass surface of the fluid cell.

Cantilever calibration is performed according to Section 3.4. The sphere is examined during experiments to assess that the sphere remains constrained during cell indentation. The laser is aligned on the sphere-attached-cantilever at an axial position of 0.8 using the top view CCD camera. The CCD camera is subsequently exchanged for a phase contrast column to allow for cell imaging. At this point, the AFM hood doors are closed and the active temperature control system is initiated.

#### 5.5.2.2 *Cell Preparation*

MC3T3-E1 osteoblasts are cultured according to the method described in Section 4.2.1. Cells are detached from the tissue culture flasks using 0.25% trypsin-EDTA and centrifuged at 2000 rpm for 4 min. The supernatant is removed and the cell pellet suspended in pre-warmed sterile PBS. Cells are counted using a haemocytometer and the cell concentration is adjusted to obtain a density of 3,500 cells/cm<sup>2</sup>.

#### 5.5.2.3 *Experimental Procedure*

Suspended cells in PBS are injected into the fluid cell via the inlet tube valve through the side portal window of hood. An additional 10 min is allowed for cell attachment to the glass substrate and system equilibration. The initial cell height is determined according to Section 4.2.3.1. The cell is then subjected to cyclic deformation at  $0\% \leq \varepsilon_H \leq 25\%$  at a frequency of 0.1 Hz (this results in a ‘sawtooth’ loading curve) for a period of 36 min, calculated according to Section 4.2.3.2. Plots of the maximum and minimum force as a function of time are constructed. The minimum force is taken as the force recorded at the start of each cycle ( $\varepsilon_H = 0\%$ ), as indicated in Figure 5.12. Maximum force is taken as the force recorded at the end of the loading half of each cycle ( $\varepsilon_H = 25\%$ ), as indicated in Figure 5.12.

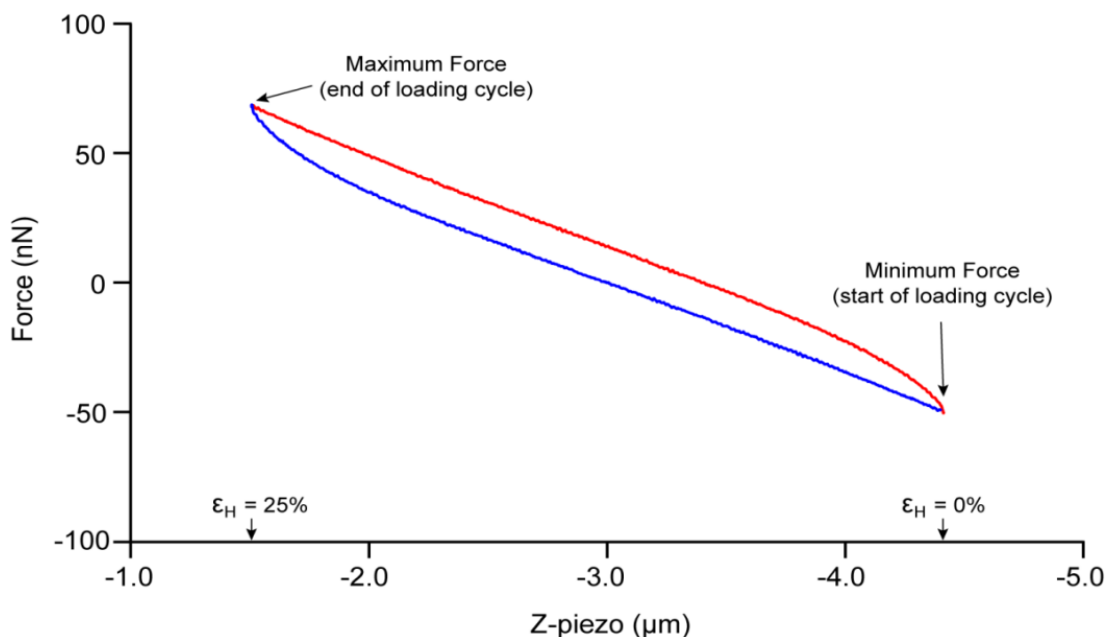


Figure 5.12: Force-displacement curve showing the loading (red) and unloading (blue) half of a cell deformation cycle. The maximum and minimum force measure points are indicated.

### 5.5.3 Results

Figure 5.13 (a, b) shows the minimum force, recorded at the beginning of each cycle and the maximum force recorded at the mid-point of each cycle for the unmodified and modified system. The initial minimum force (3.0 nN) for the unmodified system decreases by 9 nN over the first 2 cycles compared to an initial minimum force (15.6 nN) for the modified system decreasing by 10.2 nN over the first 5 cycles. Following this rapid decrease, the rate of reduction is 7.8 times larger for the unmodified system compared to the modified system.

Regarding the maximum force, the initial values are 120.6 nN and 75.0 nN for the unmodified and modified systems, respectively. Both systems exhibited an initial decrease within the first 10 cycles of deformation. Following local minima, the force in the unmodified system steadily increases in subsequent cycles, reaching a value of 175.8 nN following 36 min. In contrast, for the modified system the measured force reaches a steady state value of 70.2 nN following 22 min of cyclic deformation. It should also be noted that spikes in maximum force are observed for the cell within the unmodified system.

From force-displacement curves taken on the substrate before and after each experiment the z-drift value can be obtained, Table 5.1. The tip-surface distance decreased by 1.50  $\mu\text{m}$  for the unmodified system versus 0.02  $\mu\text{m}$  for the modified system, as shown in Figure 5.13 (g). This resulted in an actual cell indentation of  $\varepsilon_H = 40.95\%$  for the unmodified system, compared to the desired value of  $\varepsilon_H = 25\%$ . In contrast, a value of  $\varepsilon_H = 25.26\%$  is achieved using the modified system.

In Figure 5.13 the first (c, d) and last (e, f) cell deformation cycles for the modified and unmodified systems are shown. For both systems the first cycle shows a non-linear increase in force during deformation. Hysteresis is observed during the unloading half of the cycle. For both systems the force value at the end of the cycle is lower than the starting point. The final cycle at 36 min reveals significant differences between the modified and unmodified system. In the unmodified system, the final cycle (e) starts at a negative force ( $\sim -42$  nN). During the early stages of the loading half-cycle the force rapidly increases to a value of 0 nN. This is followed by an intermittent plateau at  $\sim 0$  nN, followed by further force increase to a peak value of 175.8 nN. In comparison the last cycle (f) in the modified system starts at 0.6 nN, beginning with a rapid increase in force and then continuing along a similar force-strain curve to that observed for the first cycle.

Table 5.1: Comparison of cell cyclic deformation for an unmodified and modified system

System setup	Initial cell height ( $\mu\text{m}$ )	Initial cell diameter ( $\pm 1.6 \mu\text{m}$ )	Sphere-surface distance change ( $\mu\text{m}$ )	Change in deformation (%)
Unmodified	9.4	17.1	1.50	15.96
Modified	9.4	18.0	0.02	0.26

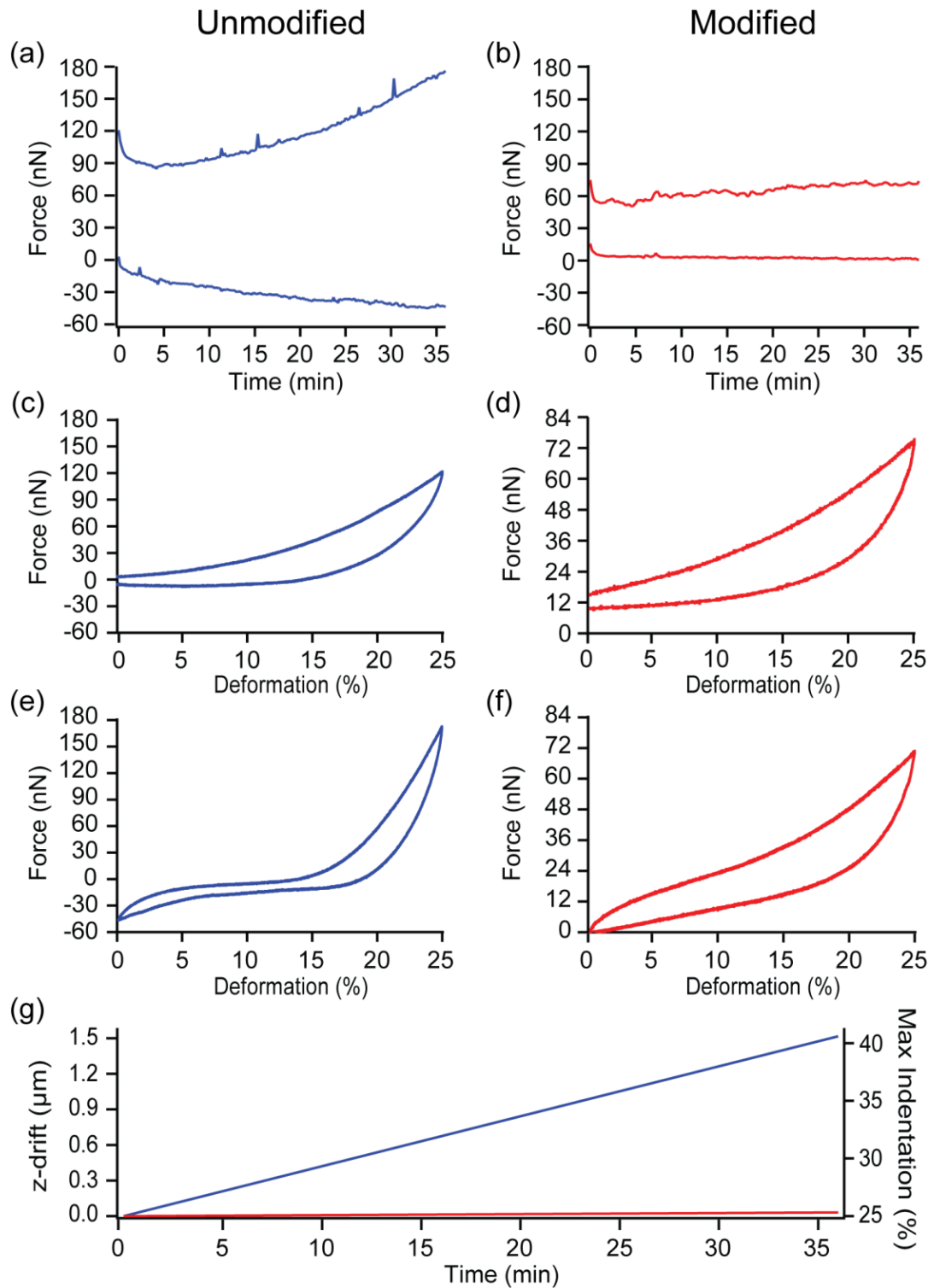


Figure 5.13: Single cell cyclic deformation experiment at  $0\% \leq \varepsilon_H \leq 25\%$  at a frequency of 0.1 Hz using a  $\varnothing 150 \mu\text{m}$  sphere within an unmodified (blue) and modified (red) system. For each system, (a, b) the minimum force (at  $\varepsilon_H = 0\%$ ) and maximum force (at  $\varepsilon_H = 25\%$ ) is shown. The first (c, d) and last (e, f) cycles during cell deformation for both systems is also highlighted. (g) A linear interpolation of z-drift and maximum indentation (relative to original cell height) is also shown.

## 5.6 Discussion

In this chapter, a readily implementable, cost effective method of modifying an AFM for z-displacement controlled operation in both air and liquid over long time scales has been successfully developed. It is demonstrated that the elimination of thermal drift and liquid instabilities is essential for all AFM studies where accurate knowledge of the tip-sample separation over long time scales is a requirement. For operation in air, it is shown that after 5 hr of equilibration, the z-drift for the unmodified system is  $111.56 \pm 112.97$  nm/hr compared to  $9.28 \pm 5.41$  nm/hr for the modified system. This represents over a 10-fold improvement in performance in air whilst not significantly altering the system noise stability ( $4.62 \pm 1.08$  nm unmodified,  $4.94 \pm 0.46$  nm modified). Furthermore, the standard deviation of the z-drift is also improved over 10-fold. For operation in fluid, a 17-fold improvement in z-drift ( $6.33 \pm 3.90$  nm/hr) and 2-fold improvement in system noise stability ( $2.40 \pm 0.29$  nm) is established when compared to the operation of an unmodified AFM system in air. For a cell of  $10 \mu\text{m}$  high, this represents a maximum of 0.5% error in indentation depth over 5 hr due to z-drift for the modified system, compared to a maximum of 13.5% error for the unmodified system. Here, it is also demonstrated, for the first time, the necessity to remove all air-liquid interfaces in order to maintain continuous displacement control in liquid environments.

To highlight the importance of precise displacement control in deformation controlled measurements of cell mechanics, cyclic cell deformation is performed for both an unmodified and modified system. For the unmodified system, the continuous increase in force occurs due a continuously increasing level of maximum cell deformation, from  $\varepsilon_H = 25\%$  at the start of the experiment to  $\varepsilon_H = \sim 41\%$  within 36 min, due to z-drift. Clearly the forces measured using the unmodified system are dominated by the influence of z-drift, preventing reliable measurement of active force changes due to cytoskeletal remodelling. A full investigation of cell response to cyclic deformation is presented in Chapter 6 but the initial data presented here indicates that the modifications presented in this chapter are essential to study the response of cell to mechanical loading over long time scales where precise force measurement and accurate control of cell strain and cell strain rate is a requirement.

Displacement controlled AFM has many applications including nano-manipulation (Hu et al. (2004)), dynamic behaviour monitoring (Mitrossilis et al. (2009)), and deformation controlled measurements (Fernández et al. (2006)). Combining the readily implementable method of performing whole cell deformation, described in Chapter 3, with the displacement controlled AFM setup presented here, the potential of this system to investigate long term whole cell mechanics is demonstrated. The long-term stability of the modified system offers the ability to apply precise mechanical stimulation and accurately monitor the evolution of cell forces. The modifications presented in this chapter can be adapted to suit any conventional AFM system. The work presented in this chapter is published in the *Review of Scientific Instruments* (Weafer et al. (2012)).

## 5.7 References

- Altmann, S. M., Lenne, P. F. and Hörber, J. K. H. (2001) Multiple sensor stabilization system for local probe microscopes. *Rev. Sci. Instrum.* 72, 142
- Charras, G. T. and Horton, M. A. (2002) Single cell mechanotransduction and its modulation analyzed by atomic force microscope indentation. *Biophys. J.* 82 (6), 2970-2981
- Choy, J. L., Parekh, S. H., Chaudhuri, O., Liu, A. P., Bustamante, C., Footer, M. J., Theriot, J. A. and Fletcher, D. A. (2007) Differential force microscope for long time-scale biophysical measurements. *Rev. Sci. Instrum.* 78, 043711
- Fernández, P., Pullarkat, P. A. and Ott, A. (2006) A master relation defines the nonlinear viscoelasticity of single fibroblasts. *Biophysical Journal.* 90 (10), 3796-3805
- Gan, Y. (2009) Atomic and subnanometer resolution in ambient conditions by atomic force microscopy. *Surf. Sci. Rep.* 64 (3), 99-121
- Hoogeman, M. S., van Loon, D. G., Loos, R. W. M., Ficke, H. G., De Haas, E., van der Linden, J. J., Zeijlemaker, H., Kuipers, L., Chang, M. F. and Klik, M. A. J. (1998) Design and performance of a programmable-temperature scanning tunneling microscope. *Rev. Sci. Instrum.* 69, 2072
- Hu, J., Zhang, Y., Li, B., Gao, H., Hartmann, U. and Li, M. (2004) Nanomanipulation of single DNA molecules and its applications. *Surface and interface analysis.* 36 (2), 124-126
- Kaunas, R., Nguyen, P., Usami, S. and Chien, S. (2005) Cooperative effects of rho and mechanical stretch on stress fiber organization. *Proc. Natl. Acad. Sci.* 102 (44), 15895-15900
- Kindt, J. H., Thompson, J. B., Viani, M. B. and Hansma, P. K. (2002) Atomic force microscope detector drift compensation by correlation of similar traces acquired at different setpoints. *Rev. Sci. Instrum.* 73 (6), 2305-2307
- McGarry, J. G., Maguire, P., Campbell, V. A., O'Connell, B. C., Prendergast, P. J. and Jarvis, S. P. (2008) Stimulation of nitric oxide mechanotransduction in single osteoblasts using atomic force microscopy. *J. Orthop. Res.* 26 (4), 513-521
- Mitrossilis, D., Fouchard, J., Guiroy, A., Desprat, N., Rodriguez, N., Fabry, B. and Asnacios, A. (2009) Single-cell response to stiffness exhibits muscle-like behavior. *Proceedings of the National Academy of Sciences.* 106 (43), 18243-18248
- Mokaberi, B. and Requicha, A. A. G. (2006) Drift compensation for automatic nanomanipulation with scanning probe microscopes. *IEEE Trans. Contr. Syst. Technol.* 3 (3), 199-207

- Munday, J. N., Capasso, F. and Parsegian, V. A. (2009) Measured long-range repulsive casimir-lifshitz forces. *Nature*. 457 (7226), 170-173
- Oulevey, F., Gremaud, G., Kulik, A. J. and Guisolan, B. (1999) Simple low-drift heating stage for scanning probe microscopes. *Rev. Sci. Instrum.* 70 (3), 1889-1890
- Rachlin, A. L., Henderson, G. S. and Goh, M. C. (1992) An atomic force microscope (afm) study of the calcite cleavage plane; image averaging in fourier space. *Amer. Mineral.* 77 (9-10), 904-910
- Schitter, G. and Stemmer, A. (2002) Eliminating mechanical perturbations in scanning probe microscopy. *Nanotechnology*. 13, 663
- Spagnoli, C., Beyder, A., Besch, S. R. and Sachs, F. (2007) Drift-free atomic force microscopy measurements of cell height and mechanical properties. *Rev. Sci. Instrum.* 78, 036111
- Sparks, A. W. and Manalis, S. R. (2004) Scanning probe microscopy with inherent disturbance suppression. *Appl. Phys. Lett.* 85, 3929
- Thundat, T., Warmack, R. J., Chen, G. Y. and Allison, D. P. (1994) Thermal and ambient-induced deflections of scanning force microscope cantilevers. *Appl. Phys. Lett.* 64 (21), 2894
- Torun, H., Finkler, O. and Degertekin, F. L. (2009) Athermalization in atomic force microscope based force spectroscopy using matched microstructure coupling. *Rev. Sci. Instrum.* 80, 076103
- Wang, J. H. C., Goldschmidt-Clermont, P., Wille, J. and Yin, F. C. P. (2001) Specificity of endothelial cell reorientation in response to cyclic mechanical stretching. *J. Biomech.* 34 (12), 1563-1572
- Weafer, P. P., McGarry, J. P., van Es, M. H., Kilpatrick, J. I., Ronan, W., Nolan, D. R. and Jarvis, S. P. (2012) Stability enhancement of an atomic force microscope for long-term force measurement including cantilever modification for whole cell deformation. *Review of Scientific Instruments*. 83 (9), 093709
- Wille, J. J., Elson, E. L. and Okamoto, R. J. (2006) Cellular and matrix mechanics of bioartificial tissues during continuous cyclic stretch. *Ann. Biomed. Eng.* 34 (11), 1678-1690
- Zepeda, S., Yeh, Y. and Orme, C. A. (2001) Atomic force microscope chamber for in situ studies of ice. *Rev. Sci. Instrum.* 72 (11), 4159-4163

## 5.8 Appendix

### 5.A Counteracting Drift based on the System Temperature

It is demonstrated in Figure 5.1 that under standard operating conditions, there is an almost linear relationship between temperature and z-displacement, that is, the z-drift per degree ( $\mu\text{m}/^\circ\text{C}$ ) is relatively constant. Therefore, using  $\mu\text{m}/^\circ\text{C}$ , the z-position could be adjusted relative to the monitored system temperature. A custom Igor program is developed to accomplish this. The  $\mu\text{m}/^\circ\text{C}$  is calculated from z-displacement and temperature data collected for a number of hours prior to an experiment. It is found that  $\mu\text{m}/^\circ\text{C}$  varied for each experiment. This variability is unpredictable and could suddenly change (Figure 5-A (a)). Furthermore, if the calculated  $\mu\text{m}/^\circ\text{C}$  is slightly miscalculated, the measured z-drift and predicted z-drift would continue to diverge over time (Figure 5-A (b)). This amount of variability and unpredictability means that it is impossible to detect the relatively small force changes due to the cell active responsiveness compared to the large force changes due to the z-position movement.

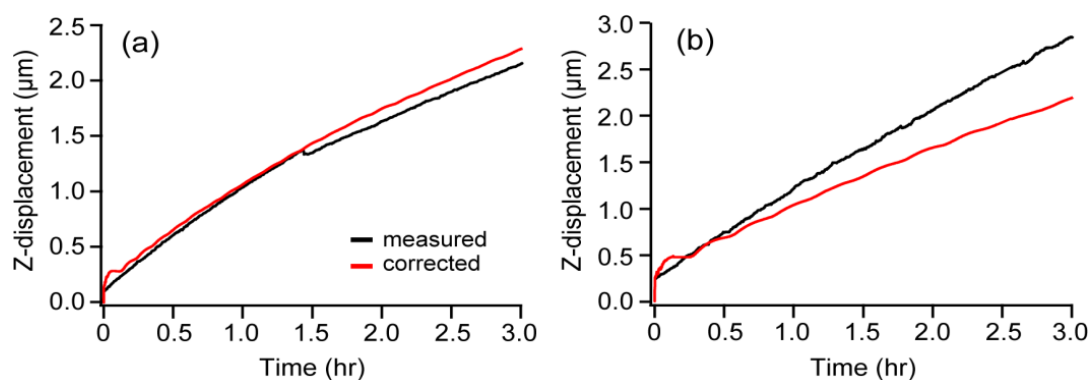


Figure 5-A: Tests to assess the fit between the predicted z-drift based on the measured system temperature change (red) and the actual measured z-drift (black). In (a) the predicted z-drift matches the measured z-drift relatively well until the drift rate suddenly changes at  $\sim 1.5$  hr. This is likely due to system movement during thermal expansion. In (b) the drift per degree is slightly off and therefore the predicted z-drift is continuously diverging from the measured z-drift.

## 5.B Quantifying Trapped Air within the System

The following procedure is used to insert a known quantity of air into a stabilised (air-free) system (Figure 5.9). Using the hood side-portal window to minimise destabilisation, air is injected into the inlet tubing of the system via the 3-way valve. The volume of trapped air within the tubing is calculated based on the length of tubing the air occupies and on the internal diameter of the inlet tubing ( $\varnothing$  1 mm). For example, the  $0.008 \text{ cm}^3$  volume of air injected in Figure 5.9 results in a length of trapped air within the inlet tubing of 1.0 cm. The known quantity of trapped air bubble is then inserted into the fluid cell and its effects on stability examined.

The same methodology is used to quantify the volume of trapped air within the fluid cell after liquid instability tests using gas permeable tubing (Figure 5.10). Directly after experiments, the fluid cell is tilted to an angle such that trapped air within the fluid cell can be drawn into the inlet tubing (making sure no additional air enters the system during this process by maintaining the ends of the inlet and outlet tubing under the reservoir liquid levels). The length of tubing the trapped air occupies is used to calculate the volume of air that was within the fluid cell.

## Chapter 6

# **Investigation of the Cellular Response to Cyclic Deformation**

## 6.1 Introduction

Dynamic mechanical loading is essential for cell function and tissue maintenance (Gabbay et al. (2006), Thorpe et al. (2008)). In an effort to characterise the response of cells to cyclic deformation several *in vitro* studies have relied on the testing of large populations of cells seeded on 2D substrates (Kaspar et al. (2002), Kurpinski et al. (2006), O'Cearbhaill et al. (2008), Lee et al. (2010), Quinlan et al. (2011)) or in 3D scaffolds and gels (Hutmacher (2000), Wille et al. (2006), Thorpe et al. (2008), Balestrini and Billiar (2009), Thorpe et al. (2010)) subjected to macroscale boundary conditions. Cyclic stretching of endothelial cell seeded silicone substrates reveal that cell morphology and the actin cytoskeleton re-align in the direction of minimum strain (Kaunas et al. (2005), Wang et al. (2001), Barron et al. (2007)). Cyclic compression of agarose gels seeded with chondrocytes has been shown to result in actin cytoskeleton disruption (Knight et al. (2006), Campbell et al. (2007)). Whereas a study by Hara et al. (2001) has shown that cyclic tensile stretching of osteoblasts induces the development of stress fibres. Furthermore, oscillatory fluid flow has been shown to induce signalling in fibroblasts, osteoblasts and osteocytes, however this response was eliminated when the actin cytoskeleton was disrupted (Ajubi et al. (1996), Malone et al. (2007)). In these aforementioned investigations of the response of large cell populations to applied loading, the actin cytoskeleton has been imaged and deformation induced remodelling has been reported; however, corresponding changes in contractile force actively generated by the actin cytoskeleton has not been quantified.

In a study by Wille et al. (2006) a collagen scaffold populated with fibroblasts was subjected to cyclic deformation at constant loading and unloading strain rates. Cyto-D was used to isolate the force contribution of the actin cytoskeleton, which was shown to be dependent on the applied strain rate. A study by Watanabe-Nakayama et al. (2011) applied step-stretching to localised regions of fibroblasts. When the cytoskeleton was disrupted using cyto-D or blebbistatin (an inhibitor of myosin II ATPase activity) a passive viscoelastic type relaxation of the cell force over time was observed. For untreated cells with intact contractile actin cytoskeletons, a passive force relaxation was not observed; rather, a gradual increase

in measured force was reported. Similar findings were also reported in the studies by Micoulet et al. (2005) and Thoumine and Ott (1997). While such characterisation of the time-dependent force response of cells to a constant applied strain is a significant contribution to the field of single cell mechanics, it should be noted that dynamic loading at a relatively high frequency (~1 Hz) is also of significant physiological relevance (You et al. (2000), Burr et al. (2002)). The study of Fernández et al. (2006) has monitored total cell forces in response to dynamic loading at a whole cell level, again revealing a deviation from a passive viscoelastic response. However, the contribution of the actin cytoskeleton to the measured reaction force was not isolated in this study.

In this study, to further the understanding of the cells' response to mechanical loading, deformation controlled cyclic loading experiments are performed on single osteoblasts at the whole cell level using the modified AFM system developed in Chapter 3 and Chapter 5. In addition to untreated cells, experiments are also performed on passive cells in which the actin cytoskeleton has been disrupted. It is demonstrated that the measured forces are highly dependent on strain rate for cells that contain a contractile actin cytoskeleton, whereas a significant strain amplitude dependence is observed for cells in which the actin cytoskeleton has been disrupted.

## **6.2 Materials and Methods**

In this section, the steps to perform whole cell cyclic deformation are described. Whole cell cyclic deformation is achieved using the customised AFM system described in Chapters 3 and 5.

### **6.2.1 AFM and Fluid Cell Setup**

All AFM and fluid cell components in direct contact with cells are sterilised and setup prior to each experiment, as described in Section 3.2.1 and Section 5.5.2.1, respectively. The AFM is setup to execute active temperature control and to log temperature change within the hood, as previously described in Section 5.2.2. From this point on, all operations (x-y stage positioning, deflection zeroing, AFM head

height adjustment, cell/chemical injection) are performed within 1 min timeframes via the hood side-portal window to prevent system destabilisation.

Temperature and z-drift logging is implemented according to Section 5.2.2. System stabilisation within 20 nm/hr for a minimum of 5 hr is required before experiment initiation. As discussed in Section 5.4.2, stabilisation takes a minimum of 10 hr. Following stabilisation, the cantilever is calibrated according to Section 3.4. At this point, the AFM system is ready for cell insertion.

### 6.2.2 Cell Preparation

MC3T3-E1 osteoblast cells are prepared according to Section 5.5.2.2. Cells are divided into three groups; control cells, cyto-D cells and dead cells.

- (i) Control cells are classified as cells that have been prepared using standard culture techniques (Section 5.5.2.2).
- (ii) Cyto-D cells are classified as cells treated with 10  $\mu\text{M}$  cyto-D for a minimum of 30 min. This treatment results in cells in which the actin cytoskeleton is disrupted.
- (iii) Dead cells are classified as cells that are left within the fluid cell for 24 hr, exhibiting an unspread rounded morphology that is distinctly different than control or cyto-D cells.

Suspended cells are added to the fluid cell via the 3-way valve to obtain a density of 3,500 cells/cm<sup>2</sup>. It is important to raise the sphere-attached-cantilever at least 10  $\mu\text{m}$  from the surface before cell injection to ensure glass bowing does not cause the cantilever to break (glass bowing results from the temporary pressure change during cell insertion). The initiation time of experiments is cell group dependent:

- (i) Control cells are left to incubate in the fluid cell for 30 min before experiments.

- (ii) Cyto-D cells are left to incubate in the fluid cell for 30 min. Cyto-D is then injected into the system and cells are left to incubate for a further 30 min before experiments.
- (iii) Dead cells are left in the fluid cell for 24 hr before experiments.

### 6.2.3 Experimental Procedure

For each cell group, cyclic deformation experiments are performed whereby cells are cyclically deformed at a constant loading and unloading nominal strain rate at a frequency of 1.0 Hz (this results in a “saw tooth” loading curve, as shown in Figure 6.1). This frequency is chosen to approximate physiologically relevant loading of osteoblasts during routine locomotion (You et al. (2000), Burr et al. (2002)). Experiments are performed for 120 min ( $T_F$ ) and a loading regime change is implemented at time  $T = T_{RC}$  (60 min). In loading regime 1, prior to the regime change ( $0 \leq T < T_{RC}$ ), cells are cyclically deformed at  $10\% \leq \varepsilon_H \leq 35\%$ . In loading regime 2, ( $T_{RC} \leq T \leq T_F$ ) cells are cyclically deformed at  $0\% \leq \varepsilon_H \leq 25\%$ . It is important to note that the nominal loading and unloading deformation rates, and hence the deformation amplitude, are identical for regime 1 and regime 2 (deformation amplitude = 25%). However, the range of applied deformation differs between the two loading regimes by a magnitude of 10%. 60 min of cyclic deformation is implemented before the regime change to ensure that a steady state response is obtained. Similarly, cyclic deformation is also implemented for 60 min following the regime change again to ensure that a steady state is again obtained for the second loading regime. Such timeframes are based on previously reported cell remodelling time scale of 30-60 min under cyclic mechanical loading (Wille et al. (2006), Kaunas et al. (2005), Wang et al. (2001)).

The modified cantilever is positioned adjacent to the cell of interest. The height of the cell of interest, and corresponding deformation ( $\varepsilon_H$ ) and deformation amplitude were calculated according to Section 4.2.3. A phase contrast image of the cell is taken before and after cyclic deformation with the sphere moved from above the cell. These images are used to calculate the change in cell spreading area and to assess any morphology changes that occur during the experiment. Additionally,

phase contrast images are taken of the cell during cyclic deformation at a capture rate of 0.01 Hz. The presence of the sphere partially blocks the light source and hence reduces the quality of such images. However, these images are of sufficient quality to reliably indicate if the cell under investigation remains centred under the sphere. The sample number ( $n$ ) tested for each cell group is seven. This sample size is in line with previous studies on single cell experiments, for example, Baik et al. (2010), Trickey et al. (2006) and Caille et al. (2002). During all experiments, the sphere position is monitored to assess that the sphere remains constrained during cell indentation. Consequently, all measured force data are corrected using the factors identified in Section 3.4.4.

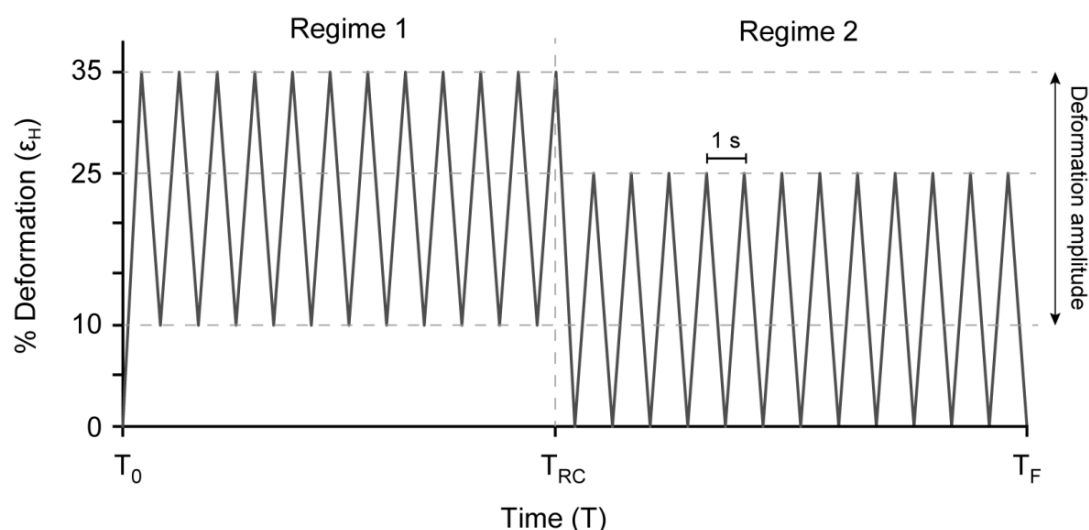


Figure 6.1: Graphical representation of the cyclic deformation experiment. The customised AFM setup is used to cyclically deform cells at a constant loading and unloading nominal strain rate at a frequency of 1.0 Hz. In loading regime 1 ( $0 \leq T < T_{RC}$ ), cells are cyclically deformed at  $10\% \leq \epsilon_H \leq 35\%$ . In loading regime 2 ( $T_{RC} \leq T \leq T_F$ ), cells are cyclically deformed at  $0\% \leq \epsilon_H \leq 25\%$ . Loading regime 1 starts at  $\epsilon_H = 0\%$  however force data collection began from  $\epsilon_H = 10\%$  of the first cycle.

#### 6.2.4 Data Analysis and Data Presentation

A change in cell height is calculated as the difference in contact point in force-displacement curves on the cell measured directly before and after a cyclic experiment. A change in surface position relative to the modified cantilever (surface drift) is calculated as the change in the contact point from force-displacement curves on glass measured directly before and after a cyclic experiment. It is found that the

thermal drift stabilisation technique presented in Chapter 5 successfully limited surface drift to values ranging from 0.02  $\mu\text{m}$  to 0.1  $\mu\text{m}$  in all experiments reported in the current chapter. This is within an acceptable range, resulting in a 0.3–1.4% error range in applied nominal cell deformation ( $\varepsilon_H$ ). Temporary lapses in thermal stabilisation of the system due to cell insertion and precise cantilever positioning over cells prior to experiments may have contributed to this small error in thermal drift stabilisation.

Plots of the maximum and minimum force as a function of time are constructed, as described in Section 5.5.2.3. The minimum force is taken as the force recorded at the start of each cycle and maximum force is taken as the force recorded at the end of the loading half of each cycle. Figure 6.2 highlights a number of force measurements and time points which are measured: (i) at the onset of cyclic deformation (measurements shown in blue) and; (ii) at the regime change (measurements shown in green).

- (i) At the onset of cyclic experiment ( $T_o$ ) the following is measured:
  - *Initial force*: Force measured for the 1<sup>st</sup> cycle of regime 1.
  - *Force reduction (60 cycles)*: Magnitude of the force reduction over the initial 60 cycles.
- (ii) At the regime change ( $T_{RC}$ ) the following is measured:
  - *Steady state 1*: Average force measured for the last 600 cycles prior to  $T_{RC}$ .
  - *Instantaneous force reduction*: Magnitude of the force reduction between the last cycle of regime 1 to the first cycle of regime 2.
  - *Force recovery*: Magnitude of the force increase from the first cycle of regime 2 until steady state 2 is reached.
  - *Time to steady state*: Time taken for the force recovery.
  - *Steady state 2*: Average force measured from the end of the force recovery to the 600<sup>th</sup> cycle of regime 2.
  - *Steady state force change*: Difference in measured force between steady state 1 and steady state 2.

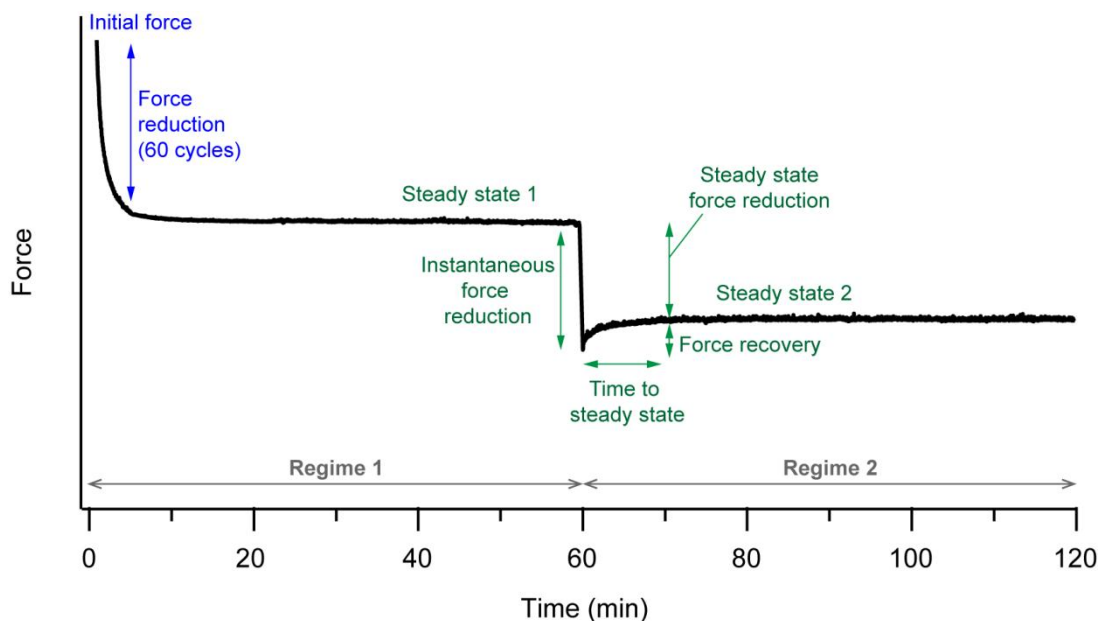


Figure 6.2: Sample cyclic force data highlighting the measurements taken at the onset of cyclic deformation (measurements in blue) and at the regime change,  $T_{RC}$  (measurements in green).

### 6.2.5 Statistical Analysis

Data is represented as the mean  $\pm$  sem of all samples within each group. One-way ANOVA tests are employed to determine statistical differences between the means of the three independent cell groups. The associated  $p$ -value is also determined in each case, and the null hypothesis rejected if  $p > 0.05$ . Statistically significant differences between the means of two cell groups are determined using the Tukey test. Significant differences between groups are indicated by  $*p < 0.01$ ,  $**p < 0.001$ ,  $***p < 0.0001$ .

## 6.3 Results

Morphological and mechanical cell response to applied cyclic deformation is presented in this section for the three cell groups: control cells, cyto-D cells and dead cells.

### 6.3.1 Cell Morphology Changes

Cell height was measured immediately before and after applied cyclic deformation. Figure 6.3 (a) shows the initial cell heights measured before the applied cyclic deformation for each cell group. The dead cells show the highest cell height

( $10.4 \pm 0.9 \mu\text{m}$ ) compared to the control cells ( $7.8 \pm 1.2 \mu\text{m}$ ) and cyto-D cells ( $8.6 \pm 1.9 \mu\text{m}$ ). However, there is no significant difference between the groups. In Chapter 4: Section 4.3.2, a significant difference is reported between control cells ( $6.3 \pm 0.8 \mu\text{m}$ ) and cyto-D cells ( $10.8 \pm 0.9 \mu\text{m}$ ). However, it is important to note that the cells tested in Chapter 4 are incubated for 24 hr prior to cyto-D treatment and height measurement. In this study, control and cyto-D cells are given a significantly reduced incubation time prior to testing (30 min for control cells, 60 min for cyto-D cells). This explains the lack of a significant difference between the groups. However, the trend of increased cell height following the inhibition of cell contractility by cyto-D is still observed for this reduced incubation time.

Figure 6.3 (b) shows that the cell height following the applied cyclic loading is found to be higher than the initial cell height by  $1.6 \pm 0.5 \mu\text{m}$  for the control cell group. In contrast, cell height decreases following applied cyclic loading by  $0.8 \pm 0.3 \mu\text{m}$  in the case of the cyto-D cells, and decreases by  $1.7 \pm 0.5 \mu\text{m}$  in the case of the dead cells. During sphere retraction at the end of experiments, it is observed that the control cells are adhered to the bottom of the sphere. Cell stretching during sphere retraction, due to adhesion to the bottom of the sphere, is most likely the cause of the increase in cell height for the control cells. A less significant level of adhesion may have also been present for the cyto-D and dead cells however the adhesion is insufficient to cause cell stretching during sphere retraction, hence the observed decrease in height. A clearer indication of cell adhesion can be observed from the minimum forces recorded during cyclic deformation, as will be discussed in Sections 6.3.2 and 6.3.4.

Figure 6.4 shows a representative example of a control ((a), (b)), cyto-D ((c), (d)) and dead cell ((e), (f)) observed directly before and after experiments. Further examples are shown in Appendix 6.A. Control cells appeared spread before the applied loading, and continued to spread slightly over the course of a cyclic deformation experiment. In comparison, cyto-D cells appeared spindly and less spread, with only minor morphology change between the start (c) and the end (d) of a cyclic deformation experiment. Dead cells appeared almost completely rounded with no morphology change observed between the start (e) and the end (f) of a cyclic

deformation experiment. These morphological changes, illustrated in Figure 6.4, are consistent with image sequences of cells recorded during experiments. It is important to note that only the results of cells that remained centred under the sphere during cyclic deformation experiments are reported in this study.

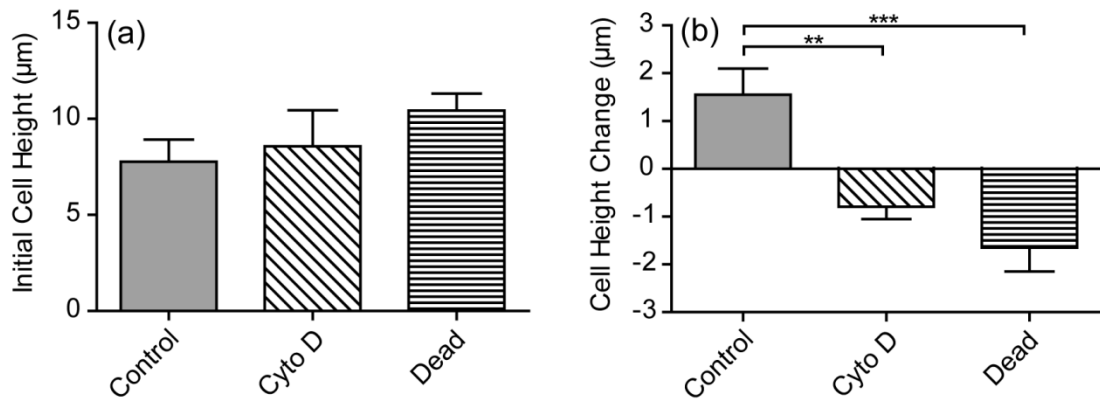


Figure 6.3: (a) Cell height measured for each cell group directly before cyclic deformation. (b) Cell height change between the initial height measured and the height measured directly after experiments.

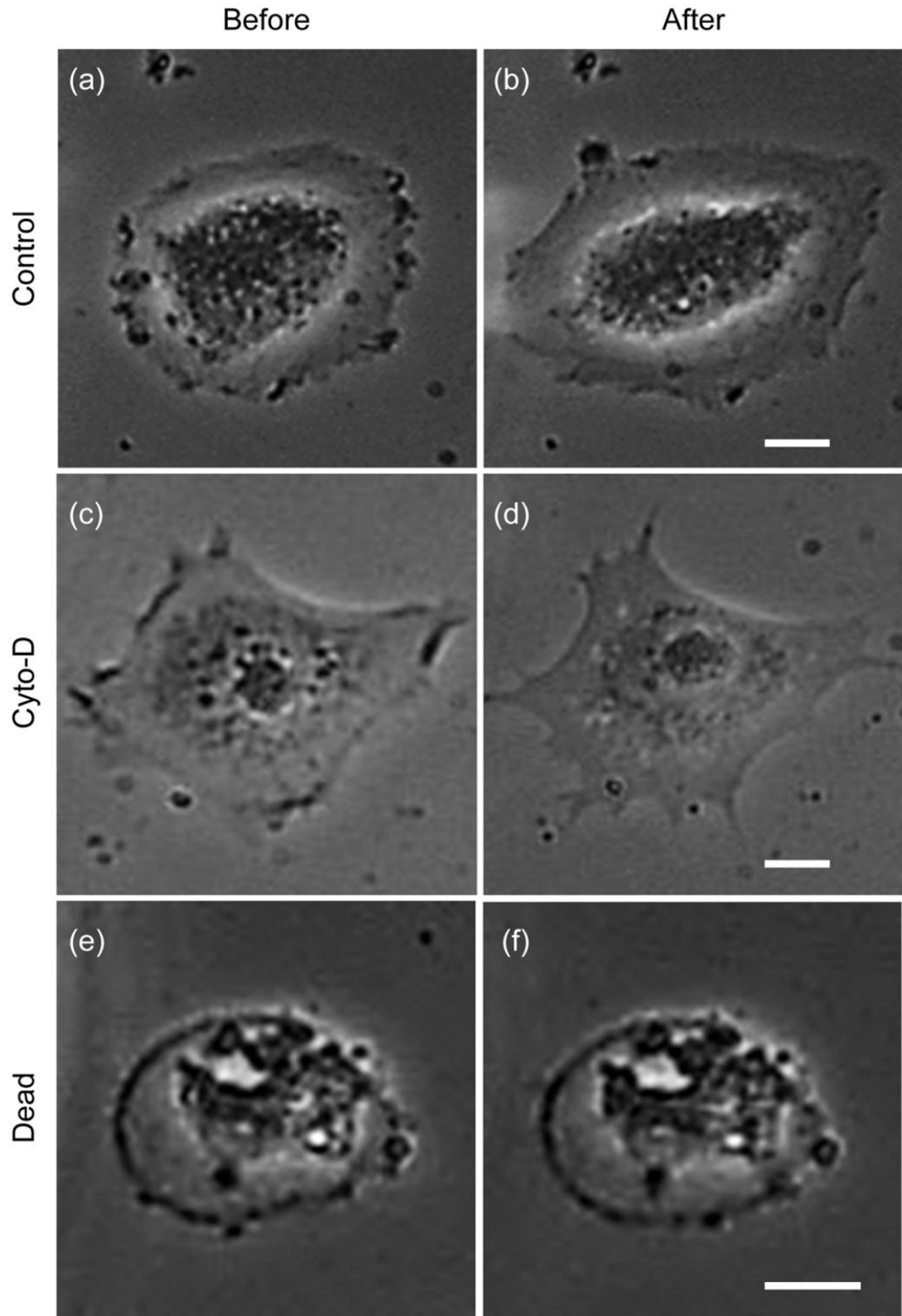


Figure 6.4: Phase contrast images of a representative cell from each cell group before (a, c, e) and after (b, d, f) cyclic deformation. Scale bar represents 10  $\mu\text{m}$ .

### 6.3.2 Effects of Cyclic Deformation over 120 min

In this section, the characteristic trends in the maximum and minimum forces recorded over the course of a cyclic deformation experiment are discussed. The forces recorded at the onset of cyclic deformation ( $T_0$ ), and at the regime change ( $T_{RC}$ ) are then examined in detail in Section 6.3.3 and Section 6.3.4, respectively.

Figure 6.5 shows a representative example of the (a) maximum and (b) minimum force recorded over 120 min for each cell group. Further examples of each cell group are provided in Appendix 6.B. A significant decrease in maximum and minimum force is observed at the onset of cyclic deformation for each cell group. The maximum and minimum force for the cyto-D (red) and dead (blue) cells subsequently stabilises to a steady state force, with only minor fluctuations in the steady state force for the cyto-D cells. However, significant fluctuations in the measured force during testing are typically observed for control cells (black), most prominently during the first 40–50 min of cyclic deformation. The fluctuations observed in the maximum force did not always correspond with the fluctuations observed for the minimum force. These fluctuations may be the result of a combination of factors including cell spreading, adhesion to the sphere and cell remodelling.

Figure 6.5 (a) shows that the pre-regime change steady state (steady state 1) maximum force, calculated as the average over the 600 cycles prior to  $T_{RC}$ , is highest for the control cells. The cyto-D and dead cells show a comparable lower steady state 1 maximum force. At  $T_{RC}$  (~60 min) a rapid decrease in maximum force occurs in all cases between the last cycle of regime 1 ( $\epsilon_H = 35\%$ ) and the first cycle of regime 2 ( $\epsilon_H = 25\%$ ). This is followed by a force recovery to a post-regime change steady state force (steady state 2). The instantaneous force drop and subsequent force recovery is most pronounced for the control cells. Dead cells showed the least recovery in maximum force.

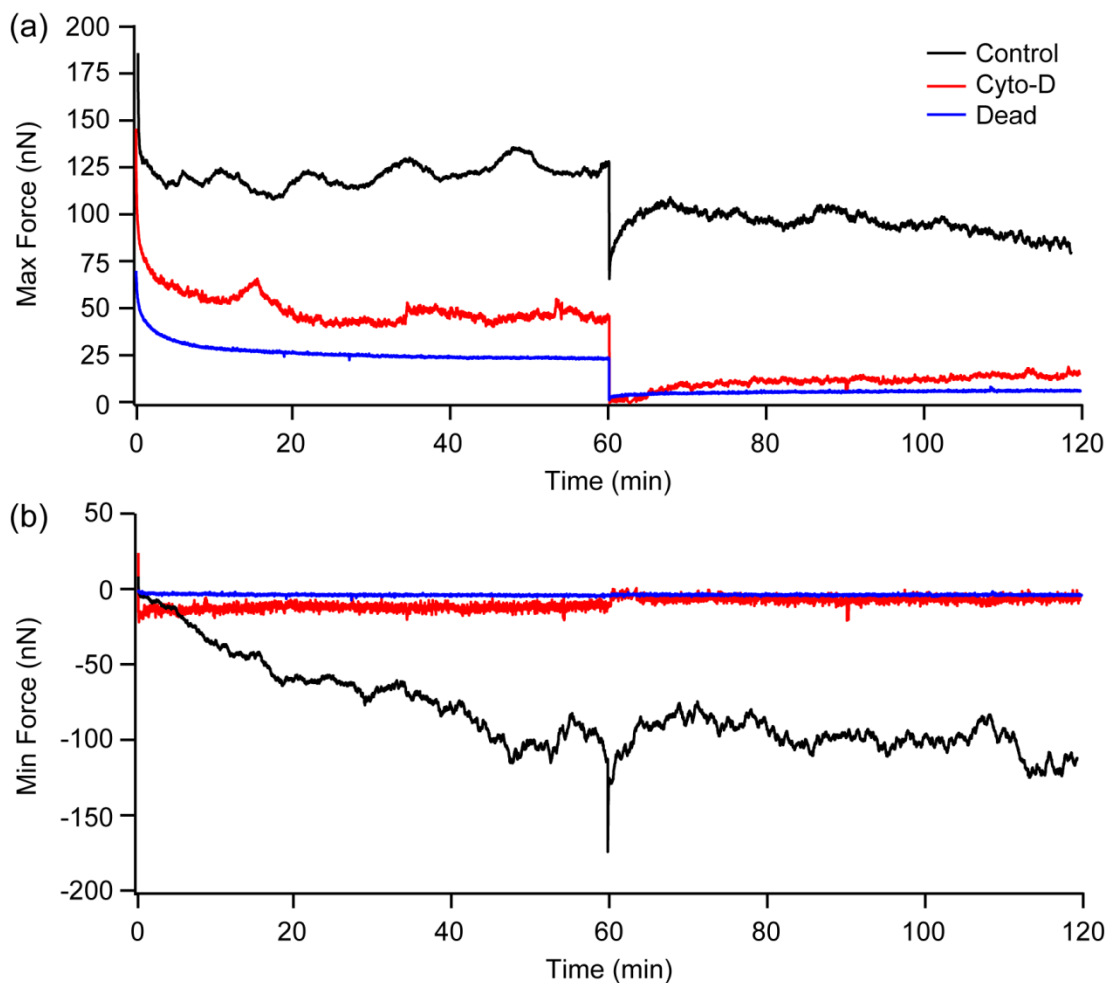


Figure 6.5: Representative examples of the (a) maximum and (b) minimum forces observed for a control (black), cyto-D (red) and dead (blue) cell over 120 min of cyclic deformation.

Figure 6.5 (b) shows that the steady state 1 minimum force is near zero for the dead cells throughout the cyclic deformation experiment. A slightly negative steady state is observed for the cyto-D cells. A negative minimum force indicates cell adhesion to the sphere, with cellular contractility applying a downwards (negative) force on the sphere. A strongly negative force is observed for the control cells, which may be attributed to cell spreading and high levels of cell contractility following adhesion to the bottom of the sphere. At  $T_{RC}$ , a rapid decrease and subsequent recovery in minimum force is observed for the control cells. This is in contrast to the cyto-D and dead cells, where no minimum force drop is observed. Instead a minor increase in the steady state force was typically observed for the cyto-D ( $n = 5$ ). No force change was observed for the dead cells. The steady state maximum and

minimum force remains relatively steady until  $T_F$ , with the control cells showing most fluctuations in the steady state force.

Figure 6.6 shows the force-deformation curves for a single loading cycle at 50 min (following 3000 cycles in regime 1), corresponding to the data shown in Figure 6.5 for each cell group. For each cell, the maximum force of the cycle is reached at the maximum deformation ( $\varepsilon_H = 35\%$ ). The maximum force is notably higher for the control cells than for the cyto-D cell (red) and the dead cell (blue). A slight hysteresis is observed during the unloading half of the cycle for each cell group. For the control cell (black), the curve begins at a strongly negative (downward) force, indicating the cell is pulling on the sphere. This tensile force decreases and becomes compressive approximately half way through the loading half-cycle. For the cyto-D cells (red), the curve begins as a weak negative force indicating a slight pulling on the sphere. No significant increase in force is observed until  $\varepsilon_H = \sim 25\%$  during the loading half-cycle. For the dead cell (blue), the near zero forces at the start of the cycle indicate the sphere may not initially be in contact with the cell. The rate of force increase with applied deformation is extremely low in comparison to control and cyto-D cells, with a maximum value of 26 nN being measured at the end of the loading half-cycle.

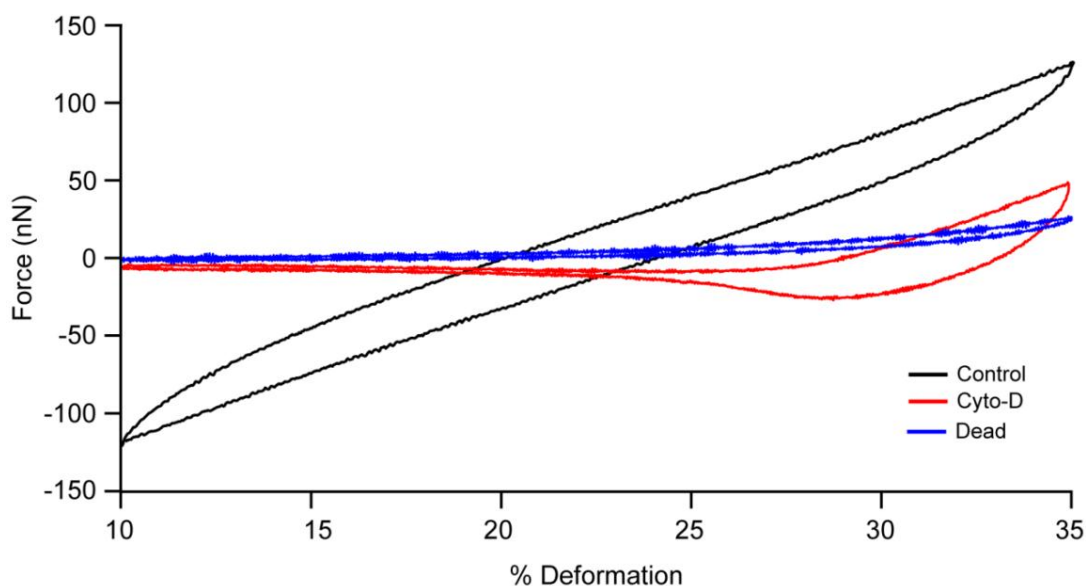


Figure 6.6: Force-displacement curves recorded at the beginning of steady state 1 ( $t = 50$  min) for the control cells (black), cyto-D cells (red) and dead cells (blue). Applied deformation is  $\varepsilon_H = 10\%$  to  $\varepsilon_H = 35\%$  within regime 1. These curves correspond to the data shown in Figure 6.5.

Data for a representative single experiment for each cell group is presented in this section (Section 6.3.2) to provide a broad introduction to the key features of the experimental results. A rigorous statistical treatment for the results for all experiments conducted will next be presented, focusing on cell behaviour during initial cycles in regime 1 (Section 6.3.3), and on cell behaviour in the vicinity of the regime change (Section 6.3.4).

### 6.3.3 Effects of Cyclic Deformation at $T_0$

In this section, the maximum recorded force values at the mid-point of a cycle and the minimum recorded force values at the end of a cycle are analysed for the initial phase of the regime 1 cyclic deformation. Results are examined in detail for control cell experiments, cyto-D cell experiments, and dead cell experiments.

Figure 6.7 shows representative maximum (top curves) and minimum (bottom curves) forces measured for the initial 60 cycles of cyclic deformation for each cell group. Further examples of such data are presented in Appendix 6.C. It is clearly observed that the force trends are comparable for each group. The initial maximum force (during the 1<sup>st</sup> cycle) is larger for the control cells than for the other two groups (Figure 6.8 (a)). However, no significant difference is observed between the groups. Furthermore, there is no significant difference between the groups in terms of the reduction in maximum force measured over the first 60 cycles of the cyclic deformation experiment (Figure 6.8 (b)).

Figure 6.9 (a) shows the initial minimum force recorded for each cell group. The initial minimum force (1<sup>st</sup> cycle) for the control cells is larger than that measured for the other two groups. However, once again no significant difference is observed. The reduction in minimum force during the first 60 cycles of the cyclic deformation experiment (Figure 6.9 (b)) is largest for the control cell, although there is again no significant difference between the three groups.

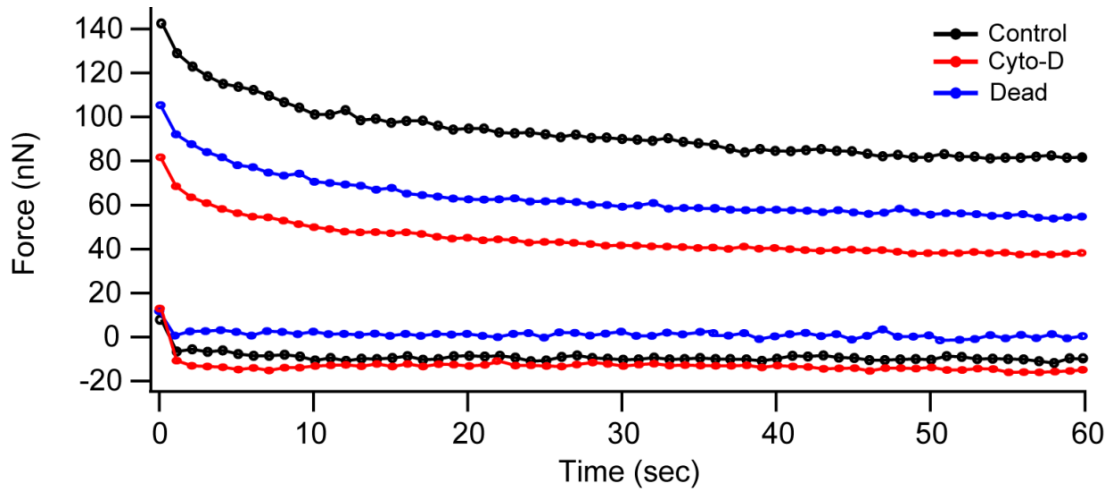


Figure 6.7: Representative maximum (top) and minimum (bottom) forces measured for the first minute (60 cycles) of cyclic deformation at  $T_0$  for a control cell (black), cyto-D cell (red) and dead cell (blue).

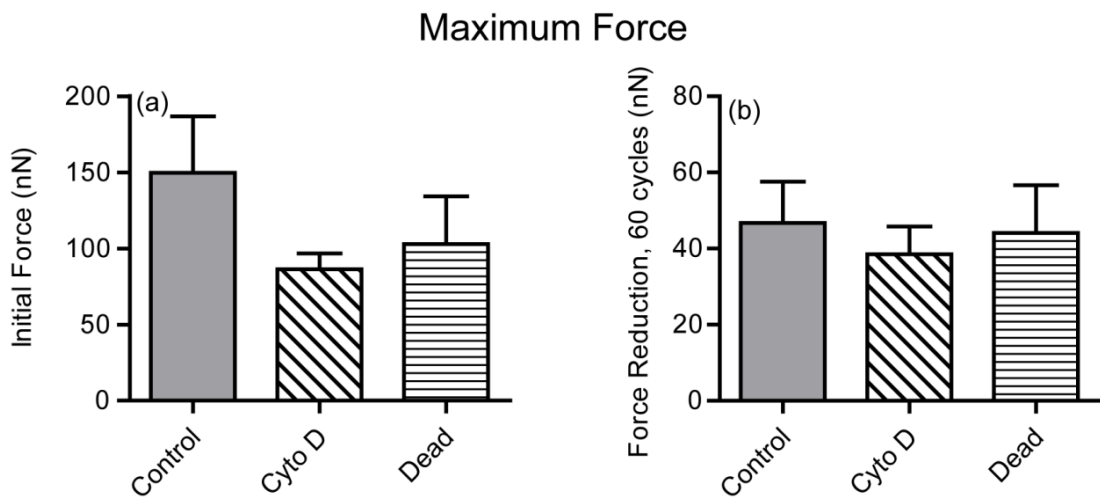


Figure 6.8: Maximum forces recorded at the initial phase of regime 1 for each cell group. (a) Maximum force measured for the first cycle of regime 1. (b) Magnitude of the reduction in maximum force over the first minute (60 cycles).

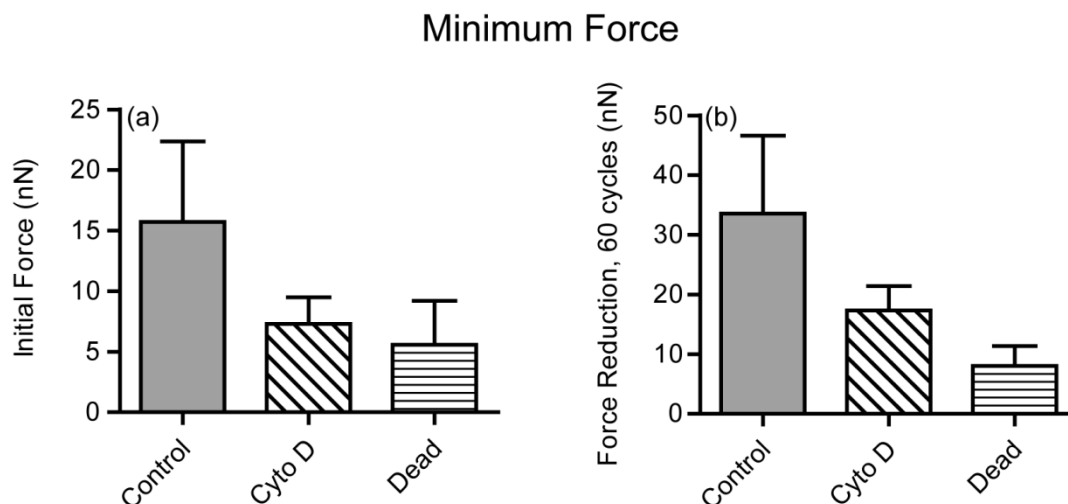


Figure 6.9: Minimum forces recorded at the initial phase of regime 1 for each cell group. (a) Minimum force measured for the first cycle of regime 1. (b) Magnitude of the reduction in minimum force over the first minute (60 cycles).

### 6.3.4 Effects of Cyclic Deformation at $T_{RC}$

A detailed examination of measured maximum and minimum forces during the final 600 cycles of regime 1 and during the first 600 cycles of regime 2 is presented in this section.

#### 6.3.4.1 Maximum and Minimum Force

Figure 10 (a-c) shows a representative example of the maximum (top curves) and minimum (bottom curves) forces recorded during the final 600 cycles of loading regime 1 and during the first 600 cycles of loading regime 2 for each cell group. Further examples of such single cell data are presented in Appendix 6.D. The pre-regime change steady state (steady state 1) maximum force is over 1.5 times higher for the control cells (Figure 10 (a); top curve) than for the cyto-D cells (Figure 10 (b); top curve) and the dead cells (Figure 10 (c); top curve). At  $T_{RC}$ , a significant rapid decrease in maximum force occurs in all cases between the last cycle of regime 1 ( $\epsilon_H = 35\%$ ) and the first cycle of regime 2 ( $\epsilon_H = 25\%$ ). This is followed by a force recovery to a post-regime change steady state force (steady state 2) in all cases. The instantaneous force drop and subsequent force recovery is most pronounced for the control cells. Dead cells showed the least recovery in maximum force. A statistical comparison of the steady state maximum forces in regime 1 and regime 2 shows that

there is no statistical difference between the forces for the control cell group. However, a statistical difference between the steady state maximum forces is measured for the cyto-D cell group ( $p < 0.001$ ) and dead cell group ( $p < 0.01$ ).

The steady state 1 minimum force is near zero for the dead cells throughout the cyclic deformation experiment (Figure 6.5 (c); bottom curve). A slightly negative (downward) steady state minimum force is observed for the cyto-D cells (Figure 6.5 (a); bottom curve). A strongly negative steady state minimum force is observed for the control cells, which may be attributed to cell spreading and high levels of cell contractility following adhesion to the bottom of the sphere. At  $T_{RC}$ , a rapid decrease and subsequent recovery in minimum force is observed for the control cells. This is in contrast to the cyto-D and dead cells, where no minimum force drop is observed. Instead, a small increase in the steady state force was typically observed for the cyto-D. No force change was observed for the dead cells.

Within this region of interest, data are compared for each group ( $n = 7$ ), with detailed analysis of the maximum and minimum forces being presented in Figure 6.11 and Figure 6.12, respectively. Figure 6.11 (a) shows that the steady state 1 force is larger for the control cells ( $78.1 \pm 19.9$  nN) than for the cyto-D cells and dead cells, which have steady state 1 forces of only  $41.3 \pm 7.7$  nN and  $41.6 \pm 11.6$  nN, respectively. The steady state 2 force (Figure 6.11 (b)) is significantly larger for the control cells ( $61.6 \pm 15.0$  nN) than for the other two groups, which have steady state force of  $15.7 \pm 4.9$  nN (cyto-D) and  $17.4 \pm 4.8$  nN (dead). Lower fluctuations in the steady state forces were observed for the dead cells compared to the control cells and cyto-D cells. The control cells show the lowest reduction in the steady state force (steady state 1 - steady state 2) ( $16.5 \pm 7.9$  nN), compared to the cyto-D ( $25.6 \pm 5.5$  nN) and dead cells ( $24.2 \pm 7.2$  nN). The similar steady state force reduction between the cyto-D cells and the dead cells should be noted. Therefore, the percentage change in steady state force is approximately three times larger for the cyto-D ( $63.0 \pm 6.7\%$ ) and dead ( $60.0 \pm 5.3\%$ ) than for the control cells ( $18.9 \pm 7.8\%$ ), see Appendix 6.E.

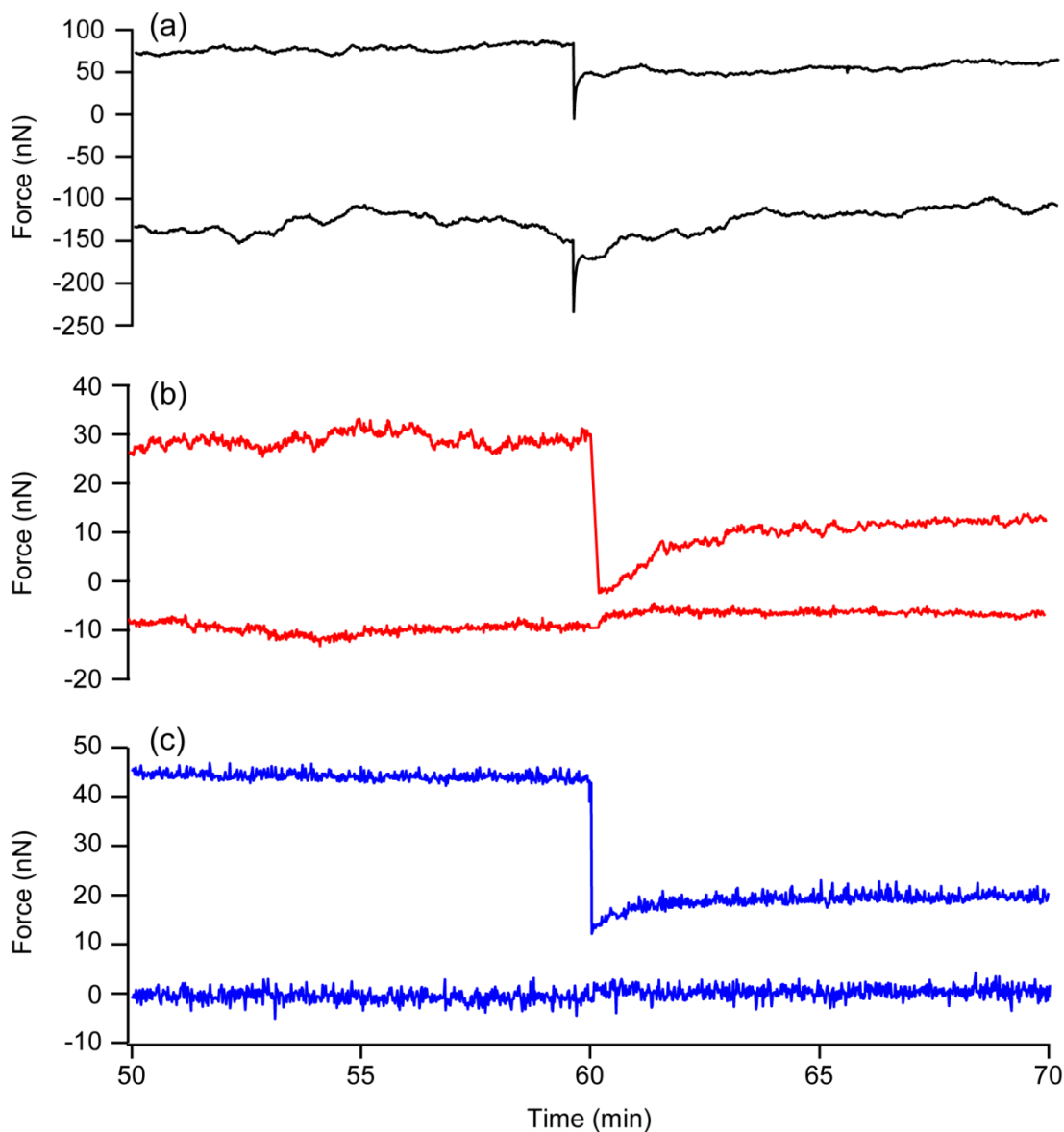


Figure 6.10: Representative maximum (top) and minimum (bottom) forces measured at the regime change for a (a) control cell (black), (b) cyto-D cell (red) and (c) dead cell (blue).

Figure 6.10 shows that at  $T_{RC}$  (60 min) an instantaneous reduction in maximum force is observed for each cell group (maximum force in cycle 3600 - maximum force in cycle 3601). The magnitude of the instantaneous force reduction (Figure 6.11 (d)) for the control cells ( $56.7 \pm 15.5$  nN) is greater than that observed for the cyto-D cells ( $36.3 \pm 6.2$ ), and is twice that observed for the dead cells ( $28.6 \pm 9.3$  nN). However, the subsequent force recovery to a steady state is found to be significantly larger for the control cells ( $40.2 \pm 8.8$  nN) compared to the cyto-D ( $10.7 \pm 1.9$  nN) and dead cells ( $4.3 \pm 2.1$  nN). In fact, the control cell force recovery is 4

fold larger than that of the cyto-D cells and 10-fold larger than that of the dead cells. The times recorded for force recovery showed no apparent trend between the groups (Figure 6.11 (f)).

Figure 6.12 (a) shows that the steady state 1 minimum force for the control cells is significantly more negative ( $-70.5 \pm 24.5$  nN) than the minimum force reported for the cyto-D cells ( $-11.9 \pm 5.1$  nN). The steady state 1 minimum force for the dead cells is approximately zero ( $-0.3 \pm 0.8$  nN). A negative minimum force indicates cell adhesion to the sphere. The strongly negative force observed for the control cells may be attributed to high levels of cell contractility, in tandem with cell spreading during the experiment, both of which will result in a significant negative (downwards) force on the sphere at the end of each cycle. Similar minimum force values are recorded for the control cells for steady state 2, following the regime change (Figure 6.12 (b)). The steady state force reductions (Figure 6.12 (c)) were small for all groups in comparison to the steady state force reduction in maximum force (Figure 6.11 (c)), with no significant difference between the cell groups. The minimum force reduces by  $1.5 \pm 2.9$  nN in the case of the control cells. However, the force increases for the cyto-D cells ( $2.4 \pm 0.6$  nN) and dead cells ( $0.3 \pm 0.7$  nN). A significant instantaneous minimum force reduction (Figure 6.12 (d)) and force recovery (Figure 6.12 (e)) is observed for the control cells compared to the other two groups. The cyto-D and dead cells exhibited only a slight force change. The times recorded for force recovery (Figure 6.12 (f)) showed no apparent trend between the groups, as also observed for the maximum forces in Figure 6.11 (f).

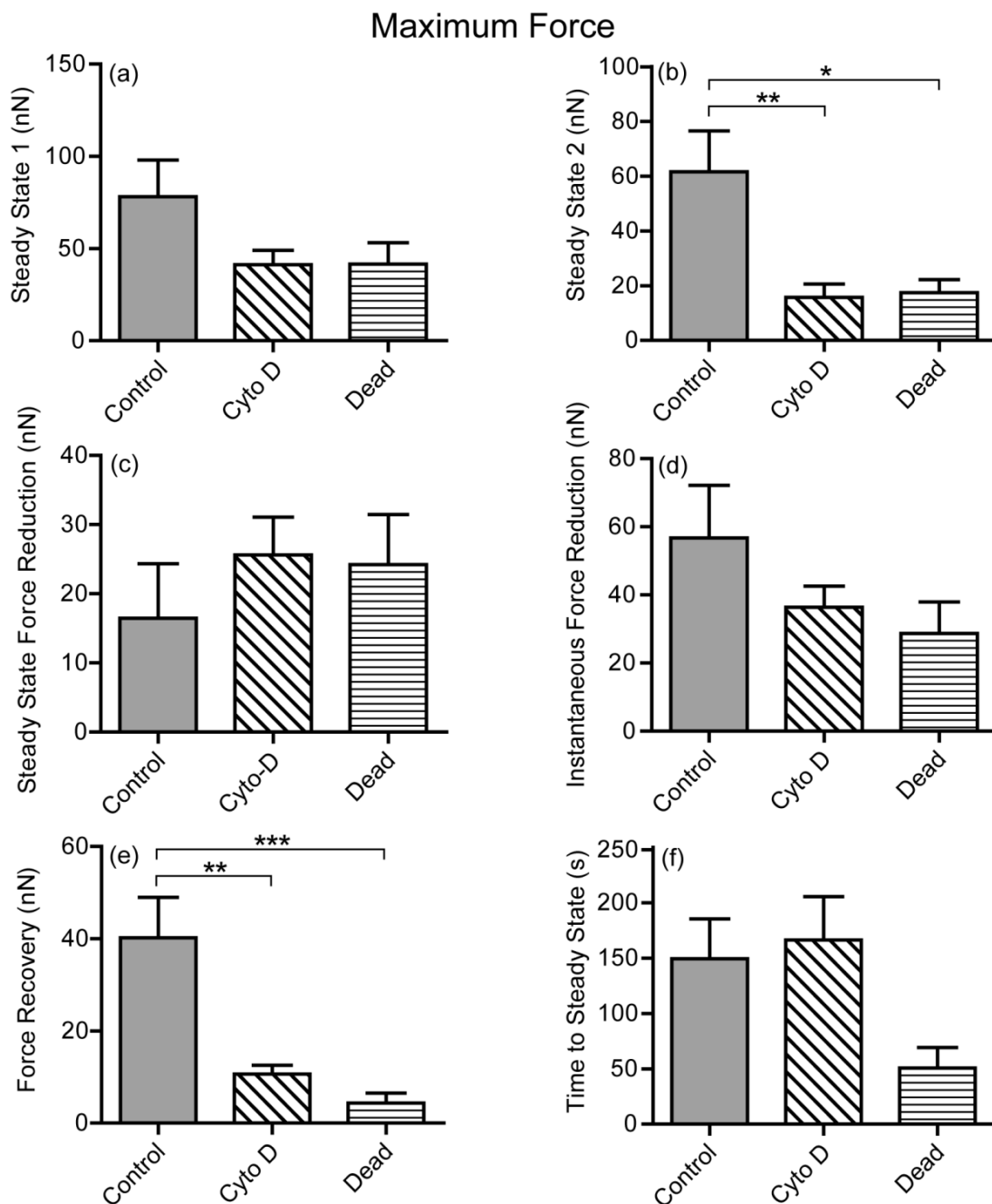


Figure 6.11: Maximum forces recorded for each cell group at the regime change region. (a) Steady state 1 and (b) steady state 2 are the force measured over the last 10 min of regime 1 and 10 min post force recovery in regime 2, respectively. (c) is the reduction in the steady state force between steady state 1 and steady state 2. (d) is the magnitude of the instantaneous reduction in maximum force between the last cycle of regime 1 and first cycle of regime 2. (e) is the recovery in maximum force from the first cycle of regime 2 until steady state 2 is reached. (f) is the time taken for the force recovery.

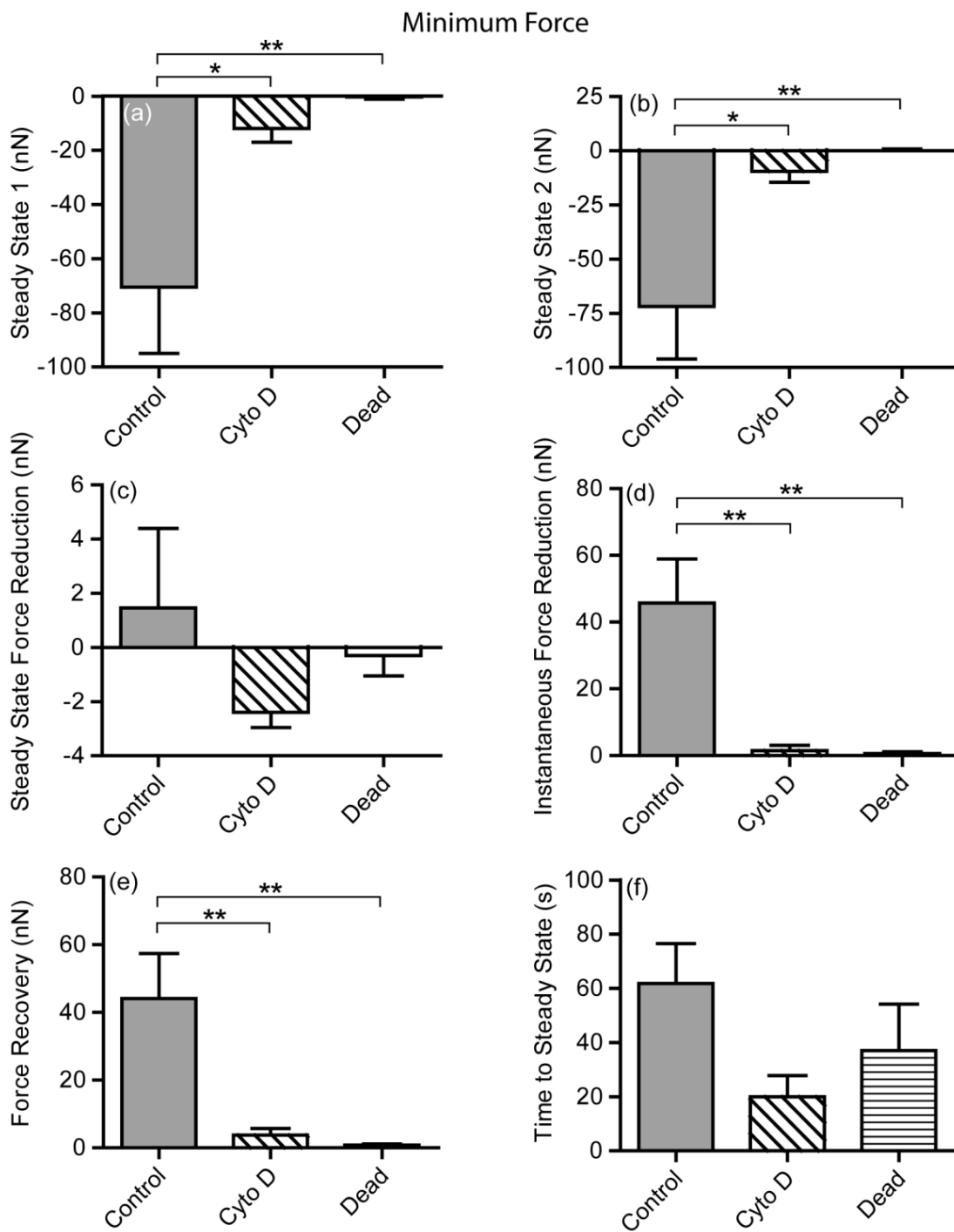


Figure 6.12: Minimum forces recorded for each cell group at the regime change region. (a) Steady state 1 and (b) steady state 2 are the force measured over the last 10 min of regime 1 and 10 min post force recovery in regime 2, respectively. (c) is the reduction in the steady state force between steady state 1 and steady state 2. (d) is the magnitude of the instantaneous reduction in minimum force between the last cycle of regime 1 and first cycle of regime 2. (e) is the recovery in minimum force from the first cycle of regime 2 until steady state 2 is reached. (f) is the time taken for the force recovery.

### 6.3.4.2 Force-Deformation Curves

Force-deformation curves measured for loading cycles at four distinct time points are shown in Figure 6.13 (a), (c), (e). The cycles shown are at the following time points: 600 cycles before the regime change ( $T_{RC}$ ) ( $T = 50$  min) (green); one cycle before  $T_{RC}$  ( $T = 59$  min 59 s) (black); one cycle after  $T_{RC}$  ( $T = 60$  min 1 s) (red); and 600 cycles after  $T_{RC}$  ( $T = 70$  min) (blue). Again, this data is presented for a single representative cell for each cell group, corresponding to the single cell data previously presented in Figure 6.12. Additional single cell data is presented in Appendix 6.F. For all cell groups, the force-deformation curves for the 600<sup>th</sup> cycle before  $T_{RC}$  (green) and last cycle before  $T_{RC}$  (black) are very similar, indicating that the cell reaction forces are at a steady state (steady state 1) during this 10 min time period.

Figure 6.13 (a) shows that, for the control cells, each cycle begins at a negative force, with the cell pulling down strongly on the sphere. The increase in negative force between the cycle immediately before  $T_{RC}$  (in which the minimum deformation is 10%) (black) and the cycle immediately after  $T_{RC}$  (in which the minimum deformation is 0%) (red), indicates that the adhered cell pulls strongly on the sphere, exerting a downwards (negative) force. In the 600 cycles following  $T_{RC}$ , a significant recovery of the measured forces is observed and the cycle resembles the steady state forces measured prior to  $T_{RC}$ . In order to directly compare the steady state force cycles before (green) and after  $T_{RC}$  (blue), the deformation axis is shifted for the cycle before (green) in Figure 6.13 (b), with force being plotted against relative deformation (where relative deformation is defined as the current deformation minus the deformation at the start of the loading cycle).

Figure 6.13 (c) shows a near zero baseline force in each force-deformation cycle for the cyto-D cells. This indicates that the cell did not exert a significant downwards force on the sphere, as contractility was inhibited in cyto-D cells. Indeed it may suggest that the cell was not in continuous contact with the sphere for the entire duration of each cycle. In the case of the force-deformation curves 600 cycles prior to  $T_{RC}$  (green) and one cycle prior to  $T_{RC}$  (black) (the maximum deformation is

$\varepsilon_H = 35\%$  in both cases), the most significant period of contact occurs after 25% deformation for each cycle. There is a significant reduction in the maximum force between the cycle immediately before (black) and cycle immediately after (red)  $T_{RC}$ , although there is no change in the minimum force over this same period. In the subsequent 600 cycles, contact increases with the cell but the measured force values do not recover to those observed prior to  $T_{RC}$ . This is highlighted in Figure 6.13 (d).

For the dead cell (Figure 6.13 (e)), the sphere appears to be in contact with the cell at all times prior to  $T_{RC}$ . Between the cycle immediately before (black) and cycle immediately after (red)  $T_{RC}$ , there is a decrease in cell contact area and drop in maximum force. The minimum force appears unchanged. In the case of the force-deformation curve 600 cycles after  $T_{RC}$ , the cell seems to remain in continuous contact with the sphere as a non-zero maximum force is recorded for all deformation levels. However the maximum force does not recover to its pre-regime change (steady state 1) value, as indicated by the superimposed cycles in Figure 6.13 (f). In general, hysteresis (indicated by reduced forces in the unloading half of a cycle) is minimal for the dead cells compared to the control cells and cyto-D cells.

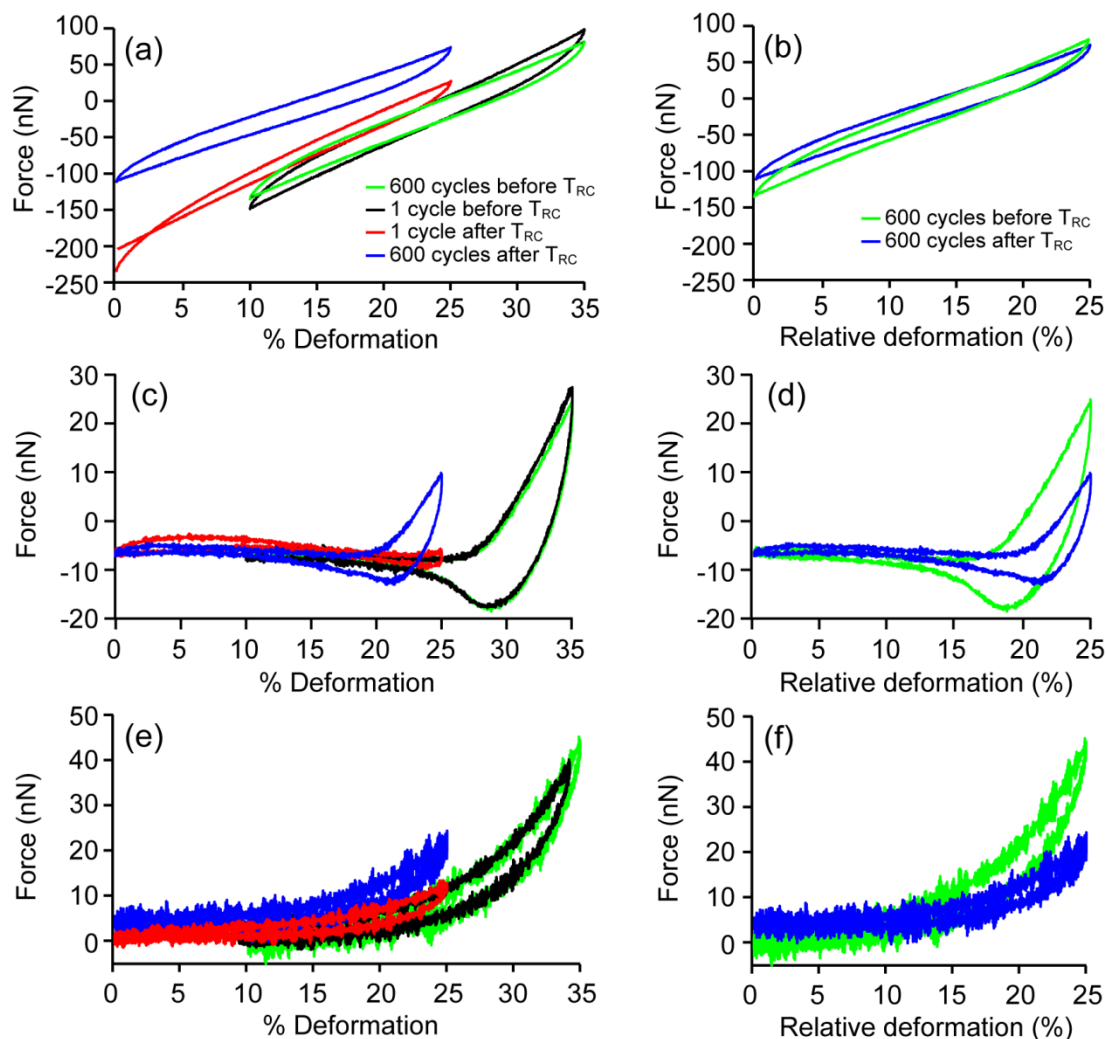


Figure 6.13: Representative force-deformation cycles within 600 cycles before and after TRC for a control (a, b), cyto-D (c, d) and dead (e, f) cell. The cycles shown in (a, c, e) correspond to the 600<sup>th</sup> cycle before (green), the cycle before (black), the cycle after (red), and 600<sup>th</sup> cycle after (blue) TRC. The curves shown in (b, d, f) are the 600<sup>th</sup> cycle before (green) and after (blue) TRC superimposed on each other with a relative % deformation. The force-deformation cycles shown correspond to the data shown in Figure 6.10.

## 6.4 Discussion

Whole cell cyclic deformation is successfully achieved using the stabilised AFM setup on three cell groups; control cells, cyto-D cells and dead cells. The forces measured for the control cells are dramatically different from those measured for the cyto-D and dead cells, indicating that the contractile actin cytoskeleton plays a critical role in the response of cells to dynamic loading. The key points of the study are as follows:

- (i) Following a shift in deformation range (from  $10\% \leq \varepsilon_H \leq 35\%$  to  $0\% \leq \varepsilon_H \leq 25\%$ .) at  $T_{RC}$ , while maintaining a constant loading and unloading strain rate, the maximum force recovers to 81% of the steady state force in the case of control cells. In contrast, cyto-D cells and dead cells recover to 37% and 40% of the steady state force, respectively.
- (ii) At steady state, control cells exhibit strongly negative (downwards) forces at the start of each cycle. In contrast, negative forces measured for cyto-D cells are 7-fold lower. Negligible forces are measured for dead cells at the start of each cycle.
- (iii) The trend in initial force reduction is comparable for all cell groups.

As outlined in key point (i) above, following the regime change, the control cells recover to 81% of their steady state maximum force. In fact, it is shown that the steady state force versus relative deformation curves are extremely similar before and after the regime change. This recovery in steady state force shows that, for control cells, which have an active contractile actin cytoskeleton, cell behaviour is primarily determined by the applied strain rate, with changes in the deformation magnitude (deformation range) having only secondary effects. The slight steady state force reduction in regime 2 is attributed to changes in the passive elastic stresses in the cell due to the change in the range of deformation. However, the remarkable similarity between the steady state behaviour in regime 1 and regime 2 suggests that if strain rate is not altered the steady state cell force remains largely unchanged, despite a change in applied deformation range. In contrast, for cyto-D cells, where the actin cytoskeleton is disrupted, the steady state force-relative deformation curves for regime 2 are very different to those of regime 1. This demonstrates that the dominant strain rate response of cell force observed for contractile control cells is not evident for passive cells, where the steady state response is primarily governed by the deformation magnitude. Steady state maximum forces in regime 1 are approximately 2-fold higher than in regime 2 for cyto-D cells. Similarly for the dead cells, which also are not actively contractile, the applied strain magnitude again dominates the

cell force, as opposed to the strain rate. These findings strongly suggest that (i) the force response is provided by the actin cytoskeleton and (ii) the active forces generated by the actin cytoskeleton are significantly higher than the strain magnitude dependent passive forces in osteoblasts.

Although only one strain rate is tested in this Chapter, the results suggest that the mechanical behaviour of contractile cells may be strain rate dependent. However, further experiments in which different strain rates are tested must be performed in order to validate this suggestion. The findings of Mitrossilis et al. (2009), in which an isolated myoblast were seeded between a rigid plate and a flexible cantilever, suggests that the actively generated tension of the actin cytoskeleton is dependent on strain rate. Interestingly, the macro-scale experiment study by Wille et al. (2006) also reports a significant strain rate dependence of the active forces generated by the actin cytoskeleton. A population of fibroblast cells were seeded in collagen scaffolds and cyclically stretched at constant strain rates. The active contribution of the cells was isolated and it was demonstrated that lower strain rates resulted in higher steady state forces following several hours of cyclic deformation. Although, a significant strain rate effect was demonstrated in the study by Wille et al. (2006), collagen remodelling and other factors may have contributed to the results of this study. Importantly, the contribution of extra-cellular factors is not a concern in the current study since single isolated cells are tested.

Strongly negative minimum forces are measured for the control cells. This negative (downward) force indicates that a cell is adhered to, and pulling on the bottom of the sphere. This negative force has two possible contributions: (i) if cell spreading occurs during the experiment and the cell remains adhered to the sphere, stretching of the spread cell between the substrate and the sphere at the end of each cycle will result in a passive force contribution due to the elasticity of the cell. (ii) In addition to this passive elastic force, the actin cytoskeleton of the cell will generate active contractile forces that will also pull downwards on the sphere. Only the former mechanism can contribute to the negative forces measured for cyto-D cells, whereas both mechanisms contribute for control cells. As the negative forces are ~7-fold higher for control cells, this suggests that the active contractile forces generated by

the actin cytoskeleton are more dominant than the passive elastic forces that result from cell spreading during the experiment. However, it is also possible that control cells may have spread more than cyto-D cells, but it is not possible to accurately measure the height change during the experiment as removal of the sphere from the control cells at the end of applied cyclic deformation results in significant deformation of the cell morphology due to strong cell adhesion to the sphere. It is highly unlikely that the ~7-fold difference in negative forces can be explained in terms of spreading and elastic deformation, suggesting the important role of the actin cytoskeleton in the force generation of cells. For the dead cells, the minimum forces recorded at the start of each cycle are approximately zero. Previous studies have investigated cell contractility by statically holding (Mitrossilis et al. (2009), Chaudhuri et al. (2009)) or stretching a cell between two surfaces (Micoulet et al. (2005), Thoumine and Ott (1997)) and monitoring the reaction force. In the study by Thoumine and Ott (1997), control cells and cyto-D cells were statically stretched between two plates. It was found that the reaction force due to the elastic deformation of the cyto-D cells was ~6-fold lower than the reaction force generated by stretching of the control cells. Similarly, in the current study measured negative forces at the end of each loading cycle are ~7-fold higher for control cells than for cyto-D cells. Similar trends are also reported in the study of Watanabe-Nakayama et al. (2011).

In the case of control cells, the initial maximum force during the first cycle (~150 nN) is similar to that measured in the monotonic deformation experiments of Chapter 4: Section 4.3.3 (~168 nN at  $\varepsilon_H = 35\%$ ). In both studies a similar trend is observed following the addition of cyto-D, whereby the maximum forces are significantly reduced. As discussed in Chapter 4, this is attributed to the significant contribution of the actin cytoskeleton to the resistance of cells to compressive deformation. During the early stages of loading regime 1 (cycles 1 to 60), a rapid reduction in both maximum and minimum force is measured for all three cell groups, with the magnitude of force reduction being similar in all cases. Also, the time taken for the maximum force reduction (~20-30 s) and the minimum force reduction (~2-3 s) is similar for each group. Such a reduction in force with deformation controlled

cyclic loading is characteristic of a viscoelastic material response. In the case of all three cell groups, viscoelastic stress relaxation is most apparent in the early cycles. However, the gradual increase in force to a steady state following the regime change is also characteristic of viscoelastic behaviour. A study by Thoumine and Ott (1997) reports a similar viscoelastic response for isolated fibroblasts subjected to stress relaxation tests. In addition, the viscoelastic characteristics found in the current study are in general agreement with other studies investigating cellular viscoelasticity (Thoumine and Ott (1997), Alcaraz et al. (2003), Peeters et al. (2005), Darling et al. (2006)).

The dead cell force data presented in this chapter exhibits no random fluctuations in any test, with measured data being highly repeatable. This confirms that the fluctuations observed for the control cells and cyto-D cells are exclusively due to cell activity and not to inaccuracies or instabilities in the experimental system, further supporting system validation presented in Chapter 5. Force data fluctuations are observed for the control cells ( $< 50$  nN), which occur most prominently over the first 40-50 min of cyclic loading. Only minor fluctuations are observed for the cyto-D cells, indicating that the actin cytoskeleton contributes to these fluctuations. Despite fluctuations during the initial phases of experiments, a steady state is achieved for 10 min prior to the regime change, and again following the regime change (as evidenced by the fact that the force-deformation curves 600 cycles prior to the regime change is identical to that 1 cycle before the regime change). Force data fluctuations are attributed to three possible interlinked contributions: (i) the area of adhesion between the cell and sphere is changing, (ii) the cell is remodelling to adapt to the cyclic loading, and (iii) the cell is spreading on the substrate. Previous studies in which an isolated cell was statically held between two surfaces have also reported an unstable response in the measured force, particularly over the first ~40 min (Thoumine and Ott (1997), Micoulet et al. (2005), Fernández et al. (2006)). However, it is highly likely that the microplate systems used in these studies cannot obtain an accurate measure of the force fluctuations since force resolution with these systems, measured by video analysis of the plate deflection, is of a similar order (~1-10nN) to the level of force fluctuation observed in the current study.

The strain applied to bone *in vivo* is typically within the range of 400-3,000 microstrain, with a corresponding strain rate of approximately  $0.01-0.03 \text{ s}^{-1}$  (Schaffler et al. (1989), Yang et al. (2011)). However, these values of strain and strain rate do not necessarily translate to that experienced by individual bone cells within the tissue. The range of strains and strain rates applied to individual bone cells is yet to be fully elucidated. In this study, although the frequency (1 Hz) is physiologically relevant in terms of locomotion, the strains chosen ( $\epsilon_{H(\max)} = 35\%$  (regime 1) and  $25\%$  (regime 2)) are much larger than those predicted to occur in bone. Subsequently, the strain rate ( $0.5 \text{ s}^{-1}$ ) is also higher than that expected physiologically. The aim of this study was to investigate the biomechanical response of single cells to a change in strain magnitude, while maintaining a constant strain rate. Applying physiologically relevant strains ( $< 0.03\%$ ) on the cell would result in a negligible reaction force change at  $T_{RC}$ . Therefore, the strains in the two regimes and the magnitude of the strain change at  $T_{RC}$  were chosen such that a clear change in the forces (instantaneous force reduction) could be observed and the corresponding force recovery in reaction force to steady state 2 could be accurately measured. Furthermore, cyclic deformation is implemented for 60 min in each regime to ensure that a steady state force is obtained in both regimes. Such timeframes are based on previously reported cell remodelling time scale of 30-60 min under cyclic mechanical loading (Wille et al. (2006), Kaunas et al. (2005), Wang et al. (2001)).

In the current study, the spreading area of the cells could not be controlled. Control of cell spreading would potentially improve the repeatability of force measurement for control cells. Preliminary attempts to control cell spreading using micropatterning have been implemented, see Appendix 6.G. However, due to the pernickety and unreliable nature of micropatterning, it was not possible to introduce this feature into the complex experimental setup within the timeframe of the project. This important consideration should be addressed in future studies using this modified AFM system. Additionally, a secondary study should be performed in which the bottom of the sphere is functionalised to elucidate the effects of cell adhesion on the cell forces (Lehenkari et al. (2000), Hsiao et al. (2008)).

In the current study, the effects of whole cell cyclic deformation on single osteoblasts are reported for the first time. It is clearly demonstrated that the measured forces for the control cells are dramatically different from those measured for the cyto-D cells and dead cells, indicating that the contractile actin cytoskeleton plays a significant role in the response of cells to dynamic loading. The current study demonstrates that the measured force in control cells, which contain an actively contractile actin cytoskeleton, is primarily a function of the strain rate, with the strain range having only a secondary effect on measured forces. Such a response is not observed when the actin cytoskeleton is chemically disrupted.

## 6.5 References

- Ajubi, N. E., Klein-Nulend, J., Nijweide, P. J., Vrijheid-Lammers, T., Alblas, M. J. and Burger, E. H. (1996) Pulsating fluid flow increases prostaglandin production by cultured chicken osteocytes—a cytoskeleton-dependent process. *Biochemical and Biophysical Research Communications*. 225 (1), 62-68
- Alcaraz, J., Buscemi, L., Grabulosa, M., Trepap, X., Fabry, B., Farré, R. and Navajas, D. (2003) Microrheology of human lung epithelial cells measured by atomic force microscopy. 84 (3), 2071-2079
- Baik, A. D., Lu, X. L., Qiu, J., Huo, B., Hillman, E., Dong, C. and Guo, X. E. (2010) Quasi-3d cytoskeletal dynamics of osteocytes under fluid flow. *Biophysical Journal*. 99 (9), 2812-2820
- Balestrini, J. L. and Billiar, K. L. (2009) Magnitude and duration of stretch modulate fibroblast remodeling. *Journal of Biomechanical Engineering*. 131 (5), 51005
- Barron, V., Brougham, C., Coghlan, K., McLucas, E., O'Mahoney, D., Stenson-Cox, C. and McHugh, P. (2007) The effect of physiological cyclic stretch on the cell morphology, cell orientation and protein expression of endothelial cells. *Journal of Materials Science: Materials in Medicine*. 18 (10), 1973-1981
- Burr, D., Robling, A. and Turner, C. (2002) Effects of biomechanical stress on bones in animals. *Bone*. 30 (5), 781-786
- Caille, N., Thoumine, O., Tardy, Y. and Meister, J. J. (2002) Contribution of the nucleus to the mechanical properties of endothelial cells. *J. Biomech*. 35 (2), 177-187
- Campbell, J. J., Blain, E. J., Chowdhury, T. T. and Knight, M. M. (2007) Loading alters actin dynamics and up-regulates cofilin gene expression in chondrocytes. *Biochem Biophys Res Commun*. 361 (2), 329-34
- Chaudhuri, O., Parekh, S. H., Lam, W. A. and Fletcher, D. A. (2009) Combined atomic force microscopy and side-view optical imaging for mechanical studies of cells. *Nature methods*. 6 (5), 383-387
- Darling, E., Zauscher, S. and Guilak, F. (2006) Viscoelastic properties of zonal articular chondrocytes measured by atomic force microscopy. *Osteoarthritis and Cartilage*. 14 (6), 571-579
- Fernández, P., Pullarkat, P. A. and Ott, A. (2006) A master relation defines the nonlinear viscoelasticity of single fibroblasts. *Biophysical Journal*. 90 (10), 3796-3805
- Gabbay, J. S., Zuk, P. A., Tahernia, A., Askari, M., O'Hara, C. M., Karthikeyan, T., Azari, K., Hollinger, J. O. and Bradley, J. P. (2006) In vitro microdistraction

- of preosteoblasts: Distraction promotes proliferation and oscillation promotes differentiation. *Tissue engineering*. 12 (11), 3055-3065
- Hara, F., Fukuda, K., Asada, S., Matsukawa, M. and Hamanishi, C. (2001) Cyclic tensile stretch inhibition of nitric oxide release from osteoblast-like cells is both g protein and actin-dependent. *Journal of Orthopaedic Research*. 19 (1), 126-131
- Hsiao, S. C., Crow, A. K., Lam, W. A., Bertozzi, C. R., Fletcher, D. A. and Francis, M. B. (2008) DNA-coated afm cantilevers for the investigation of cell adhesion and the patterning of live cells. *Angewandte Chemie International Edition*. 47 (44), 8473-8477
- Hutmacher, D. W. (2000) Scaffolds in tissue engineering bone and cartilage. *Biomaterials*. 21 (24), 2529-2543
- Kaspar, D., Seidl, W., Neidlinger-Wilke, C., Beck, A., Claes, L. and Ignatius, A. (2002) Proliferation of human-derived osteoblast-like cells depends on the cycle number and frequency of uniaxial strain. *Journal of Biomechanics*. 35 (7), 873-880
- Kaunas, R., Nguyen, P., Usami, S. and Chien, S. (2005) Cooperative effects of rho and mechanical stretch on stress fiber organization. *Proc. Natl. Acad. Sci.* 102 (44), 15895-15900
- Knight, M. M., Toyoda, T., Lee, D. A. and Bader, D. L. (2006) Mechanical compression and hydrostatic pressure induce reversible changes in actin cytoskeletal organisation in chondrocytes in agarose. *J Biomech.* 39 (8), 1547-51
- Kurpinski, K., Chu, J., Hashi, C. and Li, S. (2006) Anisotropic mechanosensing by mesenchymal stem cells. *Proceedings of the National Academy of Sciences*. 103 (44), 16095-16100
- Lee, C. F., Haase, C., Deguchi, S. and Kaunas, R. (2010) Cyclic stretch-induced stress fiber dynamics - dependence on strain rate, rho-kinase and mlck. *Biochemical and Biophysical Research Communications*. 401 (3), 344-349
- Lehenkari, P. P., Charras, G. T., Nykänen, A. and Horton, M. A. (2000) Adapting atomic force microscopy for cell biology. *Ultramicroscopy*. 82 (1-4), 289-295
- Malone, A. M. D., Batra, N. N., Shivaram, G., Kwon, R. Y., You, L., Kim, C. H., Rodriguez, J., Jair, K. and Jacobs, C. R. (2007) The role of actin cytoskeleton in oscillatory fluid flow-induced signaling in mc3t3-e1 osteoblasts. *American Journal of Physiology - Cell Physiology*. 292 (5), C1830-C1836
- Micoulet, A., Spatz, J. P. and Ott, A. (2005) Mechanical response analysis and power generation by single-cell stretching. *ChemPhysChem*. 6 (4), 663-670

- Mitrossilis, D., Fouchard, J., Guirouy, A., Desprat, N., Rodriguez, N., Fabry, B. and Asnacios, A. (2009) Single-cell response to stiffness exhibits muscle-like behavior. *Proceedings of the National Academy of Sciences*. 106 (43), 18243-18248
- O'Cearbhaill, E. D., Punched, M. A., Murphy, M., Barry, F. P., McHugh, P. E. and Barron, V. (2008) Response of mesenchymal stem cells to the biomechanical environment of the endothelium on a flexible tubular silicone substrate. *Biomaterials*. 29 (11), 1610-1619
- Peeters, E. A. G., Oomens, C. W. J., Bouten, C. V. C., Bader, D. L. and Baaijens, F. P. T. (2005) Viscoelastic properties of single attached cells under compression. *J Biomech Eng*. 127 (2), 237-243
- Quinlan, A. M. T., Sierad, L. N., Capulli, A. K., Firstenberg, L. E. and Billiar, K. L. (2011) Combining dynamic stretch and tunable stiffness to probe cell mechanobiology in vitro. *PLoS One*. 6 (8), e23272
- Schaffler, M., Radin, E. and Burr, D. (1989) Mechanical and morphological effects of strain rate on fatigue of compact bone. *Bone*. 10 (3), 207-214
- Thorpe, S. D., Buckley, C. T., Vinardell, T., O'Brien, F. J., Campbell, V. A. and Kelly, D. J. (2008) Dynamic compression can inhibit chondrogenesis of mesenchymal stem cells. *Biochemical and Biophysical Research Communications*. 377 (2), 458-462
- Thorpe, S. D., Buckley, C. T., Vinardell, T., O'Brien, F. J., Campbell, V. A. and Kelly, D. J. (2010) The response of bone marrow-derived mesenchymal stem cells to dynamic compression following  $\text{tgf-}\beta\text{3}$  induced chondrogenic differentiation. *Annals of biomedical engineering*. 38 (9), 2896-2909
- Thoumine, O. and Ott, A. (1997) Time scale dependent viscoelastic and contractile regimes in fibroblasts probed by microplate manipulation. *J Cell Sci*. 110 (17), 2109-2116
- Trickey, W. R., Baaijens, F. P. T., Laursen, T. A., Alexopoulos, L. G. and Guilak, F. (2006) Determination of the poisson's ratio of the cell: Recovery properties of chondrocytes after release from complete micropipette aspiration. *Journal of Biomechanics*. 39 (1), 78-87
- Wang, J. H. C., Goldschmidt-Clermont, P., Wille, J. and Yin, F. C. P. (2001) Specificity of endothelial cell reorientation in response to cyclic mechanical stretching. *J. Biomech*. 34 (12), 1563-1572
- Watanabe-Nakayama, T., Machida, S., Harada, I., Sekiguchi, H., Afrin, R. and Ikai, A. (2011) Direct detection of cellular adaptation to local cyclic stretching at the single cell level by atomic force microscopy. *Biophys. J*. 100 (3), 564-572

- Wille, J. J., Elson, E. L. and Okamoto, R. J. (2006) Cellular and matrix mechanics of bioartificial tissues during continuous cyclic stretch. *Ann. Biomed. Eng.* 34 (11), 1678-1690
- Yang, P., Bruggemann, G. and Rittweger, J. (2011) What do we currently know from in vivo bone strain measurements in humans. *J Musculoskelet Neuronal Interact.* 11 (1), 8-20
- You, J., Yellowley, C., Donahue, H., Zhang, Y., Chen, Q. and Jacobs, C. (2000) Substrate deformation levels associated with routine physical activity are less stimulatory to bone cells relative to loading-induced oscillatory fluid flow. *Journal of Biomechanical Engineering.* 122 (4), 387

## 6.6 Appendix

### 6.A Images of Cells Before and After Cyclic Deformation

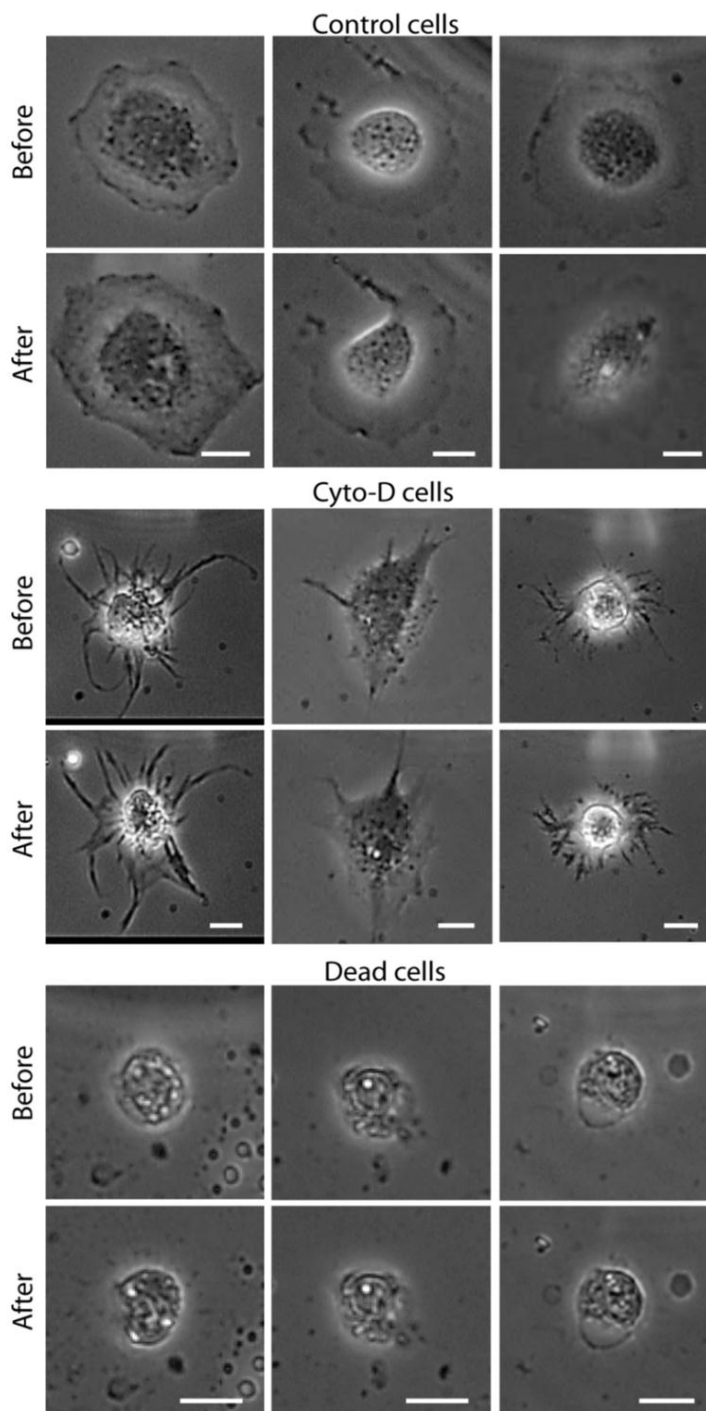


Figure 6-A: Phase contrast images of control (top), cyto-D (middle) and dead cells (bottom). Images were taken immediately before (top row) and immediately after (bottom row) cyclic deformation. Scale bar is 10  $\mu\text{m}$ .

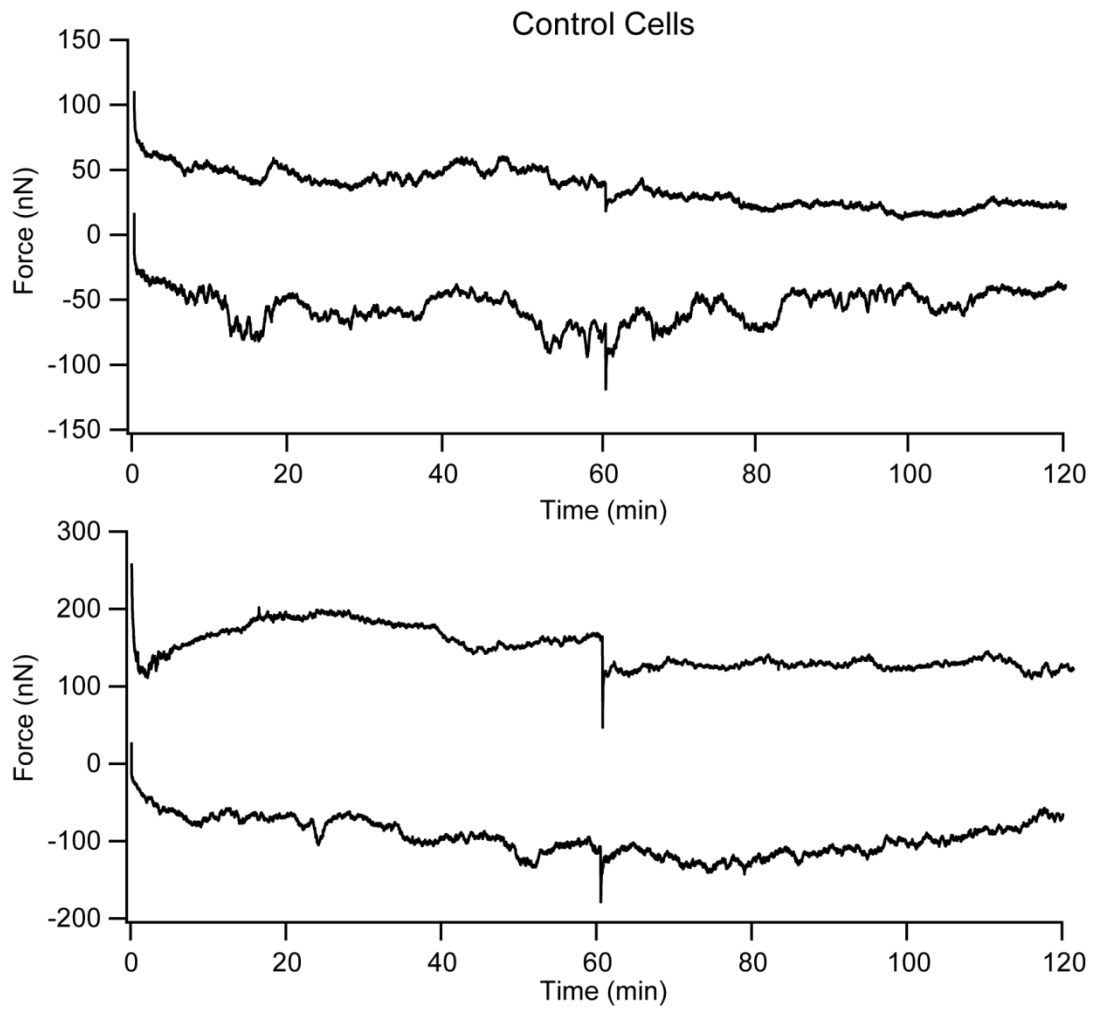
**6.B Effects of Cyclic Deformation over 120 min**

Figure 6-B: Further examples of the maximum and minimum forces observed for control cells over 120 min of cyclic deformation.

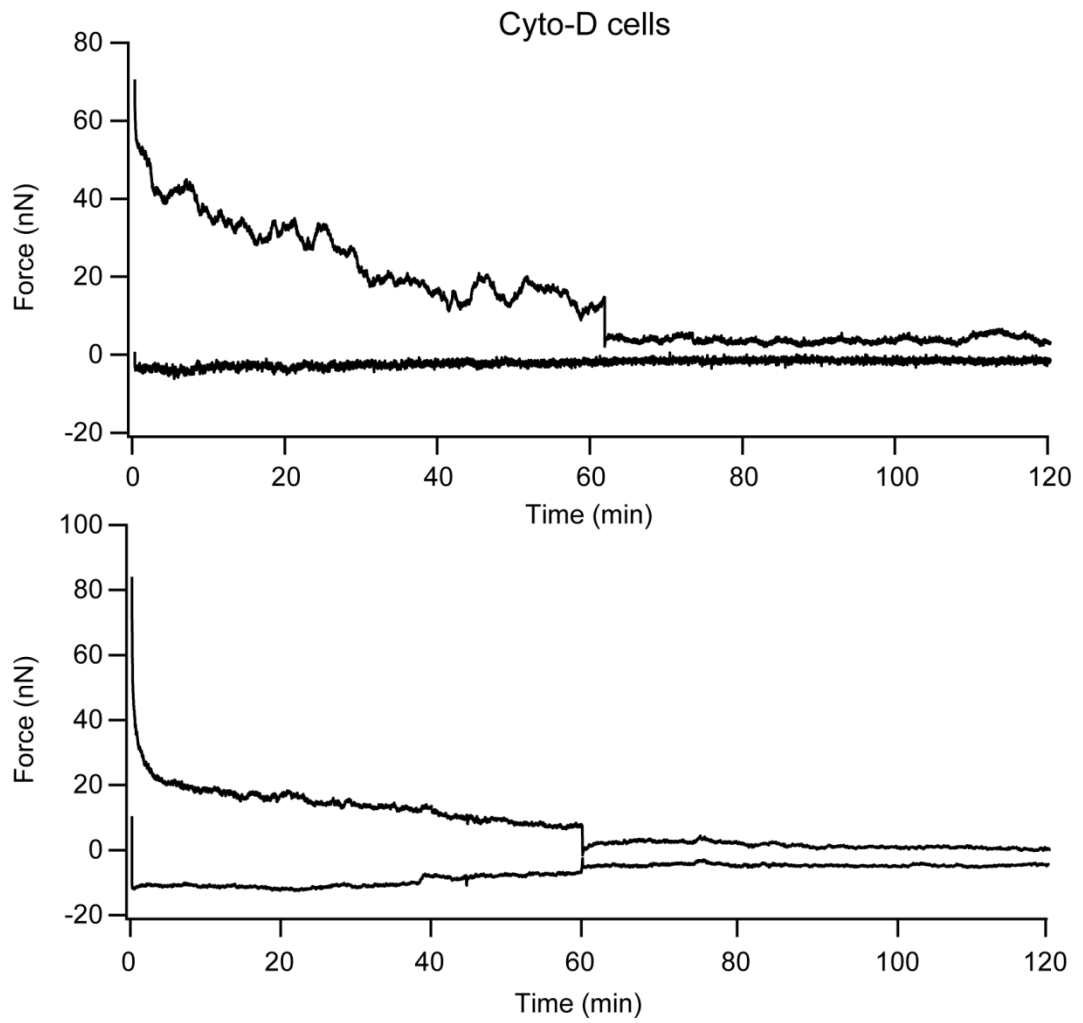


Figure 6-C: Further examples of the maximum and minimum forces observed for cyto-D cells over 120 min of cyclic deformation.

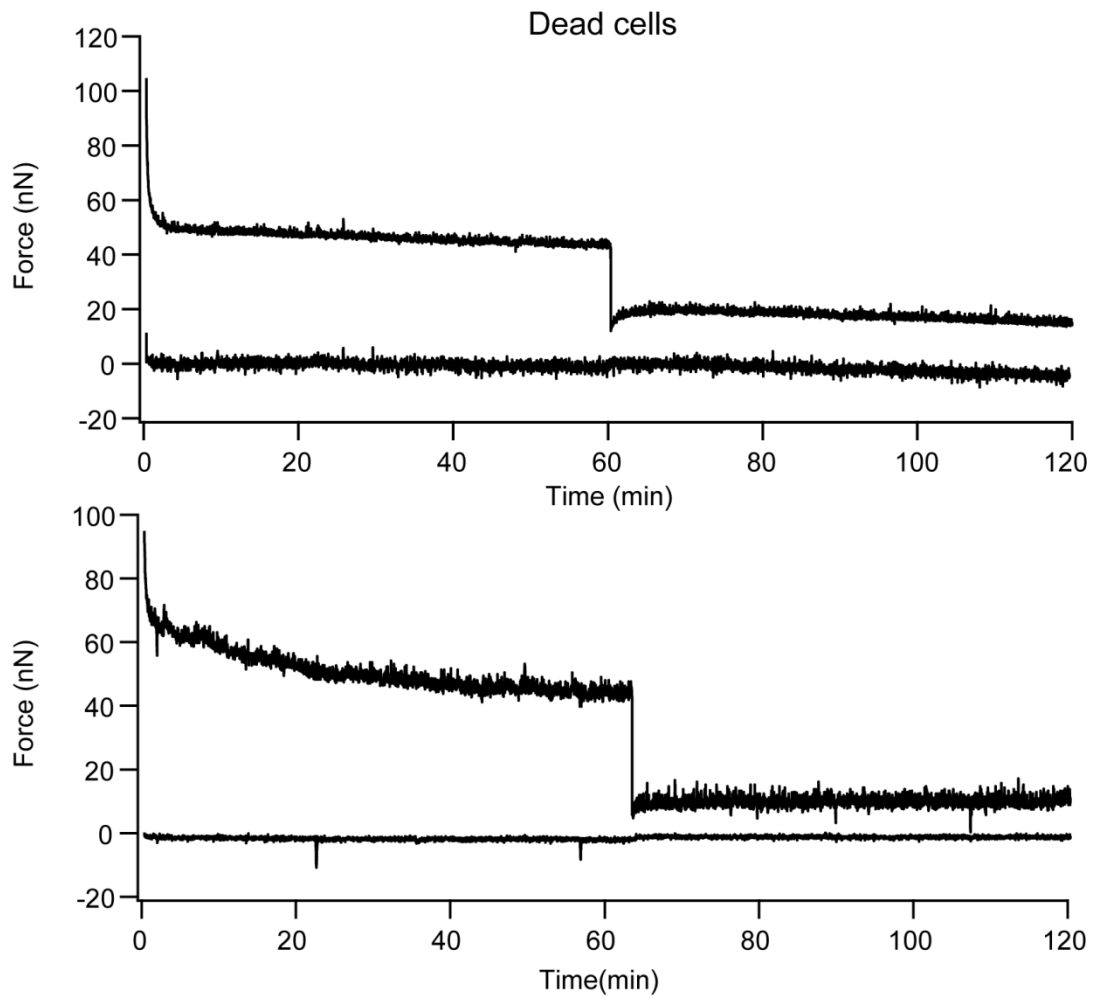


Figure 6-D: Further examples of the maximum and minimum forces observed for dead cells over 120 min of cyclic deformation.

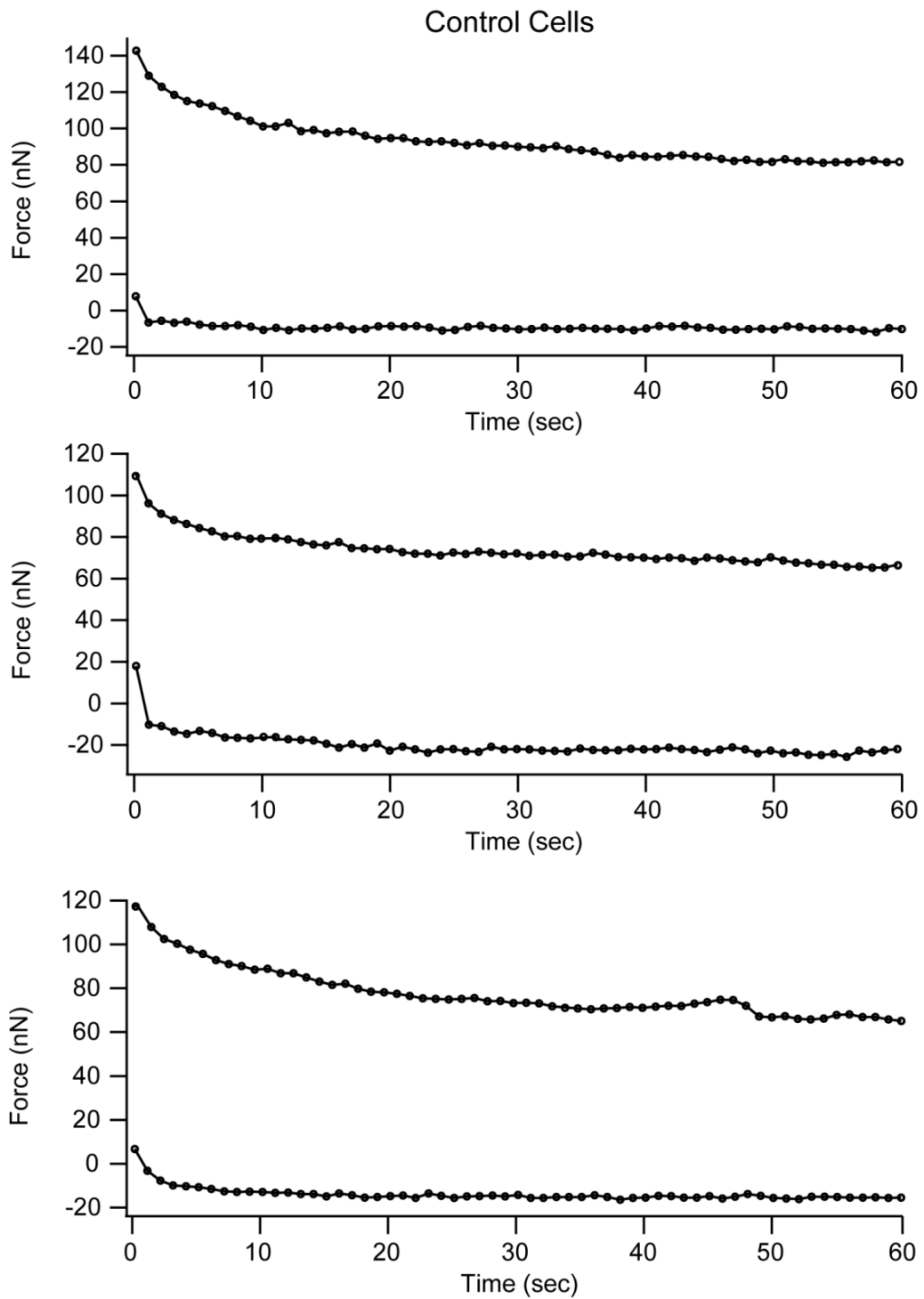
**6.C Effects of Cyclic Deformation at  $T_0$** 

Figure 6-E: Further examples of the maximum and minimum forces observed for control cells over the initial 60 s of cyclic deformation.

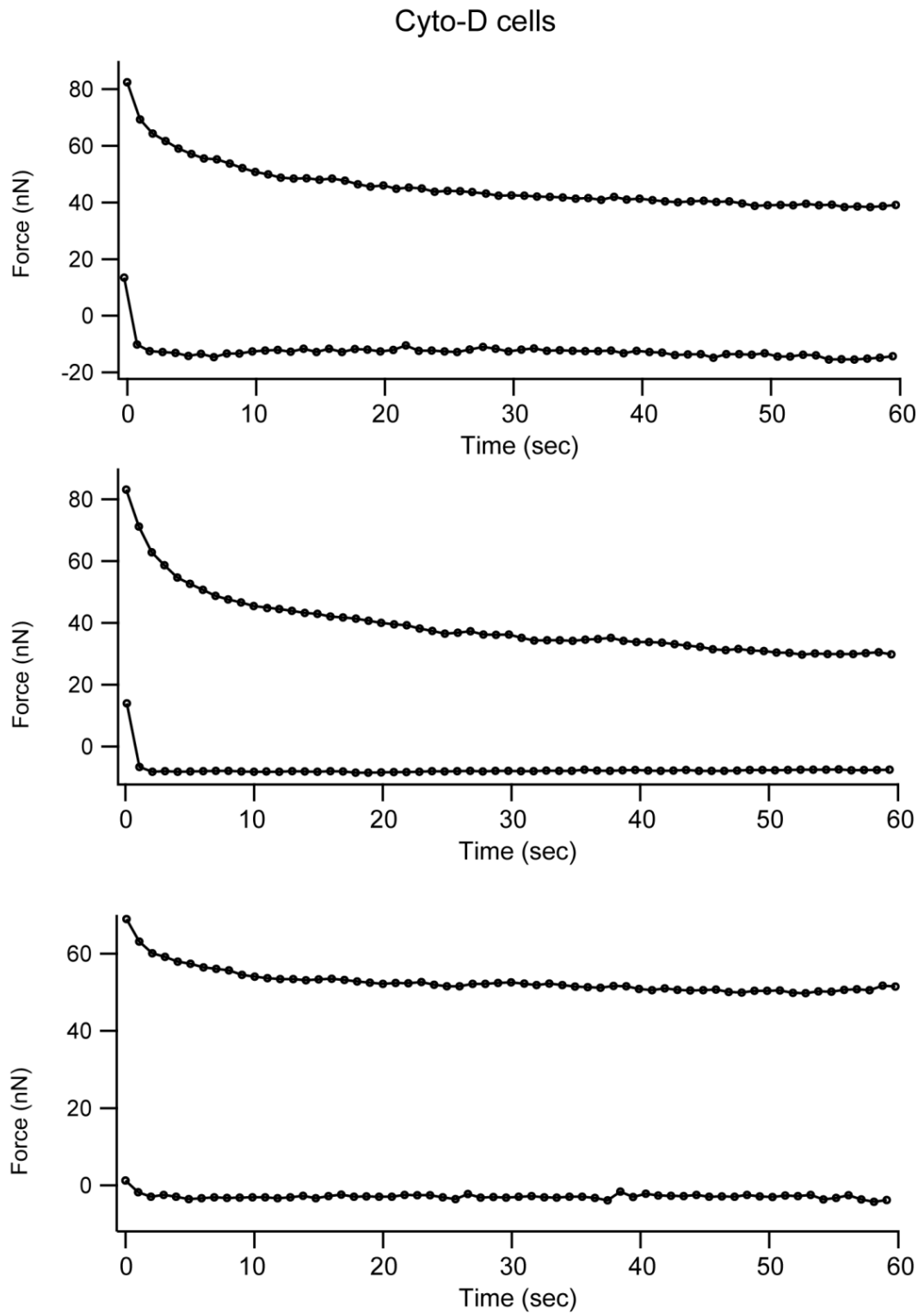


Figure 6-F: Further examples of the maximum and minimum forces observed for cyto-D cells over the initial 60 s of cyclic deformation.

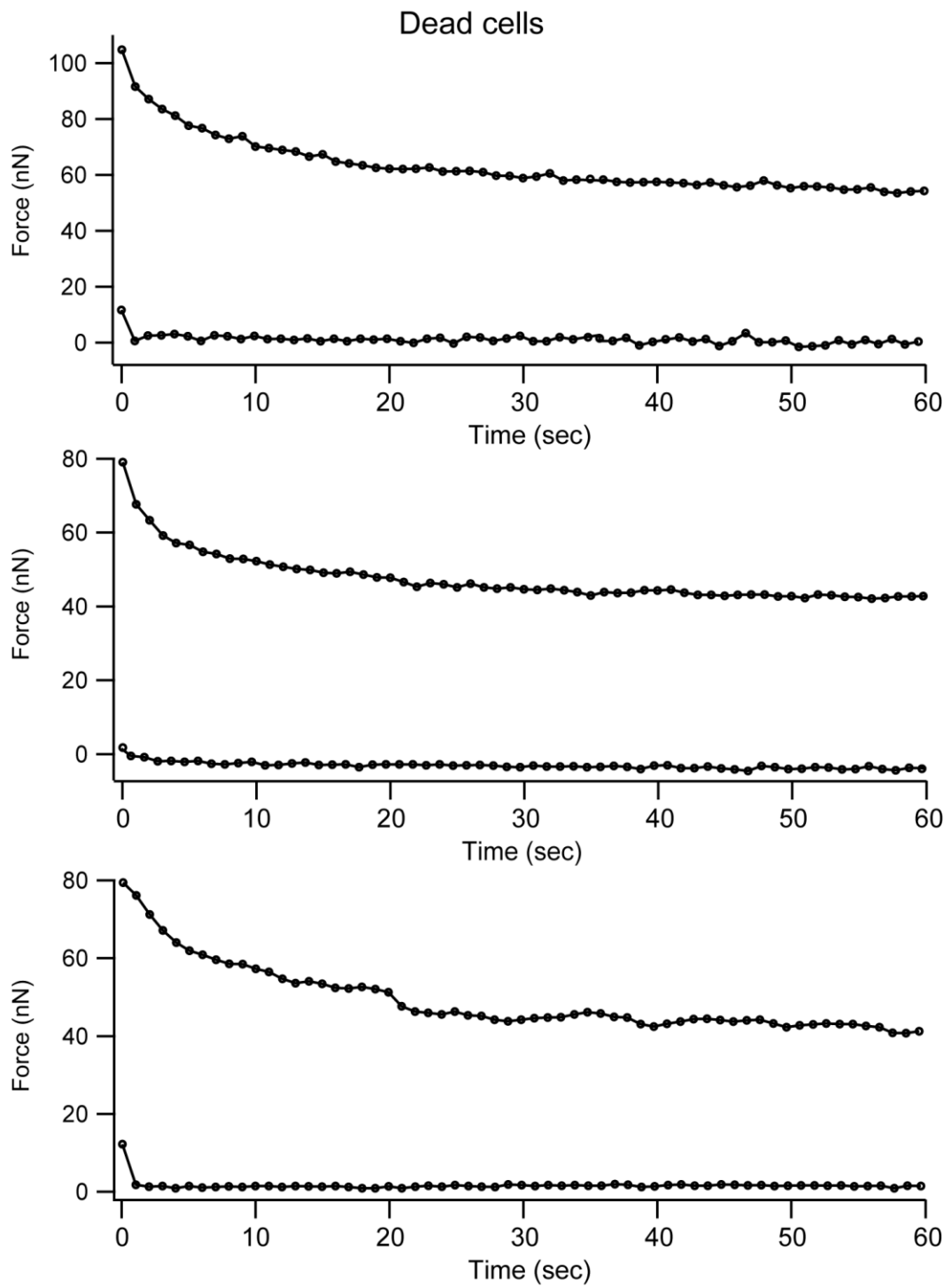


Figure 6-G: Further examples of the maximum and minimum forces observed for dead cells over the initial 60 s of cyclic deformation.

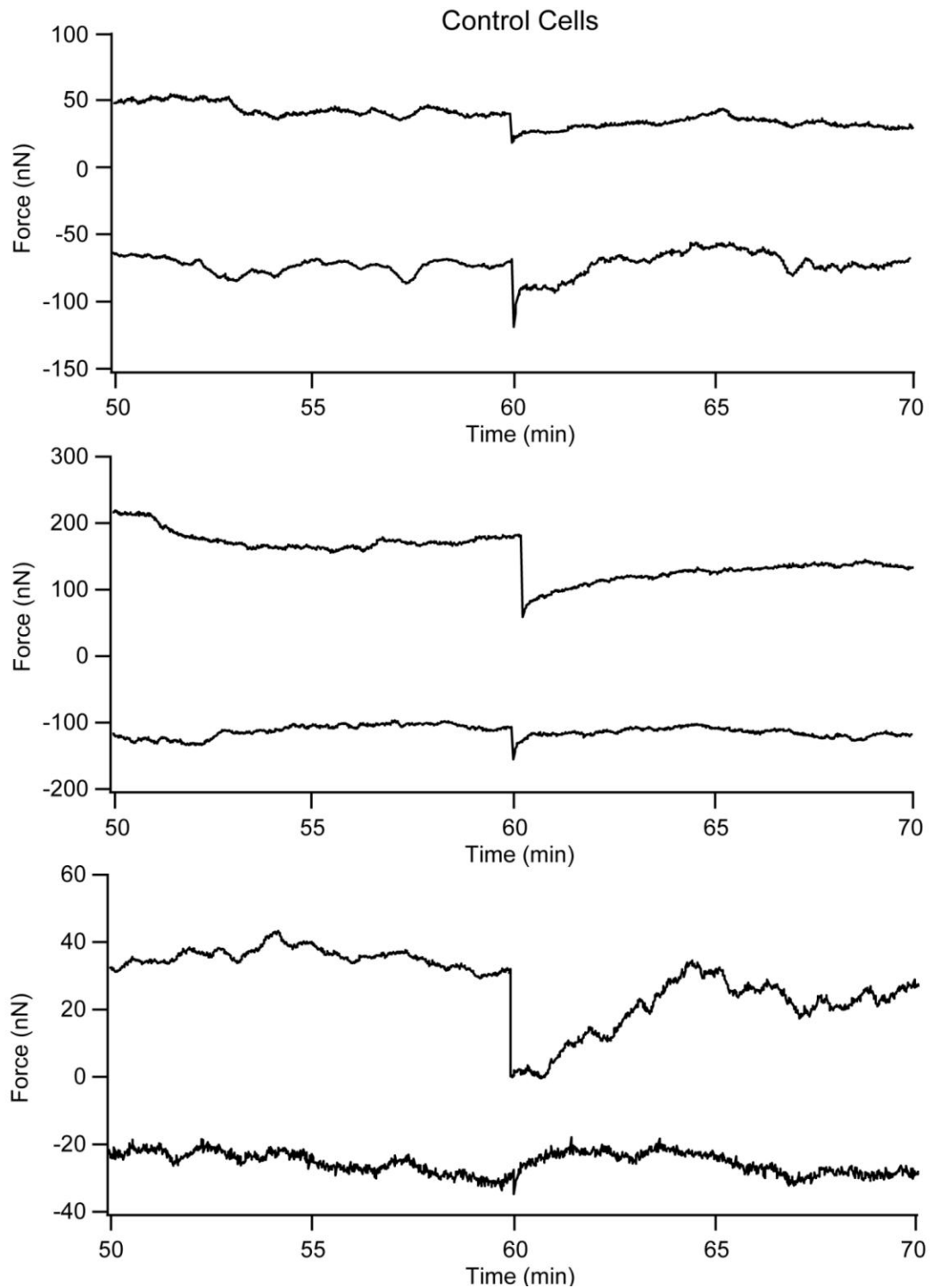
**6.D Effects of Cyclic Deformation at  $T_{RC}$** 

Figure 6-H: Further examples of the maximum and minimum forces observed for control cells at the regime change ( $T_{RC}$ ).

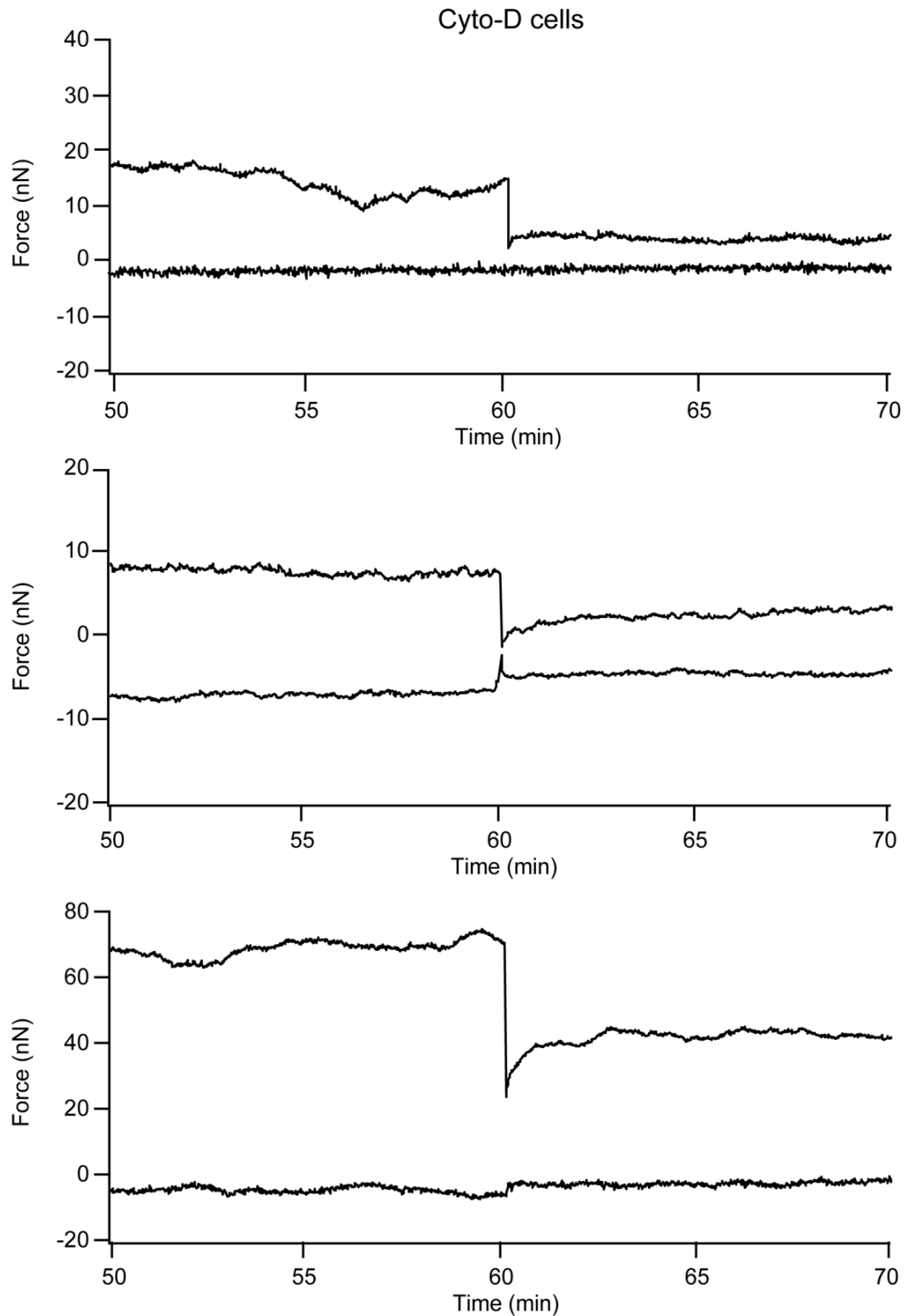


Figure 6-I: Further examples of the maximum and minimum forces observed for cyto-D cells at the regime change ( $T_{RC}$ ).

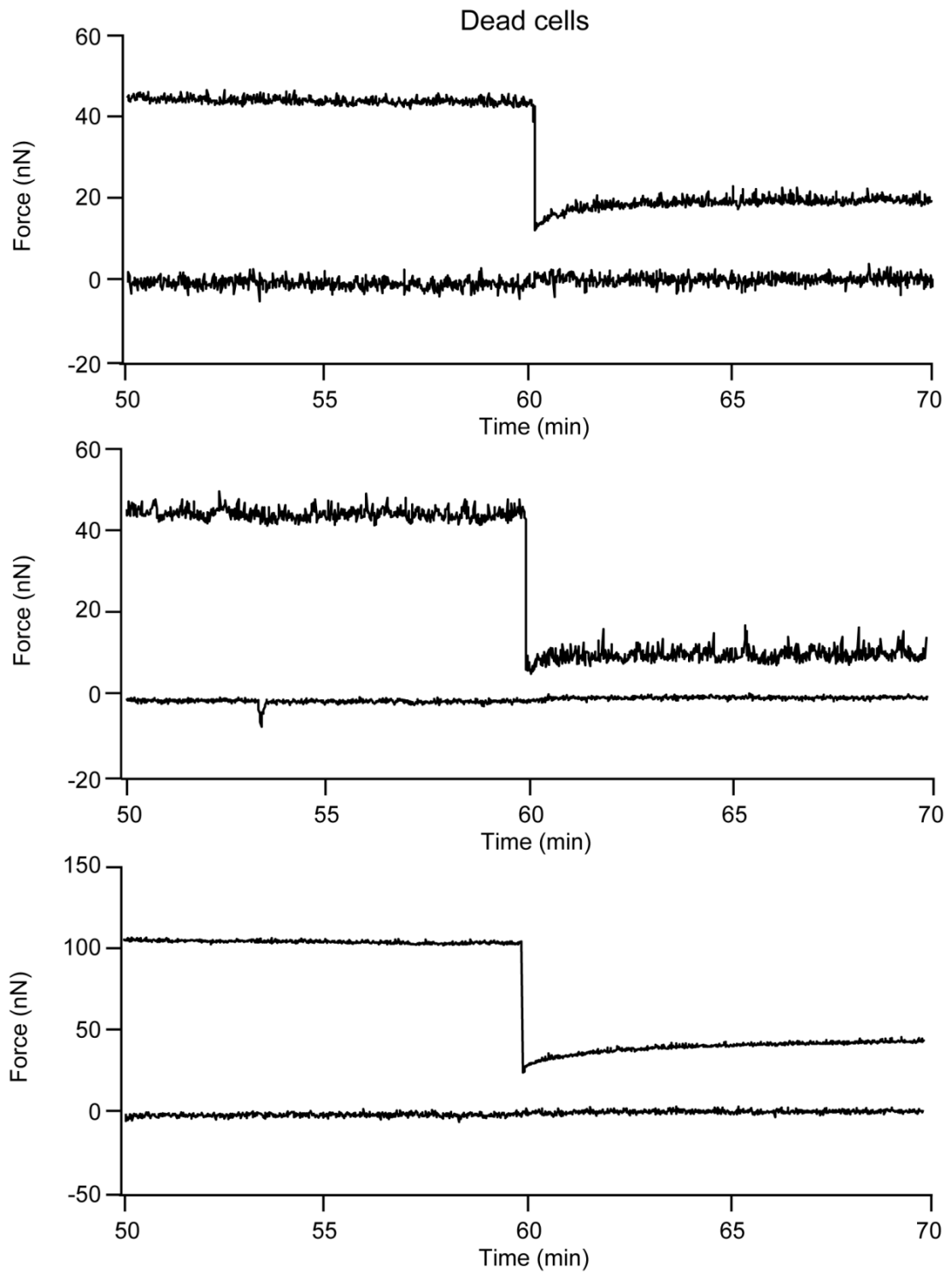


Figure 6-J: Further examples of the maximum and minimum forces observed for dead cells at the regime change ( $T_{RC}$ ).

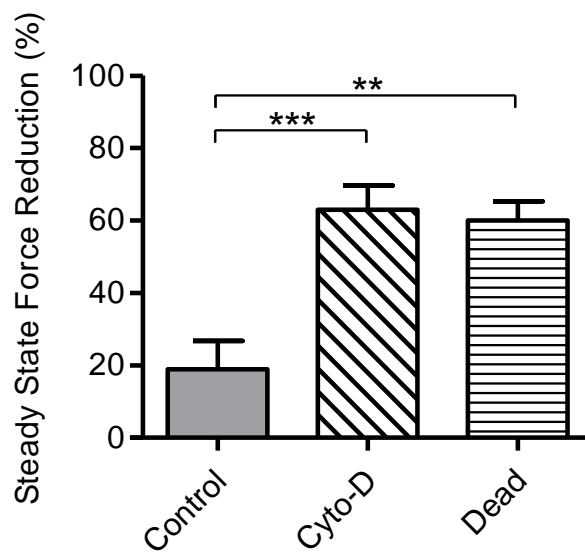
**6.E Steady State Maximum Force Reduction (%)**

Figure 6-K: Percentage reduction in the steady state maximum forces (steady state 1 - steady state 2) for the three cell groups.

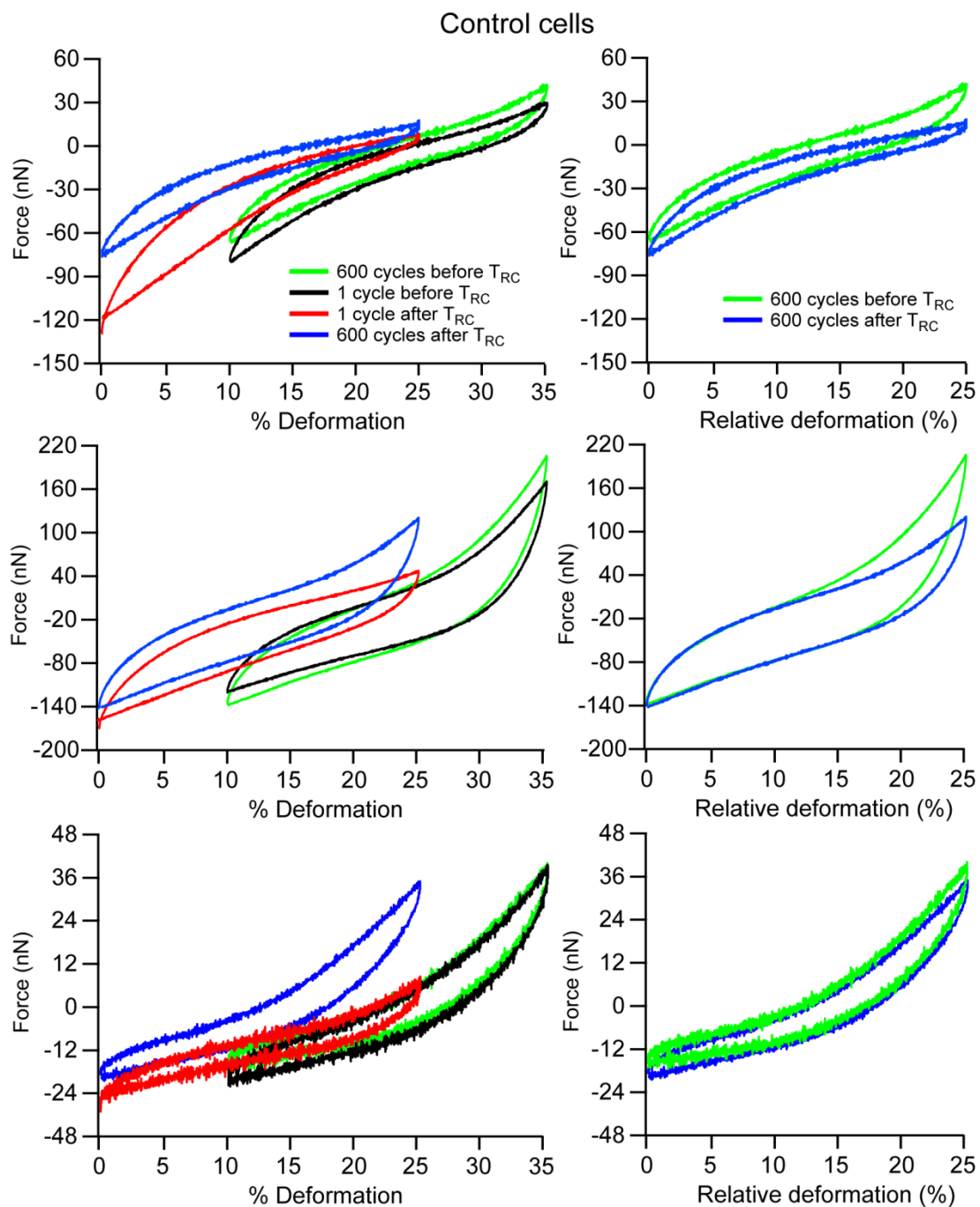
6.F Force-Deformation Curves at  $T_{RC}$ 

Figure 6-L: Force-deformation cycles within 600 cycles before and after  $T_{RC}$  for three control cells. The cycles shown (left) correspond to the 600<sup>th</sup> cycle before (green), the cycle before (black), the cycle after (red), and 600<sup>th</sup> cycle after (blue)  $T_{RC}$ . The curves shown (right) are the 600<sup>th</sup> cycle before (green) and after (blue)  $T_{RC}$  superimposed on each other with a relative % deformation.

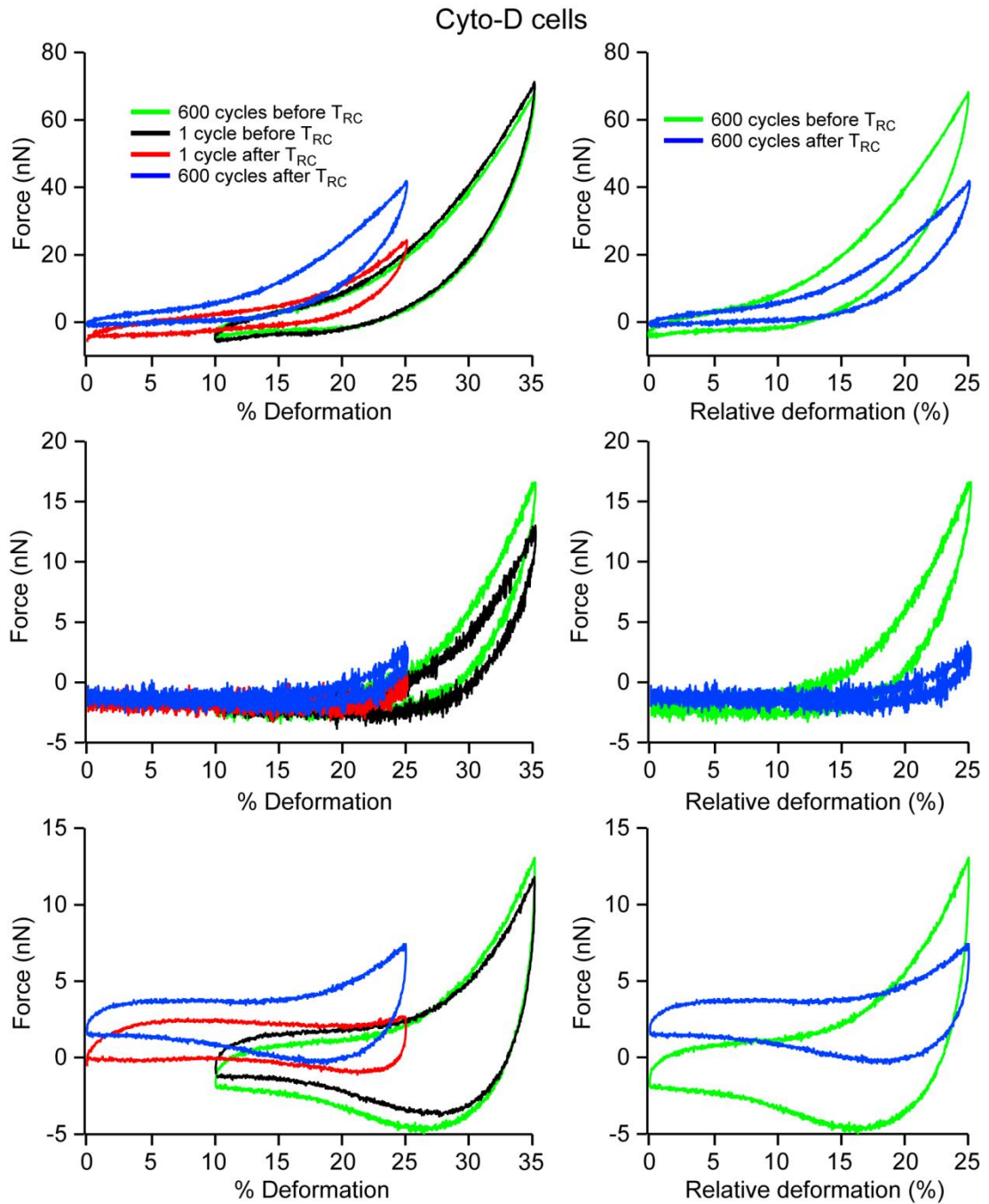


Figure 6-M: Force-deformation cycles within 600 cycles before and after  $T_{RC}$  for three cyto-D cells. The cycles shown (left) correspond to the 600<sup>th</sup> cycle before (green), the cycle before (black), the cycle after (red), and 600<sup>th</sup> cycle after (blue)  $T_{RC}$ . The curves shown (right) are the 600<sup>th</sup> cycle before (green) and after (blue)  $T_{RC}$  superimposed on each other with a relative % deformation.

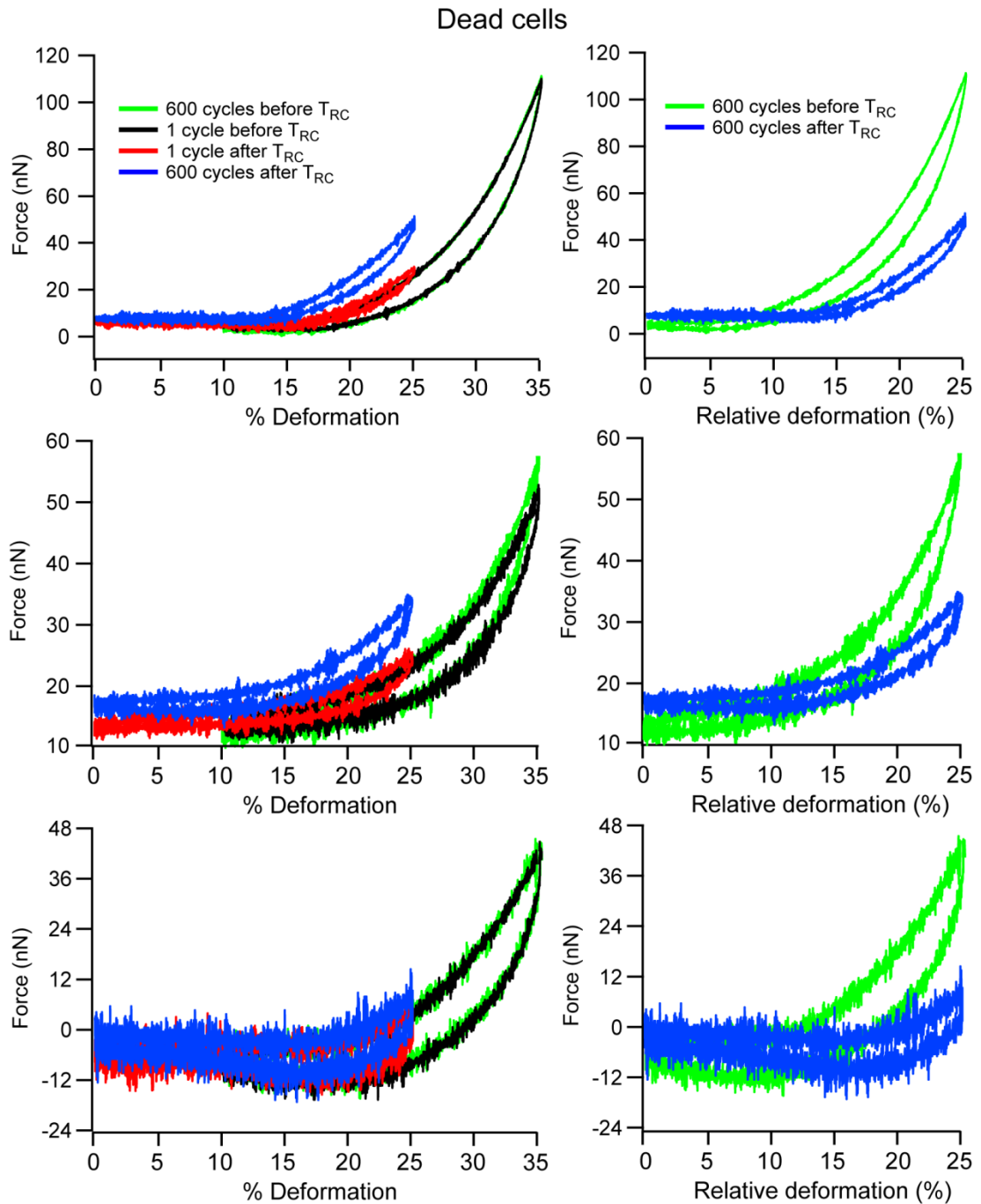


Figure 6-N: Force-deformation cycles within 600 cycles before and after  $T_{RC}$  for three cyto-D cells. The cycles shown (left) correspond to the 600<sup>th</sup> cycle before (green), the cycle before (black), the cycle after (red), and 600<sup>th</sup> cycle after (blue)  $T_{RC}$ . The curves shown (right) are the 600<sup>th</sup> cycle before (green) and after (blue)  $T_{RC}$  superimposed on each other with a relative % deformation.

### 6.G Control of Cell Spreading: Micropatterning

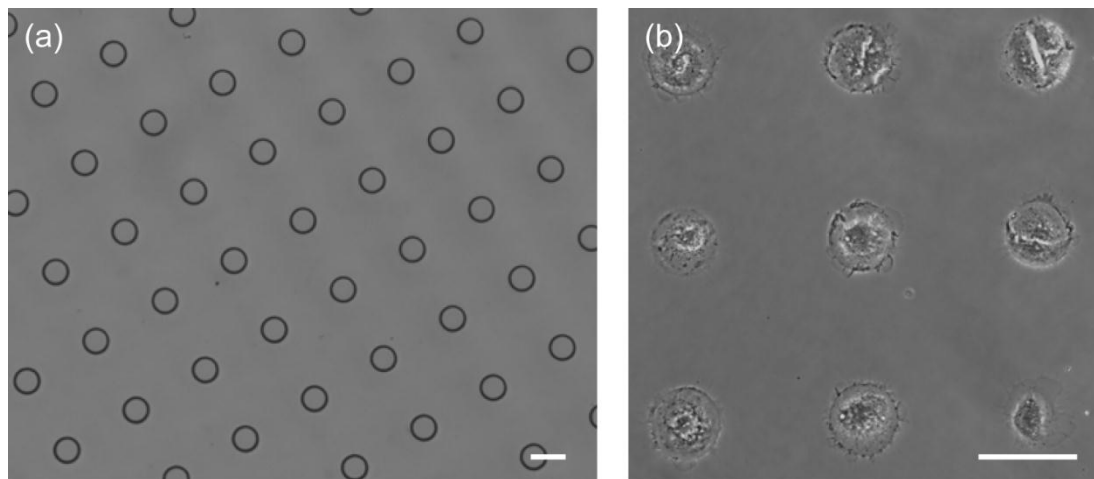


Figure 6-O: (a) PDMS stamp with  $\text{\O}35\ \mu\text{m}$  protruding posts (photolithography patterned masters kindly donated by Professor N. Spencer, ETH, Zürich, Switzerland). A microcontact printing technique was applied to micropattern the substrate with fibronectin islands. PLL-g-PEG was used to inhibit cell spreading beyond the micropatterned islands. (b) MC3T3 cells conforming to the shape of the micropatterned fibronectin islands. Scale bar represents  $50\ \mu\text{m}$ .

## Chapter 7

### **Discussion**

## 7.1 Discussion

The work presented in this thesis can be divided into two categories: (i) instrument development, and (ii) experimental cell biomechanics. In terms of instrument development, the first key contribution of this thesis is the adaptation of a standard AFM to apply high precision mechanical loading at the whole cell level. Importantly, appropriate correction factors for default AFM measurements are determined. The second key contribution in terms of instrument development is the stability enhancement of a standard AFM system to achieve accurate displacement control over long time scales. Taking advantage of the unrivalled precision of the AFM combined with the system modifications mentioned above, a series of novel *in vitro* single cell experiments are performed. Firstly, monotonic deformation experiments are implemented, giving rise to the key finding that the actin cytoskeleton contributes significantly to the mechanical response of cells to compressive deformation. Additionally it is shown that the actively generated contractility of the actin cytoskeleton has a pronounced influence on cell and nucleus morphology. Following from monotonic cell experiments, cyclic single cell deformation is then implemented, with a constant loading and unloading strain rate being applied to the cell. The range of applied deformation is altered during the experiment without altering the strain rate. It is demonstrated that the steady state cell forces are largely unaffected by this change in deformation range. This phenomenon is not observed for non-contractile cyto-D cells; passive cyto-D cell forces are found to be highly dependent on the applied deformation range. These findings suggest that the forces actively generated by the actin cytoskeleton in contractile cells responded to the strain rate rather than the strain magnitude. Detailed discussions of analyses and results are presented in each technical chapter of the thesis (Chapters 3-6). The purpose of this final chapter is to provide an overview of the importance of the key findings in the broader context of AFM experimentation and cell mechanics. Additionally, some recommendations for future work are provided.

The modified AFM successfully developed in **Chapter 3** allows single cell mechanics to be investigated at the whole cell level with high precision force and

displacement resolution. The sphere attached to the AFM cantilever has a significantly larger diameter ( $\text{\O} 150 \mu\text{m}$ ) than the typical diameter of a spread osteoblast ( $\sim \text{\O} 70 \mu\text{m}$ ). The sphere therefore provides a close approximation to a planar compression surface, and deformation is applied at a whole cell level. This is in contrast to previous AFM cell mechanics studies in which smaller spheres ( $< \text{\O} 60 \mu\text{m}$ ) are used and the resulting cell deformation is more localised (Lehenkari et al. (2000), Lulevich et al. (2006), Jaasma et al. (2006), Zimmer et al. (2012)). Previous whole cell loading systems, where the measured force is calculated from video analysis of the deflection of a flexible probe, offer a force resolution of approximately 1-10 nN (Thoumine and Ott (1997), Ofek et al. (2009)). The modified AFM system proposed in this thesis provides whole cell loading with sub-nanometre displacement precision (Colton et al. (1997), Gan (2009)) and pico-Newton force resolution (Lim et al. (2006), Mostaert et al. (2006), Simon and Durrieu (2006)). Also in Chapter 3, an in-depth experimental investigation reveals that the standard AFM optical lever system assumption of free-ended cantilevering is inappropriate when the sphere becomes constrained, resulting in an additional moment being applied to the cantilever's free-end. This serious issue, which can significantly alter the reported force measurements and perceived indentation depth, has not been considered in previous AFM studies where a sphere is attached to the cantilever (Lehenkari et al. (2000), Lulevich et al. (2006), Jaasma et al. (2006), Zimmer et al. (2012)). In this thesis, for the first time, an appropriate correction factor is proposed for AFM experiments in which the attached sphere is constrained. Observation of the front edge of the sphere during sample indentation is required to indicate if the sphere is sliding or constrained. In this study, it is demonstrated that uncorrected force-indentation data may result in a dramatic  $\sim 18$ -fold underestimation of a sample's Young's modulus. These findings illustrate, for the first time, the necessity of careful interpretation of reported measurements in all future AFM studies where sphere attachment is performed. The findings of this study are reported in Weafer et al. (2012).

High precision *in vitro* experiments using the modified AFM are performed in **Chapter 4** to directly investigate the role of the actin cytoskeleton in the

compression resistance of osteoblasts. By monotonically loading the same cells, both before and after cyto-D disruption of the actin cytoskeleton, it is found that the actin cytoskeleton contributes significantly in the resistance of osteoblasts to compression. The measured compression force is ~40-60% higher for untreated cells than for cyto-D cells. To the author's knowledge, this study is the first time whole cell loading experiments have been performed on osteoblasts. The compression value measured for osteoblasts is higher than that reported for whole cell compression (to similar levels of deformation) of fibroblasts (Deng et al. (2010)) and endothelial cells (Caille et al. (2002)), but lower than that reported for highly contractile myoblasts (Peeters et al. (2005)). A computational study by Ronan et al. (2012) reveals that an increase in compression resistance is strongly dependent on the level of cell contractility. The high compression forces measured in this study suggest that osteoblasts are more contractile than fibroblasts and endothelial cells but less so than myoblasts. Furthermore, this study also provides detailed measurements of the significant morphological changes that occur following the disruption of the actin cytoskeleton. These changes indicate that the actin cytoskeleton has a pronounced influence on cell and nucleus morphology. Significant nucleus deformation due to actin cytoskeleton contractility is observed in the present study. Similarly, in the work of Avalos et al. (2011), nuclei in contractile fibroblasts are shown to be significantly flatter than spherical nuclei observed in treated cyto-D cells. In contrast to the study presented in this thesis, Avalos et al. (2011) does not implement applied deformation and force measurement in order to uncover the mechanical contribution of the actin cytoskeleton. The detailed measurement of cell and nucleus shape change following disruption of the actin cytoskeleton reported in this chapter is of particular importance in light of studies that have reported a link between the cytoskeleton, nucleus deformation and gene expression ((Thomas et al. (2002), Vergani et al. (2004), Houben et al. (2007), Makale (2007), Roca-Cusachs et al. (2008)). Furthermore, these detailed morphology measurements allow for a unique calibration of the active and passive properties of osteoblasts, as presented in a joint experimental-computational study by Weafer and Ronan et al. (2013). Such an approach provides an enhanced insight into the mechanisms underlying the response of cells to mechanical loading. In the specific case of osteoblasts, the accurate

characterisation of the active and passive cell mechanical behaviour is an important step in the tissue engineering of bone, where cell function and extra-cellular-matrix synthesis is highly influenced by the physical environment and applied loading (You et al. (2000), Mullender et al. (2004), McGarry et al. (2005), Mullender et al. (2006), You et al. (2008)).

In **Chapter 5**, a readily implementable, cost effective method of modifying an AFM for z-displacement controlled operation in both air and liquid over long time scales is successfully developed. It is demonstrated that the elimination of thermal drift and liquid instabilities is essential for all AFM studies where accurate knowledge of the tip-sample separation over long time scales is a requirement. The stability measurements recorded for a standard unmodified AFM indicate that substantial thermal drift occurs even after several hours, which would significantly affect any long-term experiments where a known tip-substrate displacement is required. Previous studies state thermal equilibration times ranging from 60 min (Munday et al. (2009), Zepeda et al. (2001)) to a few hours (Rachlin et al. (1992), Gan (2009)); however, results presented in this thesis demonstrate that substantially longer timeframes may be required in order to reach thermal equilibrium in the absence of stability enhancement. Additionally, for the first time, the issue of liquid related instabilities is reported, which is shown to result in significant perturbations (of the order of 100 nm) in the measured deflection. The combination of active temperature control and a customised fluid cell results in a substantial 17-fold enhancement in system z-drift stability ( $6.33 \pm 3.90$  nm/hr) compared to a standard unmodified AFM ( $111.56 \pm 112.97$  nm/hr). For a cell of height 10  $\mu\text{m}$ , this represents a maximum indentation depth error of 0.5% over 5 hr for the modified system, compared to a maximum error of 13.5% for the unmodified system (Weafer et al. (2012)). The stability enhancing modifications developed in this study are important not only for AFM experimentation, but for all high precision techniques in which displacement control over long time scales is a requirement (Hu et al. (2004), Fernández et al. (2006), Thoumine et al. (1999)).

The range of whole-cell based experiments that can be performed using this modified AFM system is similar to that achievable using the microplate technique.

However, the superior displacement precision and force resolution capabilities of the modified AFM system allow cell behaviours to be measured that are undetectable using other techniques. For example, the force fluctuations observed during the cyclic deformation of cells in Chapter 6 (attributed to cell activities such as cell remodelling, cell spreading, and cell remodelling) cannot be measured using techniques such as microplates since these fluctuations are below its force resolution threshold (1-10 nN). Furthermore, in long time scale experiments, techniques are susceptible to stability issues, and typically a number of hours are required to reach thermal equilibrium (Rachlin et al. (1992), Micoulet et al. (2005), Gan (2009)). For example, microplate systems, although generally not reported, are susceptible to stability issues, particularly when experiments are performed at 37 °C. Micoulet et al. (2005) attempted to reduce z-drift for the microplate system using two heating wires; however, the system remained unstable (~700 nm/hr) after a 5 hr equilibration period. During this equilibration period, the cells are left in the system, preventing mechanical testing at an earlier stage of cell insertion into the system. In the system presented here, high precision deformation controlled experiments can be performed within 10 min of cell insertion into the system. While not the focus of the present study, such an efficient system could potentially facilitate the investigation of mechanical behaviour during cell spreading. Additionally, since chemicals and dyes can be added to the system without affecting the system stability, real-time deformation controlled experiments following chemical treatments (e.g. cytoskeleton inhibitors) can also be performed to investigate the biomechanical response of cells.

A series of novel single cell cyclic deformation experiments using the enhanced AFM setup are presented in **Chapter 6**. Cyclic deformation is applied to a cell with a constant loading and unloading strain rate. The range of applied deformation is altered during the experiment without altering the strain rate. It is demonstrated that the steady state cell forces are largely unaffected by this change in deformation range. This phenomenon is not observed for non-contractile cyto-D cells; passive cyto-D cell forces are found to be highly dependent on the applied deformation range. These findings suggest that the forces actively generated by the actin cytoskeleton in contractile cells are more responsive to strain rate than to a

change in strain magnitude. The findings of the current study are important not just for the field of cell mechanics, but also from the viewpoint of tissue level bone biomechanics. A relationship between mechanical loading and bone function has been commonly reported whereby strenuous exercise increases bone mass (Lanyon (1996), Courteix et al. (1998)) and disuse due to inactivity reduces bone mass (Zerwekh et al. (2009)). Tissue level experiments have investigated the effects of both strain magnitude (Mosley and Lanyon (1998)) and strain rate on bone function (Turner et al. (1995), Judex et al. (2007)). Turner et al. (1995) found that bone formation was strain rate dependent, with the amount of newly formed bone increasing proportionally with the strain rate applied to the bone tissue. Furthermore, a study by Judex et al. (2007) reports that bone formation dependent on strain rate rather than on strain magnitude. Therefore, the findings of the current study, which characterises the response of single osteoblasts to dynamic loading, may have important implications from a clinical and an orthopaedic device design viewpoint.

While this thesis presents a number of advances in the field of AFM characterisation of osteoblast biomechanical behaviour, some follow-on studies should be considered to further advance the work presented here. In this thesis, dynamic loading is performed in which the strain magnitude is altered while keeping the strain rate constant. Further investigations where different combinations of strain rate and strain magnitude should be investigated to further investigate the strain rate dependence of cells and of the actin cytoskeleton. While not implemented in the current study, the strain rate could be altered by altering the frequency of deformation while maintaining a constant deformation range. However, it is possible that altering the frequency of cyclic deformation may alter the frequency of cell signal activation. Previous studies have shown that dynamic loading of osteoblasts results in signal activation (Mullender et al. (2006), Sato et al. (2007), McGarry et al. (2008)). Dynamic compression of chondrocytes has been shown to result in exponentially decaying intracellular calcium signalling (Roberts et al. (2001)). Therefore in experiments where the frequency is altered, it is suggested that cell signalling should be monitored while measuring the biomechanical response of the cell. The modified system presented in this thesis is equipped to perform such

experiments; fluorescence dyes can be injected into the closed fluid cell without destabilising the system, and high resolution fluorescence microscopy is possible via the glass coverslip base of the customised fluid cell. This follow-on study may uncover a possible link between strain rate and cell signalling activation. In this thesis, it is shown that the actin cytoskeleton contributes significantly to the strain-dependent response. In order to further investigate the contribution of the actin cytoskeleton, live cell imaging should be performed in which the actin cytoskeleton is transfected with a fluorescent tag, similar to the studies by Icard-Arcizet et al. (2008), Huang et al. (2010), and Watanabe-Nakayama et al. (2011). This would allow cell remodelling to be observed while simultaneously measuring the reaction force of the cell. A recent study by Pravincumar et al. (2012) combined micropipette aspiration and fluorescence microscopy to observe actin cytoskeleton remodelling in living chondrocytes following applied strain. Additionally, a study by Chaudhuri et al. (2009) developed a system based on the AFM technique which enabled simultaneous side-view fluorescence microscopy. This system was used to measure cell contractility between a static tipless cantilever and the substrate whilst simultaneously observing the remodelling of the actin cytoskeleton. However, due to the narrow width of the cantilever and its angle of inclination to the substrate, an accurate measurement of the total actively generated contractile stress normal to the substrate is not provided. The use of a modified cantilever, as proposed in this thesis, would overcome such limitations. Side-view imaging would represent a significant enhancement to the system presented in this thesis. With the current system, it is not possible to view the side-profile of the cell morphology, or monitor the interaction between the cell and the sphere. A study by Baik et al. (2010) developed a side-view profiling technique in which the standard bottom-up optical pathway is reflected  $90^\circ$  using a glass prism. However, due to the minimal clearance between the AFM cantilever holder and the substrate, this technique would require major alteration of a standard AFM system. To overcome such a hurdle, perhaps an objective with an extra-long working distance, or a glass prism with a sub-millimetre height could be utilised. A study by Chaudhuri et al. (2009), as discussed above, developed a system which allowed combined AFM-side view fluorescent imaging. However, in general, modifying an AFM to implement the imaging techniques reported by Chaudhuri et

al. (2009) is not feasible from a practical viewpoint for an AFM system that is required for both its imaging and force-spectroscopy capabilities.

In conclusion, in this thesis a standard AFM has been adapted to apply high precision mechanical loading at the whole cell level. An in-depth experimental investigation reveals that the standard AFM optical lever system assumption of free-ended cantilevering is inappropriate when a sphere is attached to the cantilever's free-end as lateral deformation of the sphere is constrained, preventing rotation of the cantilever free-end. This issue has not been considered in previous AFM studies in which a sphere is attached to a cantilever (Lehenkari et al. (2000), Lulevich et al. (2006), Jaasma et al. (2006), Zimmer et al. (2012)). In the current study an appropriate correction factor is proposed to deal with the issue of a constrained sphere. Furthermore, it is demonstrated that uncorrected force-indentation data may result in a dramatic ~18-fold underestimation of a samples elastic modulus. Using this modified AFM, high precision whole cell monotonic deformation is applied to osteoblasts. It is found that the actin cytoskeleton contributes significantly (~40-60%) to the whole cell compression force for osteoblasts. Additionally it is shown that the actively generated contractility of the actin cytoskeleton has a pronounced influence on cell and nucleus morphology. This is of particular importance in light of studies that have reported a link between the cytoskeleton, nucleus deformation and gene expression ((Thomas et al. (2002), Vergani et al. (2004), Houben et al. (2007), Makale (2007), Roca-Cusachs et al. (2008)). AFM modifications are also performed in order to achieve precise displacement control over long time scales. It is demonstrated that the elimination of thermal drift and liquid instabilities is essential for all AFM studies where accurate knowledge of the tip-sample separation over long time scales is a requirement. The combination of active temperature control and a customised fluid cell results in a substantial 17-fold enhancement in system z-drift stability. This represents a maximum indentation depth error of 0.5% over 5 hr for the modified system (cell height of 10  $\mu\text{m}$ ), compared to a maximum error of 13.5% for the unmodified system. The readily implementable, cost effective stability modifications proposed in this thesis can be applied to any system in which displacement control over long time scales is a requirement (Hu et al. (2004),

Fernández et al. (2006), Mitrossilis et al. (2009)). Using the modified AFM presented in this thesis, cyclic strain rate controlled experiments are performed on single osteoblasts. In the case of untreated contractile osteoblasts, it is shown that the steady state force response is largely unaffected by a change in cyclic deformation range when the unloading and loading strain rate is unchanged. In contrast, when the actin cytoskeleton is disrupted, a change in cyclic deformation range results in a significant change in measured steady state forces, despite an unchanged cyclic strain rate. Results demonstrate that the mechanical response of the active contractile actin cytoskeleton is based on the strain rate and dominates the cellular response of osteoblasts during dynamic loading. A fundamental understanding of the response of bone cells to dynamic loading is essential in order to further understand the mechanotransduction mechanisms underlying bone remodelling. It is important to note that bone remodelling has also been shown to depend on cyclic strain rate applied at the tissue level (Mosley and Lanyon (1998)). Furthermore, the findings of this thesis may have important implications for the tissue engineering of bone, given the importance of *in vitro* loading regimes on matrix synthesis (Mullender et al. (2004), Gabbay et al. (2006)).

## 7.2 References

- Avalos, P. G., Reichenzeller, M., Eils, R. and Gladilin, E. (2011) Probing compressibility of the nuclear interior in wild-type and lamin deficient cells using microscopic imaging and computational modeling. *Journal of Biomechanics*. 44 (15), 2642-2648
- Baik, A. D., Lu, X. L., Qiu, J., Huo, B., Hillman, E., Dong, C. and Guo, X. E. (2010) Quasi-3d cytoskeletal dynamics of osteocytes under fluid flow. *Biophysical Journal*. 99 (9), 2812-2820
- Caille, N., Thoumine, O., Tardy, Y. and Meister, J. J. (2002) Contribution of the nucleus to the mechanical properties of endothelial cells. *J. Biomech.* 35 (2), 177-187
- Chaudhuri, O., Parekh, S. H., Lam, W. A. and Fletcher, D. A. (2009) Combined atomic force microscopy and side-view optical imaging for mechanical studies of cells. *Nature methods*. 6 (5), 383-387
- Colton, R. J., Baselt, D. R., Dufrêne, Y. F., Green, J. B. D. and Lee, G. U. (1997) Scanning probe microscopy. *Current opinion in chemical biology*. 1 (3), 370-377
- Courteix, D., Lespessailles, E., Peres, S. L., Obert, P., Germain, P. and Benhamou, C. (1998) Effect of physical training on bone mineral density in prepubertal girls: A comparative study between impact-loading and non-impact-loading sports. *Osteoporosis international*. 8 (2), 152-158
- Deng, Z., Lulevich, V., Liu, F.-T. and Liu, G.-Y. (2010) Applications of atomic force microscopy in biophysical chemistry of cells. *The Journal of Physical Chemistry B*. 114 (18), 5971-5982
- Fernández, P., Pullarkat, P. A. and Ott, A. (2006) A master relation defines the nonlinear viscoelasticity of single fibroblasts. *Biophysical Journal*. 90 (10), 3796-3805
- Gabbay, J. S., Zuk, P. A., Tahernia, A., Askari, M., O'Hara, C. M., Karthikeyan, T., Azari, K., Hollinger, J. O. and Bradley, J. P. (2006) In vitro microdistraction of preosteoblasts: Distraction promotes proliferation and oscillation promotes differentiation. *Tissue engineering*. 12 (11), 3055-3065
- Gan, Y. (2009) Atomic and subnanometer resolution in ambient conditions by atomic force microscopy. *Surf. Sci. Rep.* 64 (3), 99-121
- Houben, F., Ramaekers, F. C. S., Snoeckx, L. H. E. H. and Broers, J. L. V. (2007) Role of nuclear lamina-cytoskeleton interactions in the maintenance of cellular strength. *Biochimica et Biophysica Acta (BBA) - Molecular Cell Research*. 1773 (5), 675-686

- Hu, J., Zhang, Y., Li, B., Gao, H., Hartmann, U. and Li, M. (2004) Nanomanipulation of single DNA molecules and its applications. *Surface and interface analysis*. 36 (2), 124-126
- Huang, L., Mathieu, P. S. and Helmke, B. P. (2010) A stretching device for high-resolution live-cell imaging. *Annals of biomedical engineering*. 38 (5), 1728-1740
- Icard-Arcizet, D., Cardoso, O., Richert, A. and Hénon, S. (2008) Cell stiffening in response to external stress is correlated to actin recruitment. *Biophysical Journal*. 94 (7), 2906-2913
- Jaasma, M. J., Jackson, W. M. and Keaveny, T. M. (2006) Measurement and characterization of whole-cell mechanical behavior. *Annals of biomedical engineering*. 34 (5), 748-758
- Judex, S., Lei, X., Han, D. and Rubin, C. (2007) Low-magnitude mechanical signals that stimulate bone formation in the ovariectomized rat are dependent on the applied frequency but not on the strain magnitude. *Journal of Biomechanics*. 40 (6), 1333-1339
- Lanyon, L. (1996) Using functional loading to influence bone mass and architecture: Objectives, mechanisms, and relationship with estrogen of the mechanically adaptive process in bone. *Bone*. 18 (1), S37-S43
- Lehenkari, P. P., Charras, G. T., Nykänen, A. and Horton, M. A. (2000) Adapting atomic force microscopy for cell biology. *Ultramicroscopy*. 82 (1-4), 289-295
- Lim, C. T., Zhou, E. H., Li, A., Vedula, S. R. K. and Fu, H. X. (2006) Experimental techniques for single cell and single molecule biomechanics. *Materials Science and Engineering: C*. 26 (8), 1278-1288
- Lulevich, V., Zink, T., Chen, H. Y., Liu, F. T. and Liu, G. (2006) Cell mechanics using atomic force microscopy-based single-cell compression. *Langmuir*. 22 (19), 8151-8155
- Makale, M. (2007) Cellular mechanobiology and cancer metastasis. *Birth Defects Res C Embryo Today*. 81 (4), 329-43
- McGarry, J. G., Klein-Nulend, J. and Prendergast, P. J. (2005) The effect of cytoskeletal disruption on pulsatile fluid flow-induced nitric oxide and prostaglandin e2 release in osteocytes and osteoblasts. *Biochemical and Biophysical Research Communications*. 330 (1), 341-348
- McGarry, J. G., Maguire, P., Campbell, V. A., O'Connell, B. C., Prendergast, P. J. and Jarvis, S. P. (2008) Stimulation of nitric oxide mechanotransduction in single osteoblasts using atomic force microscopy. *J. Orthop. Res*. 26 (4), 513-521

- Micoulet, A., Spatz, J. P. and Ott, A. (2005) Mechanical response analysis and power generation by single-cell stretching. *ChemPhysChem*. 6 (4), 663-670
- Mitrossilis, D., Fouchard, J., Guiroy, A., Desprat, N., Rodriguez, N., Fabry, B. and Asnacios, A. (2009) Single-cell response to stiffness exhibits muscle-like behavior. *Proceedings of the National Academy of Sciences*. 106 (43), 18243-18248
- Mosley, J. R. and Lanyon, L. E. (1998) Strain rate as a controlling influence on adaptive modeling in response to dynamic loading of the ulna in growing male rats. *Bone*. 23 (4), 313-318
- Mostaert, A., Higgins, M., Fukuma, T., Rindi, F. and Jarvis, S. (2006) Nanoscale mechanical characterisation of amyloid fibrils discovered in a natural adhesive. *Journal of Biological Physics*. 32 (5), 393-401
- Mullender, M., El Haj, A., Yang, Y., van Duin, M., Burger, E. and Klein-Nulend, J. (2004) Mechanotransduction of bone cells in vitro: Mechanobiology of bone tissue. *Medical and biological engineering and computing*. 42 (1), 14-21
- Mullender, M. G., Dijcks, S. J., Bacabac, R. G., Semeins, C. M., Van Loon, J. J. W. A. and Klein-Nulend, J. (2006) Release of nitric oxide, but not prostaglandin e<sub>2</sub>, by bone cells depends on fluid flow frequency. *Journal of Orthopaedic Research*. 24 (6), 1170-1177
- Munday, J. N., Capasso, F. and Parsegian, V. A. (2009) Measured long-range repulsive casimir-lifshitz forces. *Nature*. 457 (7226), 170-173
- Ofek, G., Wiltz, D. C. and Athanasiou, K. A. (2009) Contribution of the cytoskeleton to the compressive properties and recovery behavior of single cells. *Biophys. J*. 97 (7), 1873-1882
- Peeters, E. A. G., Oomens, C. W. J., Bouten, C. V. C., Bader, D. L. and Baaijens, F. P. T. (2005) Mechanical and failure properties of single attached cells under compression. *J. Biomech*. 38 (8), 1685-1693
- Pravincumar, P., Bader, D. L. and Knight, M. M. (2012) Viscoelastic cell mechanics and actin remodelling are dependent on the rate of applied pressure. *PLoS One*. 7 (9), e43938
- Rachlin, A. L., Henderson, G. S. and Goh, M. C. (1992) An atomic force microscope (afm) study of the calcite cleavage plane; image averaging in fourier space. *Amer. Mineral*. 77 (9-10), 904-910
- Roberts, S. R., Knight, M. M., Lee, D. A. and Bader, D. L. (2001) Mechanical compression influences intracellular ca<sup>2+</sup> signaling in chondrocytes seeded in agarose constructs. *J Appl Physiol*. 90 (4), 1385-1391

- Roca-Cusachs, P., Alcaraz, J., Sunyer, R., Samitier, J., Farré, R. and Navajas, D. (2008) Micropatterning of single endothelial cell shape reveals a tight coupling between nuclear volume in g1 and proliferation. *Biophysical Journal*. 94 (12), 4984-4995
- Ronan, W., Deshpande, V. S., McMeeking, R. M. and McGarry, J. P. (2012) Numerical investigation of the active role of the actin cytoskeleton in the compression resistance of cells. *Journal of the Mechanical Behavior of Biomedical Materials*. 14, 143-157
- Sato, K., Adachi, T., Ueda, D., Hojo, M. and Tomita, Y. (2007) Measurement of local strain on cell membrane at initiation point of calcium signaling response to applied mechanical stimulus in osteoblastic cells. *Journal of Biomechanics*. 40 (6), 1246-1255
- Simon, A. and Durrieu, M. C. (2006) Strategies and results of atomic force microscopy in the study of cellular adhesion. *Micron*. 37 (1), 1-13
- Thomas, C. H., Collier, J. H., Sfeir, C. S. and Healy, K. E. (2002) Engineering gene expression and protein synthesis by modulation of nuclear shape. *Proceedings of the National Academy of Sciences*. 99 (4), 1972-1977
- Thoumine, O. and Ott, A. (1997) Time scale dependent viscoelastic and contractile regimes in fibroblasts probed by microplate manipulation. *J Cell Sci*. 110 (17), 2109-2116
- Thoumine, O., Ott, A., Cardoso, O. and Meister, J. J. (1999) Microplates: A new tool for manipulation and mechanical perturbation of individual cells. *J. Biochem. Bioph. Meth.* 39 (1-2), 47-62
- Turner, C. H., Owan, I. and Takano, Y. (1995) Mechanotransduction in bone: Role of strain rate. *American Journal of Physiology-Endocrinology And Metabolism*. 269 (3), E438-E442
- Vergani, L., Grattarola, M. and Nicolini, C. (2004) Modifications of chromatin structure and gene expression following induced alterations of cellular shape. *The international journal of biochemistry & cell biology*. 36 (8), 1447-1461
- Watanabe-Nakayama, T., Machida, S., Harada, I., Sekiguchi, H., Afrin, R. and Ikai, A. (2011) Direct detection of cellular adaptation to local cyclic stretching at the single cell level by atomic force microscopy. *Biophys. J.* 100 (3), 564-572
- Weafer, P. P., McGarry, J. P., van Es, M. H., Kilpatrick, J. I., Ronan, W., Nolan, D. R. and Jarvis, S. P. (2012) Stability enhancement of an atomic force microscope for long-term force measurement including cantilever modification for whole cell deformation. *Review of Scientific Instruments*. 83 (9), 093709

- Weafer, P. P., Ronan, W., Jarvis, S. P. and McGarry, J. P. (2013) Experimental and computational investigation of the role of stress fiber contractility in the resistance of osteoblasts to compression. *Bulletin of Mathematical Biology*. DOI: 10.1007/s11538-013-9812-y
- You, J., Yellowley, C., Donahue, H., Zhang, Y., Chen, Q. and Jacobs, C. (2000) Substrate deformation levels associated with routine physical activity are less stimulatory to bone cells relative to loading-induced oscillatory fluid flow. *Journal of Biomechanical Engineering*. 122 (4), 387
- You, L., Temiyasathit, S., Coyer, S., García, A. and Jacobs, C. (2008) Bone cells grown on micropatterned surfaces are more sensitive to fluid shear stress. *Cellular and Molecular Bioengineering*. 1 (2), 182-188
- Zepeda, S., Yeh, Y. and Orme, C. A. (2001) Atomic force microscope chamber for in situ studies of ice. *Rev. Sci. Instrum.* 72 (11), 4159-4163
- Zerwekh, J. E., Ruml, L. A., Gottschalk, F. and Pak, C. Y. C. (2009) The effects of twelve weeks of bed rest on bone histology, biochemical markers of bone turnover, and calcium homeostasis in eleven normal subjects. *Journal of Bone and Mineral Research*. 13 (10), 1594-1601
- Zimmer, C. C., Shi, L. F., Shih, Y. P., Li, J. R., Jin, L. W., Lo, S. H. and Liu, G. Y. (2012) F-actin reassembly during focal adhesion impacts single cell mechanics and nanoscale membrane structure. *Science China Chemistry*. 1-11